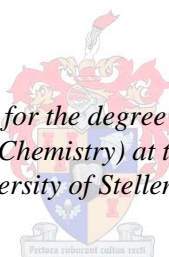


Photoelectrochemical detection of inorganic mercury in aqueous solutions

by
Jessica Chamier

*Dissertation presented for the degree of Doctor of Philosophy
(Chemistry) at the
University of Stellenbosch*



Promoter: Prof. Andrew M. Crouch
Co-promoter: Dr. Joy J. Leaner
Faculty of Science
Department of Chemistry and Polymer Science

December 2010

Declaration

By submitting this dissertation electronically, I declare that the entirety of the work contained therein is my own, original work, and that I have not previously in its entirety or in part submitted it for obtaining any qualification.

December 2010

Copyright © 2010 University of Stellenbosch

All rights reserved

Abstract

Due to the adverse human health effects associated with mercury (Hg) toxicity, an innovative method for inorganic mercury (Hg^{2+}) determination in aqueous solutions was investigated. The method of Hg^{2+} determination involved the use of a Hg^{2+} selective chemosensor immobilised onto an indium tin oxide (ITO) coated electrode in a photoelectrochemical cell. Upon light activation and in the presence of Hg^{2+} the fluorescent chemosensor absorbed a photon, and charge separation would occur according to the nature of the semiconductive material coated onto the ITO substrate. The charge separators and semiconductors investigated were an n-type carrier TiO_2 , polyaniline (PANI) and copolymers of polyaniline and 2-bromoaniline (P[A-co-2-BrA]s) with different monomer ratios.

The polymer and copolymer coated ITO working electrodes used in the Hg^{2+} sensitive photoelectrochemical cell were electrochemically evaluated. The results demonstrated that the ITO coated with PANI had superior conductive and semiconductive properties compared to ITO coated with P[A-co-2-BrA]s. The ITO glass substrates were coated with TiO_2 , PANI or P[A-co-2-BrA]s, followed by the fluorescent chemosensor, a rhodamine 6G derivative (RS). The electrodes were subsequently photoelectrochemically evaluated in a photoelectrochemical cell in the presence of Hg^{2+} . The PANI-RS coated electrode behaved as a photocathode in the presence of Hg^{2+} under illumination. The PANI-RS photoresponse increased with increasing Hg^{2+} concentration in the range 10 to 150 $\mu\text{g L}^{-1}$, with a limit of detection of 6 $\mu\text{g L}^{-1}$.

ITO coated with TiO_2 (ITO/ TiO_2) followed by a composite of PANI and RS had a linear photoanodic response in the Hg^{2+} concentration range of 10 to 200 $\mu\text{g L}^{-1}$ and a limit of detection of 5 $\mu\text{g L}^{-1}$. ITO and ITO/ TiO_2 coated with the P[A-co-2-BrA]s and RS had considerably lower photoresponses towards Hg^{2+} in aqueous solutions compared to PANI-RS. The photoresponses decreased with increasing 2-bromoaniline content.

The PANI and P[A-co-2-BrA]s coated ITO and ITO/ TiO_2 electrodes were then also coated with another rhodamine 6G derivative with a thiolactone moiety (RT). The PANI coated electrode yielded a photocathodic response in the Hg^{2+} concentration

range 0.2 to 5 $\mu\text{g L}^{-1}$. ITO coated with TiO_2 had no photoresponse towards Hg^{2+} due to repulsive forces between TiO_2 and the RT molecules.

The photoresponses of the working photoelectrodes towards Hg^{2+} were further evaluated in a custom photoelectrochemical Hg^{2+} detector. The photoresponses of PANI-RS and PANI-RT gave qualitative results for the presence of Hg^{2+} in aqueous solutions in concentrations as low as 2 $\mu\text{g L}^{-1}$.

Opsomming

Weens die negatiewe gesondheids aspekte toegeskryf aan Hg^{2+} vergiftiging is 'n nuwe innoverende metode van Hg^{2+} deteksie in wateroplossings ondersoek. Die voorgestelde metode van Hg^{2+} deteksie behels die gebruik van 'n Hg^{2+} selektiewe chemosensor geïmmobiliseer op ITO elektrodes in 'n fotoelektrochemiese sel.

Met lig aktivering en in die teenwoordigheid van Hg^{2+} , absorbeer die fluoreseerende chemosensor 'n foton, gevolg deur lading skeiding, soos bepaal deur die aard van die halfgeleidende material wat op die ITO plaatjies bedek is. Die halfgeleiers wat ondersoek was, was TiO_2 , PANI en ko-polimere van PANI met 2-bromoanilien.

Die polimeer en kopolimeer bedekte ITO werkende elektrodes wat in die Hg^{2+} sensitiewe fotoelektrochemiese sel gebruik is, is elektrochemies geëvalueer. Daaruit is gevind dat ITO bedek met PANI superieure geleier en halfgeleier eienskappe het in vergelyking met die ITO wat bedek is met P[A-co-2-BrA] kopolimere. Die ITO glas plaatjies is bedek met TiO_2 , PANI en die P[A-co-2-BrA] kopolimere gevolg deur die fluoreseerende chemosensor, RS. Die elektrodes is onderskeidelik fotoelektrochemies getoets in 'n fotoelektrochemiese sel in die teenwoordigheid van Hg^{2+} . Die PANI-RS elektrode het soos 'n fotokatode opgetree in die teenwoordigheid van Hg^{2+} onder beligting. Die foto-reaksie van die PANI-RS elektrode teenoor Hg^{2+} het liniêr toegeneem van 10 $\mu\text{g L}^{-1}$ tot 150 $\mu\text{g L}^{-1}$ met 'n limiet van deteksie op 6 $\mu\text{g L}^{-1}$.

ITO/ TiO_2 wat bedek is met 'n samestelling van PANI en RS het 'n fotoanodiese reaksie gehad teenoor Hg^{2+} in die liniêre reeks van 10 tot 200 $\mu\text{g L}^{-1}$ met 'n deteksie

limiet van $5 \mu\text{g L}^{-1}$. ITO en ITO/TiO₂ bedek met die P[A-co-2-BrA] kopolimere het heelwat laer fotoreaksies getoon teenoor Hg²⁺ in waterige oplossings Die fotoreaksie het afgeneem met toeneemende 2-bromoanilien inhoud van die kopolimeer.

Die PANI en P[A-co-2-BrA] kopolimere bedekte ITO en ITO/TiO₂ elektrodes is verder bedek met 'n tweede rhodamine 6G afgeleide, RT. Die ITO/PANI bedek met RT het weer 'n fotokatodiese reaksie gehad teenoor Hg²⁺ in die konsentrasie interval 0.2 tot $5 \mu\text{g L}^{-1}$. Die ITO/TiO₂ elektrode bedek met die PANI-RT samestelling het geen fotoreaksie gehad teenoor Hg²⁺ weens afstotende kragte tussen die TiO₂ and RT molekules.

Die fotoreaksies van die verskeie werkende elektrodes teenoor Hg²⁺ is verder getoets in 'n tuisgemaakte fotoelektrochemiese Hg²⁺ detektor. Die fotoreaksies van die PANI-RS en PANI-RT samestellings op ITO het kwalitatiewe resultate gelewer vir die teenwoordigheid van Hg²⁺ in waterige oplossings in konsentrasies tot so laag soos $2 \mu\text{g L}^{-1}$.

Acknowledgements

- ❖ I wish to express my sincere appreciation to my promoters Prof. A.M Crouch and Dr. J. J. Leaner for their assistance, guidance and encouragement throughout the project.

- ❖ I would like to acknowledge the financial assistance of the Council for Scientific and Industrial Research (CSIR) and the University of Stellenbosch.

- ❖ I would also like to thank my co-workers in the Natural Resources and the Environment group (NRE) at the CSIR, and Dr A. Buica from the analytical separations group (University of Stellenbosch) for their support and encouragement.

- ❖ To my husband, Andries, my friends and family, for your support and love that carried me when knowledge alone could not.

List of Abbreviations

A	Area (cm ²)
AA	Atomic absorption
C	Concentration
C _d	Capacitance of the double layer
CB	Conduction band
CHEF	Chelation enhancement of fluorescence
CHEQ	Chelation enhancement of quenching
CV	Cyclic Voltammetry
CVAAS	Cold vapour atomic absorption spectrometry
CVAFS	Cold vapour atomic fluorescence spectrometry
D	Diffusion coefficient (cm ² s ⁻¹)
DMA	Direct Mercury Analyzer
DMF	Dimethyl formamide
DMSO	Dimethyl sulfoxide
DSSC	Dye sensitised solar cell
E _g	Energy band gap
E _{1/2}	Mean of Electron reaction (Volt)
EDX	Energy dispersive X-ray analysis
EB	Emeraldine base
ES	Emeraldine salt
EtOH	Ethanol
eV	Electron volt
F	Faraday constant
FE	Fluorescent enhancement
FB	Flat-band potential
FTIR	Fourier Transform Infrared
GC	Gas chromatography
Hg	Mercury
Hg ²⁺	Inorganic mercury
h	Hours
HPLC	High-performance liquid chromatography

ITO	Indium tin oxide
ICP-AES	Inductively coupled plasma atomic emission spectrometry
ICP-MS	Inductively coupled plasma mass spectrometry
ICT	Internal charge transfer
ITO	Indium tin oxide
I	Current
I_p	Peak current
IAS	Integrated analytical system
K_a	Association constant
LEB	Leucoemeraldine base
LOD	Limit of detection
M	Molar (mol dm^{-3})
MeHg	Methylmercury
min	Minutes
MMHg	Dimethylmercury
n	Number of electrons involved in redox reaction
NMP	N-Methylpyrrolidone
PA-co-2-BrA	Polyaniline-co-2-bromoaniline
PANI	Polyaniline
P-2-BrA	Poly-2-bromoaniline
PEC	Photoelectrochemical cell
PEMD	Photoelectrochemical mercury detector
PEG	Polyethylene glycol
PNB	pernigraniline base
ppb	Parts per billion
ppt	Parts per trillion
PZC	Point of zero charge
R	Gas constant
R6G	Rhodamine 6G
Redox	Reduction and oxidation couple
RGHg	reactive gaseous Hg
RS	Rhodamine 6G hydrazone derivative chemosensor
rpm	revolutions per minute

RS-Hg ²⁺	Hg ²⁺ complexed RS
RT	Rhodamine 6G thioactone derivative
RT-Hg	Hg ²⁺ complexed RT
s	Seconds
SEM	Scanning electron microscopy
SHE	Standard hydrogen electrode
SRB	Sulphate reducing bacteria
T	Temperature
t	Time (seconds)
TTAB	Tetradecyltrimethylammonium bromide
US EPA	United States Environmental Protection Agency
v	scan rate (millivolts per second)
VB	Valence band
WHO	World Health Organization
XRS	X-Ray Emission Spectroscopy

Table of contents

Author's declaration	I
Abstract	II
Opsomming	III
Acknowledgements	V
List of abbreviations	VI
Table of contents	IX
List of figures	XV
List of tables	XXII

Chapter 1: Introduction and objectives

1.1 Problem statement.....	1
1.2 Objectives.....	1
1.3 Layout of the dissertation.....	2
1.4 Outputs of this dissertation	4
1.5 References.....	5

Chapter 2: Historical and theoretical background

2.1 Introduction.....	7
2.2 Mercury problem statement	
2.2.1 Mercury in the environment.....	8
2.2.2 Mercury in South Africa.....	10
2.2.3 The health risks of Hg in the environment.....	10
2.3 Current methods for determining mercury.....	11
2.4 The principle of photoelectrochemical detection.....	12
2.5 The fluorescence-based chemosensor.....	14
2.6 TiO ₂ as semiconductive material and charge separator	
2.6.1 Semiconductor electrochemistry.....	18
2.6.2 TiO ₂ , an n-type semiconductor.....	20
2.7 Polyaniline (PANI) and substituted polymers as hole conductors.....	23
2.8 References.....	27

4.5	References.....	64
-----	-----------------	----

Chapter 5: Electrochemical evaluation of composite TiO₂/ poly(aniline-co-2-bromoaniline) coated ITO electrodes

5.1	Introduction	
5.1.1	Polyaniline and 2-bromo substituted polyaniline (P[A-co-2-BrA]s)	67
5.1.2	Background for the electrochemical evaluation.....	68
5.2	Materials and methods	
5.2.1	Materials.....	72
5.2.2	Instrumentation.....	73
5.2.3	Synthesis of poly(aniline-co-2-bromoaniline) copolymers.....	73
5.2.4	Coating of ITO and ITO/TiO ₂	74
5.3	Results and discussion	
5.3.1	Copolymer characterization.....	75
5.3.2	Morphology studies of P[A-co-2-BrA]s.....	76
5.3.3	UV analysis of the ITO coated electrodes.....	78
5.3.4	Electrochemical evaluation of ITO/copolymer electrodes with a standard ferricyanide redox probe.....	81
5.3.5	Electrochemical evaluation of ITO/TiO ₂ /copolymer electrodes with the ferricyanide redox probe.....	84
5.3.6	Charge transfer coefficients, α	88
5.3.7	Diffusion coefficients of the ferricyanide redox probe for ITO/TiO ₂ /copolymer electrodes.....	89
5.4	Conclusions.....	90
5.5	References.....	91

Chapter 6: Photoelectrochemical determination of mercury (II) with an ITO/polyaniline-rhodamine derivative composite electrode

6.1	Introduction.....	95
6.2	Materials and methods	
6.2.1	Materials	97
6.2.2	Instrumentation.....	97

6.2.3 Procedure for electrode preparation.....	98
6.3 Results and discussion	
6.3.1 Surface morphology.....	98
6.3.2 Spectrophotometric properties of the RS-Hg ²⁺ complex with PANI....	100
6.3.3 Electrochemical evaluation of RS-Hg ²⁺ complex.....	102
6.3.4 Photoresponse of ITO/PANI-RS coated electrodes.....	103
6.3.5 Photoresponse of P[A-co-2-BrA] copolymers.....	108
6.4 Conclusions.....	109
6.5 References.....	110

Chapter 7: Photoelectrochemical determination of mercury (II) with a TiO₂/ polyaniline/rhodamine derivative composite electrode

7.1 Introduction.....	112
7.1.1 Phosphate doped TiO ₂	116
7.2 Materials and methods	
7.2.1 Materials.....	117
7.2.2 Instrumentation.....	117
7.2.3 Coating of electrodes.....	117
7.3 Results and discussion	
7.3.1 Electrode characterization.....	118
7.3.2 Spectrophotometric responses of RS with PANI and TiO ₂	119
7.3.3 Photoresponse of ITO/TiO ₂ /PANI-RS composite coated electrodes.....	122
7.3.4 Selectivity of the ITO/TiO ₂ /PANI-RS electrode	124
7.3.5 Hg ²⁺ evaluation with RS and TiO ₂ sol-gel in phosphate buffer.....	126
7.3.6 Photoelectrochemical evaluation of the ITO/TiO ₂ /P[A-co-2-BrA] electrodes.....	130
7.4 Conclusions.....	131
7.5 References.....	132

Chapter 8: Photoelectrochemical evaluation of an ITO/polyaniline-rhodamine 6G thiolactone composite electrode

8.1 Introduction.....	136
-----------------------	-----

8.2	Materials and methods	
8.2.1	Materials.....	138
8.2.2	Instrumentation.....	138
8.2.3	Coating of the electrodes.....	139
8.3	Results and discussion	
8.3.1	Characterization of PANI-RT composite electrode.....	139
8.3.2	Photo response of PANI-RT composite electrode.....	142
8.3.3	Photoelectrochemical evaluation of RT copolymer composites.....	145
8.4	Conclusions.....	146
8.5	References.....	146

Chapter 9: Prototype photoelectrochemical mercury detector

9.1	Introduction.....	148
9.2	Materials and methods	
9.2.1	Materials.....	148
9.2.2	Prototype design.....	149
9.2.3	Electrode evaluation with the photoelectrochemical mercury detector...	150
9.2.4	Sample collection and preparation.....	150
9.3	Results and discussion	
9.3.1	Electrode evaluation of PANI-RS and PANI-RT in the prototype photoelectrochemical mercury detector.....	151
9.3.2	Evaluation of environmental samples.....	152
9.4	Conclusions.....	154
9.5	References.....	155

Chapter 10: Conclusions and recommendations for future work

10.1	Conclusions	
10.1.1	The selection, synthesis and characterization of the chemosensor.....	156
10.1.2	Electrochemical evaluation of polyaniline and substituted polyaniline copolymers.....	156
10.1.3	Photoelectrochemical evaluation of ITO coated with PANI and P[A- <i>co</i> -2-BrA] copolymers in composite with RS.....	157

10.1.4 Photoelectrochemical evaluation of ITO/TiO ₂ coated with PANI and P[A- <i>co</i> -2-BrA] copolymers in composite with RS.....	158
10.1.5 Photoelectrochemical evaluation of ITO coated with PANI and P[A- <i>co</i> -2-BrA] copolymers in composite with RT.....	158
10.1.6 The prototype photoelectrochemical mercury detector.....	159
10.2 Scientific contributions.....	160
10.3 Recommendations for future work.....	160

List of Figures

Figure 1.1:	A schematic representation of the thesis layout.....	4
Figure 2.1:	A simplified model illustrating the global cycling of mercury.....	9
Figure 2.2:	An adaptation of the scheme suggested by Grätzel.....	13
Figure 2.3:	Schematic layout of A) a chemical sensor and B) the binding event of a chemosensor producing a complex with altered optical properties.....	16
Figure 2.4:	A) Electron energy diagram for the conductance and valence band and B) the electronic difference between a conductor, semiconductor and insulator.....	19
Figure 2.5:	The possible a) cathodic response (n-type semiconductor) and b) photoanodic (p-type semiconductor) of the working electrode in a PEMD.....	20
Figure 2.6:	The three crystal structures of TiO ₂ : anatase, rutile and brookite.....	20
Figure 2.7:	Schematic representation of competing processes at a TiO ₂ /electrolyte interface.....	22
Figure 2.8:	The oxidation forms of polyaniline.....	24
Figure 2.9:	The A) substituted aniline and B) aniline monomers that are added in different feed ratios to synthesize PANI-co-substituted PANI copolymers.....	25
Figure 3.1:	Spirolactam ring opening of the Hg ²⁺ selective rhodamine derivative.....	38
Figure 3.2:	The synthesis route for compound RS.....	40
Figure 3.3:	The synthesis route for compound RT.....	41
Figure 3.4:	¹ H NMR spectrum of RS.....	42
Figure 3.5:	¹³ C NMR spectrum of RS.....	43
Figure 3.6:	UV absorption and fluorescence emission of RS alone ((a) and (c)) and RS-Hg ²⁺ ((b) and (d)). The fluorescent emission is scaled 650:1 for comparison.....	44
Figure 3.7:	¹ H NMR spectrum of RT.....	45
Figure 3.8:	¹³ C NMR spectrum of RT.....	45

Figure 3.9: UV absorption of a) RT alone, b) RT-Hg ²⁺ and c) RT-Hg ²⁺ after 15 minutes. The fluorescent emission for d) RT-Hg ²⁺ is scaled 450:1 for comparison.....	46
Figure 4.1: The fate and transport of the excited electrons in rhodamine dyes after the absorption of a photon.....	50
Figure 4.2: A) The three oxidation states of PANI: (a) a fully reduced LEB; (b) a fully oxidised PNB, and (c) a half oxidised/half reduced EB state. B) The i) bipolaron and ii) polaron structures in EB polyaniline.....	52
Figure 4.3: A) The absorbance peaks of a) TiO ₂ -RS, b) TiO ₂ and RS-Hg ²⁺ and c) RSHg ²⁺ in 0.005 M phosphate buffer. B) The fluorescence emission of TiO ₂ a) with RS b) and with RS-Hg ²⁺ after excitation at 520 nm.....	55
Figure 4.4: A) The fluorescent quenching of RS-Hg ²⁺ by increasing the concentration of TiO ₂ . B) The Stern-Volmer plot for of quenched fluorescence intensity versus the addition of 0.03 M TiO ₂ in DMF.....	56
Figure 4.5: A) The absorption peaks of a) TiO ₂ -RS, b) TiO ₂ and RS-Hg ²⁺ and c) TiO ₂ -RS-Hg ²⁺ with additional RS-Hg ²⁺ in 0.005 M phosphate buffer. B) The emission intensity of TiO ₂ a) with RS and b) with RS-Hg ²⁺ in phosphate buffer after excitation at 520 nm.....	57
Figure 4.6: A) The absorption peaks of a) DMSO-PANI-RS, b) DMSO-PANI and RSHg ²⁺ and c) RS-Hg ²⁺ in 1:1 aqueous DMF. B) The fluorescence emission for DMSO-PANI a) with RS and b) with RS-Hg ²⁺ after excitation at 520 nm.....	58
Figure 4.7: A) The absorption peaks of a) NMP-PANI-RS, b) NMP-PANI and RS-Hg ²⁺ and c) RS-Hg ²⁺ in 1:1 aqueous DMF. B) The fluorescence emission for NMP-PANI a) with RS and b) with RS-Hg ²⁺ after excitation at 520 nm.....	59
Figure 4.8: A) Fluorescent quenching of RS-Hg ²⁺ with PANI-DMSO in 1:1 aqueous DMF. B) The Stern-Volmer plot for the addition of PANI-DMSO to RS-Hg ²⁺	59

Figure 4.9: A) The UV absorbance and B) fluorescence emission of 2.4×10^{-5} M RT 1:25 DMF a) with TiO_2 , b) with excess Hg^{2+} and c) added to TiO_2 after complexed with Hg^{2+}	60
Figure 4.10: A) The UV absorbance and B) fluorescent emission of 2.4×10^{-5} M RT 1:25 DMF:0.005 M phosphate buffer a) with TiO_2 , b) with excess Hg^{2+} and c) added to TiO_2 after complexed with Hg^{2+}	61
Figure 4.11: A) The UV absorbance of 2.4×10^{-5} M RT in 1:1 DMF: H_2O a) with PANI/NMP, b) Hg^{2+} and c) added to PANI/NMP after complexed with an excess Hg^{2+} . B) The fluorescent emission of RT in 1:1 DMF: H_2O a) with PANI/NMP, b) Hg^{2+} and c) added to PANI/NMP after complexed with an excess Hg^{2+}	62
Figure 4.12: A) The fluorescent quenching of RT-Hg with increasing PANI-DMSO. B) The Stern-Volmer plot for the quenched fluorescent intensities with increasing PANI concentration.....	63
Figure 5.1: FTIR spectra of the P[A-co-2-BrA] copolymers.....	76
Figure 5.2: SEM images of ITO/ TiO_2 coated with the various copolymers. a) Bare TiO_2 , b) P[A-co-2-BrA] 10, c) P[A-co-2-BrA] 25, d) P[A-co-2-BrA] 50, e) P[A-co-2-BrA] 70 and f) P-2-BrA.....	77
Figure 5.3: A) UV-vis spectrum of ITO/ TiO_2 coated with P[A-co-2-BrA] 10. B) UV-vis spectrum of P[A-co-2-BrA] 10 dissolved in DMF illustrating the absorption of P[A-co-2-BrA] 10 at 614 nm.....	79
Figure 5.4: Cyclic voltammograms of 10 mM $\text{K}_2\text{Fe}(\text{CN})_6$ on ITO electrodes coated with the various polymers; A) ITO alone , PANI and P-2-BrA and B) P[A-co-2-BrA] 10, P[A-co-2-BrA] 25, P[A-co-2-BrA] 50, P[A-co-2-BrA] 70, P-2-BrA measured at 100 mV s^{-1} at pH 7.5.....	82
Figure 5.5: Cyclic voltammograms of 10 mM $\text{K}_2\text{Fe}(\text{CN})_6$ on ITO electrodes coated with the various polymers; A) ITO alone , PANI and P-2-BrA and B) P[A-co-2-BrA] 10, P[A-co-2-BrA] 25, P[A-co-2-BrA] 50, P[A-co-2-BrA] 70, P-2-BrA measured at 100 mV s^{-1} at pH 3.5.....	82
Figure 5.6: A) ΔE_p , and, (B) $E_{1/2}$ values for the $\text{Fe}(\text{CN})_6^{3-/4-}$ redox peaks on the various ITO/polymer electrodes at pH 3.5, ●, and pH 7.5, ▲.	83
Figure 5.7: Cyclic voltammograms of 10 mM $\text{K}_2\text{Fe}(\text{CN})_6$ on ITO/ TiO_2 electrode coated with the various polymers A) ITO, ITO/ TiO_2 , P-2-BrA and B) P[A-co-2-BrA] 10, P[A-co-2-BrA] 25, P[A-co-2-BrA] 50, P[A-	

- co-2-BrA] 70 and P-2-BrA measured at 100 mV s^{-1} in the presence of $10 \text{ mM K}_2\text{Fe(CN)}_6$ at pH 7.5..... 86
- Figure 5.8:** Cyclic voltammograms of $10 \text{ mM K}_2\text{Fe(CN)}_6$ on ITO/TiO₂ electrode coated with the various polymers A) ITO, ITO/TiO₂, P-2-BrA and PANI, and B) P[A-co-2-BrA] 10, P[A-co-2-BrA] 25, P[A-co-2-BrA] 50, P[A-co-2-BrA] 70 and P-2-BrA measured at 100 mV s^{-1} in the presence of $10 \text{ mM K}_2\text{Fe(CN)}_6$ at pH 3.5..... 86
- Figure 5.9:** $E_{1/2}$ and ΔE_p for the redox couple on the various ITO/TiO₂/ P[A-co-2-BrA] electrodes at pH 7.5 and pH 3.5 measured at 1 mV s^{-1} 87
- Figure 5.10:** The $\sqrt{\text{scan rate}}$ dependence of the ferricyanide oxidation peak current density measured at A) pH 7.5, 0.05 M KNO_3 and B) pH 3.5, H_2SO_487
- Figure 5.11:** A) A typical Tafel plot measured at 1 mV s^{-1} used to determine α values for the oxidation and reduction of the ferricyanide couple on TiO₂/ P[A-co-2-BrA] 70 at pH 7.5. B) α values for the TiO₂/P[A-co-2-BrA] copolymers determined at pH 3.5 and pH 7.5: ■—■ α_r at pH 7.5, ●—● α_o at pH 7.5, ■---■ α_r at pH 3.5 and ●---● α_o at pH 3.5..... 89
- Figure 5.12:** A) Oxidation chronoamperograms measured in 0.05 M KNO_3 and $10 \text{ mM K}_3\text{Fe(CN)}_6$ for ITO/TiO₂ electrodes coated with the various copolymers used to determine diffusion coefficients at pH 3.5 and pH 7.5. B): — (D_r) at pH 7.5, — (D_o) at pH 7.5, ■---■ (D_r) at pH 3.5 and ●---● (D_o) at pH 3.5. 90
- Figure 6.1:** SEM images of the PANI-RS dye composite on the ITO surface: A) magnification $\times 100$ and B) magnification $\times 500$99
- Figure 6.2:** Surface profile of the ITO electrode coated with $40 \mu\text{L}$ of PANI-RS composite..... 100
- Figure 6.3:** Photoresponse for the PANI-RS composite measured for various applied potential in $0.1 \text{ mM K}_3\text{Fe(CN)}_6$ 0.05 M KNO_3 to determine the FB..... 101
- Figure 6.4:** Proposed energy diagram for the photoelectrochemical Hg^{2+} detector.....102
- Figure 6.5:** Cyclic voltammograms measured for an ITO electrode at 100 mV s^{-1} in 0.05 M phosphate buffer pH 7.5: A) with buffer alone, B) in the

	presence of 1 mM RS without 100 $\mu\text{g L}^{-1}$ HgCl_2 and C) with 100 $\mu\text{g L}^{-1}$ HgCl_2	103
Figure 6.6:	Photoresponse for an ITO/PANI-RS electrode measured at various Hg^{2+} concentrations in 0.05 M KNO_3	104
Figure 6.7:	The photovoltage response of the ITO/PANI-RS electrode in 100 $\mu\text{g L}^{-1}$ Hg^{2+} under constant illumination, highlighting the decay to an intermediate level.....	105
Figure 6.8:	pH evaluation of the ITO/PANI-RS electrode saturated with 10 $\mu\text{g L}^{-1}$ HgCl_2 measured in 0.01 M phosphate buffer.....	106
Figure 6.9:	The photoresponse of the ITO/PANI-RS sensor in the presence of 500 $\mu\text{g L}^{-1}$ potential interfering ions.....	107
Figure 6.10:	A) The photoresponses of P[A-co-2-BrA] copolymers in composite with RS and PANI-RS towards increasing Hg^{2+} concentration in 0.05 M KNO_3 . B) The photoresponse of the P[A-co-2-BrA] composite copolymers measured up to 10 $\mu\text{g L}^{-1}$ Hg^{2+}	109
Figure 7.1:	The surface functional groups of TiO_2 , depending on pH.....	114
Figure 7.2:	SEM images of the ITO/ TiO_2 electrode surface coated with PANI-RS: A) magnification $\times 58$ and B) magnification $\times 2000$	118
Figure 7.3:	Proposed energy diagram for the photoelectrochemical detection of Hg^{2+} with an ITO/ TiO_2 /PANI-RS composite electrode.....	119
Figure 7.4:	The absorbance A) and emission spectra (excitation 520 nm) B) of 0.04 mM TiO_2 with a) RS, b) RS- Hg^{2+} and c) of RS- Hg^{2+} alone in 1:1 aqueous DMF. The absorbance C) and emission spectra (excitation 530 nm) D) of 0.25 g L^{-1} PANI with a) RS, b) RS- Hg^{2+} and c) of RS- Hg^{2+} alone in 1:1 aqueous DMF.....	121
Figure 7.5:	The photoresponse measured for an ITO/ TiO_2 /PANI-RS electrode for (a) short (± 2 s) light pulses for various Hg^{2+} concentrations and 0.05 M KNO_3 . (b) The photoresponse of an ITO/ TiO_2 /PANI-RS electrode for short pulses followed by continuous illumination in 1 $\mu\text{g L}^{-1}$ of added Hg^{2+}	122
Figure 7.6:	The photoresponse of an ITO/ TiO_2 /PANI-RS electrode measured at various Hg^{2+} concentrations in 0.05 M KNO_3	123

Figure 7.7: Photoresponse of the ITO/TiO ₂ /PANI-RS electrode in the presence of interfering ions in 0.05 M KNO ₃ with ■) and without □) 20 µg L ⁻¹ HgCl ₂	124
Figure 7.8: pH dependence of the ITO/TiO ₂ /PANI/RS electrode in A) 0.01 M phosphate buffer alone and B) 0.01 M phosphate and 10 µg L ⁻¹ Hg ²⁺	125
Figure 7.9: UV-vis spectra of A) RS in TiO ₂ /phosphate in various concentration of phosphate buffered at pH 6.5, B) RS in TiO ₂ /phosphate with the addition of excess Hg ²⁺	127
Figure 7.10: The fluorescent emission spectra for A) TiO ₂ in phosphate buffer with increasing RS and B) TiO ₂ and RS in phosphate buffer at pH 6.5 with increasing Hg ²⁺	127
Figure 7.11: UV absorbance of a) TiO ₂ and RS, b) TiO ₂ , RS and Hg ²⁺ and c) RS-Hg ²⁺ in 0.005 M phosphate buffer.....	128
Figure 7.12: UV absorbance spectra of TiO ₂ in phosphate buffer with 0.0015 M RS-Hg ²⁺ measured for pH 4 to pH 8.....	129
Figure 7.13: Photoresponses of the ITO/TiO ₂ coated with P[A-co-2-BrA]s and RS measured for 0.2 µg L ⁻¹ Hg ²⁺ and 0.05 M KNO ₃	130
Figure 7.14: Photoresponses of ITO/TiO ₂ coated with P[A-co-2-BrA]s and PANI in 10 µg L ⁻¹ Hg ²⁺ and 0.05 M KNO ₃	130
Figure 8.1: 3D images of A) RT and B) RS chemosensors in their 1) unbound and 2) ligated form with Hg ²⁺	138
Figure 8.2: SEM images of the PANI-RT electrode: A) magnification × 500 and B) magnification × 2000. SEM images of PANI-RT electrode after Hg ²⁺ evaluation: C) magnification × 500 and D) magnification × 2000.....	140
Figure 8.3: Surface profiles of A) PANI-RT composite coated onto ITO and B) a used ITO/PANI-RT electrode.....	140
Figure 8.4: Cyclic voltammograms for ITO electrode in TTAB/DMF with A) 1 mM RT and B) RT-Hg ²⁺	141
Figure 8.5: Photovoltammetric responses of ITO coated with the PANI-RT composite in 0.05 M KNO ₃ and 0.2 to 5 µg L ⁻¹ Hg ²⁺	142
Figure 8.6: The photoresponses of ITO coated with a PANI-RT composite.....	143

Figure 8.7: The photoresponses of PANI-RT on ITO measured at various pHs in 0.005 M phosphate buffer in A) the absence of Hg^{2+} and B) in $10 \mu\text{g L}^{-1} \text{Hg}^{2+}$	144
Figure 8.8: The photoresponse of ITO/PANI-RT in 1 mg L^{-1} background ions and $10 \mu\text{g.L}^{-1} \text{Hg}^{2+}$	145
Figure 8.9: The A) photoresponses of the P[A-co-2-BrA] copolymers in 0.05 M KNO_3 and increasing Hg^{2+} concentration [Hg^{2+}]. B) The photoresponse of the P[A-co-2-BrA] copolymers towards $10 \mu\text{g L}^{-1} \text{Hg}^{2+}$	146
Figure 9.1: The electronic circuit board design of the PEMD.....	149
Figure 9.2: The PEMD prototype.....	150

List of Tables

Table 5.1:	The bromine content of PANI and the P[A-co-2-BrA] copolymers.....	75
Table 5.2:	Film thickness, nm, for the various ITO/TiO ₂ /copolymer coated electrodes.....	78
Table 5.3:	Energy band-gap energies calculated for the various absorptions of P[A-co-2-BrA] in DMF and coated on the ITO/TiO ₂ surfaces.....	79
Table 5.4:	Wavelengths (nm) at which the electrodes start to absorb in the UV region.....	80
Table 9.1:	The voltage responses of the PANI-RS coated ITO electrodes towards Hg ²⁺ samples in the custom PEMD prototype.....	151
Table 9.2:	The voltage responses of the PANI-RT coated ITO electrodes towards Hg ²⁺ samples in the custom PEMD prototype.....	151
Table 9.3:	The pH and conductivity values for the collected environmental samples.....	152
Table 9.4:	The photovoltage responses of the PANI-RS and PANI-RT electrodes in the PEMD toward environmental samples compared to the Hg ²⁺ concentrations determined by DMA.....	153
Table 9.5:	The photovoltage responses of the PANI-RS and PANI-RT electrodes in the PEMD toward environmental samples with 2 µg.L ⁻¹ additional Hg ²⁺ compared to the Hg ²⁺ concentration determined with DMA.....	154

Chapter 1

Introduction and objectives

1.1 Problem statement

Mercury (Hg) is a global pollutant that occurs both naturally and anthropogenically in the environment with the latter source currently exceeding inputs from the former [1]. Mercury salts are characterised by extreme toxicity, altering the biological activity of important constituents of living cells, such as proteins and nucleic acids [2]. Methylmercury, one of the most toxic forms of Hg, bioaccumulates up the aquatic food chain, and is the primary source of Hg exposure to humans, generally through the consumption of fish and seafood products [3, 4]. The exposure limit for inorganic Hg (Hg^{2+}) in drinking water is set at 2 ppb ($2 \mu\text{g L}^{-1}$) by the United States Environmental Protection Agency (US EPA).

Due to its toxicity, environmental monitoring of Hg^{2+} at low detection limits, with accuracy and high precision, is needed. Many high performance and sensitive detection methods, based on sophisticated and expensive instrumentation, are currently used for Hg^{2+} detection [4-9]. These methods, however, have various shortcomings such as high cost and lack of mobility. New, inexpensive Hg^{2+} detection methodologies or tools for use in aqueous solutions and biological samples are important when quick and reliable techniques for Hg^{2+} determination are sought.

Recently great strides have been made in the development and applications of sensors, especially chemical sensors, for metal ion detection [10-14]. Innovative and creative designs for single molecule chemical sensors, known as chemosensors, have been made and synthesised by the organic chemistry community. In this study the use of such detection tools as an alternative method for determining aqueous Hg^{2+} is investigated.

1.2. Objectives

The overall objective of this study was to develop an inexpensive, quick and reliable method that utilises chemosensors for the on-site determination of Hg^{2+} in aqueous solutions. Fluorescent chemosensors were used as the detection device in existing photoelectrochemical technology, and were used to design a portable

photoelectrochemical cell (PEC) that is capable of detecting Hg^{2+} in aqueous solutions, at the $2 \mu\text{g L}^{-1}$ level.

In order to achieve the objective of this study, a suitable Hg^{2+} selective fluorescent chemosensor was identified and synthesised, followed by the design and construction of the PEC. The design and construction of the PEC involved the combination of the fluorescent chemosensor with suitable charge separators, and immobilization onto an indium tin oxide (ITO) electrode.

To achieve the above-mentioned goals, the following tasks were identified:

- A literature review of existing fluorescent chemosensors that are currently used for Hg^{2+} determination
- The synthesis and characterization of the chemosensor.
- Immobilization of the chemosensor with polyaniline (PANI), a well published conductive polymer and charge separator, onto ITO
- The characterization and photoelectrochemical evaluation of ITO coated with PANI and the selected chemosensor toward Hg^{2+} in aqueous solution
- Photoelectrochemical evaluation of composites of the chemosensor with other substituted PANI semi-conductive materials to optimise charge separation
- Immobilization of the chemosensor in composite with PANI onto titanium dioxide (TiO_2) coated ITO
- The characterization and photoelectrochemical evaluation of the ITO/ TiO_2 electrode coated with the PANI and chemosensor composite toward Hg^{2+} in aqueous solution
- The synthesis and characterization of a second chemosensor, and its evaluation using a similar approach to that used for first chemosensor
- Design and construction of a portable PEC, with an optimized working electrode
- Evaluation of the prototype photoelectrochemical mercury detector (PEMD).

1.3 Layout of the dissertation

Because Hg in aquatic ecosystems poses a human health risk, reliable and quick methods are needed to detect Hg^{2+} in aqueous solutions. Results of the study should provide a reliable and quick alternative to the current methods used for determining Hg^{2+} in aqueous solutions.

The layout of this document is as follows

Chapter 2 presents a background to Hg in the environment, fluorescent chemosensors, photoelectrochemical cells and charge separators.

Chapter 3 provides a synopsis of the synthetic procedure used to prepare the selected chemosensors and their characterization.

Chapter 4 provides a description of the spectrophotometric influences of TiO_2 and PANI on the fluorescent chemosensors.

PANI is generally the most favoured hole conductor to be used in PECs, but due to its low processability and pH dependence, o-bromo substituted polyaniline copolymers were used. Chapter 5 describes their electrochemical evaluation, and comparison to PANI.

The coated ITO working electrodes were characterised and photoelectrochemically evaluated as described in Chapters 6 and 7, respectively. The first fluorescent chemosensor, a rhodamine 6G hydrazone derivative (RS), was then replaced by another chemosensor, a rhodamine 6G thiolactone (RT), and the influence of the chemosensor structure on the photovoltage response was determined as described in Chapter 8.

The devised photoelectrochemical detection method was then transferred to the prototype PEMD. Details of the design, construction and photoelectrochemical responses of this PEMD are given in Chapter 9. Chapter 10 comprises a short summary of all observations and conclusions to the study. A schematic representation of the layout of this dissertation is given in Figure 1.1.

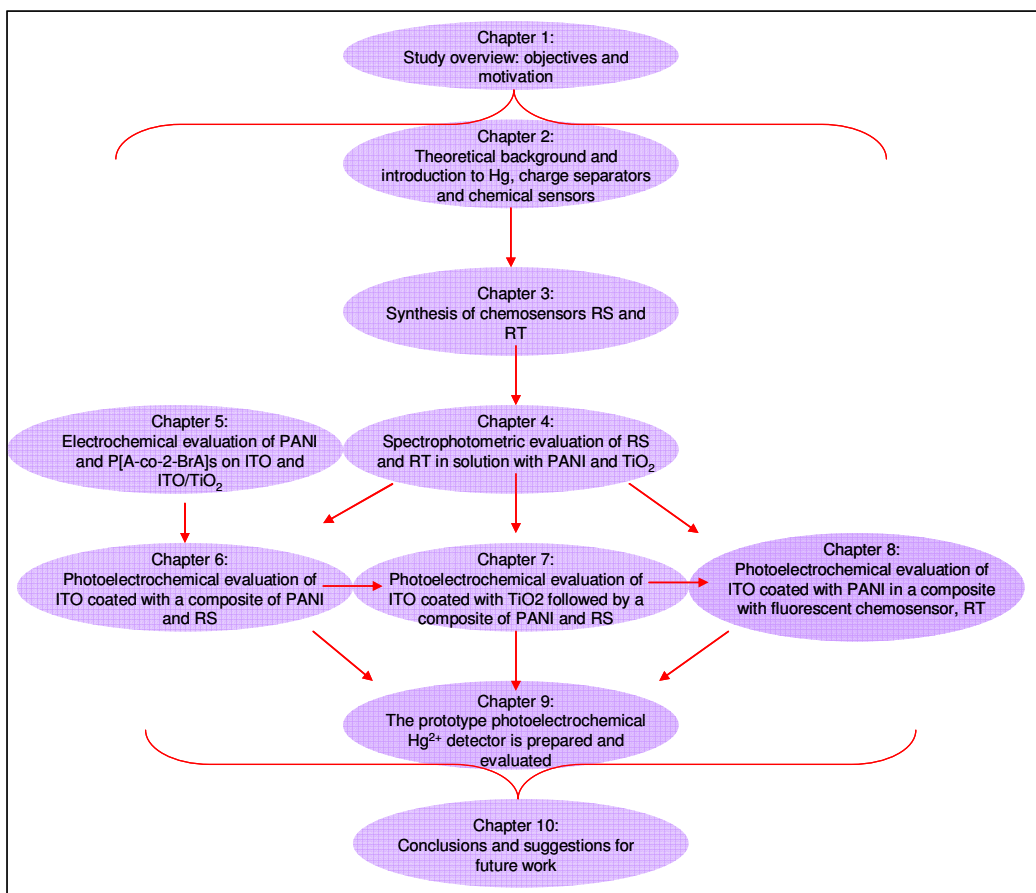


Figure 1.1: Schematic representation of the layout of this dissertation.

1.4 Outputs of this dissertation

1.4.1 Papers for publication

- I) *Photoelectrochemical determination of inorganic mercury in aqueous solutions*, by J. Chamier, J. J. Leaner and A. M. Crouch. *Analytica Chimica Acta* 661 (2010) 91 - 96.
- II) *Photo-electrochemical determination of mercury (II) with a TiO₂/ polyaniline/Rhodamine derivative composite electrode*, by J. Chamier and A. M. Crouch. Submitted to *Sensors and Actuators B: Chemical*.
- III) *Photoelectrochemical detection of Hg²⁺ with thiolactone bearing rhodamine 6G derivative*, by J. Chamier, J. J. Leaner and A. M. Crouch, To be submitted to *Electrochimica Acta*.
- IV) *Electrochemical and photoelectrochemical evaluation of polyaniline/2-*

bromo polyaniline copolymers, by J. Chamier, A. M. Crouch and G. Summers. To be submitted to Journal of Electroanalytical Chemistry.

1.4.2 Contributions to conferences

- I) Kinetics in Analytical Chemistry (KIC). *Electron kinetics in the photoelectrochemical detection of inorganic mercury*. Poster presentation. Cape Town, South Africa, 2-4 December 2009
- II) Southern and Eastern African Network of Analytical Chemists (SEANAC). *Photo-electrochemical determination of mercury (II) in aqueous solutions using immobilized rhodamine 6G derivative/polyaniline composite on TiO₂*. Oral presentation. Swaziland, 5-8 July 2009.
- III) 9th International Conference on Mercury as a Global Pollutant. *Photo-electrochemical determination of inorganic mercury in aqueous solutions*. Poster presentation. Quiyang, China, 7-12 June 2009.
- IV) South African Chemical Institute (SACI). *Photo-electrochemical determination of mercury (II) in aqueous solutions*. Poster Presentation. Stellenbosch, South Africa, 30 November – 5 December 2008.
- V) International Society of Electrochemistry (ISE) annual meeting. *Immobilized fluorescent chemosensor on TiO₂ for on-site determination of mercury (II) in aqueous solutions*. Oral Presentation. Seville, Spain, 5-11 September 2008.
- VI) ElectrochemSA. *Electrochemical evaluation of substituted polyaniline copolymers on ITO/TiO₂ surfaces*. Cape Town, South Africa, Oral presentation. 21-23 July 2007.

1.5 References

- [1] M.F. Wolfe, S. Schwarzbach, R.A. Sulaiman, Environ. Toxicol. Chem., 17 (1998) 146-160.
- [2] D.C. Rice, Environ. Res., 95 (2004) 406-413.
- [3] R. Dietz, F. Riget, M. Cleemann, A. Aarkrog, P. Johansen, J.C. Hansen, Sci. Total Environ., 245 (2000) 221-231.

- [4] M.V.B. Krishna, M. Ranjit, D. Karunasagar, J. Arunachalam, *Talanta*, 67 (2005) 70-80.
- [5] H. Morita, H. Tanaka, S. Shimomura, *Spectrochim. Acta Part B: At. Spectrosc.*, 50 (1995) 69-84.
- [6] N. Daskalova, I. Boevski, *Spectrochim. Acta. Part B: At. Spectrosc.*, 54 (1999) 1099-1122.
- [7] S.Y. Ly, S.K. Kim, T.H. Kim, Y.S. Jung, S.M. Lee, *J. Appl. Electrochem.*, 35 (2005) 567-571.
- [8] J. Qvarnstrom, L. Lambertsson, S. Havarinasab, P. Hultman, W. Frech, *Anal. Chem.*, 75 (2003) 4120-4124.
- [9] L. Jian, W. Goessler, K.J. Irgolic, *Fresenius J. Anal. Chem.*, 366 (2000) 48-53.
- [10] R.W. Cattrall, *Chemical Sensors*, Oxford University Press, Oxford, U.K., 1997, p. 2-29.
- [11] B.R. Eggins, *Chemical sensors and biosensors*, John Wiley & Sons Ltd, Chichester, England, 2002, p. 1-34.
- [12] Y.Q. Weng, Y.L. Teng, F. Yue, Y.R. Zhong, B.H. Ye, *Inorg. Chem. Commun.*, 10 (2007) 443-446.
- [13] J.S. Wu, I.C. Hwang, K.S. Kim, J.S. Kim, *Org. Lett.*, 9 (2007) 907-910.
- [14] Z. Xu, G.H. Kim, S.J. Han, M.J. Jou, C. Lee, I. Shin, J. Yoon, *Tetrahedron*, 65 (2009) 2307-2312.

Chapter 2: Historical and theoretical background

2.1 Introduction

Mercury (Hg) is a widespread and highly toxic pollutant. Although industrial use of Hg has been reduced and its use is limited by legislation, Hg contamination still occurs due to its release from natural and anthropogenic sources. These sources include oceanic and volcanic emissions, fossil fuel combustion and solid waste incineration [1].

In an aqueous environment inorganic Hg (Hg^{2+}) may be converted by sulphate reducing bacteria to methylmercury (MeHg) [2]. MeHg is known to bioaccumulate and biomagnify up the aquatic food chain, with fish at the top of the food chain containing higher MeHg concentrations than those found at the bottom end of the food chain [3]. When ingested, MeHg targets the advanced central nervous system, and causes severe lesions at the nerve centres of humans. As a result, MeHg toxicity in organisms, including humans, is symptomised by serious sensory, motor and cognitive disorders [4].

The above-mentioned human health risks have led to the need for analytical methods that are sensitive and selective to determine Hg^{2+} in aqueous solutions. Commonly used methods for Hg^{2+} determination such as Cold Vapour Atomic Fluorescence Spectrometry (CVAFS) [3, 5] and Inductively Coupled Plasma Atomic Emission Spectrometry (ICP-AES) [6] have been proven to be sensitive and accurate. These techniques, however, require tedious sample pre-treatment, sophisticated performance and expensive equipment, and are not suited for on-site screening or on-line Hg^{2+} analysis.

A simple method for the sensitive and selective determination of Hg^{2+} in aqueous environments is proposed. In this study, a Hg^{2+} selective chromophore was immobilised onto an ITO-working electrode, in a photoelectrochemical cell (PEC). A prototype photoelectrochemical mercury detector (PEMD) was constructed and investigated as a possible inexpensive tool for on-site pre-screening of Hg^{2+} in water.

2.2 Mercury problem statement

2.2.1 Mercury in the environment

Mercury has a higher electron affinity than all other transition metals. The different Hg forms in the environment include elemental Hg^0 , inorganic Hg(I) and Hg(II) [Hg^{2+}] and organic Hg(II). Hg^{2+} is generally ligated to counterions such as S^{2-} , Cl^- , OH^- , NO_3^- , while organic Hg(II) is ligated to methylgroups and other dissolved organic matter [7].

Three types of Hg are identified in the atmosphere based on their physical and chemical properties: gaseous Hg^0 , gaseous ionic divalent Hg (reactive gaseous Hg or RGHg) and particulate Hg. Speciation of RGHg is unknown, but is assumed to be gaseous HgCl_2 or other mercuric halides. Hg^0 and inorganic Hg^{2+} enter the atmosphere through anthropogenic processes such as mining, coal combustion for power generation, chloralkali production, degassing mineral deposits, waste incineration, urban discharges, and pesticides [8]. Anthropogenic Hg emissions account for ca. 70% of the 5,500 metric tons of Hg that are released to the earth's atmosphere each year [9].

Hg is released into the environment in various forms which form part of a global Hg cycle shown as a simplified model in Figure 2.1. With a lifetime of hours to days, RGHg is rapidly removed from the atmosphere, whereas less reactive Hg^0 has a residence time of up to a year. RGHg has high surface reactivity and water solubility (compared to Hg^0) [10]. Hg^0 is oxidised to ionic Hg^{2+} by halogen radical (much the same at ozone depletion mechanisms) and is subsequently deposited [11]. Dissolved Hg^{2+} species can be reduced to Hg^0 in surface waters. If the waters become saturated with Hg^0 , then a substantial fraction is returned to the atmosphere via evaporation [12]. The final step in the global Hg cycle, involving the bioaccumulation of MeHg in larger fish, results in the largest source of exposure of humans to Hg.

In aquatic environments Hg^{2+} is methylated to MeHg by sulphate reducing bacteria (SRB) under anaerobic conditions, in the presence of high molecular mass fulvic and humic acids [2]. The extent of methylation is, however, determined by the bioavailability of Hg^{2+} to the SRB, the activity of the bacteria,

pH, dissolved oxygen, redox activity, the presence of electron donors (e.g. organic carbon) and electron acceptors (Fe^{3+} , SO_4^{2-} , NO_3^-), temperature and the composition of the water/soil source. Methylation rates are however not dependant on Hg^{2+} concentrations [7]. Although the actual mechanism by which bioavailable Hg^{2+} is formed, as well as its fate and transport in the environment is still being widely investigated [12, 13].

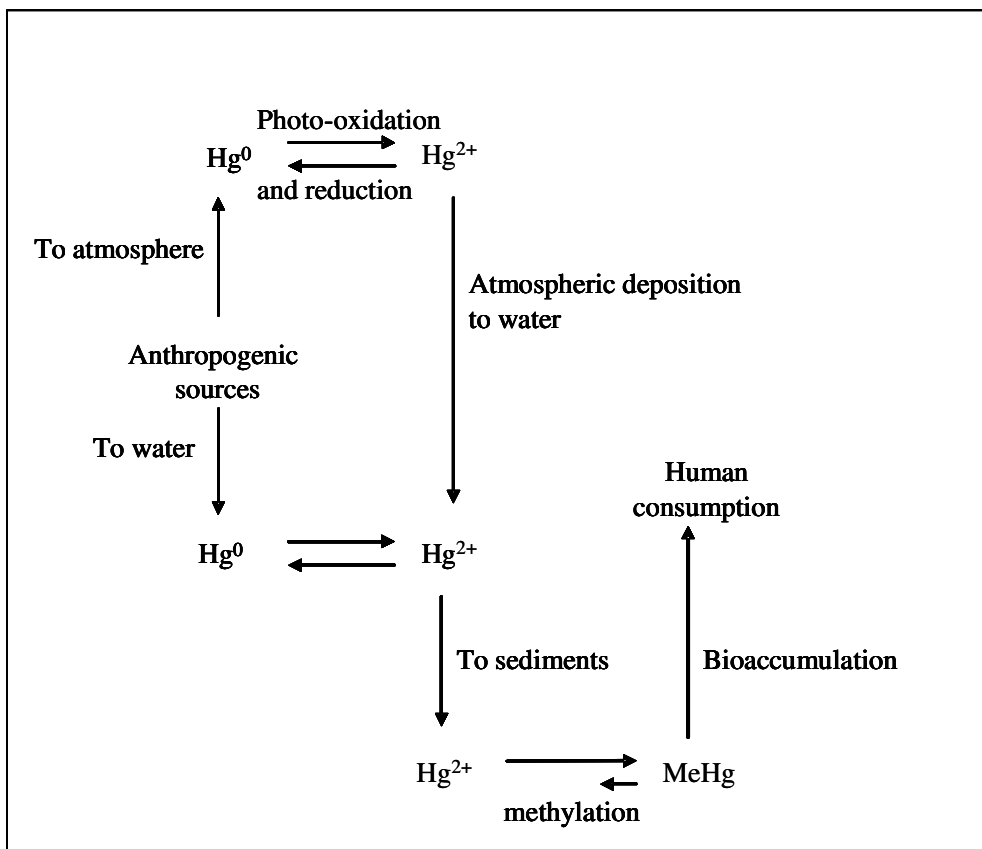


Figure 2.1: A simplified model illustrating the global cycling of mercury [13].

2.2.2 Mercury in South Africa

South Africa was previously regarded as the country with the second highest Hg emissions in the world [14]. This has caused much concern and has resulted in much research being undertaken on Hg sources and impacts in the country. As the most common source of Hg is cinnabar (HgS), which is found in coal and hydrocarbons, the assumption of South Africa's Hg footprint was based on estimates of the total Hg emissions derived primarily from gold mining and coal combustion. More than 112.3 Mt y^{-1} of coal, with an estimated Hg content of 0.2

mg kg⁻¹, is burned in all South African power plants per year to supply more than 90% of South Africa's energy needs. The estimated average emission of Hg from South Africa's coal-fired power plants is estimated at 9.8 t y⁻¹. South African power plants are designed to burn low-grade coal [15] with no prior coal washing and with limited emission control devices. Currently all large-scale extraction of gold in South Africa relies on a cyanidation leaching process [16] and other adsorption processes and any Hg emissions from gold processing facilities are significantly less compared to emissions from coal combustion.

2.2.3 The health risks of Hg in the environment

Although all forms of Hg are poisonous, the ecological and human health effects of Hg are generally related to the environmentally transformed Hg²⁺, the toxic and biomagnification-prone, MeHg and dimethylmercury (MMHg) [17, 18]. These methylated Hg forms bioaccumulate and biomagnify in the marine food chain, and generally reach high concentrations in predatory fish such as swordfish, tuna, king mackerel, and shark [19-22]. Consumption of Hg-contaminated fish has been reported to be the major route of human exposure to MeHg and MMHg.

Hg salts are characterised by extreme toxicity (nephrotoxicity, neurotoxicity), which alters the biological activity of important constituents of cells, such as proteins and nucleic acids [23]. MeHg derivatives target the advanced central nervous system by passing through the blood brain barrier, causing severe lesions of the nervous system [24]. Symptoms of MeHg poisoning include distal sensory disturbances, constriction of visual fields, ataxia, dysarthria, auditory disturbances, and tremors. Infants with Hg poisoning show symptoms such as mental retardation, cerebellar ataxia, primitive reflexes, dysarthria, and hyperkinesias [25]. Studies have also shown that MeHg affects the sex ratio of offspring at birth and causes stillbirth. Male foetuses are more susceptible to MeHg poisoning in utero, which could therefore possibly explain the altered sex ratio [26]. Recent studies have also suggested that MeHg exposure results in an elevated risk of cardiovascular disease [27]. Furthermore, Hg²⁺ has been shown to suppress immune functions and to induce autoimmunity in many animal species [28]. Although the symptoms and health effects of Hg-related exposure is well known [29], many uncertainties in terms of the risk assessment exist.

2.3 Current methods for determining mercury

Current Hg analyses are commonly performed by a hyphenated system consisting of a chromatographic separation and a highly sensitive spectrometric detection. The most popular chromatographic separation of mercury species includes gas chromatography (GC) [30] and high-performance liquid chromatography (HPLC) [31-34]. Coupled techniques include CVAFS [35, 36], cold-vapour atomic absorption spectrometry [3, 37] and inductively coupled plasma-mass spectrometry (ICP-MS) [30, 38, 39]. The CVAFS method is more sensitive and more selective, and has a wider range of linear response to the concentration of Hg^{2+} than that of conventional atomic absorption and is therefore the most commonly preferred detection technique [35, 40, 41]. Other conventional methods for detecting Hg^{2+} include the use of enzyme-based biosensors [42], fiber optic probes, optical sensors [43, 44] and stripping electrochemistry [45].

Although the above-mentioned methods have been proven to be selective and accurate, several drawbacks need to be considered. For example, most chromatographic techniques require relatively large sample volumes for analysis, as well as tedious sample preparation [46, 47]. As there is a time lapse between sample collection and analysis, these techniques are not suitable for on-line monitoring. Therefore rapid measurements of trace Hg concentrations are challenging. Environmental water samples generally contain Hg^{2+} concentrations of 0.1 to 100 ng L^{-1} , therefore rendering the need for preconcentration of samples when Hg^{2+} is to be monitored. For example, when using CVAFS, Hg is preconcentrated onto gold traps, and released into expensive argon feedgas, after which it is collected for detection and quantification.

The detection of Hg in solutions using anodic stripping voltammetry has been reported, using several different electrodes, including glassy carbon and gold electrodes [48, 49]. Although electrochemical techniques are simpler to use and more suitable for on-line analysis, the reproduction of reliable results poses a challenge. Electrode preparation techniques such as polishing, chemical modification or electrode pretreatment consistently change the electrode surfaces. The reproducibility is further influenced by the formation of calomel (Hg_2Cl_2) on

the electrode surface during anodic stripping, which is highly insoluble and obstructs further detection.

The detection of Hg using innovative and inexpensive methodologies for use in aqueous solutions and biological samples is an important goal. It has been established that fluorescence is a suitable optical method for monitoring low levels of heavy metal ions due to its sensitive, simple and rapid responses [50, 51]. Here the sensitivity of fluorescence is combined with the selectivity of small chemical sensors to develop an inexpensive simple method for on-site Hg^{2+} determination. The Hg-selective optical sensor is immobilised in a closed electrochemical cell in which photon excitation is converted into an electron transfer.

2.4 The principle of photoelectrochemical detection

The use of photoelectrochemical detection was explored as an option to determine Hg^{2+} in aqueous solutions. Photoelectrochemical cells (PECs) extract electrical energy from light. The most common PECs are dye-sensitized solar cells (DSSCs), which extract their energy from sunlight. The principle of energy conversion is the photogeneration of charge carriers (electrons and holes) upon absorption of a photon and then separation of the charge carriers to a conductive contact that will transmit the electricity (a photovoltaic effect). Development of solar cells is now in its third generation, due mainly to the significant research contributions of Michael Grätzel and coworkers [52, 53]. DSSCs are PECs that use photosensitization of wide-band-gap mesoporous oxide semiconductors to convert sunlight into an electrical current. These PECs offer the advantages of low cost and simple instrumentation.

The Grätzel cell or DSSC (Figure 2.2) realises the optical absorption and the charge separation processes through the association of the sensitizer, which acts as a light-absorbing material, with a wide-band-gap semiconductor of nanocrystalline morphology [54].

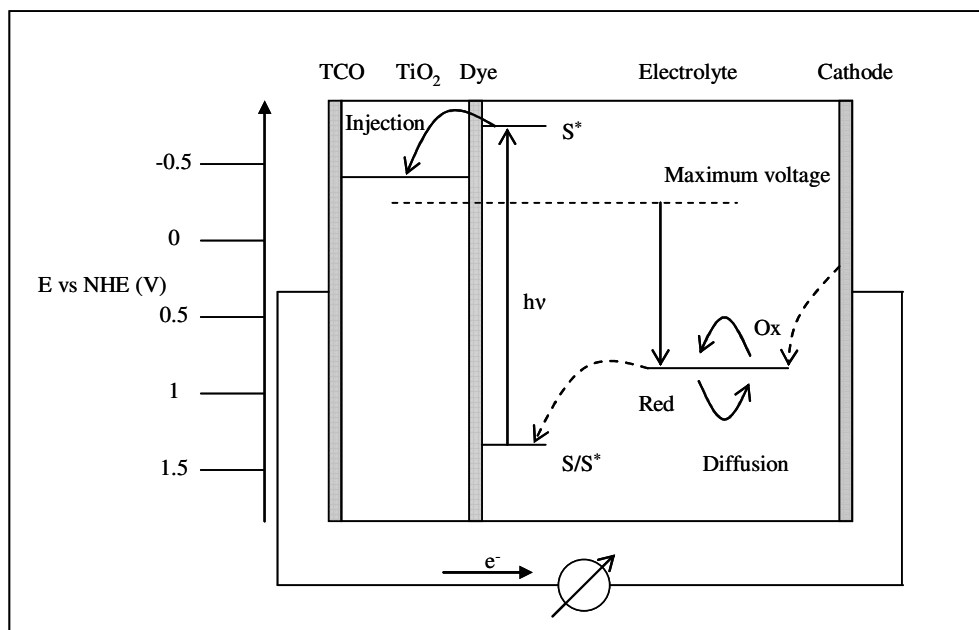


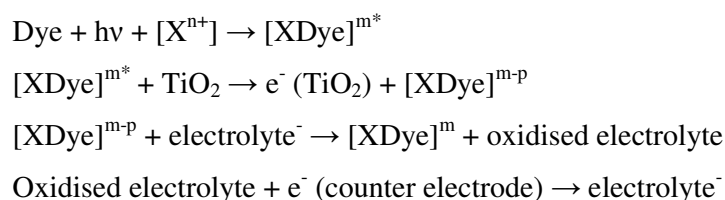
Figure 2.2: An adaptation of the scheme suggested by Grätzel

The primary agent is the mesoporous oxide layer composed of nanometer-sized particles, which have been sintered together to allow for electron conduction to occur. The oxide layer can be composed of titanium dioxide (TiO_2), zinc oxide (ZnO) [55] or niobium pentoxide (Nb_2O_5) [56], and has a monolayer of charge transfer dye attached to it. Photoexcitation (electrons transit from ground state to excited state) of the dye results in the injection of an electron into the conduction band of the oxide. The electrons diffuse through the oxide film to the glass electrode coated with a translucent conductive oxide (TCO), after which they are transferred through an external circuit to the counter electrode. The dye is restored by electron donation from the electrolyte, and the electrolyte is replenished by the counter electrode. The voltage generated under illumination corresponds to the difference between the Fermi level of the electron in the solid and the redox potential of the electrolyte [57]. The Fermi level is the energy level midway between the conduction band and valence band. In this way, the device generates an electric current from light without undergoing any permanent chemical transformation. The highest energy conversion for Grätzel cells is based on a TiO_2 semiconductor and ruthenium bipyridyl-based dyes (11%) [58].

Fluorescence is a powerful optical analytical technique, and when combined with a Hg^{2+} selective molecule it leads to fluorescent-based probes that are capable of detecting extremely low Hg^{2+} concentrations [59, 60].

Photoelectrochemical detection of certain compounds, following changes in the fluorescence of surface bound probes, has been described and evaluated [61]. The cell comprised an electrode, active nanoparticles or branched polymers that are capable of carrying photoelectrochemically active molecules that produce a photocurrent when exposed to light in an electric field, and a surface bound recognition probe. In a novel solar cell, the presence of a selective chemical of interest was determined by the change in the original electrical parameters of the solar cells, such as photoelectrical current or photoelectric voltage [62].

The sequence of reactions expected in a photoelectrochemical detector for compound $[\text{X}^n]$ is as follows:



2.5 The fluorescence-based chemosensor

A major need exists for the sensitive and accurate detection of pollutants and contaminants that threaten human health and safety, e.g. Hg. This need for continuous monitoring and the challenge to achieve lower and more accurate detection limits has led to the major field of sensor development. A sensor is a device that detects or measures a physical property and then records, indicates or otherwise responds to it. Although sensors are found in a multitude of applications, they can generally be divided into three types [63], e.g.:

- a) Physical sensors for measuring distance, mass, temperature, pressure, etc.;
- b) Chemical sensors which measure chemical substances by chemical or physical changes; and
- c) Biosensors which measure chemical substances by using a biological sensing element.

Generally, a sensor consists of a recognition element, a transducer and an actuator or signal processor. A transducer is the part of the sensor device that converts the observed chemical or physical change from the recognition element into a

measurable signal that can be processed [60]. This processable signal can then be used for the qualitative or quantitative determination of the analyte [64].

A chemical sensor consists of a chemically selective layer, of which either the chemical or physical properties changes on interaction with an analyte, and a transducer. Chemical sensors form a simple integrated analytical system that integrates the reaction and measurement steps, without a break in continuity [65]. Simple and innovative chemical sensor designs have led to the development of low cost analytical instrumentation, coupled with fast and robust analytical procedures. All chemical sensor designs comprise of two equally important parts: the receptor or recognition element and the transducer. The receptor is the area in which the chemical reaction occurs and produces a signal, which could transmit as a colour change, light emission, electrical potential, electron flow etc. The transducer responds to the recognition signal and translates the magnitude of the signal into a measure of the amount of analyte [60, 66]. Chemical sensors can be further categorised according to the transducer type: electrochemical, optical, mass sensitive and/or heat sensitive.

Chemical sensors that contain a synthetic recognition material are referred to as chemosensors, while those that contain biomaterials are known as biosensors [65]. Chemosensors can be defined as molecules in which the sensing element is chemically linked to the transducer. An optical chemosensor consists of a molecule incorporating a binding site, a chromophore or fluorophore, and a mechanism for communication between the two. Figure 2.3 is a schematic representation of the working mechanism of a chemical sensor and an optical chemosensor. The optical properties of the chemosensor will therefore change in the presence of the analyte. The optical changes/responses include shifts in the wavelength or intensity of the absorbance of the optode and/or a quenching or enhancement of fluorescence emission.

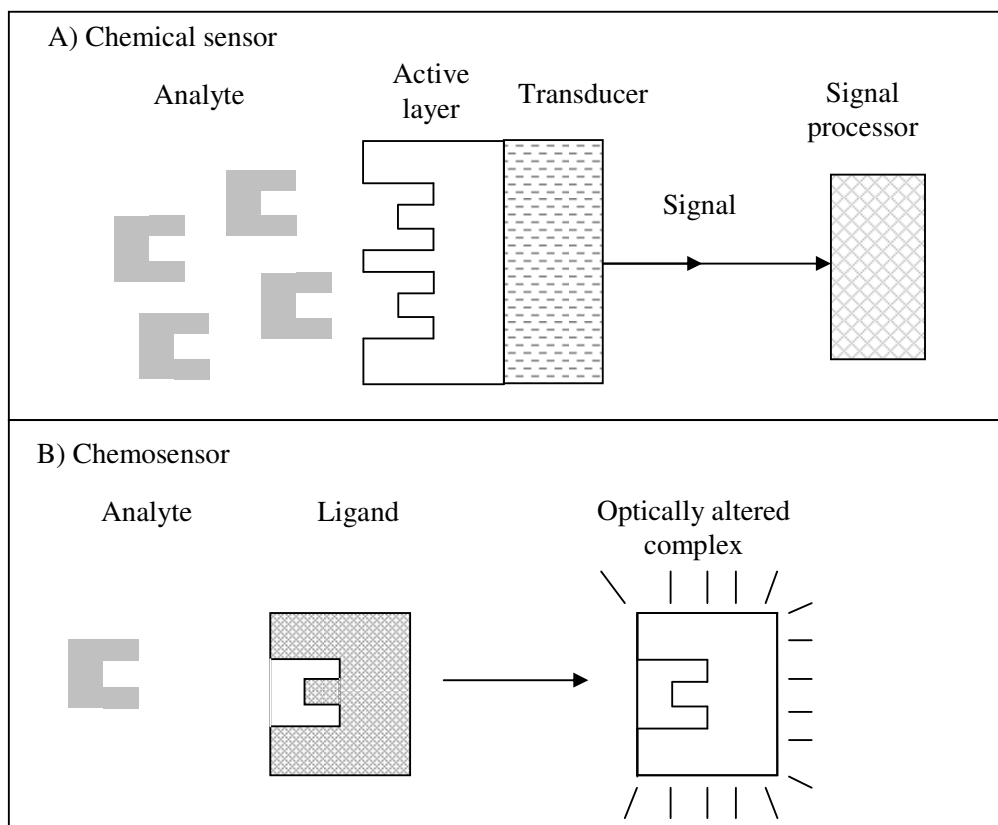


Figure 2.3: Schematic layout of A) a chemical sensor and B) the binding event of a chemosensor producing a complex with altered optical properties.

A fluorescent chemosensor, also called a fluoroionophore, consists of a recognition moiety (ionophore) linked to a fluorescent moiety (fluorophore). A fluorophore is the optical transducer because it converts the binding process of the ionophore to an optical signal. The fluorophore contains a functional group in a molecule that will absorb energy of a specific wavelength and re-emit energy at a different wavelength. The amount and wavelength of the emitted energy depend on both the fluorophore and its chemical environment. Fluorescent chemosensors are widely used as complexing agents for metal ions [67-71]. Transition metal ions, in particular, form highly coloured complexes with optically active chemosensors due to the possible *d*-electron transitions [66]. The creative design and synthesis of fluorescent chemosensors, which either fluoresce or quench upon ligation with selective ions, has received considerable attention. Fluorescence spectrophotometry is extremely sensitive and fluorescent chemosensors have been used for measurements in various media, including aqueous and biological [72-

74]. The key features by which a fluorescent chemosensor is measured are the following: selectivity, range of linear response, sample conditions, response time, recovery, lifetime and accuracy.

Fluorescent chemosensors are among the most developed areas in photometric sensors and biosensors, and present the following advantages:

- No reference electrode is needed
- There is no electrical interference
- Some analytes can be detected in equilibrium
- They are highly stable with respect to calibration
- Multi-wavelength measurements can be made to monitor changes in the state of the reagent [63]
- Optodes allow transmission of optical signals over large distances and are therefore ideal for remote sensing.

For the purposes of this study it is recommended to exchange the light sensitive dye in the DSSC with a fluorescent based chemosensor that is Hg^{2+} selective. Fluorescence offers an optimal route to metal ion sensing in aqueous solutions since it requires simple instrumentation, and offers high sensitivity and selectivity. In the unbound form the Hg^{2+} selective fluoroionophore is photoinactive. In the presence of Hg^{2+} the ionophore complexes with Hg^{2+} and the fluoroionophore rearranges, releasing the fluorophore. In the presence of light the newly formed fluorophore will absorb light and then emit at a slightly longer wavelength. The excited photon will be harvested in a way similar to the light sensitive material in DSSC (mentioned in Section 2.3), in which the charge separator leads to an electron current. The photovoltage of the PEMD will be equivalent to the concentration of Hg^{2+} . The size of the photovoltage also depends on the quantum yield of the fluorophore. Quantum yield is the number of emitted photons relative to the absorbed photons [75]. The larger the quantum yield (unity = 1) the brighter the emission.

2.6 TiO₂ as semiconductor and charge separator

2.6.1 Semiconductor electrochemistry

Solid materials, depending on their electronic structure, can be divided into, conductors and dielectrics (which includes semiconductors and insulators). In dielectrics there is a gap (energy band-gap, E_g) between the highest filled energy band, the valence band (VB), and the lowest unoccupied band, the conduction band (CB). Figure 2.4 (A) shows the relationship between the various bands and Figure 2.4 (B) illustrates the classification of the solid materials based on their energy states.

The VB is occupied by valence electrons and the CB is associated with the excited state energy levels. The conductivity of electrons is proportional to the electron mobility and electron concentration in the CB. After absorption of a photon vacancies called valence holes are formed in the VB, which make movement in the VB possible. The current flow in a semiconductor is therefore the sum of the motion of electrons in the CB, and holes in the VB. Excitation of electrons or the creation of holes can be achieved thermally or optically.

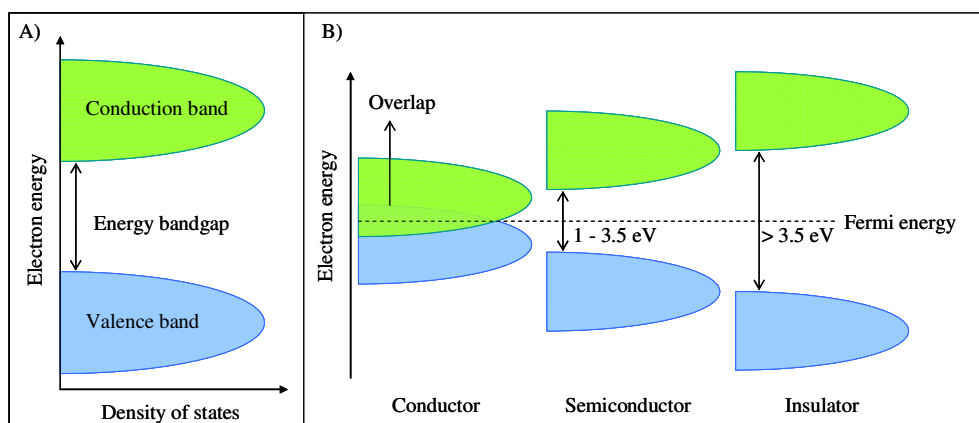


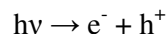
Figure 2.4: A) Electron energy diagram for the conductance and valence band and B) the electronic difference between a conductor, semiconductor and insulator.

Materials with band-gap energies between a conductor (0 eV) and an insulator (> 3.5 eV) are called semiconductors, which can be grouped into two types depending on their majority charge carriers: n-type and p-type. For n-type semiconductors the electrons dominate the carrier transport, whereas holes are the

majority carriers in p-type semiconductors. The minority carrier of the semiconductors can be created by the absorption of a photon, sufficient in energy to raise an electron in the VB to the CB. The absorbed energy must be higher than the E_g of the specific semiconductor [76].

The semiconductors can be used as light sensitive anodes or cathodes depending on their majority carrier. The majority carrier flows through the electrical load to the metallic electrode and drives an electrochemical reaction. The minority carrier flows to the semiconductor surface and drives another electrochemical reaction [77]. Semiconductors with donor character and electrons as major charge carriers are n-type, whereas electron accepting behaviour indicates holes as the major charge carrier and are therefore p-type semiconductors [78]. In semiconductors, current can be carried either by the flow of electrons or by the flow of positively charged "holes" in the electron structure of the material.

When the sensitized film is illuminated with photons of higher energy than the (E_g) of the semiconductor an electron is excited to the CB generating free electron-hole pairs ($e^- - h^+$):



In the PEMD the direction of electron transport is determined by the electron accepting or donating nature of the working photoelectrode. If the photoelectrode is coated with an electron acceptor, like TiO_2 , electrons will move from the excited dye, through the electron acceptor, to the ITO back contact, creating a photo-anode. If the working electrode is coated with a hole acceptor or electron donor then the donor will transfer electrons to the electron holes in the VB of the excited complex. When the electrons are transported through the electrolyte to the counter electrode the working photoelectrode is a photocathode. The possible photoresponses of different working electrodes are shown in Figure 2.5 a) and b).

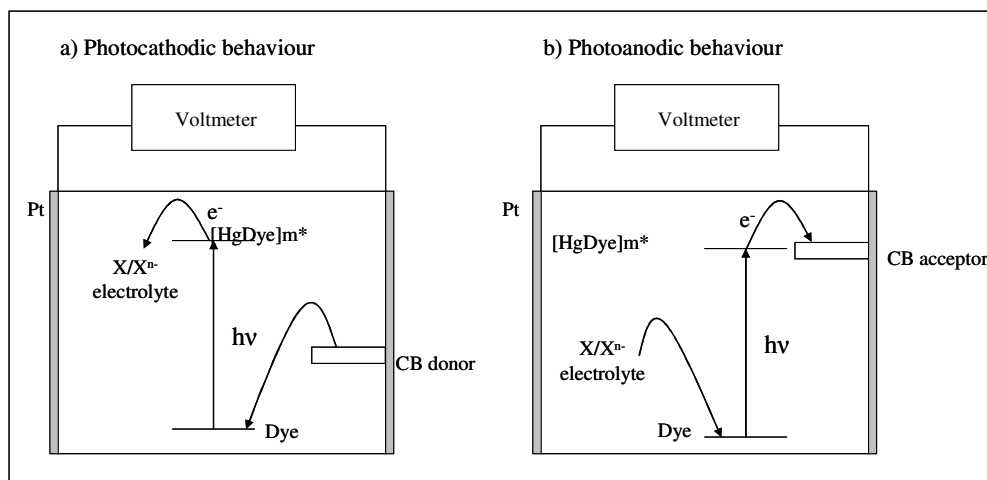


Figure 2.5: The possible a) cathodic response (n-type semiconductor) and b) photoanodic (p-type semiconductor) of the working electrode in a PEMD.

2.6.2 TiO_2 , an n-type semiconductor

TiO_2 is an n-type, large band-gap (3–3.2 eV) semiconductor which has three crystal structures; rutile, anatase and brookite. The Ti^{4+} ions are disorderedly surrounded by six O^{2-} , which create octahedral TiO_6 building blocks. The number of edges shared by the octahedra increases from 2 (out of 12) for rutile, to 4 in anatase [79]. The crystal structures of TiO_2 that are formed by the different octahedral building blocks of TiO_6 are illustrated in Figure 2.6 [80].

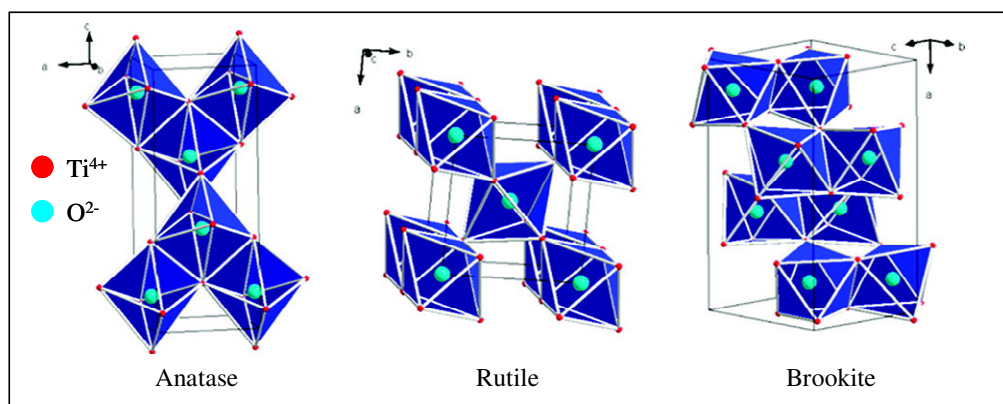


Figure 2.6: The three crystal structures of TiO_2 : anatase, rutile and brookite [80]

Electron transport is slower in the rutile layer than in the anatase layer due to differences in the extent of interparticle connectivity associated with the particle packing density. TiO_2 is transparent to visible light, it has a high refractive index,

and only absorbs in the ultraviolet part of light. Although rutile is less expensive to produce and has superior light-scattering characteristics, the anatase form is the preferred choice of material for DSSCs because of its superior surface chemistry and higher CB edge energy [81]. Recently, the uses of TiO₂ nanoparticles and nanowires have also been investigated [82]. The nanoparticles can provide large surface areas for dye adsorption, while the incorporated nanowires can enhance the light harvesting, electron transport rate, and also the mechanical properties of the films.

The properties of TiO₂ have resulted in it being a widely used and well studied semiconductor used in PECs. For efficient charge separation TiO₂ as an n-type semiconductor, will conduct the electron carriers upon photoexcitation. The actual fate and transport of the electron carriers in the TiO₂ matrix after excitation is complex, and the sum of various intermittent processes.

Upon photoexcitation of adsorbed dye molecules, electrons are injected into the CB of the TiO₂ with a time constant τ_{inj} (femto to pico seconds). The injected electrons can be captured by the trap states in the TiO₂ film, τ_t , or they can be thermally emitted back to the CB (detrapped), τ_{dt} . The photo-injected electron spends most of its time in the trap states. As the electrons are trapped and detrapped in the interconnecting network of TiO₂ particles they move towards the conductive back contact with a time constant τ_{cc} . The competing alternative is electrons that recombine with the holes in either the oxidised dye or the redox couple in the electrolyte. Generally, recombination with the oxidised dye is prevented by even faster neutralization of the dye with a suitable redox couple. Recombination occurs with a time constant τ_r at the semiconductor/electrolyte interface and occurs principally via trap states rather than the CB. The competition between the recombination and traversing of the electron through the trap states towards the contact determines, to a large extent, the photon to current efficiency. A summary of the competing processes is given in Figure 2.7.

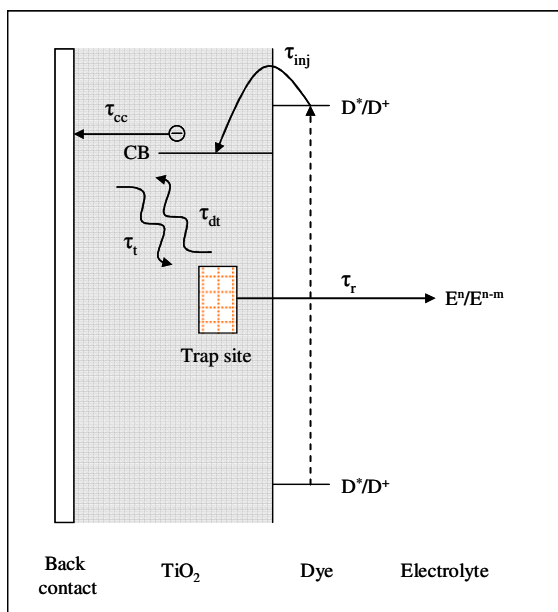


Figure 2.7: Schematic representation of competing processes at a TiO_2 /electrolyte interface.

Microscopically, an accumulation layer resembling an ohmic contact in TiO_2 at the back contact/ TiO_2 interface can be observed. As such, two potential drops exist over the TiO_2 semiconductor layer: at the accumulation layer at the back contact/ TiO_2 interface and the Helmholtz double layer at the TiO_2 /electrolyte interface. But, on the larger scale, the Fermi level of the TiO_2 layer closest to the back contact/ TiO_2 interface is in equilibrium with the Fermi-level of the back contact. The interface is transparent for electrons, and the flow of electrons in either direction over the interface is determined by the applied bias e.g. voltage [83-86].

TiO_2 has been widely used in PECs [82, 87, 88]. Nano-structured TiO_2 has high transparency, and the UV absorptivity increases with increasing geometric area. Nano-sized TiO_2 colloidal sol is the ultimate dispersion; it has high sunscreen capability, is stable at neutral pH and suppresses photocatalytic activity. Nano-sized TiO_2 colloidal sol can be synthesized via the sol-gel process, hydrothermal processes or, more recently, by wet synthesis [89]. TiO_2 is chemically stable, non-toxic and simple and inexpensive to synthesise.

2.7 Polyaniline and substituted polymers as hole conductors

A conducting polymeric material with a large band-gap, sufficient conductivity, homogeneous surface and small size clusters is desirable as a hole conductor in PECs. Polyaniline (PANI) is unique among conducting polymers due to its chemical and environmental stability, good redox reversibility, tuneable electrical conductivity [90, 91], and optical properties [92]. PANI is easy to synthesise, stable in water and air, and shows a pronounced colour change upon change in electrical potential [93-95]. These properties make it favourable for applications in rechargeable batteries, electrocatalysis, electrochromic devices, chemical sensors and the conversion of light to electricity [96-99].

In the proposed PEMD, PANI will facilitate the charge separation to produce an electron current. PANI has been used as a hole conductor in DSSCs [100, 101]. The photovoltaic behaviour of PECs is strongly influenced by the conductivity and pore filling by PANI on the photoelectrode. PANI absorbs strongly in the infrared and visible regions and can be used in the photosensitization of semiconductor nano-TiO₂ films and in the preparation of solar energy photocatalysts [102]. The conductive form of PANI exists when the pH of the medium is lower than 3. PANI has five different oxidation states as shown in Figure 2.8, but generally occurs in two forms: the emeraldine base (EB) and emeraldine salt (ES, both polaronic and bipolaronic), which can be interchanged by treating with acid or base.

The electrical conductivity of PANI is considered to be the result of motions of polarons and bipolarons [103]. Polarons are formed when a charge within the polymer chain influences the local nuclear geometry, causing an attenuation of nearby bonds. Polarons are therefore polar semiconductors. As the electrons move through the polymer matrix the induced polarization causes distortion of the polymer chain. Bipolarons are the part of the polymer chain that contains two positive charges in the conjugated system [104]. The polymeric forms of PANI with intermediate conductivity in the semiconductor region are more suitable for PECs than those close to the conductor or insulator regions.

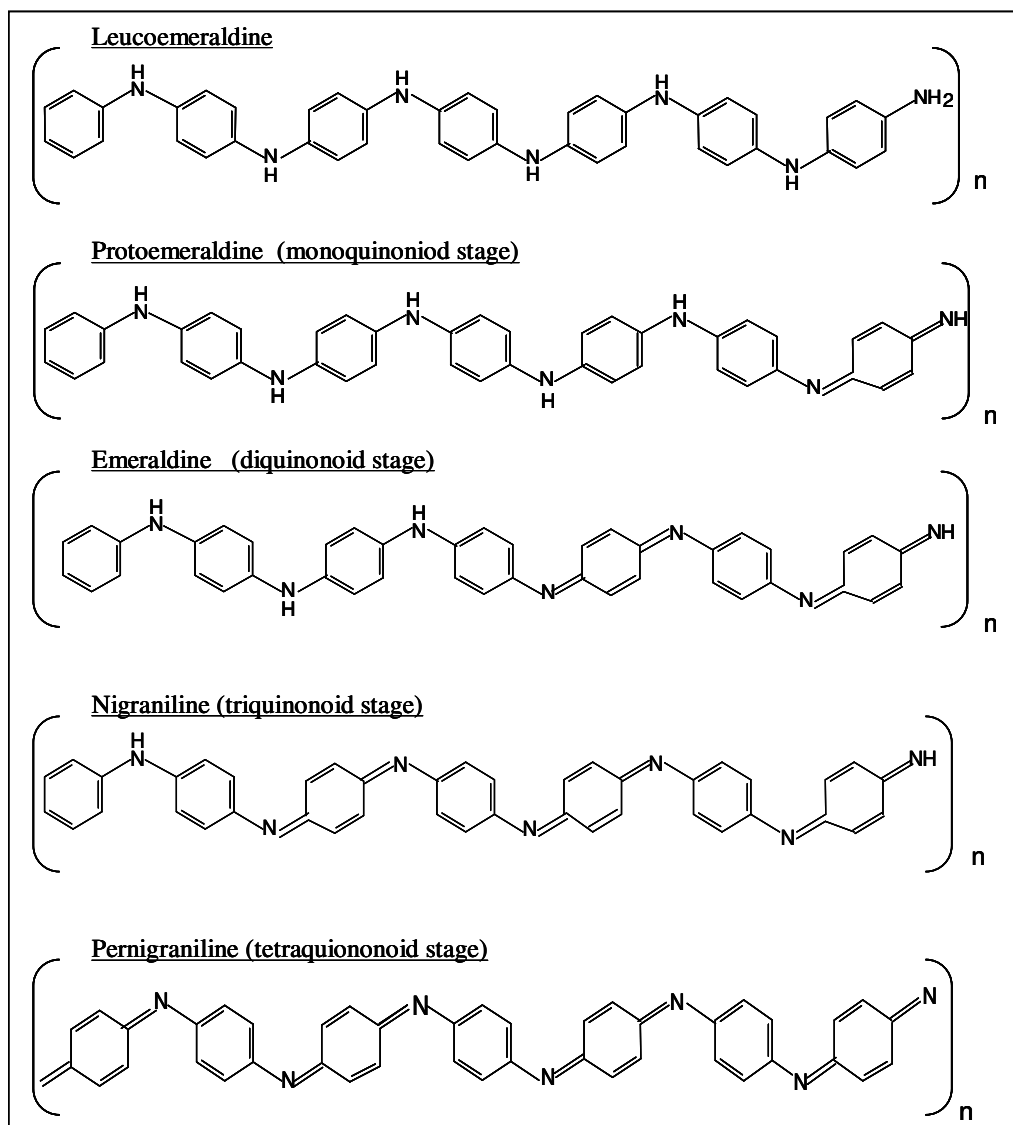


Figure 2.8: The oxidation forms of polyaniline [104].

The application of PANI has been limited because its conductivity, energy density, catalytic activity, electrochromic properties and energy conversion are highly pH dependent. PANI is also insoluble in most organic solvents which decrease its processability [105]. PANI can exist as bulk films or as dispersions; in dispersions however, particle aggregation further limits possible applications [106].

There is an overwhelming interest in synthesising copolymers of *ortho*- and *meta*-substituted PANIs that maintain the fundamental conducting backbone of PANIs, while allowing for property and functionality enhancing derivatization [105, 107,

108]. The derivatizations aim to increase solubility, optimise processability, and introduce recognition elements to improve the performances of sensors [109].

It is generally considered that copolymers of PANI containing electron withdrawing groups (for example CN⁻) are redox inactive [110-112], except in highly acidic solutions and with higher monomer content [111, 113]. The low redox activity limits electro-polymerization, as well as the conductive properties of the various polymers. Substituent groups affect the polymerizability of substituted aniline derivatives. If steric hindrance is minimal, an electron donating group increases the polymerization rate, whereas electron withdrawing substituents retard the polymerization [114]. Copolymers with a higher content of halogenated monomer show little conductivity. Bromine functionalized polymer samples are thermally more stable than the parent PANI derivative due to the introduction of the bromine onto the polymer backbone. In addition, the presence of the halogen atom in the ring of aniline units can produce polymers with better solubility in common organic solvents [112]. Figure 2.9 illustrates the monomers that can be added, in different feed ratios, for the synthesis of PANI-substituted PANI copolymers.

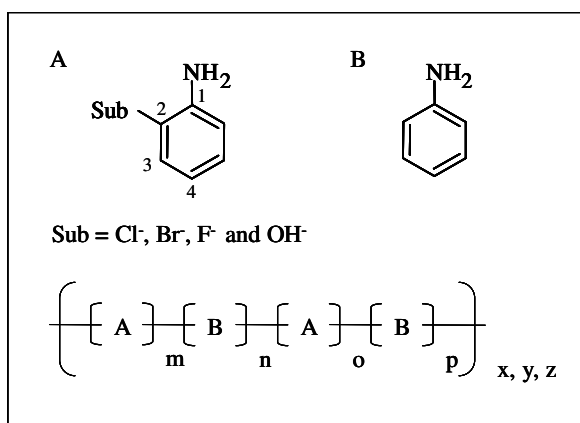


Figure 2.9: The A) substituted aniline and B) aniline monomers that are added in different feed ratios to synthesise PANI-co-substituted PANI copolymers.

Copolymers of aniline and 2-bromoaniline with different monomer feed ratios will be investigated as possible substitutes for hole conduction in the proposed PEMD. Polyaniline-co-2-bromoaniline (P[A-co-2-BrA]) polymers will be electrochemically evaluated to determine the conductive properties of the

copolymers containing monomer feed ratios aniline:2-bromoaniline; 10:90, 25:75, 50:50 and 70:30.

The P[A-co-2-BrA] copolymers will be photoelectrochemically evaluated in corporation with the Hg²⁺-selective organic dye to determine their electron donating capability in a PEC. PANI copolymers with higher solubility and higher processibility will simplify the making of the sensitized electrodes, reduce the cost of the electrodes, as well as increase reproducibility due to smoother film formation.

2.8 References

- [1] M.F. Wolfe, S. Schwarzbach, R.A. Sulaiman, Environ. Toxicol. Chem., 17 (1998) 146-160.
- [2] R. Ebinghaus, H. Hintelmann, R.D. Wilken, Fresenius J. Anal. Chem., 350 (1994) 21-29.
- [3] M.V.B. Krishna, M. Ranjit, D. Karunasagar, J. Arunachalam, Talanta, 67 (2005) 70-80.
- [4] T.W. Clarkson, L. Magos, G.J. Myers, N. Engl. J. Med., 349 (2003) 1731-1737.
- [5] H. Morita, H. Tanaka, S. Shimomura, Spectrochim. Acta, Part B: At. Spectrosc., 50 (1995) 69-84.
- [6] N. Daskalova, I. Boevski, Spectrochim. Acta. Part B: At. Spectrosc., 54 (1999) 1099-1122.
- [7] J.C. Andrews, in: D.A. Atwood (Ed.), Structure and Bonding, Springer, Berlin, 2006, p. 1-35.
- [8] W.F. Fitzgerald, R.P. Mason, Met. Ions Biol. Syst., 34 (1997) 53-112.

- [9] Assessment Global Mercury, Geneva: UNEP (2002), accessed 01-09-2009, available at <http://www.chem.unep.ch/mercury/Report/revdraft-afterWG/assessment-report-4Oct02.pdf>.
- [10] O.R. Bullock Jr., W.G. Benjey, M.H. Keating, in: J.E. Baker (Ed.), Atmospheric deposition of contaminants to the Great Lakes and Coastal Waters. SETAC Press, Pensacola, Florida, 1997, p. 323-347.
- [11] R.P. Mason, M.L. Abbott, R.A. Bodaly, O.R. Bullock Jr, C.T. Driscoll, D. Evers, S.E. Lindberg, M. Murray, E.B. Swain, Environ. Sci. Technol., 39 (2005) 14-22.
- [12] R.P. Mason, G.R. Sheu, Global Biogeochem. Cycles, 16 (2002) 1093.
- [13] M.S. Gustin, A. Kolker, K. Gårdfeldt, Appl. Geochem., 23 (2008) 343-344.
- [14] J.M. Dabrowski, P.J. Ashton, K. Murray, J.J. Leaner, R.P. Mason, Atmos. Environ., 42 (2008) 6620-6626.
- [15] R. Spalding-Fecher, D.K. Matibe, Energy Policy, 31 (2003) 721-734.
- [16] G. Hilson, A.J. Monhemius, J. Clean. Prod., 14 (2006) 1158-1167.
- [17] M. Leermakers, W. Baeyens, P. Quevauviller, M. Horvat, Trends Anal. Chem., 24 (2005) 383-393.
- [18] T.W. Clarkson, L. Magos, CRC Crit. Rev. Toxicol., 36 (2006) 609-662.
- [19] R. Dietz, F. Riget, M. Cleemann, A. Aarkrog, P. Johansen, J.C. Hansen, Sci. Total Environ., 245 (2000) 221-231.
- [20] C.C. Gilmour, G.S. Riedel, Arch. Environ. Contam. Toxicol., 39 (2000) 53-59.
- [21] R.P. Mason, J.R. Reinfelder, F.M.M. Morel, Water Air Soil Pollut., 80 (1995) 915-921.
- [22] R.M. Neumann, S.M. Ward, J. Freshwat. Ecol., 14 (1999) 487-497.
- [23] D.C. Rice, Environ. Res., 95 (2004) 406-413.

Chapter 2 – Historical and Theoretical background

- [24] L. Magos, in: A. Sigel (Ed.), Mercury and its effects on environment and biology, Marcel Dekker Inc, New York, 1997, p. 321-370.
- [25] M. Harada, Teratology, 18 (1978) 285-288.
- [26] Y. Itai, T. Fujino, K. Ueno, Y. Motomatsu, Environ. Sci, 11 (2004) 83-97.
- [27] A.H. Stern, Environ. Res., 98 (2005) 133-142.
- [28] E.K. Silbergeld, I.A. Silva, J.F. Nyland, Toxicol. Appl. Pharmacol., 207 (2005) 282-292.
- [29] D. Mergler, H.A. Anderson, L.H.M. Chan, K.R. Mahaffey, M. Murray, M. Sakamoto, A.H. Stern, J. Human Environ., 36 (2007) 3-11.
- [30] Y. Li, S.J. Liu, D.Q. Jiang, Y. Jiang, X.P. Yan, Chin. J. Anal. Chem., 36 (2008) 793-798.
- [31] J. Qvarnstrom, L. Lambertsson, S. Havarinasab, P. Hultman, W. Frech, Anal. Chem., 75 (2003) 4120-4124.
- [32] P. Ugo, L.M. Moretto, P. Bertoncetto, J. Wang, Electroanalysis, 10 (1998) 1017-1021.
- [33] C. Chiou, S. Jiang, K.S. Kumar Danadurai, Spectrochim. Acta Part B: At. Spectrosc., 56 (2001) 1133-1142.
- [34] T. Stoichev, D. Amouroux, R.C.R. Martin-Doimeadios, M. Monperrus, O.F.X. Donard, D.L. Tsalev, Appl. Spectrosc. Rev., 41 (2006) 591-619.
- [35] S. Han, W. Gan, X. Jiang, H. Zi, Q. Su, J. Anal. At. Spectrom., 23 (2008) 773-776.
- [36] E.L. Witt, R.K. Kolka, E.A. Nater, T.R. Wickman, Environ. Sci. Technol., 43 (2009) 1776-1782.
- [37] T.H. Nguyen, J. Boman, M. Leermakers, W. Baeyens, Fresenius J. Anal. Chem., 360 (1998) 199-204.

- [38] L. Jian, W. Goessler, K.J. Irgolic, Fresenius J. Anal. Chem., 366 (2000) 48-53.
- [39] Y. Li, C. Chen, B. Li, J. Sun, J. Wang, Y. Gao, Y. Zhao, Z. Chai, J. Anal. At. Spectrom., 21 (2006) 94-96.
- [40] I. Karadjova, P. Mandjukov, S. Tsakovsky, V. Simeonov, J.A. Stratis, G.A. Zachariadis, J. Anal. At. Spectrom., 10 (1995) 1065-1068.
- [41] W. Geng, T. Nakajima, H. Takanashi, A. Ohki, J. Hazard. Mater., 154 (2008) 325-330.
- [42] S. Pirvutoiu, I. Surugiu, E.S. Dey, A. Ciucu, V. Magearu, B. Danielsson, Analyst, 126 (2001) 1612-1616.
- [43] N.M. Hanumegowda, I.M. White, X. Fan, Sens. Actuators, B, 120 (2006) 207-212.
- [44] C. Cano-Raya, M.D. Fernández-Ramos, J. Gómez-Sánchez, L.F. Capitán-Vallvey, Sens. Actuators, B, 117 (2006) 135-142.
- [45] S.Y. Ly, S.K. Kim, T.H. Kim, Y.S. Jung, S.M. Lee, J. Appl. Electrochem., 35 (2005) 567-571.
- [46] R. Ito, M. Kawaguchi, N. Sakui, N. Okanouchi, K. Saito, Y. Seto, H. Nakazawa, Talanta, 77 (2009) 1295-1298.
- [47] S.F. Boulyga, Anal. Bioanal. Chem., 387 (2007) 731-732.
- [48] S. Meyer, F. Scholz, R. Trittler, Fresenius J. Anal. Chem., 356 (1996) 247-252.
- [49] A. Giacomino, O. Abollino, M. Malandrino, E. Mentasti, Talanta, 75 (2008) 266-273.
- [50] R.H. Yang, Y. Zhang, K.A. Li, F. Liu, W.H. Chan, Anal. Chim. Acta, 525 (2004) 97-103.
- [51] R. Yang, K. Li, K. Wang, F. Zhao, N. Li, F. Liu, Anal. Chem., 75 (2003) 612-621.

- [52] A. Kay, M. Grätzel, *Chem. Mater.*, 14 (2002) 2930-2935.
- [53] G.P. Smestad, M. Grätzel, *J. Chem. Educ.*, 75 (1998) 752-756.
- [54] M. Grätzel, *Nature*, 414 (2001) 338-344.
- [55] M. Law, L.E. Greene, J.C. Johnson, R. Saykally, P. Yang, *Nat. Mater.*, 4 (2005) 455-459.
- [56] M. Wei, Z. Qi, M. Ichihara, H. Zhou, *Acta Mater.*, 56 (2008) 2488-2494.
- [57] M. Grätzel, *J. Photochem. Photobiol. C*, 4 (2003) 145-153.
- [58] M. Grätzel, *Inorg. Chem.*, 44 (2005) 6841-6851.
- [59] M.K. Nazeeruddin, D. Di Censo, R. Humphry-Baker, M. Grätzel, *Adv. Funct. Mater.*, 16 (2006) 189-194.
- [60] P.A. Lieberzeit, F.L. Dickert, *Anal. Bioanal. Chem.*, 387 (2007) 237-247.
- [61] S. Franzen, D.L. Feldheim, Light addressable electrochemical detection of duplex structures, 10/236,205 (2002) 1-4.
- [62] R. Danz, B. Elling, Solar cell sensors, process for their manufacture and their use, 9/626,897 (2002) 1-7.
- [63] B.R. Eggins, *Chemical sensors and biosensors*, John Wiley & Sons Ltd, Chichester, England, 2002, p. 1-34.
- [64] J. Janata, M. Josowicz, P. Vanysek, D.M. DeVaney, *Anal. Chem.*, 70 (1998) 179-208.
- [65] S. Alegret, *Rev. Mex. Fis. S*, 52 (2006) 99-103.
- [66] R.W. Cattrall, *Chemical Sensors*, Oxford University Press, Oxford, U.K., 1997, p. 2-29.
- [67] H. Mu, R. Gong, Q. Ma, Y. Sun, E. Fu, *Tetrahedron Lett.*, 48 (2007) 5525-5529.

- [68] Y. Yu, L.R. Lin, K.B. Yang, X. Zhong, R.B. Huang, L.S. Zheng, *Talanta*, 69 (2006) 103-106.
- [69] Z. Xu, G.H. Kim, S.J. Han, M.J. Jou, C. Lee, I. Shin, J. Yoon, *Tetrahedron*, 65 (2009) 2307-2312.
- [70] Y.Q. Weng, Y.L. Teng, F. Yue, Y.R. Zhong, B.H. Ye, *Inorg. Chem. Commun.*, 10 (2007) 443-446.
- [71] L. Basabe-Desmonts, D.N. Reinhoudt, M. Crego-Calama, *Chem. Soc. Rev.*, 36 (2007) 993-1017.
- [72] L. Zeng, E.W. Miller, A. Pralle, E.Y. Isacoff, C.J. Chang, *J. Am. Chem. Soc.*, 128 (2006) 10-11.
- [73] C. He, W. Zhu, Y. Xu, T. Chen, X. Qian, *Anal. Chim. Acta*, 651 (2009) 227-233.
- [74] J.K. Tusa, H. He, *J. Mater. Chem.*, 15 (2005) 2640-2647.
- [75] J.R. Lakowicz, *Principles of fluorescence spectroscopy*, 2nd edition, Kluwer Academic/Plenum Publishers, New York, 1999, p. 24-94.
- [76] M.S. Wrighton, *J. Chem. Educ.*, 60 (1983) 877-881.
- [77] M.A. Butler, D.S. Ginley, *J. Mater. Sci.*, 15 (1980) 1-19.
- [78] S.M. Sze, K.K. Ng, *Physics of semiconductor devices*. 3rd edition edition, Wiley-Interscience, India, 2007, p. 7-62.
- [79] A. Verma, S.B. Samanta, A.K. Bakhshi, S.A. Agnihotry, *Sol. Energy Mater. Sol. Cells*, 88 (2005) 47-64.
- [80] A. Di Paola, G. Cufalo, M. Addamo, M. Bellardita, R. Campostrini, M. Ischia, R. Ceccato, L. Palmisano, *Colloids Surf. Physicochem. Eng. Aspects*, 317 (2008) 366-376.
- [81] N.G. Park, J. Van de Lagemaat, A.J. Frank, *J. Phys. Chem. B*, 104 (2000) 8989-8994.

- [82] B. Tan, Y. Wu, *J. Phys. Chem. B*, 110 (2006) 15932-15938.
- [83] J. Van de Lagemaat, N.G. Park, A.J. Frank, *J. Phys. Chem. B*, 104 (2000) 2044-2052.
- [84] P.E. De Jongh, D. Vanmaekelbergh, *Phys. Rev. Lett.*, 77 (1996) 3427-3430.
- [85] P.E. De Jongh, D. Vanmaekelbergh, *J. Phys. Chem. B*, 101 (1997) 2716-2722.
- [86] J. Nelson, *Phys. Rev. B*, 59 (1999) 15374-15380.
- [87] S. Mori, K. Sunahara, Y. Fukai, T. Kanzaki, Y. Wada, S. Yanagida, *J. Phys. Chem. C*, 112 (2008) 20505-20509.
- [88] V. Thavasi, V. Renugopalakrishnan, R. Jose, S. Ramakrishna, *Mater. Sci. Eng. R.*, 63 (2009) 81-99.
- [89] Y. Ishibai, T. Nishikawa, S. Miyagishi, *J. Dispersion Sci. Technol.*, 27 (2006) 1093-1098.
- [90] A. Pud, N. Ogurtsov, A. Korzhenko, G. Shapoval, *Prog. Polym. Sci.*, 28 (2003) 1701-1753.
- [91] A. Pron, P. Rannou, *Prog. Polym. Sci.*, 27 (2002) 135-190.
- [92] A.G. MacDiarmid, *Synth. Met.*, 84 (1997) 27-34.
- [93] R.L.N. Chandrakanthi, M.A. Careem, *Thin Solid Films*, 417 (2002) 51-56.
- [94] P.R. Somani, R. Marimuthu, U.P. Mulik, S.R. Sainkar, D.P. Amalnerkar, *Synth. Met.*, 106 (1999) 45-52.
- [95] Y. He, *Mater. Chem. Phys.*, 92 (2005) 134-137.
- [96] N. Oyama, T. Tatsuma, T. Sato, T. Sotomura, *Nature*, 373 (1995) 598-600.
- [97] G. Bidan, E.M. Genies, M. Lapkowski, *J. Chem. Soc. Chem. Commun.* (1988) 533-535.

- [98] M.M. Ayad, A.H. Gemaey, N. Salahuddin, M.A. Shenashin, *J. Colloid Interface Sci.*, 263 (2003) 196-201.
- [99] J. Huang, S. Virji, B.H. Weiller, R.B. Kaner, *Chem. Eur. J.*, 10 (2004) 1314-1319.
- [100] S. Tan, J. Zhai, B. Xue, M. Wan, Q. Meng, Y. Li, L. Jiang, D. Zhu, *Langmuir*, 20 (2004) 2934-2937.
- [101] S.X. Tan, J. Zhai, M.X. Wan, L. Jiang, D.B. Zhu, *Synth. Met.*, 137 (2003) 1511-1512.
- [102] X. Li, D. Wang, G. Cheng, Q. Luo, J. An, Y. Wang, *Appl. Catal., B*, 81 (2008) 267-273.
- [103] S. Quillard, G. Louarn, S. Lefrant, A.G. MacDiarmid, *Phys. Rev. B*, 50 (1994) 12496-12508.
- [104] A.S. Alexandrov, N.F. Mott, *Polarons & bipolarons*, World Scientific Cambridge, 1999, .
- [105] V. Rajendran, S. Prakash, A. Gopalan, T. Vasudevan, W.C. Chen, T.C. Wen, *Mater. Chem. Phys.*, 69 (2001) 62-71.
- [106] D. Li, R.B. Kaner, *J. Am. Chem. Soc.*, 128 (2006) 968-975.
- [107] D.S. Lin, S.M. Yang, *Synth. Met.*, 119 (2001) 111-112.
- [108] W.A. Gazotti Jr., R. Faez, M.A. De Paoli, *J. Electroanal. Chem.*, 415 (1996) 107-113.
- [109] A.A. Athawale, M.V. Kulkarni, *Sens. Actuators, B*, 67 (2000) 173-177.
- [110] D.V. Zhuzhel'skii, V.D. Ivanov, V.V. Malev, *Russian J. Electrochem.*, 42 (2006) 699-707.
- [111] H. Tanaka, H. Katsuura, S. Torii, *Electrochim. Acta*, 42 (1997) 2019-2026.

Chapter 2 – Historical and Theoretical background

[112] A.H. Kwon, J.A. Conklin, M. Makhinson, R.B. Kaner, *Synth. Met.*, 84 (1997) 95-96.

[113] M. Sato, S. Yamanaka, J.I. Nakaya, K. Hyodo, *Electrochim. Acta*, 39 (1994) 2159-2168.

[114] B.C. Roy, M.D. Gupta, J.K. Ray, *Macromolecules*, 28 (1995) 1727-1732.

Chapter 3

Synthesis and characterization of rhodamine 6G derivative fluorescent chemosensors

3.1 Introduction

An inorganic mercury (Hg^{2+}) selective chemical sensor will respond to Hg^{2+} in a selective way, through a chemical reaction, and can be used for the qualitative and quantitative determination of Hg^{2+} . Chemosensors are single type molecules containing both the recognition element as well as the transducer. The recognition of a chemosensor towards a particular analyte is most commonly transduced to an optical response or a change in electric potential [1]. Of all the potential optical responses, fluorescence is the most sensitive and also allows for visual indication. The selection of a suitable fluorescent chemosensor is an important objective and is crucial for the design and construction of the photoelectrochemical detector.

3.1.1 Selection of the chemosensor

The use of chemical sensors of which the chemical properties change upon identification of an analyte have been used in the pre-screening of certain hazardous or poisonous substances [2]. The selected chemosensor will transduce the Hg^{2+} binding event into a measurable signal. Hg^{2+} has no optical spectroscopic signature because of its closed-shell d^{10} configuration, but the $5d^{10}6s^2$ electronic configuration can accommodate a range of coordination numbers and geometries. Optical detection of Hg^{2+} therefore follows changes in solution fluorescence or UV-Vis spectroscopy resulting from Hg^{2+} -induced perturbation of the chromophore functional group in the ligand. The use of a Hg^{2+} responsive small molecule ligand provides immediate optical feedback, thus eliminating the need for sophisticated instrumentation. Small molecule ligands for Hg^{2+} complexation can therefore be engineered into assay kits, portable fiber optic devices and commercial indicators. These products will facilitate rapid on-site Hg^{2+} detection.

The affinity and selectivity of the chemosensor can be tuned by modifications of the Hg^{2+} binding unit (ionophore). Currently, extensive research on the design and synthesis of Hg^{2+} selective fluorescence molecule sensors capable of detecting Hg^{2+} in a variety of matrixes (aqueous and non aqueous) is being carried out [3-9].

Most fluorescent chemosensors are capable of chelating metal ions, and two types can be distinguished: chelation enhancement of fluorescence (CHEF) and chelation enhancement of quenching (CHEQ). Enhancement (“turn-on”) is the preferred method for fluorescence detection of Hg^{2+} , as oppose to fluorescence quenching (“turn-off”). The reason is that in the case of CHEF there is less chance of false positives, and is more amenable to multiplexing, i.e. the simultaneous use of several detectors that uniquely respond to different analytes.

The design of sensors that give fluorescent enhancement (FE) upon Hg^{2+} binding presents a particular challenge because, like many other heavy metals, Hg^{2+} often causes fluorescent quenching via several mechanisms that can be attributed to electron transfer [10]. The most common mechanism relevant to the FE effect of Hg^{2+} is enhanced spin-orbit coupling associated with the heavy atom effect, which will facilitate the intersystem crossing process [11]. For fluorescent indicators, the excitation and emission wavelengths are dictated by the choice of fluorophore, and the brightness is defined as the product of the quantum yield and extinction coefficient. Mechanisms commonly used to explain the response of optical sensors to Hg^{2+} are electron transfer and charge transfer. These general categories include photoinduced electron transfer, internal charge transfer, and photoinduced charge transfer [12]. Some desirable features of a fluorescent metal ion probe include a positive and selective fluorescence response for the analyte, reversibility, high selectivity and sensitivity for the analyte of interest in the presence of background ions, and water solubility [13].

Criteria for a fluorescent chemosensor are as follows:

- The fluorescence based chemosensor must be activated by a fluorescence enhancement (“turn-on”) mechanism.
- The sensor must be Hg^{2+} selective in the presence of other background cations.
- Fluorescence enhancement must be proportional to the Hg^{2+} concentration. Calibration of the optical responses is crucial for validation of the detection method.
- A fluorescent chemosensor must have a high quantum yield (~ 1) and therefore high brightness for the Hg^{2+} complex.

- The photoresponses of the chemosensor toward Hg^{2+} need to be quantitatively reproducible from batch to batch of made chemosensors.
- The chemosensor must have a relatively low detection limit (preferably $2 \mu\text{g L}^{-1}$) for Hg^{2+} .
- The sensor must also be relatively pH-independent, to avoid the requirement for the addition of buffers on-site and enable direct detection to be made.
- Generally, water solubility for direct analyte addition is favoured. For implementation in a photoelectrochemical detector however, heterogeneous interaction between the fluorophore and the Hg^{2+} is required.
- Ideally, the chemosensor needs to be reusable. A reversible chemical reaction introduces the possibility of regenerating the sensor, making it environmentally friendly as well as cost effective.

These above-mentioned criteria are the primary considerations. Others factors that could also be taken into account are a good response time, suspension in a substrate, simple synthesis, and matrix effects.

3.1.2 Rhodamine chemosensors

Rhodamine derivatives have large molar extinction coefficients and high fluorescent quantum yields and are therefore ideal for constructing “off-on” fluorescent chemosensors [14]. Rhodamine derivatives are generally non-fluorescent and colourless, whereas ring opening of the spirolactam gives rise to the strong fluorescent xanthene moiety and various red to pink colours [15, 16]. Spirolactam to fluorescent amide ring opening of the rhodamine derivatives has been utilised for the selective detection of Hg^{2+} [17, 18]. Figure 3.1 is an illustration of the ring opening upon complexation of Hg^{2+} with the rhodamine 6G derivative synthesised by Wu *et al.* [17].

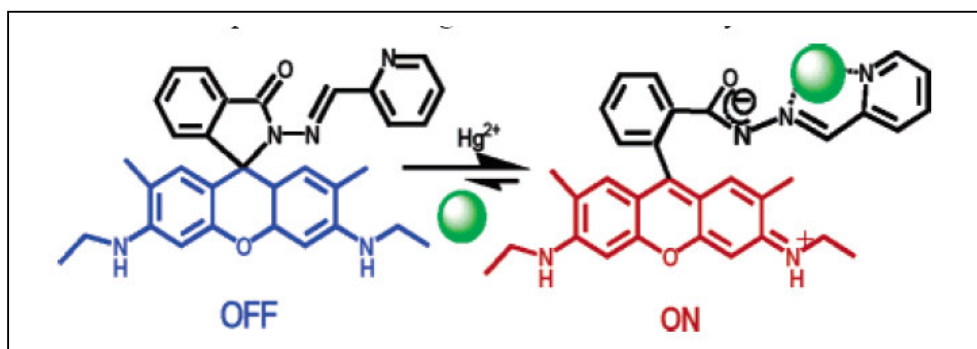


Figure 3.1: Spirolactam ring opening of the Hg²⁺ selective rhodamine derivative [17].

Rhodamine compounds and their derivatives are inexpensive to make and have long wavelengths (> 500 nm) for both absorption and emission. As both the rhodamine absorption and emission wavelengths are in the visible region, naked eye inspection as well as spectroscopic determination of Hg²⁺ is possible. The binding units of the rhodamine derivatives most often contain imino nitrogen, carbonyl oxygen and thioether or thiourea-sulphur groups [14, 17].

3.1.3 Rhodamine 6G derivative chemosensors for use in photoelectrochemical cells

Two rhodamine 6G Hg²⁺ selective chemosensors were selected for use in the photoelectrochemical mercury detector (PEMD). The first was a derivative containing a carbohydrazone block synthesised by Wu *et al.* [17]. The rhodamine 6G hydrazone derivative (RS) sensor is highly selective (50-fold) towards Hg²⁺ in the presence of background cations and can detect levels of 2 µg L⁻¹ (2 ppb or 10 nM). RS is a suitable bis-chelating Schiff based receptor for Hg²⁺ in which the nitrogen affinity of Hg²⁺ is combined with the amide deprotonation ability of Hg²⁺. The association constant, K_a , for the 2:1 binding process with mercury is $2.4 \times 10^9 \text{ M}^{-2}$. Wu *et al.*'s [17] RS is pH insensitive in the range pH 5 to 10. RS can serve as a visual indicator for the presence of Hg²⁺ and has a high quantum yield of 0.42. The response of the sensor towards Hg²⁺ in DMF/H₂O is currently irreversible.

The second chemosensor selected for use in the PEMD was the rhodamine 6G derivative containing a thiolactone moiety (RT), as synthesised by Chen *et al.* [18]. The spirothiolactone ring opened on coordination of Hg²⁺ with two sulphur atoms from neighbouring RT molecules. The limit of detection was 1 nM to 10 nM, which makes RT an excellent screening sensor. RT has a 2:1 binding event with Hg²⁺ and

has a 200-fold selectivity for Hg^{2+} in the presence of background cations. The thiophilic nature of Ag^+ leads to a small fluorescent enhancement, but due to the low natural abundance of Ag^+ this effect is negligible. Because the RT sensor was used for detection of Hg^{2+} in biological samples the pH was fixed at pH 7.14. The sensor could be regenerated with four equivalent amounts of potassium iodide (KI).

Sensors RS and RT were synthesised and characterised as described in the following section. Then RS and RT were immobilised on the surface of indium tin oxide (ITO) glass substrates and evaluated for their responses towards Hg^{2+} in aqueous solutions, as described in Chapters 6 to 8.

3.2 Materials and methods

3.2.1 Materials

All chemicals and organic solvents used were of analytical reagent grade and were obtained from Sigma-Aldrich, South Africa. All aqueous solutions were prepared using ultrapure water obtained using a Milli-Q RO purification system.

3.2.2 Instrumentation

The spectrometric properties of RS and RT were determined using a Cintra Double beam UV-Vis spectrometer and a Perkin Elmer L550B Fluorimeter. ^{13}C and ^1H Nuclear Magnetic Resonance (NMR) spectra of RS, in DMSO-d_6 , and RT, in CDCl_3 , were determined with a 400 MHz Oxford NMR instrument. Values of RS and RT (complexed and uncomplexed) were compared to the previously published spectroscopic data and NMR spectra [17, 18]. Molecular ions for both RS and RT were determined by electron spray ionization mass spectroscopy ESI-MS with a Waters API Quattro Micro instrument.

3.2.3 Synthesis of rhodamine 6G derivative sensors

The RS sensor was synthesised according to a procedure of Wu *et al.* [17] with minor modifications and is briefly illustrated in Figure 3.2.

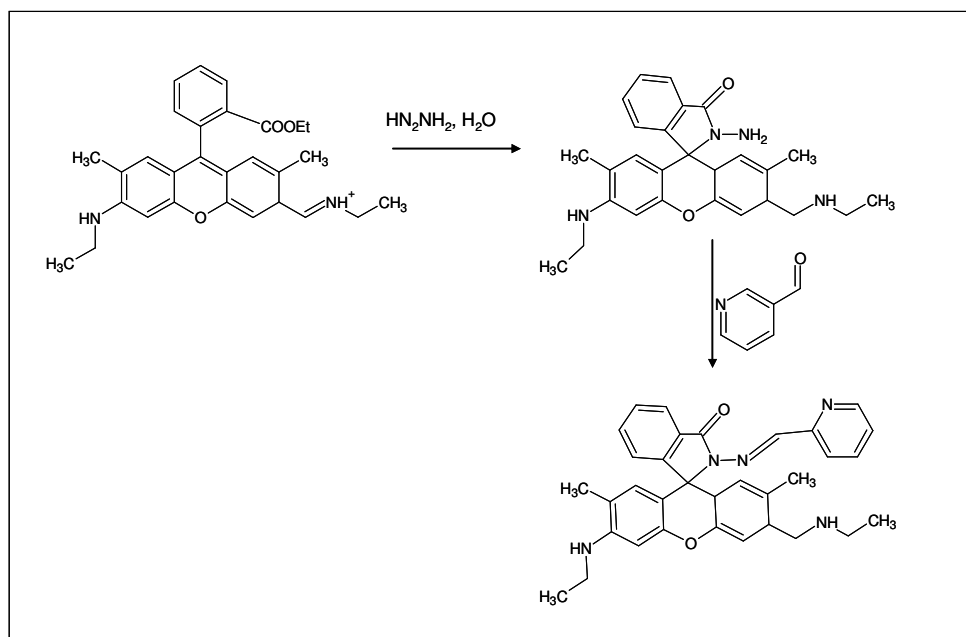


Figure 3.2: The synthesis route for compound RS.

The synthesis of the rhodamine 6G hydrazone was carried out according to a modified literature procedure [19] in which the pH of the solution was modified to increase the yield of rhodamine 6G hydrazone. Approximately 2 mmol 0.958 g Rhodamine-6G was dissolved in 30 mL ethanol in a 50 mL round-bottom flask. Under vigorously stirring at room temperature, 3 mL (excess) hydrazine monohydrate (85%) was then added dropwise to the reaction flask. The mixture was heated and allowed to reflux for 2 h. A purple solution formed. The mixture was then cooled overnight, and a pink precipitate formed. The precipitate was filtered off and washed three times with 15 mL EtOH/ water (1/1). The product was then dried over P_2O_5 in vacuum. The yield was approximately 90% rhodamine-6G hydrazone (Mr 428.26).

A 50 mL flask was charged with 0.428 g rhodamine 6G hydrazone, 0.15 g 2-pyridinecarboxaldehyde, 3 drops of acetic acid and 15 mL methanol. The mixture was stirred vigorously and then heated at 40 °C for 8 h, after which a further 0.5 g of 2-pyridinecarboxaldehyde was added. The mixture was allowed to react for an additional 8 hrs after which it was cooled to room temperature. The yield could be increased by extending the reaction time. The low boiling point of 2-pyridinecarboxaldehyde requires that approximately 0.5 g 2-pyridinecarboxaldehyde be added to the mixture every 8 h. An off-white to yellow coloured product was

formed after filtration with methanol/ ether (1:1), and drying over P_2O_5 in vacuum. The product was then purified by passing through a 20 cm column, made in a burette plugged with glass wool and filled with silica gel (Merck) 230-400 mesh, 60 Å. n-Hexane/ ethylacetate (1:1) was used as the eluent. The first fraction contained the product; after evaporation a white product was obtained.

The rhodamine 6G thiolactone derivative (RT) was synthesised according to the procedure described by Chen *et al.* [18] without modification. The synthesis route for RT is shown in Figure 3.3.

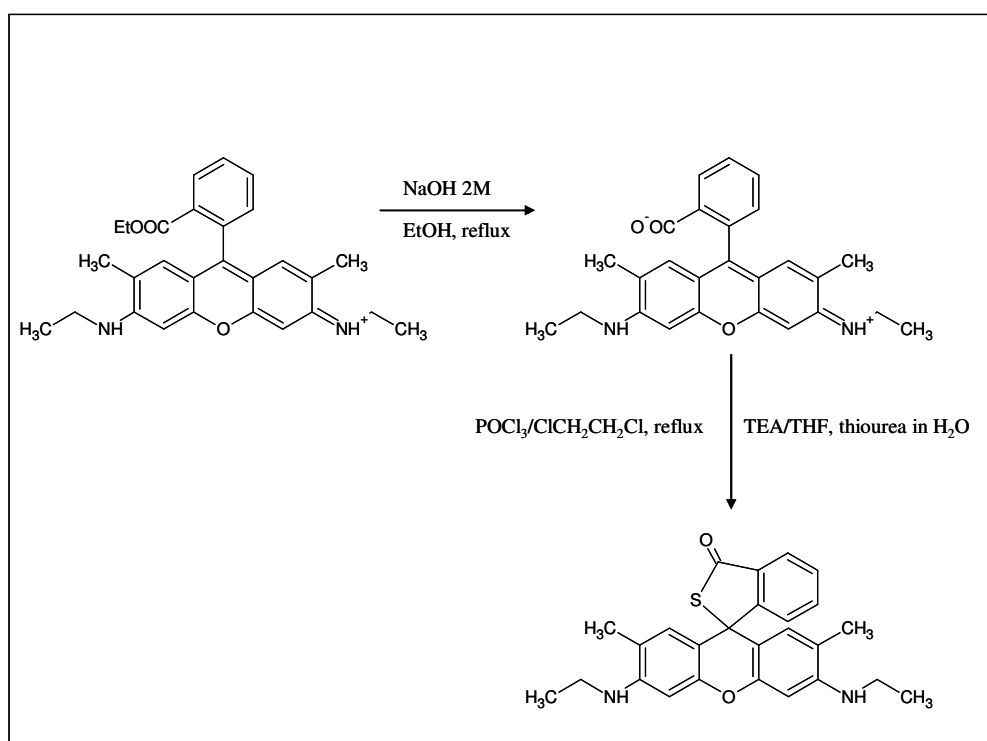


Figure 3.3: The synthesis route for compound RT.

3.3 Results and discussion

3.3.1 Characterization of the of rhodamine 6G hydrazone derivative (RS) sensor

NMR was used to verify the synthesis of the RS sensor, and was compared to the NMR spectrum published by Wu *et al.* [17]. The compound was synthesized with 95 to 98% purity.

The NMR spectra of RS are shown in Figure 3.4 and 3.5 and the characterization peaks obtained were as follows:

$^1\text{H-NMR}$ (DMSO-d_6): 8.44 (1 H, d, $J = 4.70$ Hz), 8.15 (1 H, s), 7.92 (1 H, d, $J = 6.16$ Hz), 7.78 (1 H, t, $J = 8.07$ Hz), 7.75 (1 H, s), 7.57 (2 H, q, $J = 7.48$ Hz), 7.30 (1H, t, $J = 4.67$ Hz), 7.01 (1 H, d, $J = 7.48$ Hz), 6.33 (2 H, s), 6.20 (2 H, s), 5.09 (2 H, t, $J = 5.43$ Hz), 3.13 (4 H, q, $J = 6.60$ Hz) 1.83 (6 H, s), 1.20 (6 H, t, $J = 7.19$ Hz); ^{13}C NMR (DMSO-d_6): 164.36, 153.44, 152.42, 151.43, 150.70, 149.55, 148.13, 144.36, 137.02, 134.48, 128.89, 127.49, 126.73, 124.46, 123.87, 123.39, 119.312, 118.65, 104.32, 96.016, 65.17, 37.63, 17.13, 14.35. ESI-MS: m/z 518.291 for $[\mathbf{1} + \text{H}]^+$.

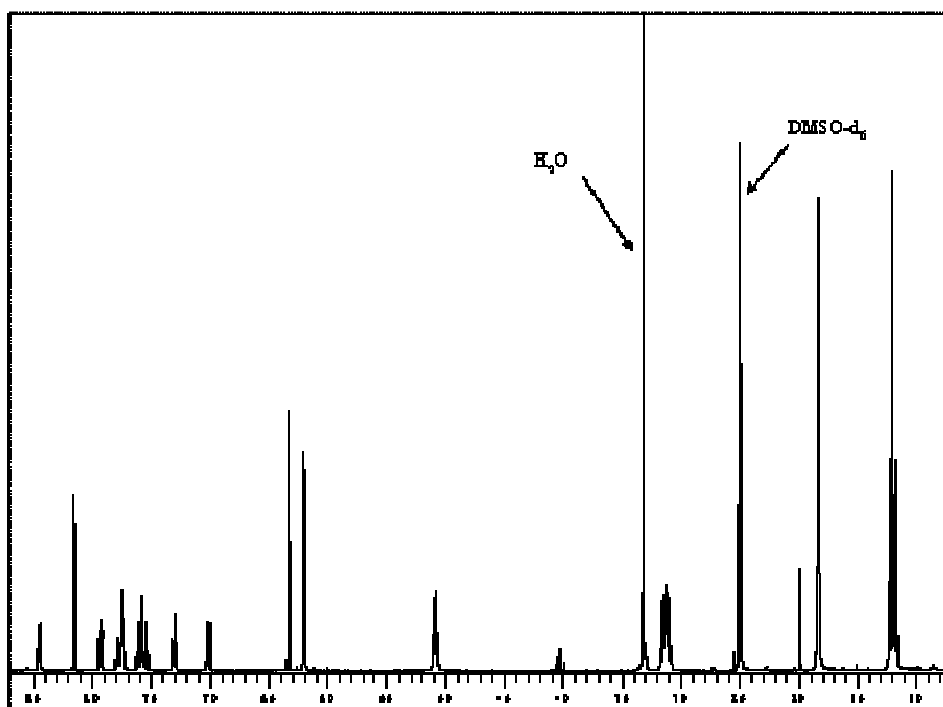


Figure 3.4: ^1H NMR spectrum of RS.

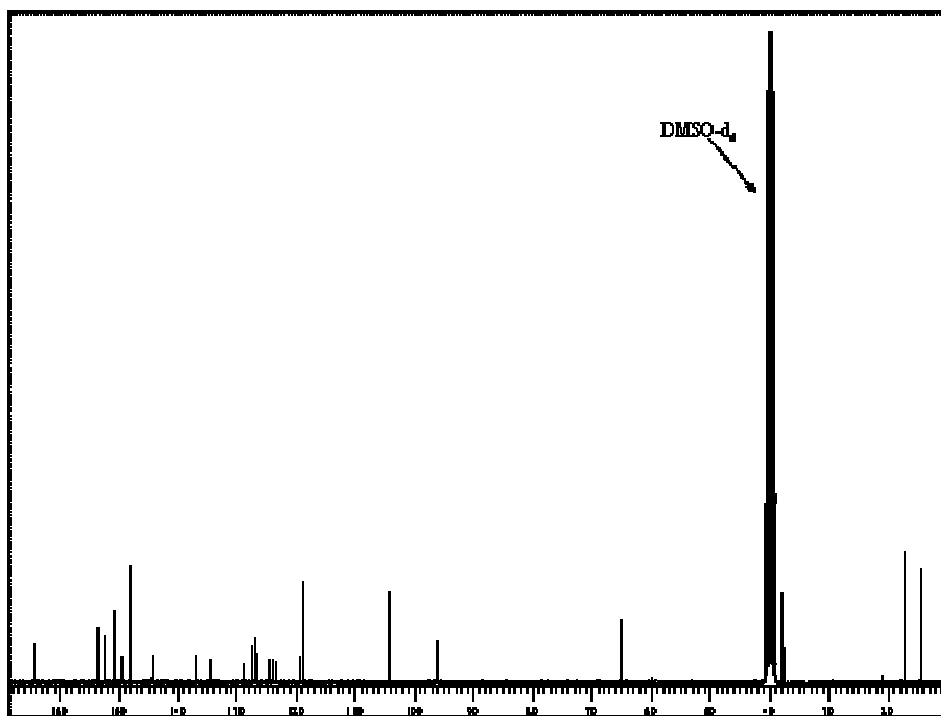


Figure 3.5: ^{13}C NMR spectrum of RS.

UV analysis of RS and the precursor, rhodamine 6G hydrazone, was performed in the presence and the absence of HgCl_2 . Rhodamine 6G hydrazone, the precursor used in the synthesis of RS, has a very strong absorbance and fluorescence. The latter were compared to the absorbance and fluorescence of RS. A wavelength scan of RS and rhodamine 6G hydrazone with Hg^{2+} was performed from 800 nm to 350 nm in a 1:1 aqueous dimethylformamide (DMF) solution. The absorption peak of the Hg-sensor complex was observed at 536 nm and the absorption peak of the Rhodamine 6G hydrazone was located at 524 nm. The absorbance for the Hg-sensor complex recorded by Wu *et al.* [17] was located at 538 nm. The peak height increased with increasing HgCl_2 added to 0.1 mM RS. The addition of HgCl_2 to rhodamine 6G hydrazone did not increase the peak absorption. The various spectrophotometric results are summarised in Figure 3.6.

For fluorescence the scan window was 520 nm to 650 nm scanned at 50 nm min^{-1} . The excitation wavelength was 500 nm with a split width of 5 nm. The emission peak for RS- Hg^{2+} was observed at 558 nm which increased with increasing HgCl_2 concentration. The concentration of the sensor was kept constant at 0.1 mM. The emission peak for the RS- Hg^{2+} complex shown in Figure 3.6 was observed in the

presence of $20 \mu\text{g L}^{-1} \text{HgCl}_2$. The Rhodamine 6G hydrazone emission peak was observed at 544 nm. The fluorescence peak of the Hg-sensor complex was comparable to 560 nm, as determined by Wu *et al.* [17].

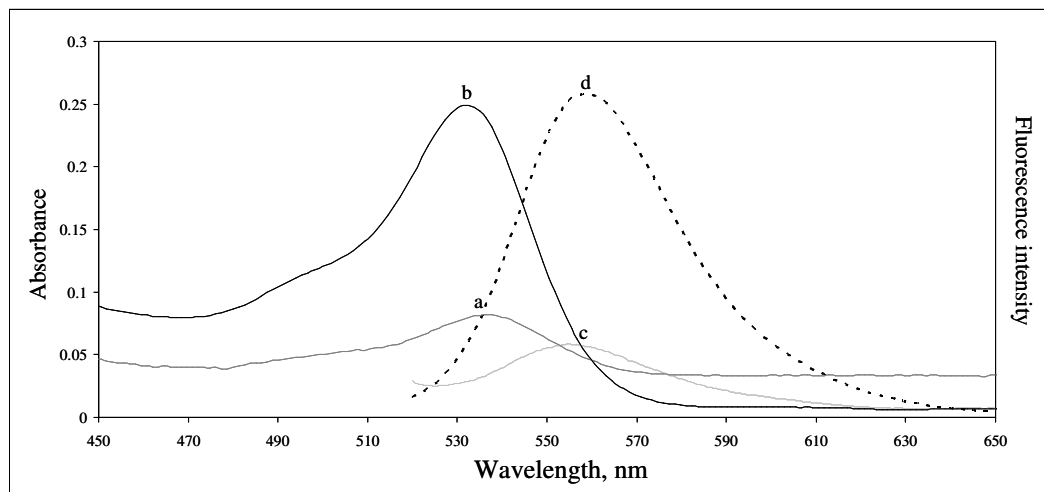


Figure 3.6: UV absorption and fluorescence emission of RS alone [(a) and (c)] and RS in the presence of HgCl_2 [(b) and (d)]. The fluorescent emission is scaled at 650:1 for comparison.

3.3.2 Characterization of the of rhodamine 6G thiolactone derivative (RT) sensor

The synthesis of the RT sensor presented fewer complications compared to the synthesis of the RS sensor. However, the RT sensor synthesis procedure resulted in a lower product yield (53%). The proton and carbon NMR spectra are shown in Figures 3.7 and 3.8 and the resultant characterization peaks obtained were as follows: $^1\text{H-NMR}$ (CDCl_3 , 400 MHz) δ (ppm): 7.86 (1 H, d, $J = 8.38$ Hz), 7.50 (2 H, m), 7.15 (1 H, d, $J = 7.11$ Hz), 6.518 (2 H, s), 6.295 (2 H, s), 3.506 (2 H, s), 3.21 (4 H, m), 1.92 (6 H, s), 1.31 (6 H, t, $J = 7.02$ Hz); $^{13}\text{C NMR}$ (CDCl_3 , 400 MHz): 198.38, 158.71, 151.03, 147.54, 135.80, 134.70, 130.08, 128.53, 127.67, 122.99, 118.49, 109.23, 96.78, 63.33, 38.77, 17.17, 15.17. ESI-MS $m/z = 431$ $[\text{M} + \text{H}]^+$.

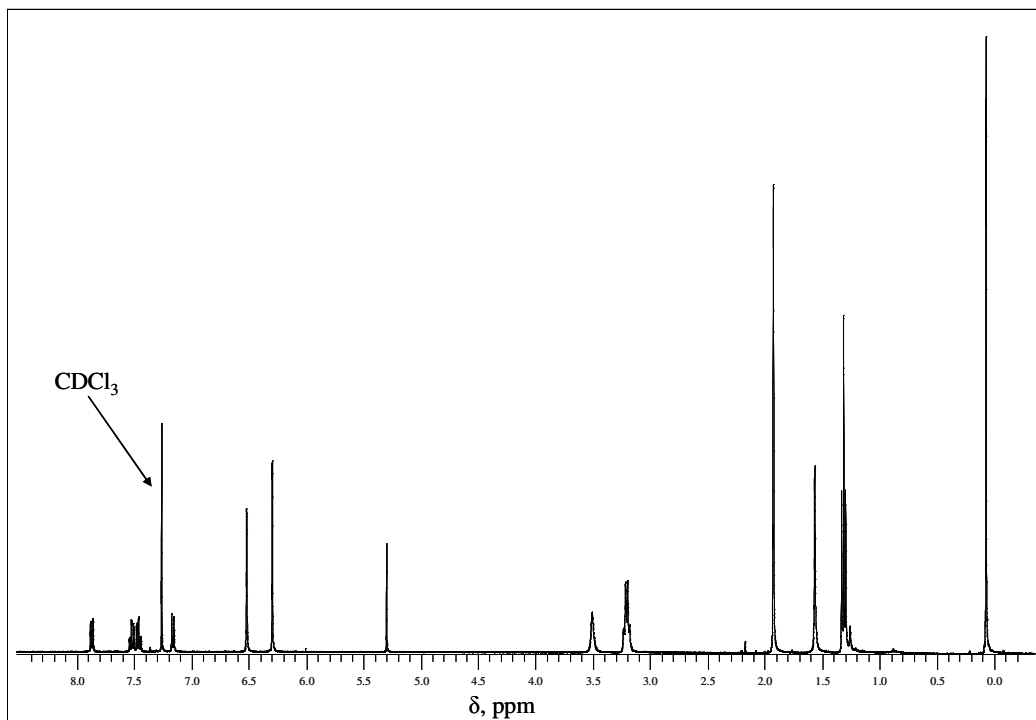


Figure 3.7: ^1H NMR spectrum of the RT sensor.

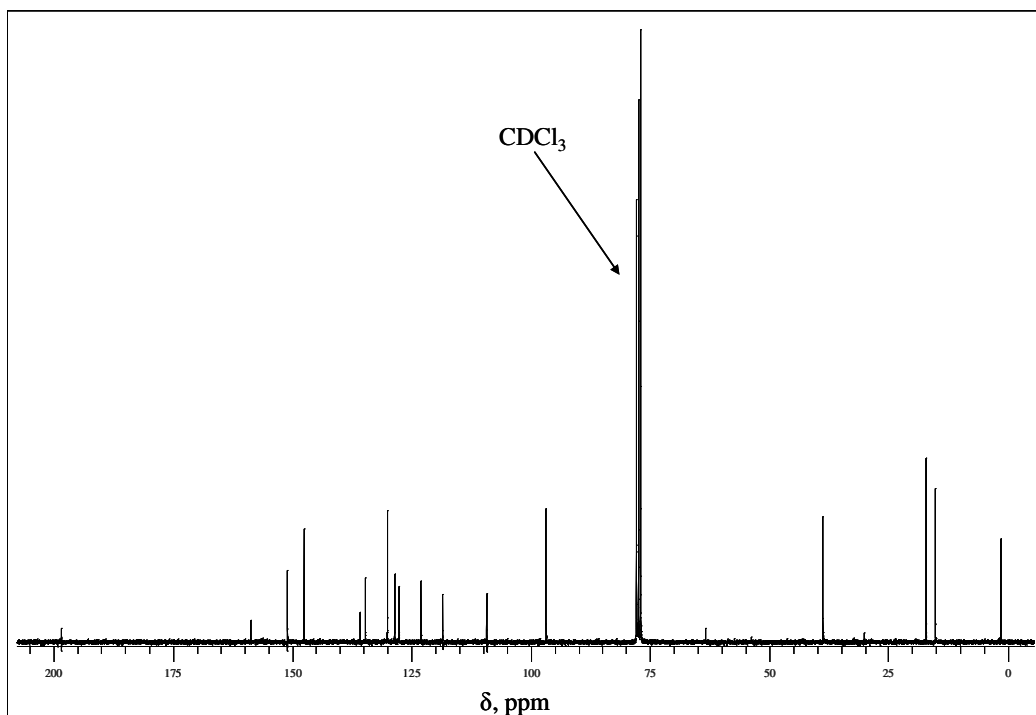


Figure 3.8: ^{13}C NMR spectrum of the RT sensor.

The spectrophotometric properties of the RT sensor in the uncomplexed and Hg-complexed form were determined in a 1:99 mixture of acetonitrile/ water. The results for the absorption and fluorescence spectra are summarised in Figure 3.9. The RT dye alone did not absorb in the visible region, but when complexed with Hg^{2+} , a strong absorption peak was observed at 529 nm. As reported in the literature [18], the complexation is a time controlled reaction that reaches a maximum absorption after 20 min reaction time. The fluorescence spectra were measured at a scan rate of 100 nm min^{-1} with a slit width of 5 nm. The excitation wavelength was 510 nm. The unreacted RT dye had a small (< 0.5 emission intensity) emission peak at 526 nm, but when ligated with Hg^{2+} , a single strong emission peak was observed at 552 nm.

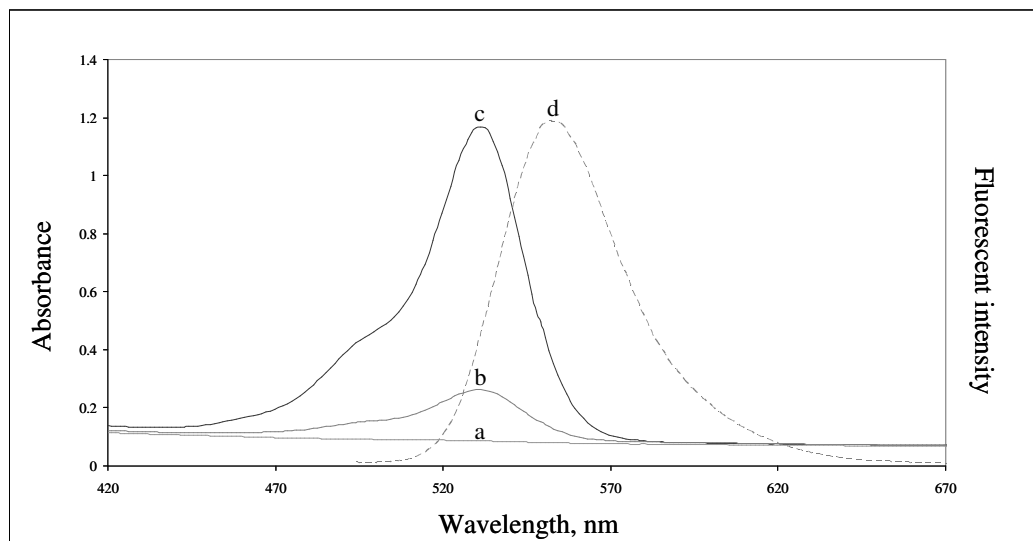


Figure 3.9: UV absorption of a) RT alone, b) RT in the presence of HgCl_2 and c) RT in the presence of HgCl_2 , complexed as RT- Hg^{2+} after 15 min. The fluorescent emission for d) RT- Hg^{2+} was scaled at 450:1 for comparison.

3.4 References

- [1] R.W. Cattrall, *Chemical Sensors*, Oxford University Press, Oxford, U.K., 1997, p. 2-29.
- [2] W.G. Holthoff, L.T. Tan, E.L. Holthoff, E.M. Cardone, F.V. Bright, in: R.A. Potyrailo and V.M. Mirsky (Eds.), *Combinatorial methods for chemical and biological sensors*, Springer, New York, 2008, p. 393-417.

- [3] E.M. Nolan, S.J. Lippard, *Chem. Rev.*, 108 (2008) 3443-3480.
- [4] K. Feng, F.L. Hsu, K. Bota, X.R. Bu, *Microchem. J.*, 81 (2005) 23-27.
- [5] L. Feng, Z. Chen, *Sens. Actuators, B*, 122 (2007) 600-604.
- [6] Y. Yu, L.R. Lin, K.B. Yang, X. Zhong, R.B. Huang, L.S. Zheng, *Talanta*, 69 (2006) 103-106.
- [7] Z.X. Cai, H. Yang, Y. Zhang, X.P. Yan, *Anal. Chim. Acta*, 559 (2006) 234-239.
- [8] J. Chen, A. Zheng, A. Chen, Y. Gao, C. He, X. Kai, G. Wu, Y. Chen, *Anal. Chim. Acta*, 599 (2007) 134-142.
- [9] C.L. He, F.L. Ren, X.B. Zhang, Z.X. Han, *Talanta*, 70 (2006) 364-369.
- [10] C.N. Burrell, M.I. Bodine, O. Elbjeirami, J.H. Reibenspies, M.A. Omary, F.P. Gabbai, *Inorg. Chem.*, 46 (2007) 1388-1395.
- [11] Y. Zhao, Z. Lin, C. He, H. Wu, C. Duan, *Inorg. Chem.*, 45 (2006) 10013-10015.
- [12] A.P. De Silva, H.Q.N. Gunaratne, T. Gunnlaugsson, A.J.M. Huxley, C.P. McCoy, J.T. Rademacher, T.E. Rice, *Chem. Rev.*, 97 (1997) 1515-1566.
- [13] E.M. Nolan, S.J. Lippard, *J. Mater. Chem.*, 15 (2005) 2778-2783.
- [14] W. Huang, C. Song, C. He, G. Lv, X. Hu, X. Zhu, C. Duan, *Inorg. Chem.*, 48 (2009) 5061-5072.
- [15] H.N. Kim, M.H. Lee, H.J. Kim, J.S. Kim, J. Yoon, *Chem. Soc. Rev.*, 37 (2008) 1465-1472.
- [16] J.S. Wu, I.C. Hwang, K.S. Kim, J.S. Kim, *Org. Lett.*, 9 (2007) 907-910.
- [17] D.W. Wu, W. Huang, C. Duan, Z. Lin, Q. Meng, *Inorg. Chem.*, 46 (2007) 1538-1540.

[18] X. Chen, S.W. Nam, M.J. Jou, Y. Kim, S.J. Kim, S. Park, J. Yoon, *Org. Lett.*, 10 (2008) 5235-5238.

[19] Y. Xiang, A. Tong, P. Jin, Y. Ju, *Org. Lett.*, 8 (2006) 2863-2866.

Chapter 4

Spectrophotometric evaluation of rhodamine 6G derivative chemosensors with polyaniline and TiO₂ in solution phase

4.1 Introduction

In Chapter 3, it was established that both the rhodamine 6G hydrazone derivative (RS) and rhodamine 6G thiolactone (RT) chemosensors synthesised and characterised were sensitive to aqueous Hg²⁺, and had a high quantum yield: However their application in photoelectrochemical cells (PECs) depend on their photometric responses in the presence of charge separators. Photoelectrochemical detection requires that the photon excitation of the chemosensor in the presence of Hg²⁺ be converted to an electron transfer. The electron transfer is achieved when the photon-induced electrons and electropositive holes are successfully separated.

The roles of the rhodamine excited states and free radicals are crucial in the mechanism of electron transport. Excitation of rhodamine dyes occurs to a singlet excited state, but relaxation of the electrons soon occurs to the triplet state. It has been reported that the lifetime of the electrons in the triplet state depends on the local environment such as the solvent environment, and it ranges from 250 ns to 3400 μs [1]. Rhodamine dye free radicals can be formed as a result of reactions of rhodamine excited states with suitable donors and acceptors. Xanthene dyes, like rhodamine 6G (R6G), are expected to form the corresponding semi-reduced forms more than the semi-oxidised forms.

Electron transfer can occur from three different states in the excited rhodamine molecule [1-4], namely:

- The excited singlet state, which would mean direct electron injection
- The triplet state, which has a longer lifetime, and
- from the formation of free radicals.

The state from which rhodamine electron transfer occur, depends mainly on its surrounding electron donating or accepting environment. The fate and transport of the excited electrons in rhodamine dyes after absorption of a photon are shown in Figure

4.1. Previous studies have shown that, in the case of radical formation, the energy transfer in rhodamine compounds occurs mainly by anionic radicals, which resemble triplet-triplet transitions [1].

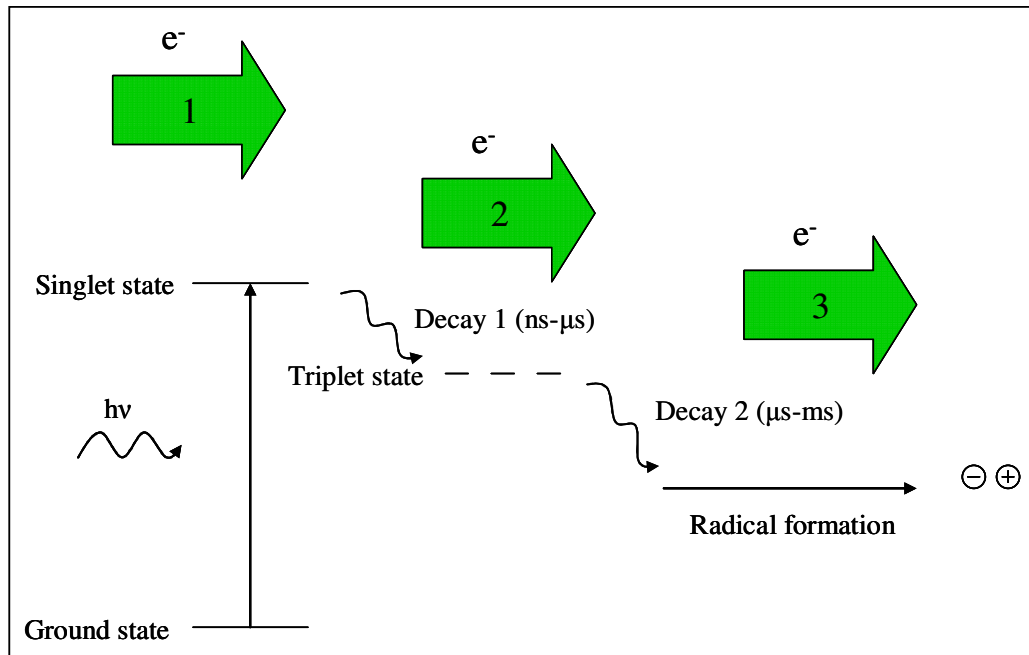


Figure 4.1: The fate and transport of the excited electrons in rhodamine dyes after the absorption of a photon.

Rhodamine dyes can also interact with each other in solution and on substrate surfaces; these interactions include forming monomers, H-dimers and J-dimers, all of which influence the photoluminescence properties of the rhodamine dyes [2, 3]. Other influences are the presence of counter ions and moving from wet solutions to dry surfaces [4].

For photoelectrochemical detection, the adsorption and interaction of the chemosensor with the charge separators are crucial for the electron transfer process. As the mechanism of electron transfer for rhodamine compounds depends on their environment, the photoresponse of the dye should differ in the presence of an n- or p-type semiconductor. To investigate the photoresponse of the chemosensors, the spectrophotometric responses were determined in the presence of two charge separators: TiO₂ and polyaniline (PANI).

4.1.1 Rhodamine 6G chemosensors, in the presence of TiO₂

TiO₂ is an electron acceptor with surface hydroxyl and oxide functional groups which can lead to various pH dependant interactions with rhodamine dyes. The interaction of the hydroxylated porous oxide surface with a cationic dye molecule is vital during the absorption process. Hamad *et al.* [5], for example, report that the R6G molecules only begin to be incorporated within the pores of TiO₂ films when the pH of the solution is either higher or at the point of zero charge (PZC) of TiO₂ [5]. According to Hamad *et al.* [5], the maximum adsorption of R6G will occur at basic pH. This is however not unexpected, due to electrostatic attraction between the cationic dye and the negatively charged surface. Hamad *et al.* [5] further reported that, during the simulations, the phenyl moiety of the R6G molecule is often inserted within the region previously occupied by the hydroxyl group. The fluorescent quenching of dyes by colloidal TiO₂ is well documented [6-8]. Kathiravan *et al.* [6] assigned the fluorescent quenching of xanthene compounds like eosin, rhodamine B and R6G to an electron transfer mechanism. Photochemical studies of dyes sensitization of TiO₂ via electron injection into the TiO₂ conduction band (CB) by an excited dye indicated that the following steps are involved [6, 7, 9, 10]:



Spectrophotometrically, the electron transfer process is therefore from the singlet excited state, which leads to a quenching of the florescent response of the xanthene dye. The electron transfer is a form of electron injection on the picosecond timescale.

4.1.2 Rhodamine 6G chemosensors, in the presence of PANI

PANI has three oxidation states (Figure 4.2 A): (a) a fully reduced leucoemeraldine base (LEB), (b) a fully oxidised pernigraniline base (PNB), and (c) a half oxidised/half reduced emeraldine base (EB) state. Of these oxidation states it is the EB that is conductive and responsible for the electropositive hole conduction in PANI. The deprotonation of the EB form of PANI leads to bipolaron and more stable polaron structures, as shown in Figure 4.2 B. A polaron structure is formed through

the successive formation of bipolaronic species and is responsible for electrical conduction through the intra-chain or inter-chain hopping mechanism in the crystalline regions in PANI [11, 12].

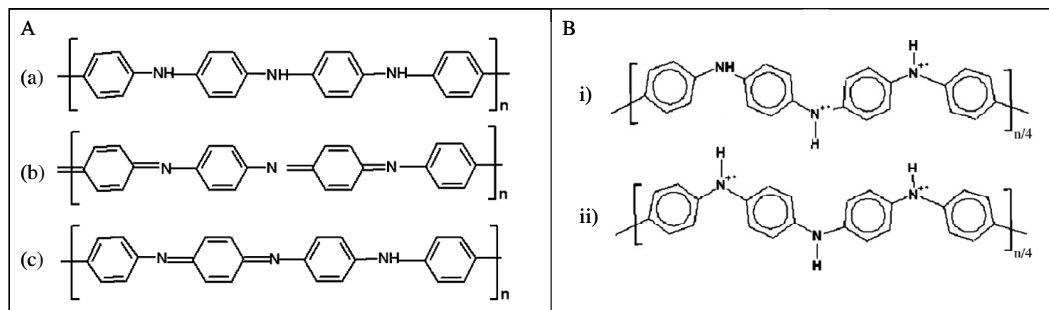


Figure 4.2: A) The three oxidation states of PANI: (a) a fully reduced LEB, (b) a fully oxidised PNB, and (c) a half oxidised/half reduced EB. B) The i) bipolaron and ii) polaron structures in EB polyaniline.

In the polaron structure a cation radical of one nitrogen acts as the hole and these holes are charge carriers. The electron from the adjacent nitrogen (neutral) neutralises the hole in the PANI. Consequently, the holes start to migrate. As a result, another hole is created on the second nitrogen. Thus, in the polaron structure an electron starts moving along the polymer chain in one particular direction and the corresponding electropositive hole is set into motion along the chain length in the opposite direction, leading to an electrical conduction along the chain. However, in the case of a bipolaron structure, this type of movement of the electron and hole is not possible since the two electropositive holes are located adjacent to each other [13].

The interaction of PANI and rhodamine dyes has not been reported previously, but it is likely that the PANI hole conduction assists in the conduction of the electropositive holes in the rhodamine dye, following the absorption of a photon. In the presence of PANI alone the mechanism of electron transfer would be more complex, and would depend on the redox couple of the electrolyte. Energy transfer would then be due to anionic radicals formed on longer timescales. Spectrophotometrically the fluorescence of the xanthene dye should also be quenched in the presence of PANI.

4.2 Materials and methods

4.2.1 Materials

All chemicals and organic solvents used were of analytical reagent grade and were obtained from Sigma-Aldrich, South Africa. The water was distilled once, followed by a deionising process with a Milli-Q RO purification system.

4.2.2 Instrumentation

The spectrometric properties of the RS and RT chemosensors were determined with a Cintra double beam UV-Vis spectrometer and a Perkin Elmer L550B fluorimeter. Spectrophotometric measurements were conducted at a scan rate of 150 nm min⁻¹, using a slit width of 5 nm, in 4 × 1 × 1 quartz cuvettes.

4.2.3 Sample preparation

The TiO₂ sol-gel was synthesised according to two procedures. The following sol-gel preparation methods were used:

- i. The method as described by Srikanth *et al.* [14], in which the sol-gel is in a strong nitric acid environment.

A dilute titanium isopropoxide solution was added dropwise to 10 mL deionized water at 0 °C, while stirring vigorously. The final ratio of titanium alkoxide, ethanol and water was 1:1:10. Thereafter, 1.5 mL of 65% aqueous HNO₃ was added and the resultant solution was heated at 80 °C for 8 h. The concentration of undiluted sol-gel was 0.3 M. The acidic sol-gel was used to determine the influence of the TiO₂ surface charge and the presence of protons in the dye-TiO₂ samples.

- ii. The method as described by Kathiravan and Renganathan [9].

In this procedure the prepared Ti precursor and organic solvent were injected directly into dimethyl formamide (DMF) and stirred for 8 h under a N₂ atmosphere. The sizes of the DMF prepared sol-gel particles were calculated by Kathiravan and Renganathan [9] to be 1.92 nm. The final concentration was 0.01 M titania stock solution. It was stable for only three days, after which it formed larger colloidal suspensions.

PANI was prepared according to standard chemical oxidation polymerization methods [15]. PANI was also dissolved either in N-methylpyrrolidone (NMP) or dimethyl

sulfoxide (DMSO) to investigate the influence of the PANI surface charge on the spectrophotometric properties of the rhodamine chemosensors.

The rhodamine selective dyes RS and RT were prepared according to the procedure set out in Section 3 and references [16] and [17]. Both dyes were dissolved in DMF, 1 g L⁻¹ RS and 1 g L⁻¹ RT. The samples were buffered in 0.005 M NaH₂PO₄- Na₂HPO₄ at pH 6.5.

For the acidic sol-gel samples, 40 µL of the TiO₂ stock was added to 5 mL of water or phosphate buffer. The dye was complexed with Hg²⁺ prior to addition to the TiO₂ samples. The DMF sol-gel was added to water or buffer at 100 µL per 5 mL sample and bubbled with N₂ gas. The samples containing PANI (dissolved either in NMP or DMSO) were added as 100 µL aliquots to 5 mL 1:1 aqueous DMF containing 100 µL of Hg²⁺ complexed dye.

4.3 Results and discussion

4.3.1 Spectrophotometric evaluation of RS and TiO₂

Detection of the RS chemosensor was achieved by the opening of the rhodamine spirolactam ring and releasing of the fluorescent xanthene. In the presence of an acidic TiO₂ sol-gel the spirolactam ring was opened and the RS sensor was converted to a zwitterion containing both positively charged amine groups and a negatively charged carbohydrazone block. The spirolactam ring opening in acidic media has been documented by Shi and Ma [18].

The spectrophotometric influence of TiO₂ on RS-Hg²⁺ was investigated using TiO₂ made in DMF, to eliminate acidic ring opening. The absorbance of RS-Hg²⁺ at 526 nm was decreased when added to TiO₂ in both buffer and water, which also resulted in a lower fluorescent intensity. The emission peak of RS-Hg²⁺ at 551 nm was red shifted to 547 nm when added to TiO₂. Although there was a slight decrease in the absorbance peak, the fluorescence was significantly quenched. The quenching of xanthene fluorescence has been reported to be due to an electron transfer mechanism [6]. The spectrophotometric results for RS-Hg²⁺ with DMF-TiO₂ are summarised in Figure 4.3. It is likely that the electron transfer occurred from the RS-Hg²⁺ excited state to either the conductive band or valence band of TiO₂. As the conductive band of

TiO₂ is already at a reasonably high energy state, transfer to the valence band of TiO₂ is far more likely.

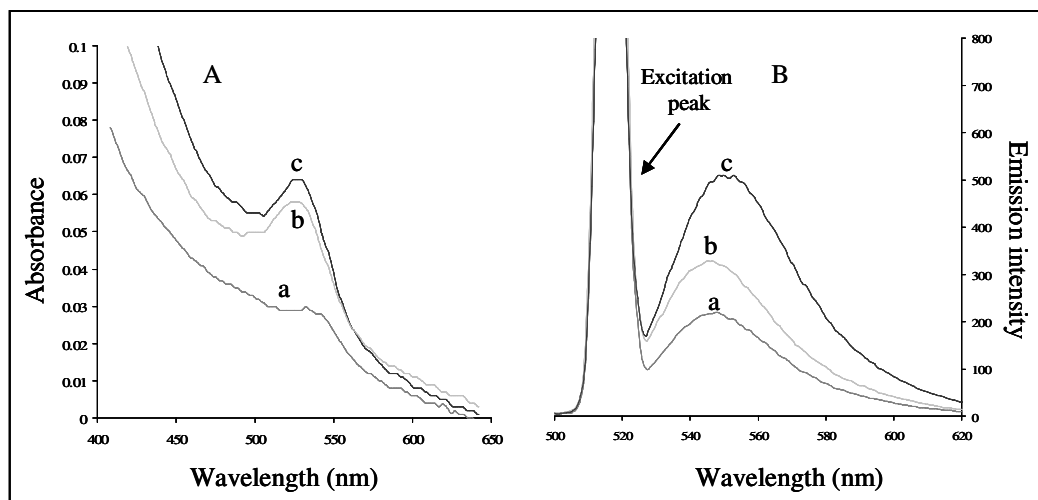


Figure 4.3: A) The absorbance peaks of a) TiO₂-RS, b) TiO₂ and RS-Hg²⁺ and c) RS-Hg²⁺ in 0.005 M phosphate buffer. B) The fluorescence emission of TiO₂ a) with RS b) and with RS-Hg²⁺ after excitation at 520 nm.

The Stern-Volmer plot of the fluorescent quenching of RS-Hg²⁺ by TiO₂ was not linear as seen in Figure 4.4. The Stern-Volmer plot is generally used to determine the rate constant for quenching [19]:

$$\frac{I_f^0}{I_f} = 1 + \frac{k_q}{k_f} [Q] \quad (1)$$

where I_f^0 : fluorescence emission of a fluorophore in solution

I_f : the quenched fluorescence emission of the solution

k_f : the rate constant of the fluorophore in solution

k_q : the rate constant of the quenched solution

[Q]: the concentration of the quencher

The lack of linearity in the Stern-Volmer plot for TiO₂ quenching indicates that the quenching is not entirely dependent on the concentration of TiO₂. The TiO₂ nanoparticles are comparable in size to the RS-Hg²⁺ complex, and hence the quenching would be limited by the physical contact of TiO₂ and the RS-Hg²⁺ molecule. It was found that the quenching increased when colloidal particles are

formed, but that the fluorescent quenching could not be determined due to increased light scattering in the fluorescent samples by the colloidal particles. Initially the Stern-Volmer plot for TiO₂ quenching appeared linear, suggesting that quenching was taking place according to the donor-acceptor model. After the addition of 20 μL of TiO₂ the graph became non-linear, suggesting that the mechanism had changed. The mechanistic change is likely due to increased TiO₂ particle size approaching a “solid state” environment for the excited dye. It would then mean that the latter part of the Stern-Volmer plot presents the quenching of the dye by a TiO₂ “solid”.

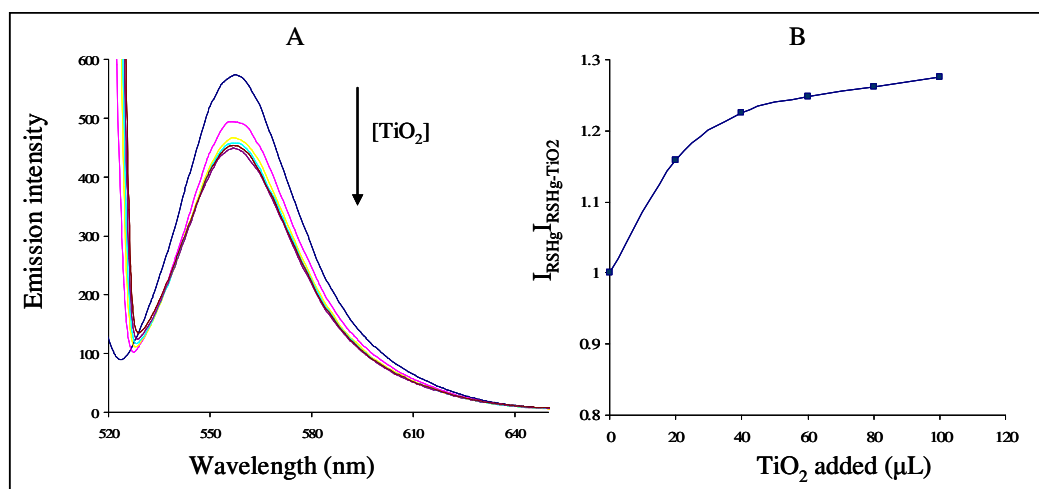


Figure 4.4: A) The fluorescent quenching of RS-Hg²⁺ by increasing the concentration of TiO₂. B) The Stern-Volmer plot of the quenched fluorescence intensity versus the addition of 0.03 M TiO₂ in DMF.

4.3.2 Effect of phosphate on the spectrophotometric properties of RS

The characteristic absorbance peak of the RS xanthene chromophore was observed at 536 nm and the fluorescent emission peak at 565 nm, in the presence of TiO₂. For TiO₂ and RS in 0.005 M phosphate buffer, an additional peak was observed upon the addition of Hg²⁺, at 505 nm. The additional absorbance peak is linked to the dimer formation of the rhodamine 6G chromophores. The dimerization was observed for the RS-Hg²⁺ complex in the presence of phosphate-rich TiO₂. The reaction as well as the activity of TiO₂ was pH dependent. At lower pH (pH 2 to pH 4) the 532 nm absorbance band was considerably higher than the band observed at 505 nm, and the band at 505 nm increased with increasing pH. It is likely that the PO₄³⁻ created an electronegative layer around the TiO₂ colloidal particle. The rhodamine dye was

accordingly polarised with the nitrogen rich group directed towards the phosphate groups. The electropositive side was freed to engage the free Hg²⁺ ions in solution. With the rhodamine groups immobilised on the TiO₂, the Hg²⁺ is likely to coordinate in a 2:1 reaction with the RS sensor, thereby creating a dimer that is immobilized onto TiO₂ with PO₄³⁻. Such binding is considerably more effective in the absence of H⁺. According to Tomás *et al.* [20], dimerization of rhodamine chromophores is also characterised by a decrease in the fluorescence response. As seen in Figure 4.5 the fluorescence of the RS xanthene chromophore was significantly reduced upon the addition of HgCl₂. An excess of rhodamine and PO₄³⁻ resulted in a decrease in active surface area of TiO₂. The absorbance shoulder observed for RS-Hg²⁺, or spiro-lactam opened RS, is due to the second vibrational state for the opened complex [19]. The selectivity of the micelle formation was almost exclusively selective for Hg²⁺ at pH 6.5. The spectrophotometric properties of TiO₂-RS in phosphate-rich solutions is summarised in Figure 4.5.

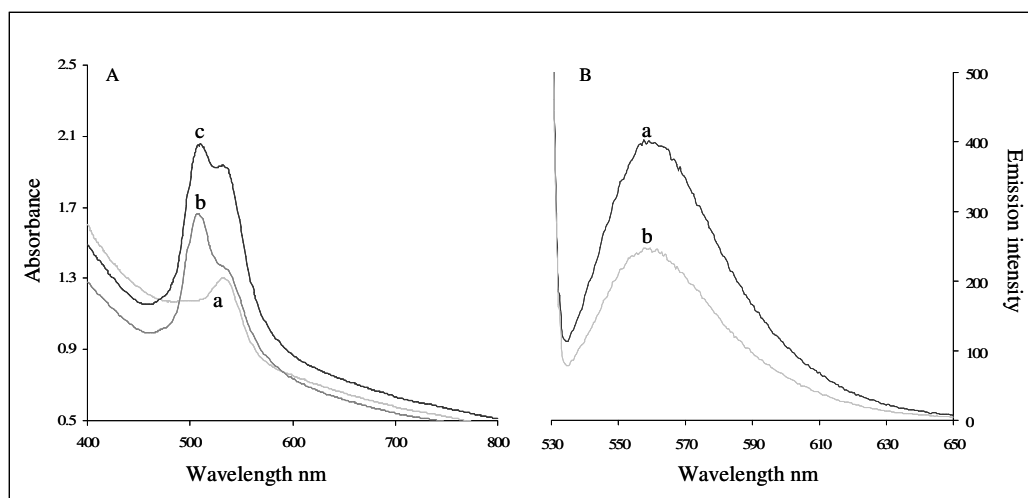


Figure 4.5: A) The absorption peaks of a) TiO₂-RS, b) TiO₂ and RS-Hg²⁺ and c) TiO₂-RS-Hg²⁺ with additional RS-Hg²⁺ in 0.005 M phosphate buffer. B) The emission intensity of TiO₂ a) with RS and b) with RS-Hg²⁺ in phosphate buffer after excitation at 520 nm.

The dimerization observed in the presence of acidic TiO₂ was not observed when the complexed dye was added to DMF-TiO₂ in phosphate buffer. This was mostly due to the lack of Ti-OH₂⁺ and Ti-OH⁺-Ti surface groups at higher pH, and the nanoparticle

size of DMF-TiO₂. The TiO₂ sol-gel particles are considerably larger than the DMF/sol-gel particles, allowing for phosphate linking as well as RS attachment.

4.3.3 Spectrophotometric evaluation of RS and PANI

The spectrophotometric influences of PANI on the RS-Hg²⁺ complex were determined with PANI in two conductive states of emeraldine. The two states were achieved by dissolving the PANI in DMSO and NMP, and they were referred to as PANI-DMSO and PANI-NMP, respectively. The PANI-DMSO, which is blue in colour, corresponds to a doped form of emeraldine in which the imine groups are protonated [21]. PANI-NMP, which is green in colour and considerably more basic, has more imine links than amine links, and is therefore slightly more oxidised.

The absorbance and fluorescence results for RS with the addition of PANI are summarised in Figures 4.6 and 4.7.

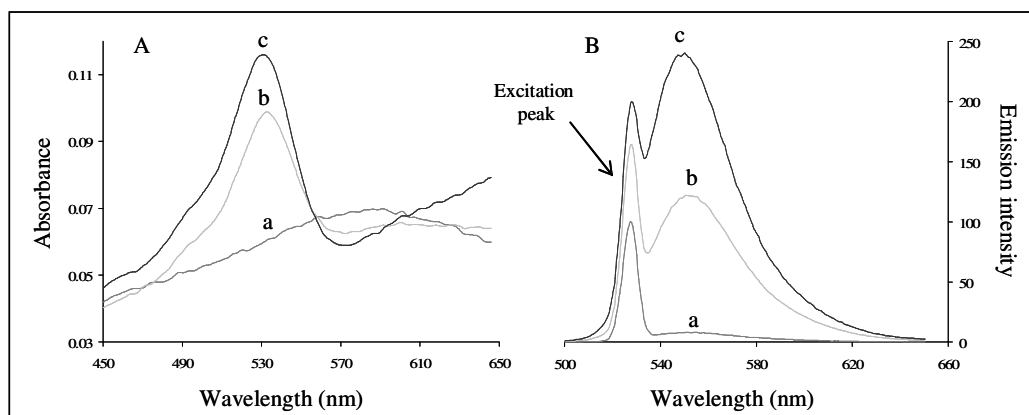


Figure 4.6: A) The absorbance peaks of a) DMSO-PANI-RS, b) DMSO-PANI and RS-Hg²⁺ and c) RS-Hg²⁺ in 1:1 aqueous DMF. B) The fluorescence emission for DMSO-PANI a) with RS and b) with RS-Hg²⁺ after excitation at 520 nm.

The absorbance peak of RS-Hg²⁺ shifted to 533 nm in aqueous DMF 1:1. It was not influenced by the presence of DMSO-PANI and blue shifted only 2 nm upon the addition of NMP-PANI. The fluorescence emission of RS-Hg²⁺ in aqueous DMF after excitation at 530 nm was observed at 550 nm, which blue shifted to 553 nm with the addition of NMP-PANI. The wavelength shifts in these spectrophotometric spectra are most likely due to changes in the nature of the solvents used. The absorbance

decreased slightly upon the addition of either form of PANI, and the fluorescence decreased significantly.

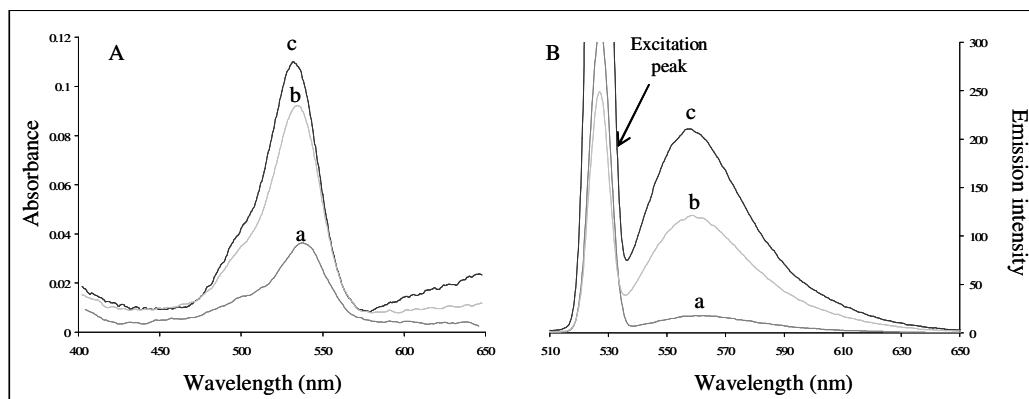


Figure 4.7: A) The absorption peaks of a) NMP-PANI, b) NMP-PANI and RS-Hg²⁺ and c) RS-Hg²⁺ in 1:1 aqueous DMF. B) The fluorescence emission for NMP-PANI a) with RS and b) with RS-Hg²⁺ after excitation at 520 nm.

The quenching of the RS-Hg²⁺ complex by PANI-DMSO was determined as a function of the PANI concentration. The quenching results are shown in Figure 4.8 A. The ratio of the intensities of the RS-Hg²⁺ complex in the presence and the absence of PANI were plotted against the PANI concentration. Results are shown in the Stern-Volmer plot presented in Figure 4.8 B.

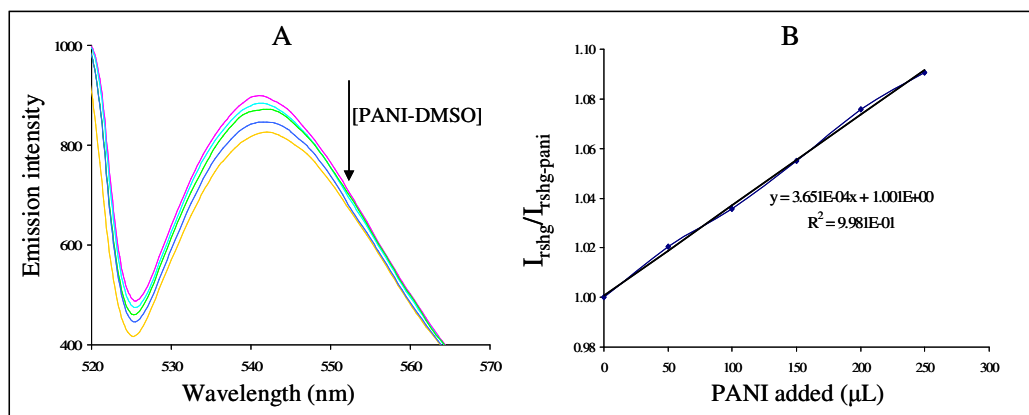


Figure 4.8: A) Fluorescent quenching of RS-Hg²⁺ with PANI-DMSO in 1:1 aqueous DMF. B) The Stern-Volmer plot for the addition of PANI-DMSO to RS-Hg²⁺.

The quenching results yielded a linear graph. The results showed a y intercept at 1, the slope of which was equal to the ratio of the rate constants of RS-Hg²⁺ in the presence and absence of the PANI-DMSO. The excited RS-Hg²⁺ molecules either rearranged in the presence of PANI, thereby resulting in a decreased fluorescence, or the electropositive holes were conducted to PANI, thereby releasing the excited electrons from the excited dye to the solvent environment.

4.3.4 Spectrophotometric evaluation of RT dye and TiO₂

The RT absorbance peak shifted to 527 nm in the presence of TiO₂ in H₂O (from 529 nm in 1:99 acetonitrile: H₂O). As a rule, the solvent determines the wavelength of the absorbance peak and not the presence of TiO₂. The small shoulder on the absorbance peak is the excitation to the second less populated vibrational state in the excited state [19]. The xanthene moiety of RT is not released in TiO₂ alone. Hence, all excitation and emission is determined by the ring-opening in the presence of Hg²⁺. The fluorescent emission peak for RT-Hg red shifted considerably to 542 nm upon excitation at 520 nm. This could be attributed to solvent interaction between H₂O and the RT chromophore. The ring-opened RT-Hg complex is polar, and solvent interaction with more polar solvents such as 1:250 DMF:H₂O compared to 1:99 acetonitrile:H₂O will influence the wavelength of emission. The spectrophotometric evaluation of RT-Hg is shown in Figure 4.9.

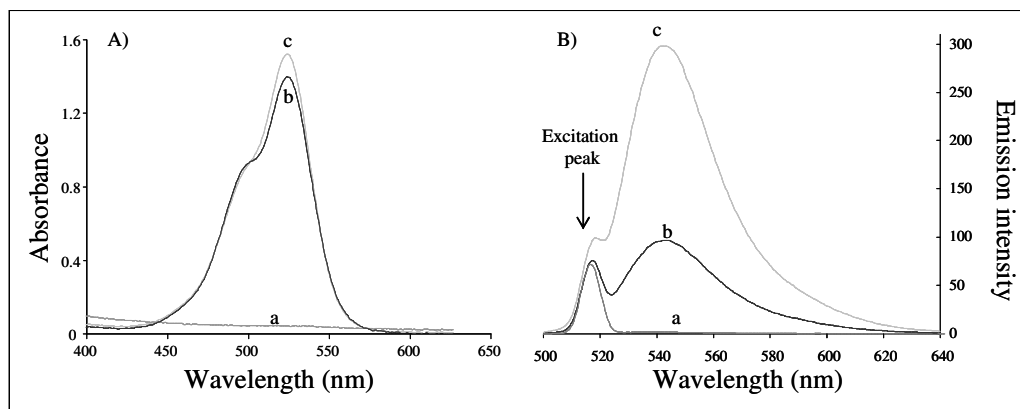


Figure 4.9: A) The UV absorbance and B) fluorescence emission of 2.4×10^{-5} M RT 1:25 aqueous DMF a) with TiO₂, b) with excess Hg²⁺ and c) added to TiO₂ after complexed with Hg²⁺. The RT samples for fluorescent emission were diluted with H₂O to 1:250 and excited at 520 nm.

The fluorescent increase in the presence of TiO₂ is most likely due to the reorganization of the moieties upon excitation and chemical interaction between the TiO₂ and the RT-Hg²⁺ molecule. The exact interaction should be monitored on short timescales by flash photolysis. From the results obtained, it was however evident that electron injection did not occur from the RT-Hg excited state into the TiO₂ valence or conductive band.

The effect of phosphate was also investigated to determine if any immobilization of RT by phosphate onto TiO₂ occurs, as seen with the RS compound in Section 4.3.2. The RT dye was added to 0.005 M phosphate buffer at pH 6.5. The spectrophotometric results are shown in Figure 4.10.

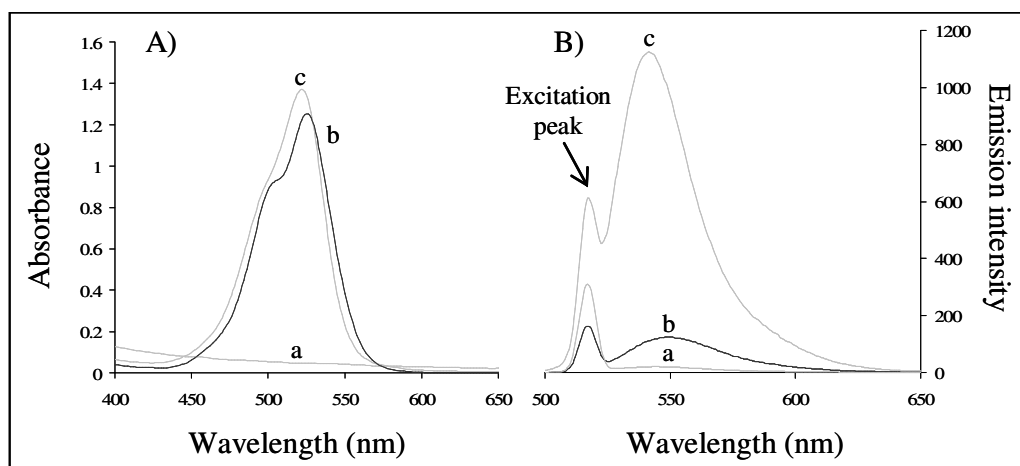


Figure 4.10: A) The UV absorbance and B) fluorescent emission of 2.4×10^{-5} M RT 1:25 DMF:0.005 M phosphate buffer a) with TiO₂, b) with excess Hg²⁺ and c) added to TiO₂ after complexed with Hg²⁺. The RT samples for fluorescent emission were further diluted with 0.005 M phosphate buffer to 1:250 and excited at 520 nm.

The absorbance peak of RT-Hg in buffer alone was observed at 526 nm, which is similar to what was observed for RT-Hg in H₂O. The RT-Hg absorbance peak however red shifted to 522 nm when it was added to phosphate-rich TiO₂. The absorbances of RT-Hg in H₂O and in phosphate buffer were identical. The fluorescence emission of RT-Hg in phosphate buffer was however significantly less (quenched) when compared to that in H₂O alone. The emission peak of the RT-Hg chromophore red shifted from 550 nm to 542 nm when added to TiO₂ in phosphate

buffer. Therefore, unlike the case of the RS chemosensor, the RT chemosensor was not immobilised onto TiO₂ via phosphate groups. This is most likely due to the stability of the spirothiolactone of the RT chemosensor in the presence of H⁺ and the differences in the Hg²⁺ binding event of the RS and RT chemosensors. The RS binding of Hg²⁺ is delocalised over the carbohydrazone block [16] whereas the RT chemosensor is bound by two sulphur atoms [17].

4.3.5 Spectrophotometric evaluation of RT dye and PANI

The spectrophotometric properties of the RT chemosensor were also evaluated in the two partially oxidised emeraldine forms of PANI. The absorbance peak for RT-Hg red shifted to 534 nm in 1:1 aqueous DMF (from 529 nm in 1:99 acetonitrile: H₂O). The absorbance peak was slightly increased when RT-Hg was added to PANI-DMSO, but remained unchanged in PANI-NMP.

The fluorescence emission peak of RT-Hg in 1:1 aqueous DMF was at 558 nm after excitation at 530 nm. The presence of PANI-NMP did not influence the position or the intensity of the fluorescent emission peak of RT-Hg. The spectrophotometric inertness of RT-Hg towards PANI-NMP in aqueous DMF is shown in Figure 4.11.

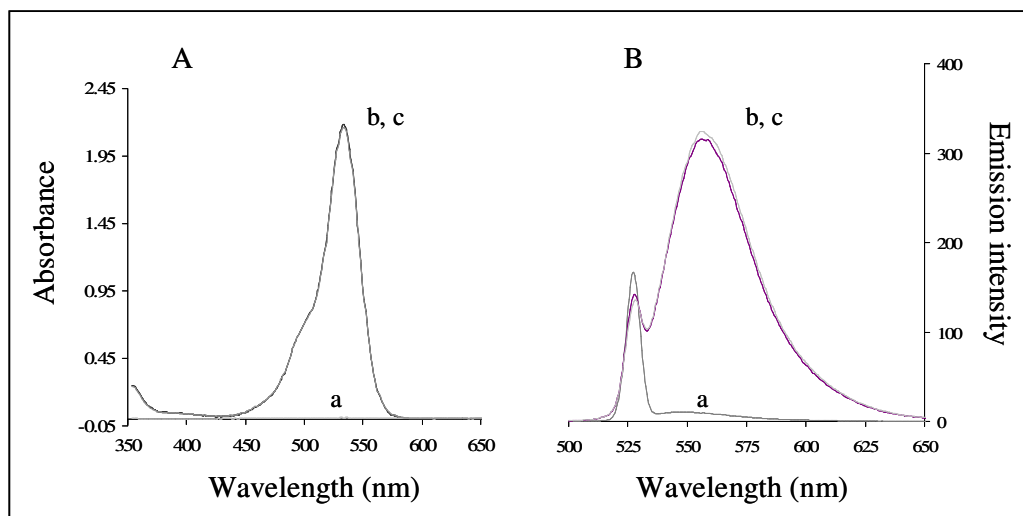


Figure 4.11: A) The UV absorbance of 2.4×10^{-5} M RT in 1:1 DMF:H₂O a) with PANI/NMP, b) Hg²⁺ and c) added to PANI/NMP after complexed with an excess Hg²⁺. B) The fluorescent emission of RT in 1:1 DMF:H₂O a) with PANI/NMP, b) Hg²⁺ and c) added to PANI/NMP after complexed with an excess Hg²⁺. The samples were diluted 1:250.

The fluorescence emission increased and blue shifted to 558 nm (from 550 nm) when the complexed RT-Hg was added to PANI-DMSO, with 1:1 aqueous DMF and excited at 530 nm. The fluorescent quenching of RT-Hg by PANI-DMSO is shown in Figure 4.12. The Stern-Volmer plot was linear, indicating that the quenching was dependent on the concentration of PANI-DMSO in solution. The quenching can most likely be ascribed to energy or electron transfer or interaction of the excited state with PANI.

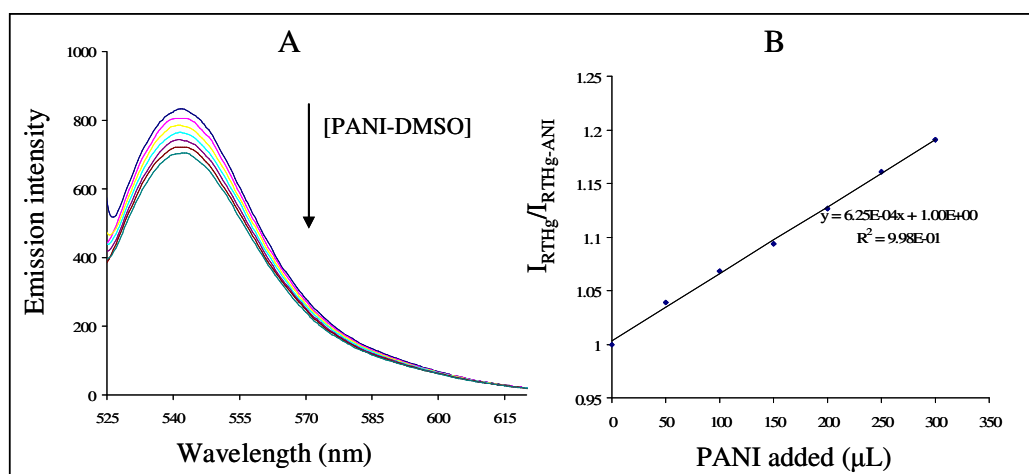


Figure 4.12: A) The fluorescent quenching of RT-Hg with increasing PANI-DMSO. B) The Stern-Volmer plot for the quenched fluorescent intensities with increasing PANI concentration.

4.4 Conclusions

In acidic medium the RS spiro lactam is protonated and ring opened to release the fluorescent xanthene. The spectrophotometric influence of TiO₂ on RS-Hg²⁺ was therefore more accurately determined for TiO₂ nanoparticles in DMF than in aqueous sol-gel. The fluorescence of the RS-Hg²⁺ was quenched with the addition of TiO₂ in DMF, and the absorbance remained relatively unaffected. Although the quenching was not according to the Stern-Volmer plot, the fluorescent quenching was most likely due to the electron transfer from the RS-Hg²⁺ excited state to the TiO₂ valence or conduction band. The quenching was also influenced by the size of the TiO₂ particulates.

In phosphate-rich TiO₂ solutions containing RS the addition of Hg²⁺ causes dimerization of the RS on the surface of TiO₂. The dimerization is dependent on the pH of the phosphate buffer as well as the size of the TiO₂ particles.

The spectrophotometric influence of PANI on RS-Hg²⁺ was only observed in its semiconductive state, dissolved in DMSO. The fluorescent response was quenched linearly with increasing PANI concentration. This was attributed either to interaction in the excited state or electron conduction to the electrolyte. The fluorescence response of RT-Hg increased with the addition of TiO₂, was most likely due to interaction between the excited RT-Hg state and TiO₂. The fluorescent intensity of RT-Hg decreased linearly with the addition of PANI-DMSO according to the Stern-Volmer equation.

The spectrophotometric responses of RS-Hg²⁺ in solution suggest that PANI and TiO₂ may be suitable charge separators for RS-Hg²⁺ in a PEC. The interactions of TiO₂ with the sulphur containing RT-Hg are more complicated than those of RS-Hg²⁺ and charge transfer may occur on longer timescales through energy transfer processes. Charge separation after excitation of RT-Hg is also likely with the addition of PANI-DMSO.

4.5 References

- [1] P.C. Beaumont, D.G. Johnson, B.J. Parsons, J. Photochem. Photobio. A, 107 (1997) 175-183.
- [2] J. Bujdak, N. Iyi, J. Phys. Chem. B, 109 (2005) 4608-4615.
- [3] J. Bujdak, N. Iyi, R. Sasai, J. Phys. Chem. B, 108 (2004) 4470-4477.
- [4] P. Čapková, P. Malý, M. Pospíšil, Z. Klika, H. Weissmannová, Z. Weiss, J. Colloid Interface Sci., 277 (2004) 128-137.
- [5] S. Hamad, J.R. Sánchez-Valencia, A. Barranco, J.A. Mejias, A.R. González-Elípe, Mol. Sim., 35 (2009) 1140-1151.

- [6] A. Kathiravan, V. Anbazhagan, M.A. Jhonsi, R. Renganathan, Z. Phys. Chem., 221 (2007) 941-948.
- [7] A. Kathiravan, R. Renganathan, Spectrochim. Acta, Part A, 71 (2008) 1106-1109.
- [8] A. Kathiravan, R. Renganathan, Spectrochim. Acta, Part A, 71 (2008) 1080-1083.
- [9] A. Kathiravan, R. Renganathan, J. Colloid Interface Sci., 331 (2009) 401-407.
- [10] P.K. Sudeep, K. Takechi, P.V. Kamat, J. Phys. Chem. C, 111 (2007) 488-494.
- [11] Z. Mandić, L. Duić, J. Electroanal. Chem., 403 (1996) 133-141.
- [12] V. Luthra, R. Singh, S.K. Gupta, A. Mansingh, Curr. Appl. Phys., 3 (2003) 219-222.
- [13] S. Bhadra, D. Khastgir, N.K. Singha, J.H. Lee, Prog. Polym. Sci., 34 (2009) 783-810.
- [14] K. Srikanth, M.M. Rahman, H. Tanaka, K.M. Krishna, T. Soga, M.K. Mishra, T. Jimbo, M. Umeno, Sol. Energy Mater. Sol. Cells, 65 (2001) 171-177.
- [15] M.C. Gupta, S.S. Umare, Macromolecules, 25 (1992) 138-142.
- [16] D.W. Wu, W. Huang, C. Duan, Z. Lin, Q. Meng, Inorg. Chem., 46 (2007) 1538-1540.
- [17] J. Chen, A. Zheng, A. Chen, Y. Gao, C. He, X. Kai, G. Wu, Y. Chen, Anal. Chim. Acta, 599 (2007) 134-142.
- [18] W. Shi, H. Ma, Chem. Commun.,(2008) 1856-1858.
- [19] P.W. Atkins, Physical chemistry, 6 th edition, Oxford University Press, U.K., 1998, p. 497-524.
- [20] S.A. Tomás, R. Palomino, R. Lozada, E.F. da Silva, E.A. de Vasconcelos, W.M. de Azevedo, C. Persson, I. Pepe, D.G.F. David, A. Ferreira da Silva, Microelectron. J., 36 (2005) 570-573.

[21] W.J. Feast, J. Tsibouklis, K.L. Pouwer, L. Groenendaal, E.W. Meijer, Polymer, 37 (1996) 5017-5048.

Chapter 5

Electrochemical evaluation of composite TiO₂/poly(aniline-co-2-bromoaniline) coated ITO electrodes

5.1. Introduction

5.1.1 Polyaniline and 2-bromo substituted polyaniline

Polyaniline (PANI) is unique amongst conducting polymers due to its chemical and environmental stability, good redox reversibility, tuneable electrical conductivity, and optical properties [1]. These properties make it favourable for its applications in rechargeable batteries, electrocatalysis, electrochromic devices, chemical sensors and the conversion of light to electricity [2-5]. The application of PANI has however been limited because its conductivity, energy density, catalytic activity, electrochromic properties and energy conversion are highly pH dependent, and PANI is insoluble in most organic solvents, which decreases its processability [6].

In an effort to introduce functionality and solubility to PANI, yet maintain some of its conductivity, copolymers of PANI and substituted PANI were prepared. Addition of a halogen atom to the ring of aniline prior to polymerization produces polymers that possess improved solubility in common organic solvents and have good thermal stability [7-9]. However, these substituted copolymers lose conductivity due to the substitution of hydrogen with an electronegative group that changes the electronic delocalization, which reduces the electron density of the phenyl ring [10].

Poly(aniline-co-2-bromoaniline) (P[A-co-2-BrA]s) was prepared electrochemically [11] and by oxidative coupling [12], [13]. Subsequently, Stejskal [10] investigated the effect of chemical heterogeneity on the conductivity of P[A-co-2-BrA]s which were synthesised by the oxidation of 2-bromoaniline in the presence of ammonium peroxydisulphate and HCl. The different P[A-co-2-BrA]s used in the present study were synthesised by chemical oxidative copolymerization of aniline and 2-bromoaniline using ammonium persulphate, in a HCl medium, with equimolar amounts of oxidant and monomer [13, 14]. The molar feed ratios of the constituent monomers were varied in order to obtain copolymers with different compositions. The 2-bromo substituent on the polymer backbone introduces flexibility into the rigid

polymer backbone structure and reduces interchain interactions, thereby increasing the solubility of the copolymers.

TiO₂ serves as the electron acceptor and transport layer in photoelectrochemical cells (PECs), especially dye-sensitized solar cells [15, 16]. The use of PANI as solid phase electrolyte to penetrate the electropositive holes between the TiO₂, to facilitate electron hole conduction and facilitate a p-n heterojunction, has been well documented [16]. PANI-TiO₂ nanocomposites have found applications in electrochromic devices, p-n heterojunction diodes, rectifiers, gas sensors, high piezoresistivity, electrorheological response, cathode electrodes in rechargeable batteries and photoelectrochemical devices [17-20]. However, the limiting factor is the overall processability and pH dependence of PANI.

The electrocatalytic activity of ITO/TiO₂ electrodes coated with P[A-co-2-BrA], containing 2-bromoaniline monomer ratios of 10:90, 25:75, 50:50 and 70:30, were investigated. The kinetics and thermodynamics of TiO₂ semiconductor and substituted PANI copolymer composites were then investigated in terms of the diffusion and charge transfer coefficients, peak separations and half peak potentials (E_{1/2}) values.

5.1.2 Background for the electrochemical evaluation

The energy band-gap (E_g) is the electronvolt (eV) energy difference between the valence band (VB) and the conductive band (CB), i.e. the amount of energy required to excite an electron from the ground state (i.e. VB) to an excited state (i.e. CB). The E_g is determined by the Planck equation:

$$E = \frac{hc}{\lambda} \quad (1)$$

with E: Energy of the absorbance in J

h: Planck's constant

$$= 6.626 \times 10^{-34} \text{ J s}$$

C: the speed of light

$$= 2.998 \times 10^8 \text{ m s}^{-1}$$

λ: the wavelength of absorbance (nm)

The energy is then converted to eV by the relationship:

$$1 \text{ eV} = 1.602 \times 10^{-19} \text{ J} \quad (2)$$

As mentioned in Section 2.6, the size of the E_g can be used to classify the conducting properties of certain materials, with higher band-gap materials ($E_g < 3.5$) described as insulators and semiconductors. According to Planck's equation, the E_g is therefore determined by the wavelength of the UV absorbance. The higher the absorbance wavelength, the smaller the E_g , and the more likely it is that the copolymer could have semiconductive properties.

In electrochemical evaluation, quick and reversible (accepting and donating) electron transfer between the absorbed species in solution and the electrode surface is desirable. Oxidation and reduction reactions (redox) are reversible on electrode surfaces when the oxidised and reduced species remain in equilibrium during the potentials scans.

In all electrochemical methods the rate of oxidation and reduction depend on the:

- rate at which and means by which soluble species reach the electrode surface (mass transport)
- kinetics of the electron transfer process at an electrode surface (electrode kinetics), which depend on the following:
 - the nature of the reaction
 - the nature of electrode surface
 - the temperature.

The following parameters are indicative of a reversible process:

- peak potential separation (ΔE_p) (= cathodic peak potential – anodic peak potential) = $58/n$ mV, with n = the amount of redox electrons, at all scan rates at 25 °C
- peak current ratio = anodic peak current (i_{pa})/cathodic peak current (i_{pc}) = 1, at all scan rates
- peak current function $i_p/v^{1/2}$ (v : scan rate) which is independent of v .

Irreversible behaviour of adsorbed species on the electrode surfaces can be due to either of the following [21, 22]:

- Slow electron transfer kinetics. Reversibility requires that the electron transfer kinetics be fast enough to maintain the surface concentrations of the oxidised and reduced species. Hence, reversibility depends on the relative values of the standard heterogeneous electron transfer rate constant (k_s) and the rate of change of potential i.e. the scan rate v . A quasi-reversible process is characterized by $\Delta E_p > 58/n$ mV, with the value increasing with increasing scan rate.
- Chemical reactions of the oxidised and reduced species.

ΔE_p values are the potential difference between the oxidised state and reduced state of the molecule. Hence, small differences require less energy to “move” between the two states. The electron energy required to move between the redox potential is therefore a measurement of the potential or energy required for charge separation. ΔE_p of the redox peaks, like the energy band-gap, is another important parameter for reversible and efficient electron transfer. ΔE_p is an indicator of the conductivity of the electrode surface.

Another parameter used for the electrochemical characterisation of electrodes is the half-wave potential ($E_{1/2}$). The $E_{1/2}$ is the point at which the current is half of its limiting value, i.e. the potential midway between the oxidation and reduction peak potential. $E_{1/2}$ is a characteristic of particular species on a specific electrode surface, and therefore an indicator of an electrode’s catalytic ability. Shifting of $E_{1/2}$ for a redox probe to higher potentials on modified electrode surfaces means that more energy is required for reversible electron transfer. The closer $E_{1/2}$ moves to zero the higher is the catalytic ability of the electrode surface.

The Randles-Sevcik equation has been used to determine the mass transport properties of the ferricyanide redox couple in the 0.05 M KNO₃/10 mM K₃Fe(CN)₆ electrolyte towards the working electrode.

The Randles-Sevcik equation is described as follows [24]:

$$I_p = 0.4463 nF(nF/RT)^{1/2}CD^{1/2}v^{1/2} \quad (3)$$

where I_p : Peak current (A)

n : number of electrons involved in the redox reaction

F : Faraday constant

R : gas constant

T : temperature (K)

C : concentration of electrolyte (mol.dm⁻³)

v : scan rate (V s⁻¹)

D : Diffusion coefficient (cm² s⁻¹)

The mass transport properties of the redox probe in the bulk electrolyte towards the electrode surface can be investigated by plotting the peak current density vs the square of the scan rate ($v^{1/2}$). Linear regressions indicate that mass transport is controlled by mass diffusion of the probe from the electrolyte to the electrode surface. The slope of the linear plot is used to determine the diffusion coefficient, and regression through zero is indicative of a reversible redox reaction.

A simple electrode reaction involves mass transport of the electroactive species to the electrode surface, the electron transfer across the interface, and the transport of the product to the bulk solution. Most electrode surfaces involve more complex reactions, including chemical and surface processes that either impede or increase electron transfer. For static voltammetric measurements, mass transport is primarily controlled by mass diffusion of the electroactive species to the electrode surface. Chronoamperometry, by way of the Cottrell equation, gives insight into the diffusion coefficient of the redox couple on the various electrode surfaces [23]:

$$I = nFACD^{1/2}\pi^{1/2}t^{-1/2} \quad (4)$$

where A is the electrode area (cm²)

Cottrell plots are constructed using chronoamperometry results. The current is plotted against the inverse of the square root of time ($t^{1/2}$), and from the slope of the plot the diffusion coefficient can be determined. Deviations from linearity in the plot of I vs $t^{1/2}$ can indicate that the redox event is associated with certain processes, such as association/dissociation of a ligand, or a change in geometry. In Chapter 5,

chronoamperometry was utilised to determine the accessibility of the electrode surface for electrolyte diffusion.

As mentioned above, the reversibility of the redox couples are determined by two factors: slow electron kinetics and mass diffusion. To further categorise the electrode surfaces, the charge transfer coefficient, α , needs to be determined. The α value is an indication of the amount of energy that is required by a system to overcome the activation energy barrier of a given reaction. These values can be determined using the Butler-Volmer equation:

$$I = I_0 [e^{\alpha n F \eta / RT} - e^{-(1-\alpha) n F \eta / RT}] \quad (5)$$

where I: The peak current (A)

I_0 : The initial peak current (A)

$\eta = E - E_{1/2}$

α : transfer coefficient

which can be rewritten as

$$\ln I = \ln i_0 - \alpha n F \eta / RT \quad (6)$$

The overpotential is the difference between the potential for the peak current and the mean value of the redox couple (the formal potential for reversible systems). For overpotentials higher than 50 mV, Tafel plots are constructed by plotting the peak potential (in this case the peak current density) against the overpotential, η .

The electrochemical properties of the different P[A-co-2-BrA]s were investigated by measuring UV absorbance, cyclic voltammetry (CV) and chronoamperometry with a ferricyanide redox couple at pH 3 and pH 7.5. The E_g energies, potential window, redox activity, mass transport and diffusion coefficients were measured by CV and compared to those obtained for PANI.

5.2. Materials and methods

5.2.1 Materials

Indium tin oxide (ITO) glass plates had a surface resistivity between 8 and 12 $\Omega \text{ sq}^{-1}$ and were purchased from Aldrich, South Africa. All chemicals and organic solvents used were of analytical reagent grade from Sigma-Aldrich, South Africa. All aqueous

solutions were prepared with ultrapure water obtained using a Milli-Q RO purification system.

5.2.2 Instrumentation

The bromine content of each copolymer sample in the salt form was determined by using a Phillips 1404 dispersive X-ray emission spectrometer in the energy dispersive X-ray emission mode. Characterization of the copolymers was carried out using a Thermo fourier transform infrared (FTIR) and attenuated total reflection (ATR) system and UV analysis was performed on a Centra double beam UV-Vis spectrophotometer. Surface imaging was performed using a Leo 1430VP scanning electron microscope (SEM) and the film thicknesses were determined by using a Veeco Dektak 6M surface profiler.

The room temperature electrical conductivity of P[A-co-2-BrA]s in the salt form was measured using the two point probe method. The samples were in the form of compressed disk pellets 12 mm in diameter and 2 mm thick. For the conductivity measurements the surfaces of the pellets were coated with a conductive Ag paint. The conductivity was measured directly by utilising a high resistive multimeter fitted with a frequency analyzer.

Electrochemical measurements were performed using an Epsilon BAS potentiostat, and EpsilonEC 2000-XP software. A three electrode cell was used for both the CV and chronoamperometry measurements. The coated ITO plates functioned as the working electrode, the Pt wire as the counter electrode and Ag/AgCl as a reference electrode. Measurements were undertaken in either a 0.05 M KNO₃ (pH 7.5) or H₂SO₄ (pH 3) solution as background electrolyte, to which 10 mM K₃Fe(CN)₆ was added. Ferricyanide (Fe(CN)₆^{3/4-}) was used as the redox probe to investigate the electrode properties and characteristics. Various scan rates were used: 100, 50, 20, 10 and 1 mV s⁻¹ for CV measurements. The chronoamperometric responses were measured at 200 and 2000 ms pulse widths.

5.2.3 Synthesis of poly(aniline-co-2-bromoaniline) copolymers

Poly-2-bromoaniline (P-2-BrA) was synthesized by oxidative chemical polymerization using ammonium persulphate in 1 M HCl, according to the procedure of Roy *et al.*

[13], with minor modifications. Ammonium persulphate (16 mmol) in 1 M HCl (100 mL) was slowly added dropwise to freshly distilled 2-bromoaniline (14 mmol) in 1 M HCl (100 mL) at 0-4 °C under continuous stirring, to maintain an approximate pH of 1. The resultant solution was stirred for 8 h and polymerization was carried out at room temperature. The resultant polymeric product was filtered, washed with small amounts of HCl, methanol and distilled water and dried in an air oven at 70 °C for 8 h to afford a 52% yield of P-2-BrA, as a green-black emeraldine salt.

A sample of the emeraldine salt was treated with 1 M NH₄OH at room temperature and stirred overnight. The resultant polymer powder was filtered, washed with methanol and distilled water, and dried at 70 °C for 8 h to afford the emeraldine base as a black powder.

The P[A-co-2-BrA] copolymers were synthesised by chemical oxidative coupling of monomers with varying mole fractions of aniline and 2-bromoaniline in aqueous solution of 1 M HCl using ammonium persulphate as the oxidant (molar ratio of monomer to oxidant = 1:1), following the procedure described by [14]. To prepare copolymers with different compositions, the mole fraction of 2-bromoaniline in the reaction mixture was varied between 0.1 and 0.7.

The P[A-co-2-BrA] copolymers used in the study contained monomer ratios of aniline:2-bromoaniline of 90:10, 75:25, 50:50 and 30:70, and were identified as P[A-co-2-BrA], followed by the 2-bromoaniline monomer content. For example, a copolymer containing 25% 2-bromoaniline would be given as P[A-co-2-BrA] 25. PANI was prepared according to standard chemical oxidation polymerization methods [24].

5.2.4 Coating of ITO and ITO/TiO₂

ITO glass plates were cut into approximately 8 × 12 mm segments and sonicated for 10 min in water, followed by ethanol and then acetone. The dried plates were coated with TiO₂ sol-gel modified with polyethylene glycol (PEG) which was synthesised according to the procedures described by Srikanth *et al.* [25]. TiO₂ paste was drop-coated onto the ITO glass plates and spun on a custom spin-coating device at an

average speed of 1000 rpm to form a TiO₂ thin film. Thereafter, the plates were annealed in a quartz tube furnace at 500 °C for 30 min to form the anatase structure.

A 5 mg sample of each copolymer was dissolved in 0.5 mL dimethylformamide (DMF) and sonicated for 10 min. The prepared ITO/TiO₂ plates were coated with 40 µL of the dissolved copolymer and the solvent was evaporated at room temperature, in a controlled atmosphere until dry (ca. 3-4 days).

5.3 Results and discussion

5.3.1 Copolymer characterization

The composition of each copolymer was determined by UV absorbance, FTIR and energy dispersive X-Ray emission spectroscopy (XRS). The bromine content as well as the electrical conductivity of the various copolymers are summarised in Table 5.1. The bromine content increased with increasing 2-bromoaniline monomer addition during the synthesis procedures, which confirmed the copolymerization of the various copolymer compositions. The electrical conductivity of the P[A-co-2-BrA]s decreased with increasing 2-bromoaniline monomer content; copolymers with 10% and 25% incorporation of 2-bromoaniline into the copolymer exhibited favourable conductivity characteristics.

Table 5.1: The bromine content of PANI and the P[A-co-2-BrA] copolymers

Polymer	Bromine content (%)	Electrical conductivity, σ (S/cm)
PANI	0	1.25×10^{-2}
P[A-co-2-BrA] 10*	2	7.3774×10^{-4}
P[A-co-2-BrA] 25	7	5.4720×10^{-4}
P[A-co-2-BrA] 50	27	2.6027×10^{-4}
P[A-co-2-BrA] 70	30	1.2366×10^{-5}
P-2-BrA	39	1.5988×10^{-6}
TiO ₂	0	

* The values given after the closing brackets i.e. 10, 25, 50 and 70 refer to the percentage 2-bromoaniline monomer added to the starting mixture.

The FTIR spectra of the copolymers between 650 cm⁻¹ and 1800 cm⁻¹ are shown in Figure 5.1. The only peak that can be assigned to aryl bromide (C-Br) stretching was observed between 1075 cm⁻¹ and 1030 cm⁻¹ [26]. The single peak located at 1065 cm⁻¹ was absent in PANI, but increased with increasing bromine content. It should be noted that FTIR is only a semi-quantitative technique and that the observed increase in the aryl bromide peak served as an approximation of the increase in bromine content. Increased imine (R₂C=N-C) character of the higher bromine content copolymers was also observed at 1650 cm⁻¹. The sharp amine peak became broader with increasing bromine content, probably due to N-Br interaction between polymer chains in the copolymers.

XRS and FTIR analyses showed that the 2-bromoaniline content was indeed incorporated into the copolymers.

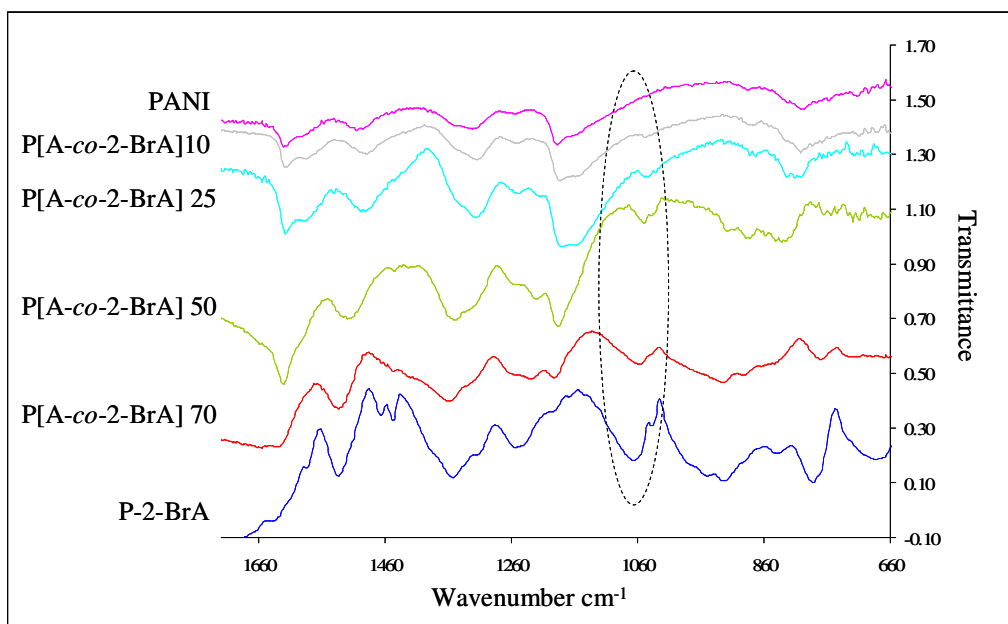


Figure 5.1: FTIR spectra of the P[A-co-2-BrA] copolymers.

5.3.2 Morphology of P[A-co-2-BrA] copolymers

The SEM images of ITO coated with TiO₂/copolymer composite electrode surfaces are shown in Figure 5.2. ITO coated with the PEG modified TiO₂ had a relatively smooth surface with a minor increase in surface roughness when compared to ITO coated with TiO₂ alone. Drop-coating of the various polymers onto the ITO/TiO₂

electrode surface increased the surface roughness considerably. The amount of clustering observed on the ITO/TiO₂/copolymer surface increased with increasing amount of 2-bromoaniline monomer. The density of the coating increased with the solubility, therefore increasing the bromine content; P-2-BrA formed a thin polymer film on the electrode surface. The solubility of the different P[A-co-2-BrA] copolymers in DMF was considerably higher when compared to PANI. PANI, being the least soluble of the polymers in the present study, led to the highest surface roughness. Due to the low solubility of PANI it was assumed that the deposited PANI contained polymer chains of low molecular weight. The P[A-co-2-BrA] coatings were more evenly distributed onto the surface of the ITO/TiO₂ electrodes than PANI.

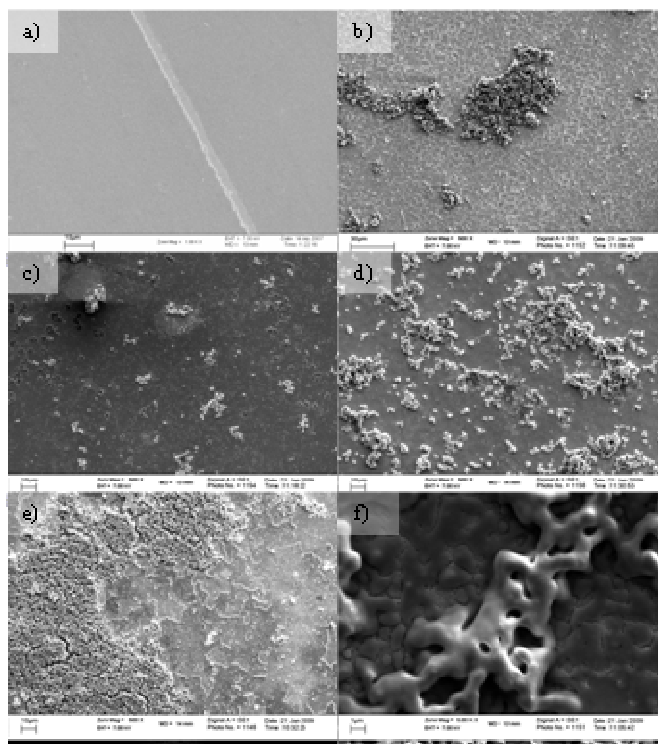


Figure 5.2: SEM images of ITO/TiO₂ coated with the various copolymers. a) Bare TiO₂, b) P[A-co-2-BrA] 10, c) P[A-co-2-BrA] 25, d) P[A-co-2-BrA] 50, e) P[A-co-2-BrA] 70 and f) P-2-BrA. Magnifications: b-d) 500×, a) and e) 1000×

The film or composite thicknesses of the various coated copolymers were measured over the length of the electrode perpendicular to the ITO surface. Results are tabulated in Table 5.2.

Table 5.2: Film thickness, μm , of the various ITO/TiO₂/copolymer coated electrodes

Polymer	Film thickness, μm
P[A-co-2-BrA] 10	1.45 ± 0.28
P[A-co-2-BrA] 25	1.74 ± 0.15
P[A-co-2-BrA] 50	2.15 ± 0.23
P[A-co-2-BrA] 70	2.59 ± 0.09
P-2-BrA	2.73 ± 0.34
TiO ₂	1.71 ± 0.10

The layer thickness increased with increasing monomer content. The film thickness of the ITO/TiO₂ electrode alone was 1.71 μm , and after coatings the thickness increased by a maximum of 37%. For the electrodes coated with the higher PANI and more particulate copolymers, the layer thickness was comparable to that of electrodes coated with TiO₂. It was therefore assumed that the particulate copolymers penetrate the pores in the TiO₂ layer, forming a composite layer rather than two coatings. As the P[A-co-2-BrA] content increases, the penetration into the TiO₂ layer was less due to more polymer film formation over the electrode surface. From Figure 5.2 it can be seen that the copolymers (except for P-2-BrA) do not coat the entire surface. Hence, the chemical and electrode surface interactions due to the presence of bare TiO₂ should always be taken into consideration in all analyses undertaken.

5.3.3 UV analysis of the ITO coated electrodes

The absorption peaks of the various copolymers were measured in (0.5 g L⁻¹) DMF as well as coated onto the ITO/TiO₂ electrodes. The polymer absorption peaks in DMF were observed between 520 nm and 620 nm, whereas the absorption peaks of the polymers deposited onto ITO/TiO₂ appeared over a wider range; between 530 nm and 890 nm. The band-gaps were determined by the Planck equation, taking the UV cut-off at high energy as the wavelength to determine the band-gaps of the deposited polymers. Figure 5.3 shows the UV-Vis spectra measured for P[A-co-2-BrA] 10 in DMF, and illustrates the shift to higher wavelength when coated onto the ITO/TiO₂ surfaces.

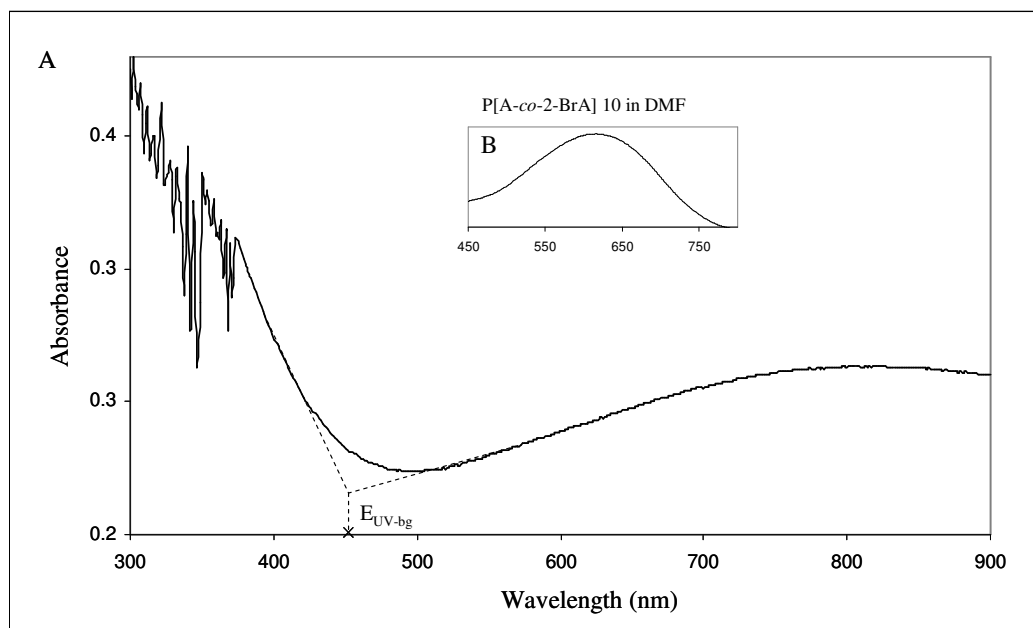


Figure 5.3: A) UV-Vis spectrum of ITO/TiO₂ coated with P[A-co-2-BrA] 10. B) The UV-Vis spectrum of P[A-co-2-BrA] 10 dissolved in DMF, illustrating the absorption of P[A-co-2-BrA] 10 at 614 nm.

The wavelengths and band-gap energies of the various polymer absorption peaks are summarized in Table 5.3.

Table 5.3: Energy band-gap energies calculated for the various absorptions of P[A-co-2-BrA] in DMF and coated on the ITO/TiO₂ surfaces

Polymer	In DMF		Coated onto ITO/TiO ₂	
	Wavelength (nm)	E (eV)	Wavelength (nm)	E (eV)
PANI	606.7	2.04	790	1.57
P[A-co-2-BrA] 10	614.4	2.02	809	1.53
P[A-co-2-BrA] 25	608.0	2.04	878	1.41
P[A-co-2-BrA] 50	600.3	2.07	591	2.10
P[A-co-2-BrA] 70	581.1	2.13	554	2.24
P-2-BrA	522.2	2.37	531	2.34
TiO ₂			344.6	3.6

The E_g increased with increasing 2-bromoaniline content while the E_g of the copolymers, similar to PANI, were significantly reduced when coated onto the ITO/TiO₂ surfaces. The deposited form of PANI occurred mostly in the oxidised form ($E_g \sim 1.4$ eV [27]), which is more semiconductive in nature.

The results demonstrated that the ITO/TiO₂/polymer electrodes absorb UV light at longer wavelengths than the ITO/polymer electrodes. The presence of the TiO₂ coating increased the region for absorbing light and increased the wavelength maximum by ca. 100 nm. Addition of the polymers increased the wavelength in which the TiO₂ absorbed UV light by 90 nm. The observed absorption wavelengths for the ITO/TiO₂/polymer and ITO/polymer are shown in Table 5.4. The values of the wavelengths used to determine the band-gap energies were estimated as in Figure 5.3.

Table 5.4: Wavelengths (nm) at which the electrodes start to absorb in the UV region.

Polymer	Coated onto ITO/TiO₂ wavelength (nm)	Coated onto ITO alone wavelength (nm)
PANI	477.6	320.4
P[A-co-2-BrA] 10	494.2	319.5
P[A-co-2-BrA] 25	532.5	318.7
P[A-co-2-BrA] 50	489.0	343.8
P[A-co-2-BrA] 70	436.5	322.3
P-2-BrA	437.8	413.4
TiO ₂	344.6	

From the results in Table 5.3 and 5.4 it is evident that the presence of the P[A-co-2-BrA] coatings added favourable intermediate energy bands to the existing 3.6 eV of the ITO/TiO₂ electrodes. The band-gap energies increased with increasing 2-bromoaniline content in the copolymers. The wider band-gap energies are therefore an indication that the conductive property of the copolymers decrease with increasing bromine content.

5.3.4 *Electrochemical evaluation of ITO/copolymer electrodes with a standard ferricyanide redox probe*

The electrochemical properties of ITO are well known [28]. The $E_{1/2}$ value for the $\text{Fe}(\text{CN})_6^{3-/4-}$ redox couple on ITO is 0.59 mV at pH 7.5, compared to 0.082 mV at pH 3 measured at a scan rate of 1 mV/s. The $\text{Fe}(\text{CN})_6^{3-/4-}$ redox peaks measured with the ITO electrode were sharper at higher pH, with the sharpness increasing with decreasing scan rate. The electrochemical reactivities of the polymer coatings were determined in $\text{K}_3\text{Fe}(\text{CN})_6$ solutions at pH 3.5 and pH 7.5 and compared to ITO. The ITO/TiO₂ electrodes were coated with copolymer films to investigate the electron-shuttling ability of the composite electrodes, as well as their electrocatalytic activity, in the presence of the ferricyanide probe. The pH values were chosen to resemble the broad spectrum of natural waters, as one of the motivations for this study is to design a PEC that was capable of Hg^{2+} measurements in the environmental samples. It is well known that PANI is highly pH dependent, and has a higher conductivity at lower pH because the pH affects the degree of protonation of the PANI polymer [29]. It is therefore important to investigate copolymers of PANI at different pH values to determine if these copolymers offer viable options for use in PECs for determining metals in environmental samples.

Due to the low solubility of PANI, PANI and P[A-co-2-BrA] were only partially dissolved in DMF; they formed particulates. PANI and P[A-co-2-BrA] 10 were therefore filtered to remove the larger particulates before being coated onto the ITO surface; they therefore had a lower concentration per centimeter of ITO.

When PANI was immersed in the $\text{Fe}(\text{CN})_6^{3-/4-}$ electrolyte it showed electrochemical properties that were typical of electrodes; the dominating property was the processes at the electrode/electrolyte interface [29]. The cyclic voltammograms measured for the various ITO/polymer electrodes are shown in Figures 5.4 and 5.5.

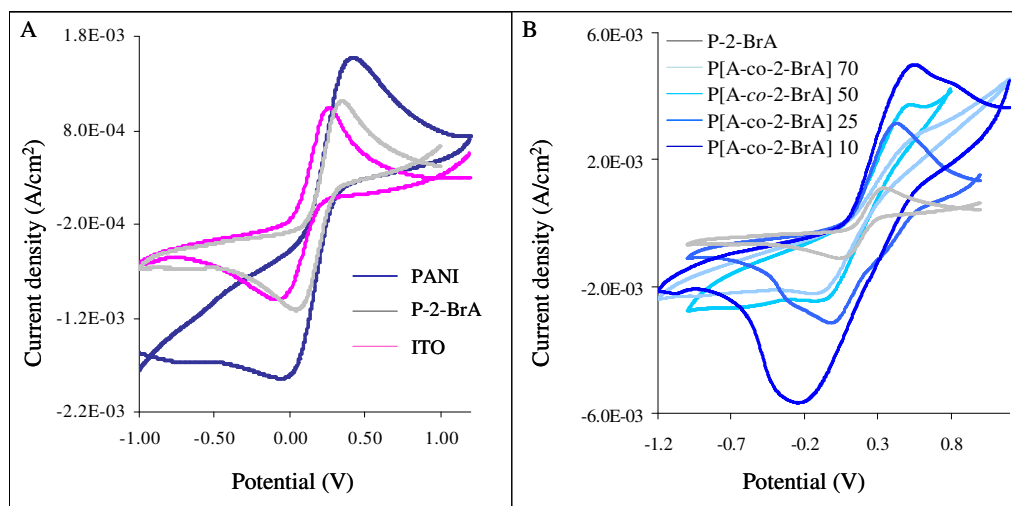


Figure 5.4: Cyclic voltammograms of 10 mM $K_2Fe(CN)_6$ on ITO electrodes coated with the various polymers; A) ITO alone, PANI and P-2-BrA and B) P[A-co-2-BrA] 10, P[A-co-2-BrA] 25, P[A-co-2-BrA] 50, P[A-co-2-BrA] 70, P-2-BrA measured at 100 mVs^{-1} in electrolyte with pH 7.5.

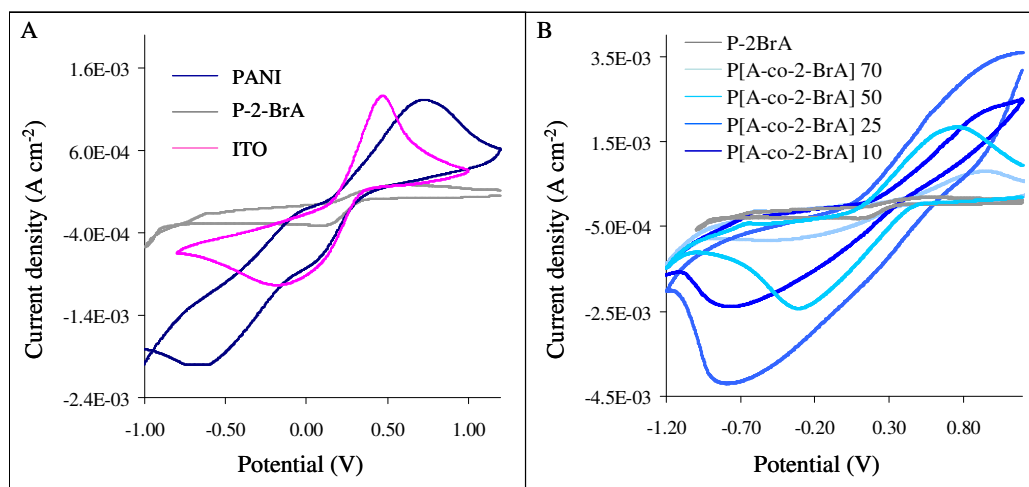


Figure 5.5: Cyclic voltammograms of 10 mM $K_2Fe(CN)_6$ on ITO electrodes coated with the various polymers; A) ITO alone, PANI and P-2-BrA and B) P[A-co-2-BrA] 10, P[A-co-2-BrA] 25, P[A-co-2-BrA] 50, P[A-co-2-BrA] 70, P-2-BrA measured at 100 mVs^{-1} in electrolyte with pH 3.5.

ITO coated with PANI showed sharp oxidation peaks, with an additional set of redox peaks observed at -750 and -350 mV. These redox peaks were sharper at lower pH, which corresponds to the oxidation and reduction of the PANI double bonded N-quinoid groups. The doubling of the current density for the ITO/PANI electrode

response to the Fe(CN)₃^{3-/4-} redox couple can be attributed to the conductive properties of PANI and the increase in active surface area on the ITO electrode.

Although the current density for the copolymer electrodes doubled, the current density for P-2-BrA remained similar to that of ITO at pH 7.5. The basic trends for the ΔE_p and the $E_{1/2}$ values versus the amount of 2-bromoaniline monomer in the copolymer are illustrated in Figure 5.6.

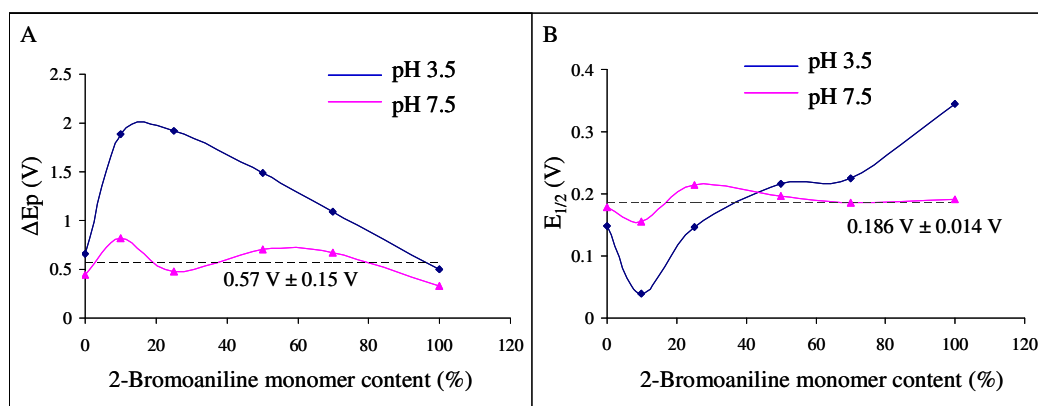


Figure 5.6: A) ΔE_p , and (B) $E_{1/2}$ values for the Fe(CN)₆^{3-/4-} redox peaks on the various ITO/polymer electrodes at pH 3.5, ●, and pH 7.5, ▲. The zero content of 2-bromoaniline represents the values of the redox couple on ITO. The average value of the peak separation and the standard deviation for the values observed at pH 7.5 are also indicated on the various plots. Values were determined at $v = 100 \text{ mVs}^{-1}$.

At pH 7.5, the ΔE_p and the $E_{1/2}$ remain roughly constant, with an average ΔE_p of $570 \text{ mV} \pm 150 \text{ mV}$ and $E_{1/2}$ of $186 \text{ mV} \pm 14 \text{ mV}$. From this result it is evident that the conductive properties of the various copolymers are most likely all restricted at higher pH. The increased ΔE_p values for the quasi-reversible redox couple with increasing scan rate for all polymers can be attributed to slow charge transfer kinetics. The transfer kinetics at pH 7.5 were faster when compared to those at lower pH, but this is only due to reduced interaction of the polymers with the ferricyanide and reduced surface activity of the PANI containing polymers.

ΔE_p of the ferricyanide redox couple on the ITO/P[A-co-2-BrA]s electrodes decreased with increasing 2-bromoaniline monomer content at pH 3.5. The rate of electron

transfer also increased with decreasing amounts of PANI, due to less interference of the PANI surface redox states, which are prevalent at lower pH. The $E_{1/2}$ value for the redox couple moved to lower overpotentials with increasing amounts of PANI. The potential of the $\text{Fe}(\text{CN})_6^{3/4-}$ redox reaction is located in the potential range of the redox reaction of the emeraldine (EM) and leucoemeraldine (LE) forms of PANI in the copolymers [30].

Figure 5.5 shows that the redox peaks for the $\text{Fe}(\text{CN})_6^{3/4-}$ redox couple became broader and moved to higher potentials when the PANI content was increased. This reduction in transfer kinetics indicates a restriction of mass diffusion to the available electrode surface. The restriction is due to repulsive forces that exist between the electrode surface and the iron complexes delaying the oxidation/reduction reaction (i.e. both the copolymer and the redox couple have negative charge) [31]. The elongated peaks are typical for semiconductive coatings [32]. The reversibility at lower pH is therefore reduced due to: i) the competition for electronic charge and ii) the continuous changing of the electrode surface oxidation state. The $E_{1/2}$ values for the redox couple on the electrode surface increased with increasing comonomer content. $E_{1/2}$ values for the redox couple are indicative of the catalytic effect of the polymer surface to facilitate electron transfer between the oxidation and reduction states. Figure 5.6 B) illustrates that the catalytic effect of the copolymers is reduced with increasing 2-bromoaniline monomer content. The redox peaks of the $\text{Fe}(\text{CN})_6^{3/4-}$ couple on copolymers that contain more than 50% 2-bromoaniline content are characterised by having sharper peaks, which approach a ratio of 1, indicating that these copolymers are not limited by mass transfer or available surface area. The reduced current density and lack of catalytic ability towards the redox probe can be attributed to lower conductivity or electron shuttling capabilities of copolymer coatings on the electrode surface.

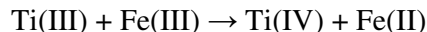
5.3.5 Electrochemical evaluation of ITO/TiO₂/copolymer electrode with the ferricyanide redox probe

Subsequently to the ITO electrodes being coated with TiO₂, 40 μl aliquots of polymer/DMF solution were coated onto the various electrode surfaces. The electrochemical responses were measured at pH 3.5 (H₂SO₄) and pH 7.5 (KNO₃).

Baez *et al.* [33] characterised the TiO₂-anatase system in Fe(CN)₆^{3-/4-} medium and demonstrated that the cathodic reaction was initiated by the surface process:



which is followed by the chemical reaction:



The surface properties of TiO₂ are also pH dependent, having increased Ti-OH⁺ surface groups for pH > 5 and carbonyl groups at pH < 5.5 [34, 35]. ΔE_p of the Fe(CN)₆^{3-/4-} redox couple on TiO₂ was increased by 50 mV compared ITO alone, but with higher current density for the redox peaks. Electron transfer was retarded due to a further distance travelled through the TiO₂ matrix. The E_{1/2} value for the redox couple on ITO/TiO₂ remained the same (0.174 V measured at 100 mV s⁻¹) for both pH values, but was characterised by sharper peaks and smaller ΔE_p at pH 7.5. The surface oxidation and reduction of the Ti=O groups was the additional redox couple observed on TiO₂ coated electrodes for potentials lower than -0.7 V. At pH 3.5, however, the peak separation was lower and the surface Ti=O reduction was shifted to more negative potentials. The Ti=O redox was not observed on P-2-BrA, as P-2-BrA formed a film that coated the entire TiO₂ surface. The P-2-BrA polymer film also retarded the rate of electron transfer from the electrolyte to the ITO surface. As such, the redox current densities were lowered considerably and had large ΔE_p values.

Figures 5.7 and 5.8 show the cyclic voltammograms of the Fe(CN)₆^{3-/4-} couple on the different TiO₂ /P[A-co-2-BrA] composite electrodes at pH 3.5 and pH 7.5. A summary of the observed peak separation and E_{1/2} is given in Figure 5.9. The ΔE_p values for the copolymer coated electrodes were increased due to the TiO₂ layer, as well as the addition of another layer through which electrons would have to travel to reach the ITO back contact.

Both the ΔE_p and E_{1/2} redox couple values were favoured at pH 7.5. At pH 7.5 the ΔE_p were again influenced by the repulsive forces between the negatively charged couple and the electrode surface. The redox peaks were also broader and had smaller current densities when compared to those at pH 3.5. The peaks are, however, considerably sharper than those observed for the ITO/copolymer. The more positive TiOH⁺ surface groups acted to counter the repulsion of the negatively charged species, thereby increasing mass diffusion to the electrode surface.

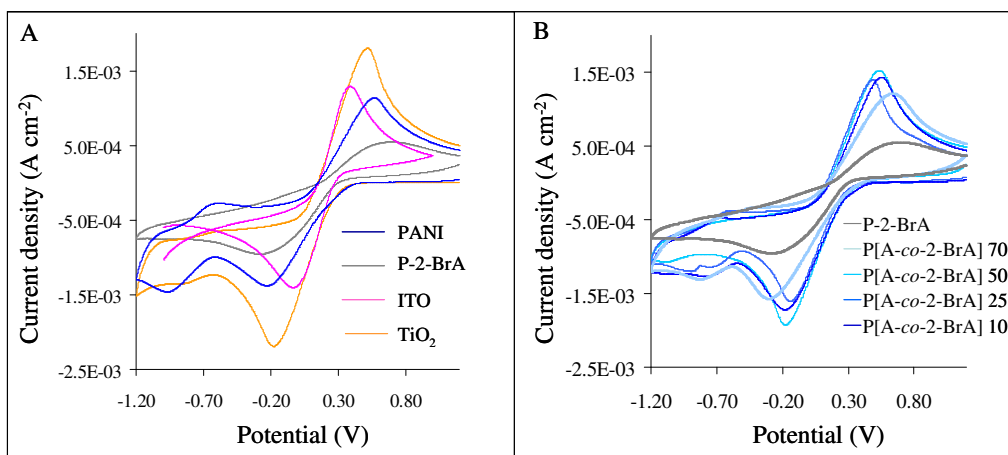


Figure 5.7: Cyclic voltammograms of 10 mM K₂Fe(CN)₆ on an ITO/TiO₂ electrode coated with the various polymers A) ITO, ITO/TiO₂, P-2-BrA and PANI and B) P[A-co-2-BrA] 10, P[A-co-2-BrA] 25, P[A-co-2-BrA] 50, P[A-co-2-BrA] 70 and P-2-BrA, measured at 100 mV s⁻¹ in the presence of 10 mM K₂Fe(CN)₆ at pH 7.5.

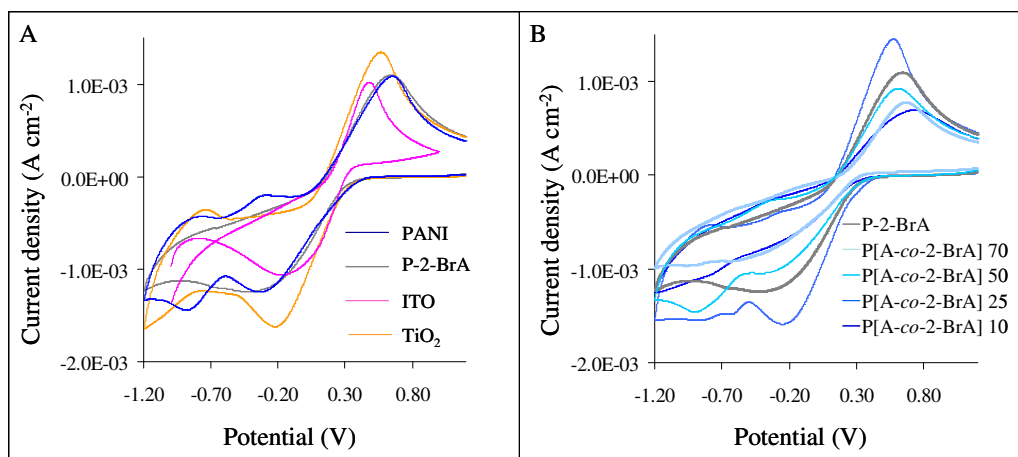


Figure 5.8: Cyclic voltammograms of 10 mM K₂Fe(CN)₆ on an ITO/TiO₂ electrode coated with the various polymers A) ITO, ITO/TiO₂, P-2-BrA and PANI, and B) P[A-co-2-BrA] 10, P[A-co-2-BrA] 25, P[A-co-2-BrA] 50, P[A-co-2-BrA] 70 and P-2-BrA, measured at 100 mV s⁻¹ in the presence of 10 mM K₂Fe(CN)₆ at pH 3.5.

The electrocatalytic abilities of the ITO/TiO₂ copolymer electrodes were similar to those observed for ITO coated copolymers. Although the E_{1/2} values were centred near 0.18 V, a slight increase with increasing 2-bromoaniline monomer content was observed at higher pH. The decrease in catalytic ability of high 2-bromoaniline content copolymers was most likely due to the attraction between the electronegative

bromine and the TiO₂ surface, which is more prevalent at lower pH. There is therefore a competition between the species in solution and the already present bromine.

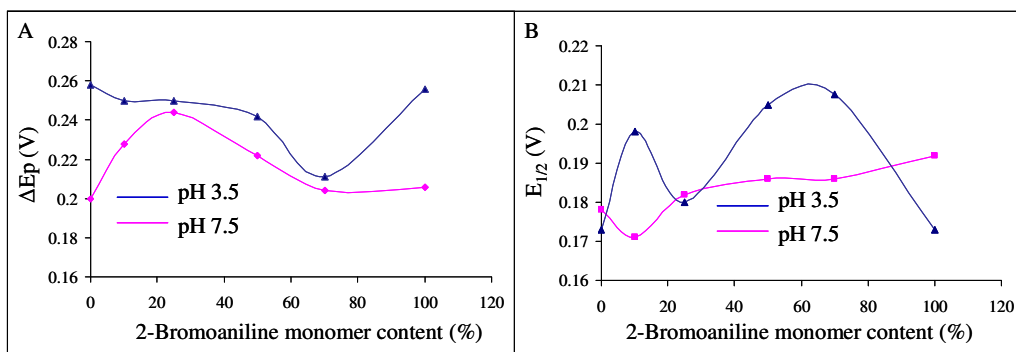


Figure 5.9: $E_{1/2}$ and ΔE_p for the redox couple on the various ITO/TiO₂/P[A-co-2-BrA] electrodes at pH 7.5 and pH 3.5 measured at 1 mV s⁻¹.

The scan rate dependence of the Fe(CN)₆^{3-/4-} couple on the different TiO₂/P[A-co-2-BrA] composite electrodes was determined, the oxidation peak dependence of which is shown in Figure 5.10. A linear increase in current density for the square root of the scan rate was observed for all of the ITO/TiO₂ electrode surfaces. The linear dependence did, however, not pass through zero, which indicated a quasi-reversible system.

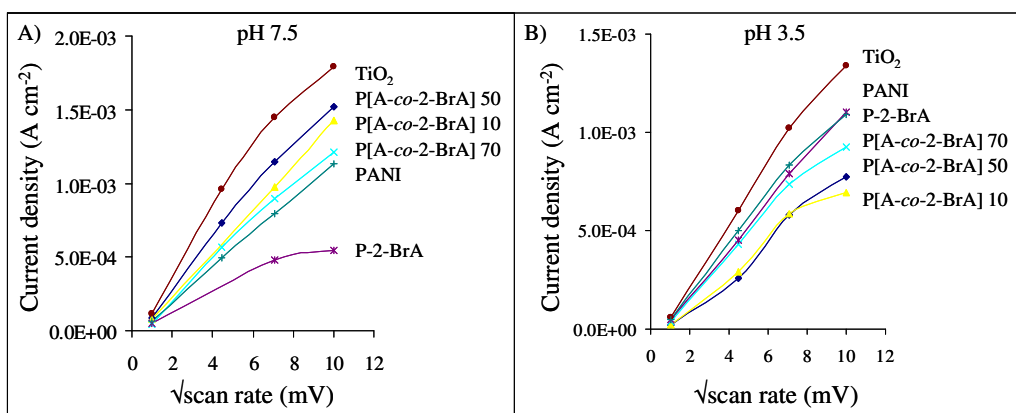


Figure 5.10: The $\sqrt{\text{scan rate}}$ dependence of the ferricyanide oxidation peak current density measured at A) pH 7.5, 0.05 M KNO₃, and B) pH 3.5, H₂SO₄.

The quasi-reversibility was caused by all or some of the following;

- surface redox reactions of Ti=O and the P[A-co-2-BrA] copolymers
- surface interactions between the various coatings (repulsion and attraction)
- interaction between the various coatings and the ferricyanide couple, i.e. decreased mass diffusion due to repulsion between electronegative species
- increased electron tunnelling distance from the redox probe to the ITO back contact

The redox behaviour of the Fe(CN)₆^{3-/4-} couple observed on the ITO/TiO₂/copolymer surfaces was to a large degree, but not completely, mass diffusion controlled.

5.3.6 The charge transfer coefficient, α

The charge transfer coefficient, α , for the Fe(CN)₆^{3-/4-} redox couple was determined on all the electrode surfaces studied. The resultant Tafel plots (e.g. Figure 5.11 (A)) were measured at a scan rate of 1 mV s⁻¹ to eliminate mass transfer effects. For simple electron transfer reactions α is assumed to have a value of about 0.5. In the present study values above 0.5 were only observed for ITO coated with TiO₂ alone, due to charge accumulation resulting from boundary resistance experienced between the TiO₂ and the Fe(CN)₆^{3-/4-} redox couple. The α values for the redox couple on TiO₂ at pH 7 were 0.48 (reduction) and 0.52 (oxidation), and together with the linear scan rate dependence of the current density, indicate mass controlled diffusion for the particular redox couple on ITO/TiO₂.

At pH 3.5 the charge transfer was influenced by the protonation of the Ti=O surface and resulted in a lower charge transfer for all electrode surfaces when compared to measurements at higher pH. At pH 3.5 a higher surface reactivity and lower electron transfer was expected. From the results illustrated in Figure 5.11 (B) it is evident that the Ti=O surface reactivity alone was not responsible for the variation in cathodic charge transfer. The charge transfer improved linearly with increasing 2-bromoaniline content at lower pH, which can be attributed to delocalising of the polarons by the bromide groups in the polymer chains. The cathodic charge transfer was retarded by the PANI surface charging at lower pH, where PANI is the most active. Overall charge transfer from the electrolyte to the electrode surface was favoured at higher pH

due to the surface protonation of Ti=O and the cathodic interference of PANI surface activity at pH 3.5.

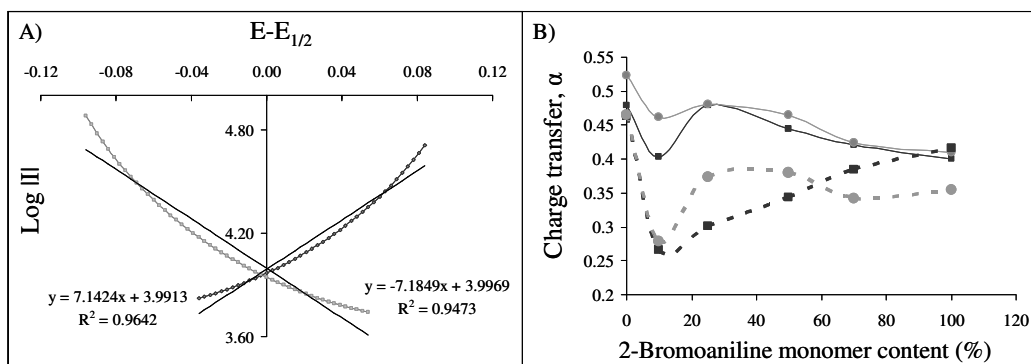


Figure 5.11: A) A typical Tafel plot, measured at 1 mV s^{-1} , used to determine α values for the oxidation and reduction of the ferricyanide couple on TiO₂/ P[A-co-2-BrA] 70 at pH 7.5. B) α values for the TiO₂/ P[A-co-2-BrA] copolymers determined at pH 3.5 and pH 7.5:— α_r at pH 7.5,— α_o at pH 7.5, ■---■ α_r at pH 3.5 and ●---● α_o at pH 3.5.

5.3.7 The diffusion coefficients of the ferricyanide redox probe for ITO/TiO₂/copolymer electrodes

The diffusion coefficients (D) of the ferricyanide couple at the various electrodes were determined by chronoamperometry, and the Cottrell equation [22]. The area of the electrodes used was 1.6 cm^2 and the concentration of the ferricyanide couple was $1.0 \times 10^{-5} \text{ mol/cm}^3$. The gradients of the Cottrell plots of I versus $t^{-1/2}$ were used to determine the diffusion coefficients for 10 mM K₃Fe(CN)₆ in H₂SO₄ (pH 3.5) and 0.05M KNO₃ (pH 7.5). Figure 5.12 A shows the chronoamperograms measured for the oxidation pulse at pH 7.5. The calculated diffusion coefficient for the oxidation (D_o) and reduction (D_r) peaks for pH 3.5 and pH 7.5 are summarised in Figure 5.12 B.

Diffusion coefficients were calculated for ITO/TiO₂/PANI coated with a single, and then a second layer of PANI to compare the influence of the layer thickness on the diffusion coefficient. The diffusion coefficient increased from $1.45 \times 10^{-6} \text{ cm}^2 \text{ s}^{-1}$ to $2.44 \times 10^{-6} \text{ cm}^2 \text{ s}^{-1}$ when another layer was added, at higher pH (pH 7.5). The diffusion coefficient was lower and remained unchanged at lower pH ($1.21 \times 10^{-6} \text{ cm}^2 \text{ s}^{-1}$).

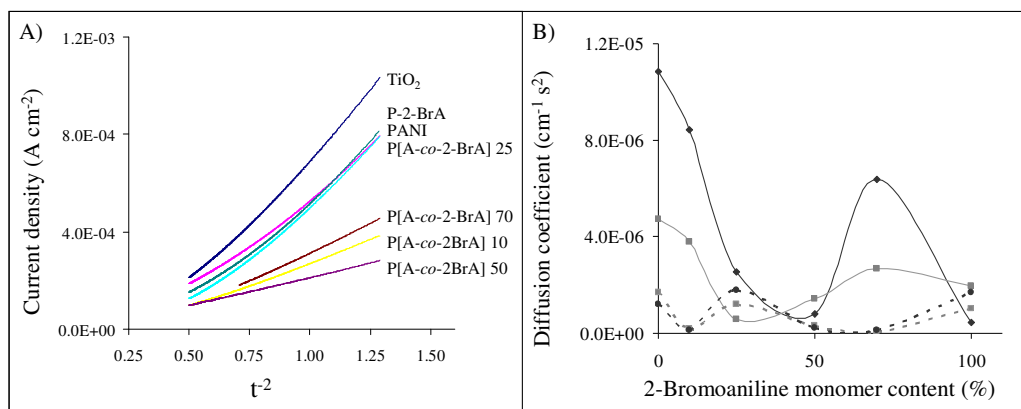


Figure 5.12: A) Oxidation chronoamperograms measured in 0.05 M KNO₃ and 10 mM K₃Fe(CN)₆ for ITO/TiO₂ electrodes coated with the various copolymers used to determine diffusion coefficients at pH 3.5 and pH 7.5. B): —(D_r) at pH 7.5, —(D_o) at pH 7.5, ■---■ (D_r) at pH 3.5 and ●---● (D_o) at pH 3.5. Zero content is ITO coated with TiO₂ alone.

Diffusion at lower pH was influenced by the activation of the PANI layer by increased polarons on the PANI surface as well as the protonation of Ti=O surface groups, which lead to repulsion of the species in solution. The diffusion coefficient at higher pH increased with decreasing amount of 2-bromoaniline content, except for P[A-co-oBrA] 50, which can be related to its thicker composite layer. It appeared that the repulsion between the fixed bromine substituent on the copolymer, and the negatively charged Fe(CN)₆^{-3/4} couple influenced the diffusion to the electrode surface. The higher 2-bromoaniline content copolymers had higher surface coverage of the TiO₂ layer as well as lower conductive properties, which led to less attraction of species to the double layer on the electrode surface.

5.4. Conclusions

P[A-co-2-BrA] copolymers were investigated for use in a PEC in terms of favourable E_g, surface morphology and electrochemical properties. The copolymers were synthesised and then characterised by XRS and FTIR, thereby indicating a clear increase in the bromine content with increasing 2-bromoaniline monomer incorporation into the copolymer. The E_g for deposited copolymers increased with increasing 2-bromoaniline content, which favoured the electron shuttling of electrons to the electrode surface.

The electrochemical properties of the ITO coated with the copolymers were similar to PANI, and was dependent on pH. At a lower pH the redox peak separation decreased with increasing 2-bromoaniline content, but the $E_{1/2}$ increased with increasing bromine content, thereby indicating a reduction in the electrocatalytic ability of the copolymers. The mass diffusion was, however, decreased due to repulsive forces between the electrode surface and the electronegative species in solution. At pH 7.5 the ITO/copolymer electrodes displayed similar electrocatalytic behaviour for all copolymer compositions.

On the TiO₂/P[A-co-2-BrA] electrodes the redox reaction was mass diffusion controlled, but was influenced by surface interactions. The electrocatalytic effect of PANI was suppressed on TiO₂ and the $E_{1/2}$ value for the ferricyanide couple remained relatively constant at pH 7.5; it increased only slightly with increasing 2-bromoaniline monomer content. With the addition of Ti=O surface groups the electrode interface became more complex, and the electrocatalytic properties were most favourable at pH 7.5.

At lower pH the charge transfer on the TiO₂/P[A-co-2-BrA] composites decreased and the oxidative charge transfer was directly influenced by the activity of PANI. This was most likely the result of the repulsion experienced between the polymer surface and the electrolyte. The slow electron transfer kinetics and lower reversibility of ferricyanide on the copolymers at lower pH is supported by the lower diffusion coefficients.

The P[A-co-2-BrA] copolymers were found to be semiconductive in nature and have higher processability when compared to PANI. Copolymers with less than 50% 2-bromoaniline content also displayed favourable electrocatalytic properties, similar to that of the parent PANI. Hence, these copolymers will be considered for use as semiconductors in the proposed PEC, for the measuring of Hg²⁺ in aqueous solutions.

5.5. References

- [1] A.G. MacDiarmid, Synth. Met., 84 (1997) 27-34.

- [2] N. Oyama, T. Tatsuma, T. Sato, T. Sotomura, *Nature*, 373 (1995) 598-600.
- [3] G. Bidan, E.M. Genies, M. Lapkowski, *J. Chem. Soc. Chem. Commun.* (1988) 533-535.
- [4] M.M. Ayad, A.H. Gemaey, N. Salahuddin, M.A. Shenashin, *J. Colloid Interface Sci.*, 263 (2003) 196-201.
- [5] J. Huang, D. Stockwell, A. Boulesbaa, J. Guo, T. Lian, *J. Phys. Chem. C*, 112 (2008) 5203-5212.
- [6] V. Rajendran, S. Prakash, A. Gopalan, T. Vasudevan, W.C. Chen, T.C. Wen, *Mater. Chem. Phys.*, 69 (2001) 62-71.
- [7] A.A. Athawale, M.V. Kulkarni, *Sens. Actuators, B*, 67 (2000) 173-177.
- [8] S. Mu, *Synth. Met.*, 143 (2004) 259-268.
- [9] Y. He, *Mater. Chem. Phys.*, 92 (2005) 134-137.
- [10] J. Stejskal, *Polym. Int.*, 54 (2005) .
- [11] Y. Sahin, S. Perçin, M. Sahin, G. Özkan, *J. Appl. Polym. Sci.*, 90 (2003) 2460-2468.
- [12] B.C. Roy, M.D. Gupta, L. Bhowmik, J.K. Ray, *J. Appl. Polym. Sci.*, 86 (2002) 2662-2669.
- [13] B.C. Roy, M.D. Gupta, J.K. Ray, *Macromolecules*, 28 (1995) 1727-1732.
- [14] U.S. Waware, S.S. Umare, *React. Funct. Polym.*, 65 (2005) 343-350.
- [15] S.E. Shaheen, C.J. Brabec, N.S. Sariciftci, F. Padinger, T. Fromherz, J.C. Hummelen, *Appl. Phys. Lett.*, 78 (2001) 841-843.
- [16] D. Wei, G. Amaratunga, *Int. J. Electrochem. Sci*, 2 (2007) 897-912.

- [17] K. Gurunathan, D.P. Amalnerkar, D.C. Trivedi, *Mater. Lett.*, 57 (2003) 1642-1648.
- [18] C. Wei, Y. Zhu, X. Yang, C. Li, *Mat. Sci. Eng. B*, 137 (2007) 213-216.
- [19] X. Zhang, G. Yan, H. Ding, Y. Shan, *Mater. Chem. Phys.*, 102 (2007) 249-254.
- [20] M.K. Ram, Ö. Yavuz, V. Lahsangah, M. Aldissi, *Sens. Actuators, B*, 106 (2005) 750-757.
- [21] A.J. Bard, L.R. Faulkner, *Electrochemical methods: fundamentals and applications*, 2nd edition, John Wiley & Sons, New York, 2001, p. 15-60.
- [22] J. Wang, *Analytical electrochemistry*, 2nd edition, John Wiley & Sons, Inc., 2000, p. 28-59.
- [23] Bioanalytical Systems, available at http://www.basinc.com/mans/EC_epsilon/index.html, Accessed 01-09-2009.
- [24] M. Dos Santos, J. Brédas, *Phys. Rev. Lett.*, 62 (1989) 2499-2502.
- [25] K. Srikanth, M.M. Rahman, H. Tanaka, K.M. Krishna, T. Soga, M.K. Mishra, T. Jimbo, M. Umeno, *Sol. Energy Mater. Sol. Cells*, 65 (2001) 171-177.
- [26] D.L. Pavia, G.M. Lampman, G.S. Kriz, *Introduction to spectroscopy*, 3rd edition, Harcourt College Publishers, Philadelphia, PA, 2001, p. 30-84.
- [27] M.C. Gupta, S.S. Umare, *Macromolecules*, 25 (1992) 138-142.
- [28] V. Christou, M. Etchells, O. Renault, P.J. Dobson, O.V. Salata, G. Beamson, R.G. Egdell, *J. Appl. Phys.*, 88 (2000) 5180.
- [29] C. Deslouis, M.M. Musiani, M. El Rhazi, B. Tribollet, *Synth. Met.*, 60 (1993) 269-278.
- [30] H.G. Huang, Z.X. Zheng, J. Luo, H.P. Zhang, L.L. Wu, Z.H. Lin, *Synth. Met.*, 123 (2001) 321-325.

- [31] Z. Mandić, L. Duić, J. Electroanal. Chem., 403 (1996) 133-141.
- [32] D. Losic, M. Cole, H. Thissen, N.H. Voelcker, Surf. Sci., 584 (2005) 245-257.
- [33] V.B. Baez, J.E. Graves, D. Pletcher, J. Electroanal. Chem., 340 (1992) 273-286.
- [34] P.A. Connor, K.D. Dobson, A.J. McQuillan, Langmuir, 15 (1999) 2402-2408.
- [35] G. Ramakrishna, H.N. Ghosh, A.K. Singh, D.K. Palit, J.P. Mittal, J. Phys. Chem. B, 105 (2001) 12786-12796.

Chapter 6:

Photoelectrochemical determination of mercury (II) with an ITO/polyaniline-rhodamine derivative composite electrode

6.1 Introduction

Photoelectrochemical detection of inorganic mercury (Hg^{2+}) offers an inexpensive, simple and portable analytical method for the determination of Hg^{2+} in aqueous media. The proposed method requires that a sensitive Hg^{2+} -selective chemosensor, in combination with a charge separator(s), be immobilised on a working electrode, followed by photoelectrochemical evaluation. Photoelectrochemical evaluation refers to the monitoring of an electron current as a result of changes in chemical properties of the system under illumination [1]. In the photoelectrochemical cell (PEC) proposed for Hg^{2+} detection, the immobilised Hg^{2+} selective rhodamine 6G derivative dye (RS) will undergo a chemical rearrangement to release a chromophore upon chelating Hg^{2+} . The newly formed Hg^{2+} complex, i.e. RS- Hg^{2+} , will therefore fluoresce under illumination. The charge separator, polyaniline (PANI), will facilitate as the transducer and convert the photochemical change into a measurable voltage response. The main aim of the following sections is to construct a working electrode for a PEC capable of qualitative as well as a quantitative response towards Hg^{2+} under illumination.

The method of the photoelectrochemical detection of Hg^{2+} is based on the extraction of electrical energy from a light-activated Hg^{2+} complex. Under illumination, rhodamine 6G (R6G) electrons are excited to the triplet state from where R6G radicals are generated [2-4]. Depending on the electron donating or accepting nature of the solvent environment of the R6G radicals, electron transfer will occur. When activated, the spiro ring of the Hg^{2+} selective RS sensor opens to establish a delocalised xanthene moiety that is identical to that of R6G [5]. It was therefore suggested that the excited electrons can be harvested either from the triplet or radical state of the activated RS- Hg^{2+} into an electron current by controlling the environment of the activated complex. To control the environment of RS- Hg^{2+} , the Hg^{2+} probe was immobilised in composite form with a selected charge separator, PANI.

In the previous chapter it was concluded that from an electrochemical point of view, PANI was a superior charge separator compared to the 2-bromoaniline copolymers. The conductive properties of PANI are well known [6, 7]. In dye-sensitised solar cells (DSSCs) PANI is routinely added as either a solid phase electrolyte or charge separator [8, 9]. In the DSSCs the PANI facilitates the electropositive hole separation, conducting electropositive holes away from the activated ruthenium bipyridyl complex towards the counter electrodes, and hence reducing the oxidised dye [10].

PANI can be found in five oxidation states, of which the emeraldine base (EB) is the most favourable as it is only partially reduced or oxidised [11]. The EB can then be protonated by a protic acid to various degrees to form conductive or semiconductive PANI. According to Tan *et al.* [10] the intermediate conductivity of PANI in the semiconductive region is more suitable for use in PECs than those closer to the conductor or insulator region. Tan *et al.* [10] suggest the intermediate level because the energy band-gap decreases with increasing conductivity, yet an increase in the conductivity accelerates the hole transfer in the polymer. Accelerated hole transfer reduces the resistance of the photoelectrochemical electrode, as well as the recombination opportunities between electropositive hole and electron. For all electron or hole conductive routes in a PEC, the transitions must be energetically favourable, with large enough energy band-gaps, and ideally situated valence bands, conductive bands and Fermi levels. The spectrophotometric and electrochemical properties of PANI and RS- Hg^{2+} are therefore used to suggest an energy diagram determining the fate of the excited photon in the PEC. Although the photometric properties of the RS- Hg^{2+} are already known (Chapter 3 and Wu *et al.* [5]), the optical responses of the optical probe need to be determined when in composite with PANI and immobilised on indium tin oxide (ITO).

A composite of PANI and RS (PANI-RS) was coated onto ITO working electrodes and subjected to photovoltage measurements in the presence and absence of Hg^{2+} . The proposed method of Hg^{2+} determination requires a limit of detection (LOD) and/or quantification (LOQ) in the region of the recommended limit by the World Health Organization (WHO), which is $6 \mu\text{g L}^{-1} \text{Hg}^{2+}$ for drinking water [12]. The selectivity of the immobilised RS in the presence of background ions as well as the pH sensitivity of the photoresponse will also be evaluated. In this part of the study, the

first steps are taken to design a Hg^{2+} selective ITO electrodes to be used in PECs, where the optical recognition is converted into a measurable signal. The photoresponses of the PANI-RS composite electrodes will also be compared to RS composites containing the polyaniline-*co*-2-bromoaniline (P[A-*co*-2-BrA]) copolymers to confirm the charge separation abilities of the polymers measured in Chapter 5.

6.2 Materials and methods

6.2.1 Materials

ITO glass plates, with a surface resistivity of between 8 and $12\Omega\text{ sq}^{-1}$, were purchased from Aldrich, South Africa. All chemicals and organic solvents used were of analytical reagent grade, as purchased from Sigma-Aldrich, South Africa. All aqueous solutions were prepared with ultrapure water obtained using a Milli-Q RO purification system.

6.2.2 Instrumentation

Surface imaging of the coated electrodes was performed with a Leo 1430VP scanning electron microscope and surface thickness was determined with a Veeco DEKTAK 6M surface profiler. The RS dye was synthesised and characterised according to procedures set out in Section 3.2.3. Electrochemical measurements were performed on an Epsilon BAS potentiostat, with EpsilonEC 2000-XP software. A three-electrode cell was used with the dye coated ITO plate as the working electrode, Pt wire as the counter electrode, and Ag/AgCl as the reference electrode. The voltammograms were measured in 0.05 M phosphate buffer (pH 7.5) containing 1 mM RS, with and without $100\text{ }\mu\text{g L}^{-1}$ HgCl_2 , at 100 mV s^{-1} scan rate. The flat-band potential for the ITO/PANI-RS electrode was determined for applied potentials of between 600 and -600 mV in 0.1 mM $\text{K}_3\text{Fe}(\text{CN})_6$ and 0.05 M KNO_3 under photo illumination. The same three-electrode set-up was used for the photoelectrochemical evaluation of the various coated electrodes. For the photoelectrochemical set-up, the electrolyte was 0.05 M KNO_3 and varying concentrations of HgCl_2 were used. An Elmo Omnigraphic 253 slide projector was used as a light source. The tungsten halogen lamp emitted 0.86 mW cm^{-2} at the point of absorption by the electrode. The collimated beam was isolated in a steel casing to eliminate background light effects. The light was pulsed at

2 s intervals and the photovoltage signals were recorded by means of a DAX data acquisition system.

6.2.3 Procedure for electrode preparation

ITO glass plates were cut into approximately 8×12 mm segments and were sonicated for 10 min in water, followed by ethanol and then acetone. PANI was prepared according to standard chemical oxidation polymerization methods [13]. A sample of 40 μL composite solution, containing 5 mg PANI and 5 mg RS in 5 mL dimethyl sulfoxide (DMSO) was drop-coated onto the ITO surface, which was then dried at room temperature for 2 to 5 days. Composites of the 2-bromoaniline copolymers, synthesised as described in Section 5.2.2 and RS were also made and coated onto ITO for photoelectrochemical evaluation. Aliquots of 50 μL of 5 g L^{-1} DMF prepared P[A-co-2-BrA] copolymers was coated onto ITO substrates together with 50 μL of RS. The electrodes were dried at room temperature and evaluated in 0.05 M KNO_3 .

6.3 Results and discussion

6.3.1 Surface morphology

The DMSO/RS drop coatings dried on the electrode surfaces to form cube-like crystals. SEM images of the crystals on the electrode surface are shown in Figure 6.1. The crystal composite did not dissolve in water and was bound to the electrode surface. The crystals were cube-like and their sizes depended on the solvent evaporation period. After 5 days of drying at 25°C the cube lengths were approximately 15 μm . The formation of crystals was favourable, because it increased the surface roughness of the coated electrode. The increased surface roughness increased the active surface area on which the RS- Hg^{2+} interaction can take place as well as contact with the PANI charge separator. In composite form with PANI the contact area was therefore increased, as opposed to having the crystals deposit onto a polymer film. Generally, a more homogeneous surface coverage is preferred [10] and the photoactivity is increased by thin compact layers [14].

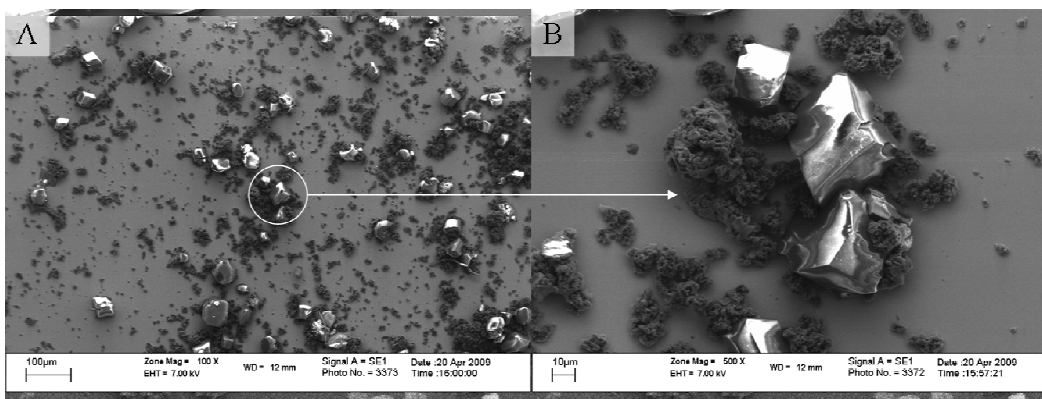


Figure 6.1: SEM images of the PANI-RS dye composite on the ITO surface: A) magnification $\times 100$ and B) magnification $\times 500$.

PANI was coated into thin composite layers under acidic conditions ($\text{pH} < 2$) but addition of RS dye to this acidic level of PANI caused the spiro ring to open, thereby releasing the fluorescent xanthene moiety that is required for Hg^{2+} detection. PANI is only partially soluble in DMF, and only low molecular weight chains of PANI in the composite were immobilised on the electrode surface.

The shorter chains tended to form bigger clusters as opposed to smooth thin film formation. A metallic deposition was observed on the crystal surfaces after analysis of Hg^{2+} samples. The deposition was irreversible, and was most likely Hg^0 , mainly due to the presence of excess of Hg^{2+} in the evaluated samples. The thickness of the composite layer generally determines the distance an electron needs to be transported from the excited molecule to the back contact [15, 16]. The surface image profile in Figure 6.2 shows a very rough particulate layer on the ITO surface. Due to the rough non-uniform distribution of the crystal composite the surface photoactivity was therefore taken as an average over a 6×10 mm electrode surface area. The average film thickness with a single $40 \mu\text{L}$ composite coating was $1.62 \mu\text{m}$.

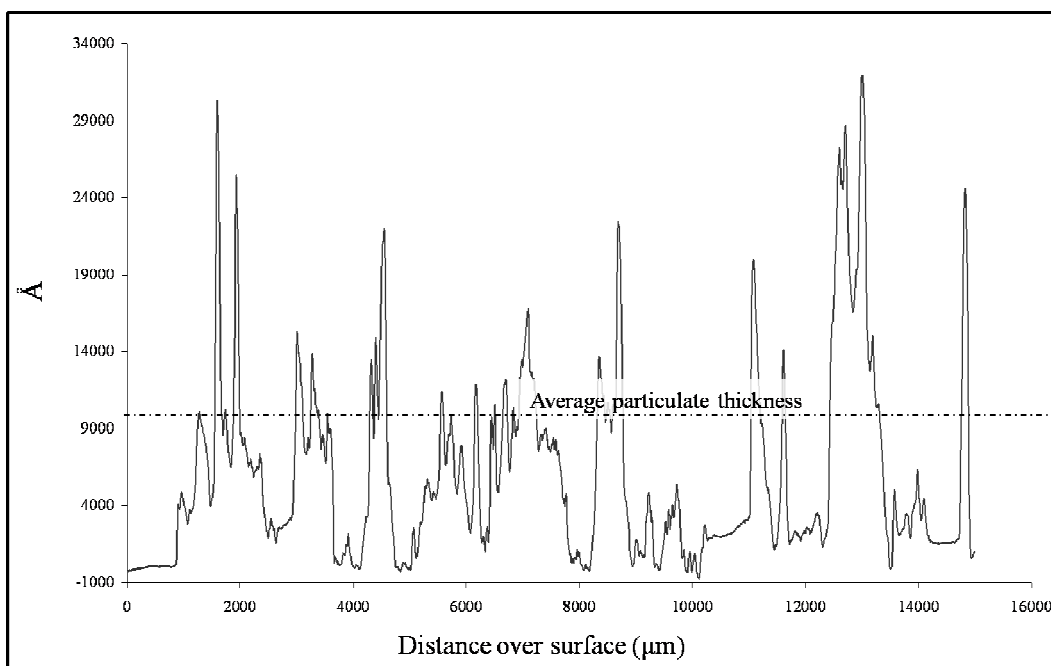


Figure 6.2: Surface profile of the ITO electrode coated with 40 μL of PANI-RS composite.

6.3.2 Spectrophotometric properties of the RS- Hg^{2+} complex with PANI

For the RS- Hg^{2+} complex, the absorbance and emission peaks were observed at 536 nm and 558 nm respectively (compared to 538 nm and 560 nm, as reported by Wu *et al.* [5]), thereby confirming the optical properties of the RS- Hg^{2+} complex. For the Hg^{2+} photoelectrochemical detector to successfully convert photoactivity to an electron transport the conversion needs to be energetically favourable. The RS- Hg^{2+} absorption at 536 nm converted to a 2.35 eV energy band-gap, using the Planck equation. For PANI it was assumed that the emeraldine form would be the photoconductive part of the PANI layer because the leucoemeraldine and pernigraniline forms behave more like insulators [17]. The flat-band potential (FB) for the emeraldine PANI was reported to be 0.63 V (vs SHE), as calculated with the Mott Schottky plots by Huang *et al.* [17]. The energy band-gap for the emeraldine form was 3.33 eV. The FB for the PANI-RS composite was determined by varying the applied potential between 0.6 V and -0.6 V and measuring the photoresponse on illumination of the electrode. From Figure 6.3, the FB for the PANI-RS composite on an ITO electrode was determined to be 0.4 V vs Ag/AgCl, or 0.61 V vs SHE. The irregular shape of the photoresponse at various applied potentials was due to

influences of other redox reactions occurring in the electrolyte. These include the Fe^{3+} to Fe^{2+} redox couple, as well as (to a lesser extent) the oxidation of nitrate. The FB was taken as the value of the applied potential at the point of zero photovoltage (the value at which the photoresponse crosses the x axis). This value is regarded as the point at which the Fermi levels of the $\text{Fe}(\text{CN})_6^{-3/4}$ redox couple and the PANI-RS composite are equal.

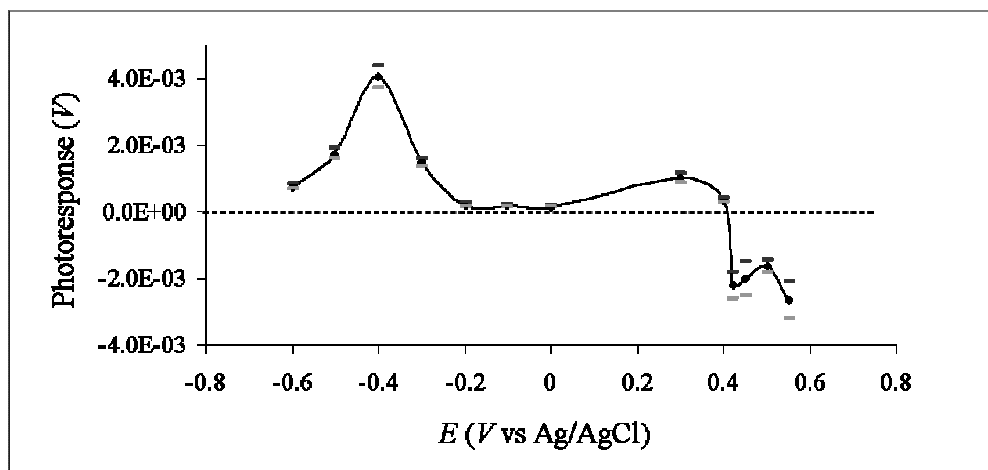


Figure 6.3: Photoresponse for the PANI-RS composite measured at various applied potential in 0.1 mM $\text{K}_3\text{Fe}(\text{CN})_6$ and 0.05 M KNO_3 to determine the FB.

Figure 6.4 represents a coated ITO electrode in an aqueous electrolyte containing mercury chloride (HgCl_2). The half peak potential ($E_{1/2}$), the potential midway between the oxidation and reduction peak potential, for the HgCl_2 redox couple on ITO was 0.225 V (vs SHE). The energy diagram suggests that in the presence of Hg^{2+} and light ($h\nu$), an electron was excited from the ground state in the chromophore (S/S^-) to an excited state (S/S^*). The $E_{1/2}$ for HgCl_2 was lower than the FB of PANI-RS and therefore excited electrons were transported in the direction of HgCl_2 , and the RS- Hg^{2+} complex formed on the electrode surface. The electrolyte containing the HgCl_2 acted as an electron acceptor. The valence band (VB) of PANI was lower than that of the RS dyes, in both the complexed and uncomplexed forms, and this energy level was then ideally positioned to transport electropositive holes from the composite to the electrolyte. The proposed energy diagram for the Hg^{2+} photoelectrochemical detector illustrates that the PANI-RS dye composite electrode to behave as a photocathode in the presence of HgCl_2 (Figure 6.4).

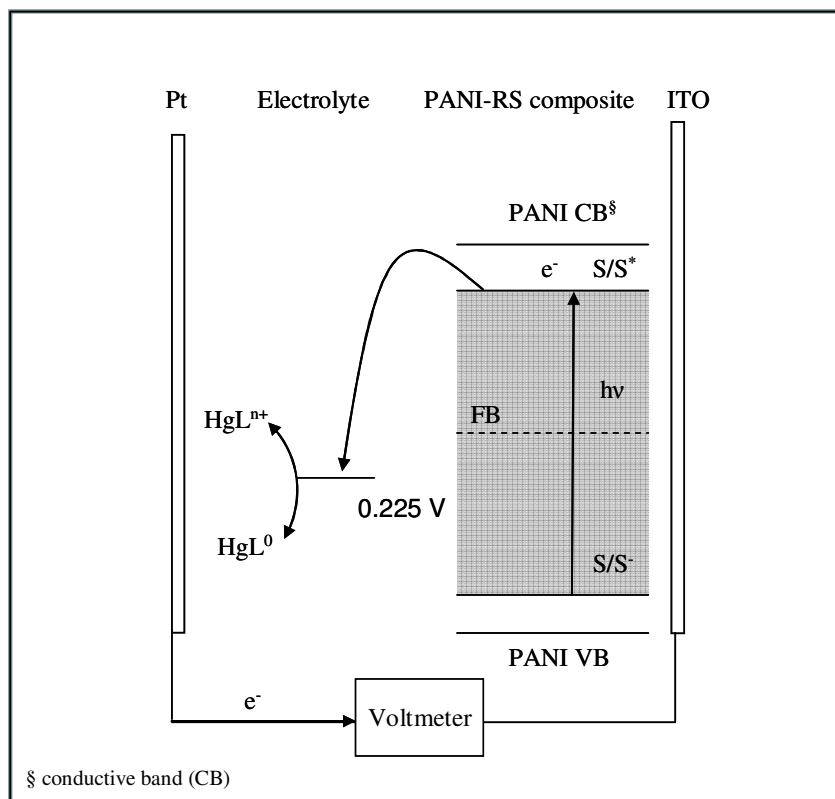


Figure 6.4: Proposed energy diagram for the photoelectrochemical Hg^{2+} detector.

6.3.3 Electrochemical evaluation of RS- Hg^{2+} complex

The electrochemical properties of RS were investigated. Electrochemical evaluations of the RS coated electrodes were conducted in 0.05 M phosphate buffer at pH 7.5. The cyclic voltammograms were measured in the presence and absence of $100 \mu\text{g L}^{-1}$ HgCl_2 , and results are shown in Figure 6.5. In 0.05 M phosphate buffer the RS solution turned pink at both 0.8 V and -0.6 V applied potential. The RS fluorophore appeared to have a single oxidation peak at 0.9 V in aqueous media. The single oxidation peak of RS indicated the position of the highest occupied molecular orbital from where an electron could be donated. In the presence of HgCl_2 the single oxidation peak either disappeared or moved to a higher applied potential. The redox values for RS- Hg^+ could not be determined due to the following factors. After 0.8 V and -0.8 V irreversible pink colour changes occurred, indicating that the RS- Hg^{2+} was permanently changed after these applied potentials. Further fouling of the ITO electrode with Hg^0 occurred at potentials lower than 0 V. As a result, the potential window to determine the redox values for RS- Hg^+ was considerably narrower than

that for RS alone. Considering the results of the electrochemical evaluation it is suggested that the binding of Hg^{2+} resulted in the delocalised ring opened xanthere moiety, which is considerably more stable than the RS dye alone. Electron transfer will therefore more likely result from the photon excitation than rearrangement of the RS- Hg^{2+} complex.

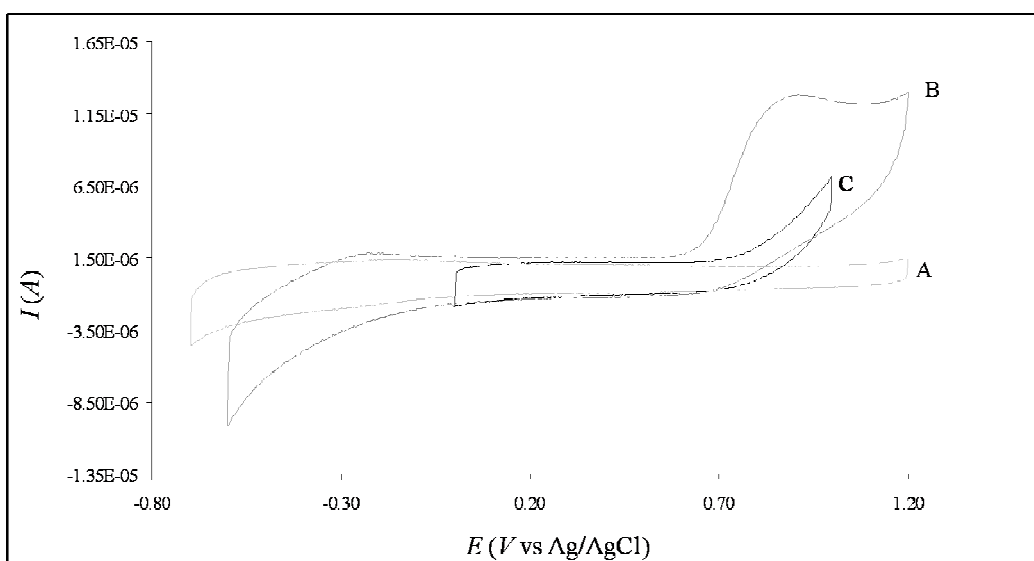


Figure 6.5: Cyclic voltammograms measured for an ITO electrode at 100 mV s^{-1} in 0.05 M phosphate buffer pH 7.5: A) with buffer alone, B) in the presence of 1 mM RS without $100 \text{ } \mu\text{g L}^{-1}$ HgCl_2 , and C) with $100 \text{ } \mu\text{g L}^{-1}$ HgCl_2 .

6.3.4 Photoresponse of ITO/PANI-RS coated electrodes

The photoresponse of ITO coated with PANI-RS was determined in 0.05 M KNO_3 containing HgCl_2 . As schematically depicted in Figure 6.4, ITO coated with PANI-RS behaved like a photo-cathode in the presence of Hg^{2+} in a closed PEC. The photoresponse increased with increasing amounts of HgCl_2 to concentrations as high as $150 \text{ } \mu\text{g L}^{-1}$, after which the reading remained relatively constant. The LOD was set to where the photoresponse of the ITO/PANI-RS electrode to Hg^{2+} was three times the value of background signal (no Hg^{2+}) in solution. Although an increase in photoactivity was observed at $0.2 \text{ } \mu\text{g L}^{-1}$ the LOD was $6 \text{ } \mu\text{g L}^{-1}$, which is the WHO maximum recommended amount of Hg^{2+} in drinking water [3]. The photoresponse of separately prepared electrodes exposed to the same amount of Hg^{2+} varied by approximately 10%. The large variation was expected due to the non-uniform distribution of the crystal composite on the electrode surface, as seen in Figure 6.1. As

the electrode surfaces were irreversibly fouled with Hg^{2+} , the reproducibility could not be determined on the same electrode. A small voltage response was always observed in the absence of Hg^{2+} . This is due to ever-present trace amounts of the ring-opened RS tautomer. The baseline for the voltage measurements increased with increasing amounts of Hg^{2+} , indicating a greater diffusion layer next to the electrode surface.

Figure 6.6 illustrates the photoresponses measured for short light pulses (± 2 s) measured at various concentrations of Hg^{2+} ($[\text{Hg}^{2+}]$).

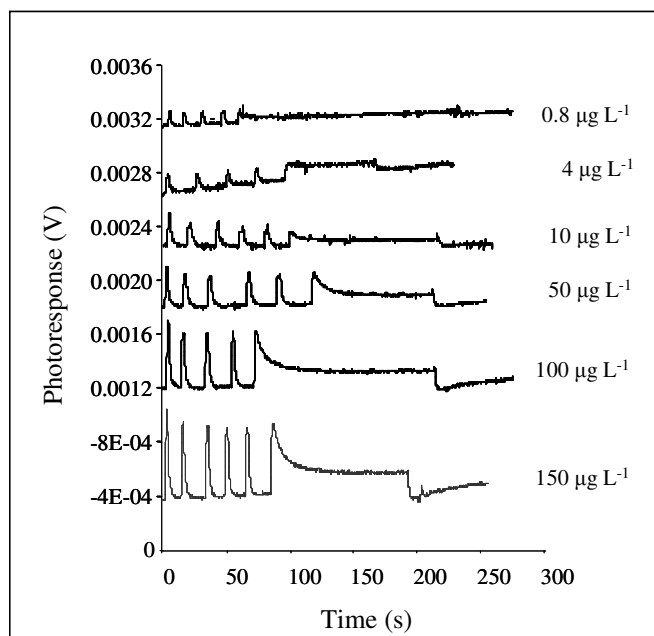


Figure 6.6: Photoresponse of an ITO/PANI-RS electrode measured at various Hg^{2+} concentrations in 0.05 M KNO_3 .

The sensor response was also determined under constant illumination following exposure to a continuous source of light. The response increased linearly from 10 to $150 \mu\text{g L}^{-1}$, and is best represented by the equation: $\text{photoresponse} = 0.0026 [\text{Hg}^{2+}] + 0.1177$, with a $R^2 = 0.9959$. After $150 \mu\text{g L}^{-1}$, the electrode surface was saturated to the point where the response became more irregular.

Under constant illumination the electrons were first activated to the excited state, but decayed almost instantly to a secondary excited state, as shown in Figure 6.7. Using the differential equation for exponential decay, the decay constant (λ) for the excited RS- Hg^{2+} complex at various Hg^{2+} concentrations could be determined. The λ varied

linearly between 0.016 and 0.043 depending on Hg^{2+} concentration (10 to $150 \mu\text{g L}^{-1}$), thereby indicating that the lifetime in the activated state is not influenced by the amount of activated complex. At higher concentrations the rate of decay was simply faster, and maintained the approximate lifetime of the excited RS-Hg^{2+} . As the lifetime remained relatively constant, the position of the excited state was the same for all concentrations. The positions of the excited states for all complexes were unique. This suggests that the photoresponse is determined by the RS-Hg^{2+} activated complex alone and not any other activated complex that may form in solution.

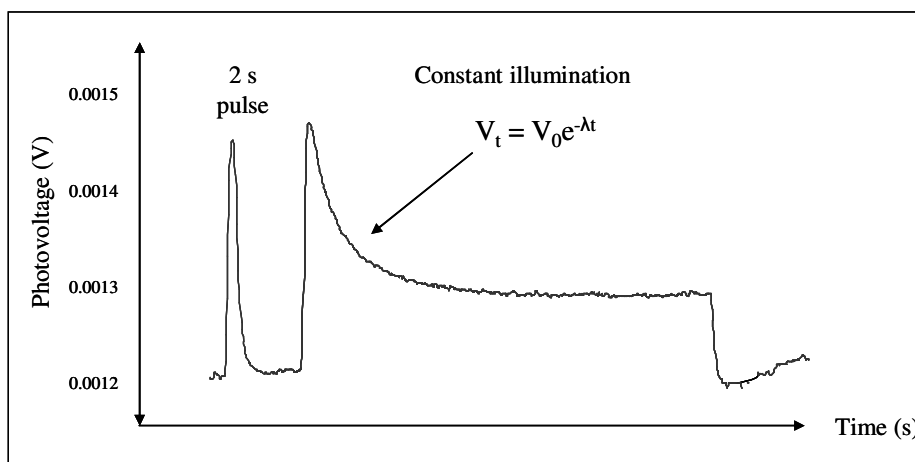


Figure 6.7: The photovoltage response of the ITO/PANI-RS electrode in $100 \mu\text{g L}^{-1}$ Hg^{2+} under constant illumination, highlighting the decay to an intermediate level.

The pH dependence of the photoresponse was determined in $0.01 \text{ M Na}_2\text{HPO}_4$, which was pH modified with $0.01 \text{ M H}_3\text{PO}_4$. As the RS sensor is pH insensitive in the range pH 5 to 10 [5], the pH dependence of the ITO/PANI-RS electrode was investigated. The electrode was saturated in $10 \mu\text{g L}^{-1} \text{ HgCl}_2$ (in $0.01 \text{ M Na}_2\text{HPO}_4$) and the photoresponse was determined between pH 4 and 9.8. Figure 6.8 shows that the photoresponse was relatively stable and decreased marginally between pH 6 and 9 (3% error). The baseline response of the coated electrode was 0.004 V , as measured in 0.05 M KNO_3 alone.

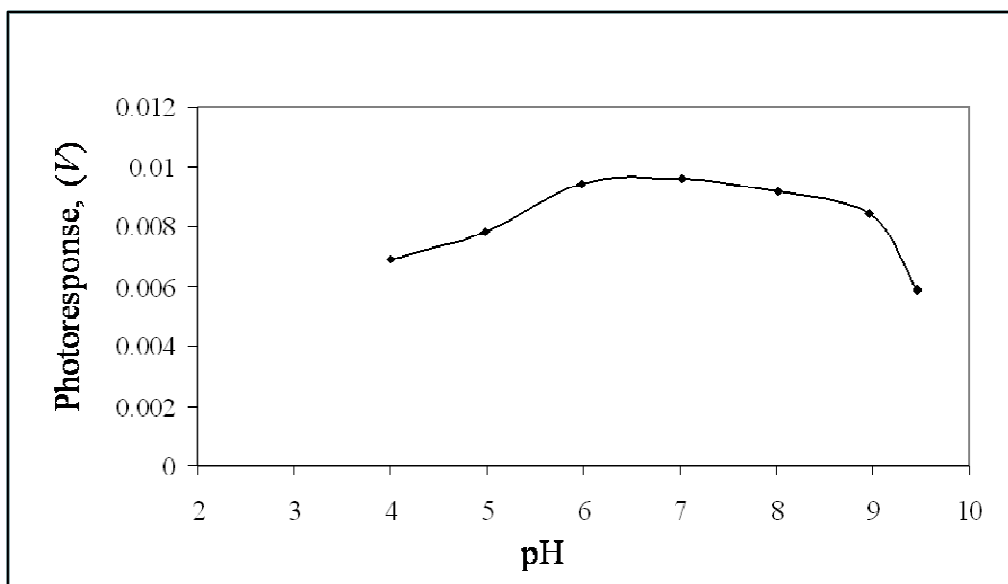


Figure 6.8: pH evaluation of the ITO/PANI-RS electrode saturated with $10 \mu\text{g L}^{-1}$ HgCl_2 measured in 0.01 M phosphate buffer.

At $\text{pH} < 6$ the photoresponse was quenched due to protonation of the PANI to a more conductive form which increased the delocalisation in the composite. At $\text{pH} > 9$ the PANI had more insulating behaviour, which inhibited electron transfer. UV analysis of the RS- Hg^{2+} complex in aqueous DMF showed that the complex was stabilised by the presence of H_3O^+ molecules prior to ring opening. At higher pH (> 8.5) the number of ring opened RS dye molecules was reduced, which decreased the absorbance as well as the fluorescence of the RS- Hg^{2+} complex. Therefore, all pH evaluations were conducted in 0.05 M KNO_3 at pH 7.2.

The photoresponse of the sensor was determined in the presence of background compounds to determine the effect of any interfering ions. Figure 6.9 shows the photoresponse of the RS electrode in the presence of $500 \mu\text{g L}^{-1}$ K^+ , Cd^{2+} , Mg^{2+} , Pb^{2+} , Ag^+ , Na^+ , Cu^{2+} , NO_3^- , Cl^- , SO_4^{2-} , PO_4^{2-} and $\text{CH}_3(\text{O})_2\text{C}^-$. All measurements were conducted in 0.05 M KNO_3 to ensure conductivity in the PEC and were therefore regarded as the baseline for all measurements.

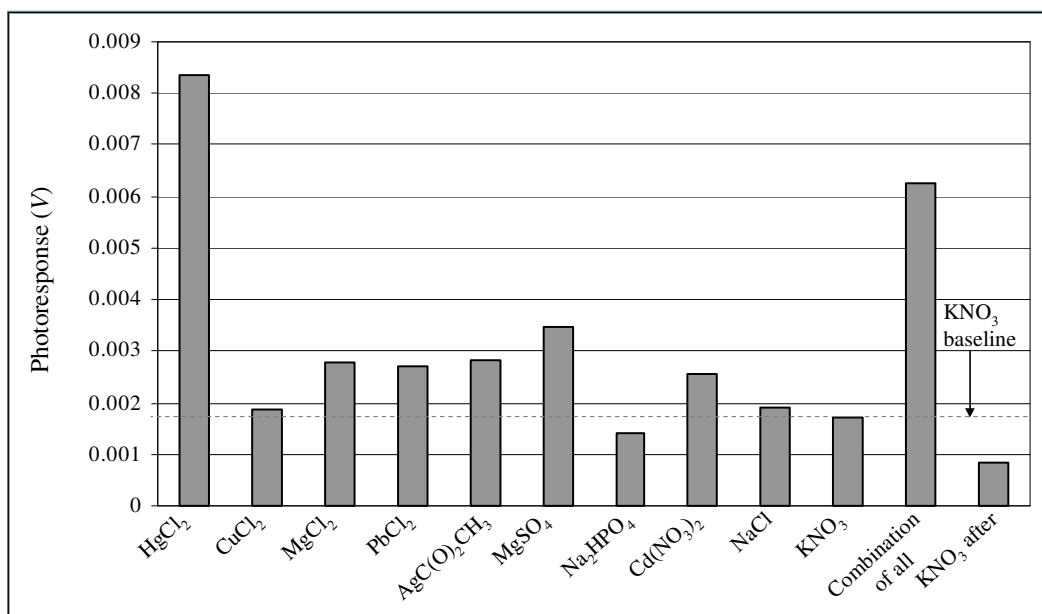


Figure 6.9: The photoresponse of the ITO/PANI-RS sensor in the presence of $500 \mu\text{g L}^{-1}$ potential interfering ions. The background response of ITO/PANI-RS (---) is the signal measured of electrolyte 0.05 M KNO_3 alone and should be subtracted from the observed response to establish the influence of each interfering ion on its own.

The photoresponse of the dye coated electrode towards Hg^{2+} alone was only approximately three times the value towards other background ions. The decrease in selectivity of the dye-coated electrode to Hg^{2+} compared to that of RS dye alone [5] was due to the formation of a double layer on the electrode surface. The electronegative surface of the dye under steady state conditions will lead to the formation of a positive counter layer in aqueous solution. In solution the RS- Hg^{2+} complex has a 2:1 binding event, but once immobilised the RS- Hg^{2+} complex is more rigid and the interaction was more heterogeneous. It is suggested that dipole interaction between the xanthene functional group and the diffusion layer may induce delocalization in the RS dye, weakening the spiro ring that is needed for the fluorescent response. It is therefore unknown at this stage whether the heterogeneous interaction is 2:1, or if the diffusion layer environment, would allow for 1:1 Hg^{2+} ring opening of the RS dye. A 1:1 binding event for immobilised RS- Hg^{2+} in the presence of a positive diffusion layer may explain the high baseline response, as well as the decreased selectivity of the RS dye in the presence of certain background ions.

Interfering ions, which could influence the determination of Hg^{2+} , are SO_4^{2-} and Ag^+ . The affinity of Ag^+ and Hg^{2+} for nitrogen compounds, and therefore the competition between these two cations for rhodamine compounds, is well known [18]. However, it is unlikely that Ag^+ will naturally occur at concentrations as high as $500 \mu\text{g L}^{-1}$ in water resources. The influence of SO_4^{2-} is most likely due to its interaction with the PANI, as well as with the RS ketone functional group, which is vulnerable to interaction in the immobilised state.

The selectivity of the PANi-RS composite could possibly be improved after investigating the addition of a TiO_2 semiconductor, inhibiting interactions with the RS ketone, and the addition of gold nanoparticles [19, 20]. Gold nanoparticles are Hg^{2+} selective, and combined with rhodamine dyes, increase the quantum yield and fluorescent response of chemosensors. The RS binding with Hg^{2+} is irreversible, but the expensive ITO glass plates can be reused without increasing the surface resistivity of the ITO coating. The electrodes can be sonicated in DMSO, followed by water and then acetone, and simply recoated with the PANI-RS composite.

6.3.5 Photoresponses of P[A-co-2-BrA] copolymers

The photoresponses of 2-bromoaniline copolymers were measured and compared to the photoresponse of the PANI-RS composite. The photoresponses of the copolymer composites were measured up to $50 \mu\text{g L}^{-1} \text{Hg}^{2+}$ in 0.05M KNO_3 . Results are shown in Figure 6.10. The photo-cathodic shape of the P[A-co-2-BrA] copolymers photoresponses was similar to that of the PANI-RS composite. The copolymers containing less than 50% 2-bromoaniline content had a linear increase up to $10 \mu\text{g L}^{-1} \text{Hg}^{2+}$ after which the surface was saturated. P[A-co-2-BrA] 50, P[A-co-2-BrA] 70 and P-2-BrA in composite with RS had smoother film-like coatings, which appeared to inhibit interaction with Hg^{2+} in solution. The charge separation in the copolymers was more efficient for copolymers containing more PANI, which had a higher conductivity as opposed to poly-2-bromoaniline, and the photoresponse was not improved by a higher RS-copolymer surface contact. The copolymer composites had more than 1000-fold lower photoresponse towards Hg^{2+} as opposed to PANI-RS.

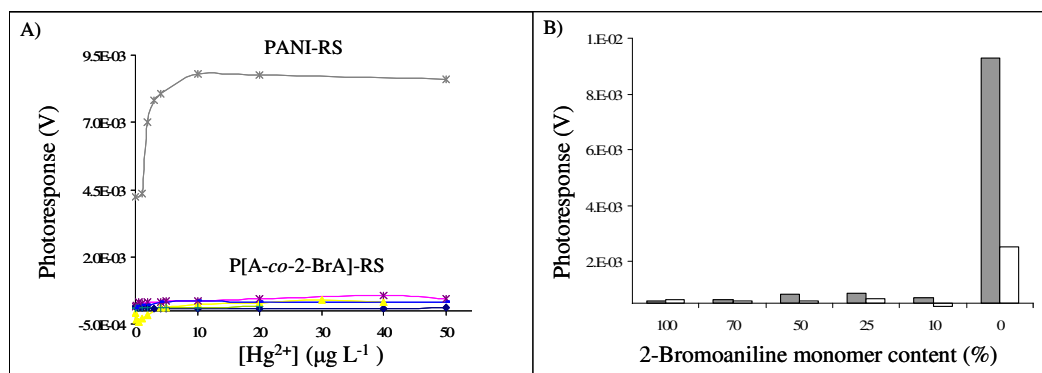


Figure 6.10: A) The photoresponses of P[A-co-2-BrA] copolymers in composites with RS and PANI-RS towards increasing Hg^{2+} concentration in 0.05 M KNO_3 . B) The photoresponse of the P[A-co-2-BrA] composite copolymers measured up to 10 $\mu\text{g.L}^{-1}$ Hg^{2+} . Zero content 2-bromoaniline represents the PANI-RS composite.

6.4 Conclusions

A method for the photoelectrochemical detection of Hg^{2+} with ITO electrodes modified with a PANI-RS composite is proposed. In a closed PEC, the photon excitation from the Hg^{2+} -sensitive dye was converted to an electron transfer process. The optical recognition of Hg^{2+} was successfully converted into a measurable photovoltage. An energy diagram for the implementation of a PEC based on a dye sensitiser was suggested. The proposed energy diagram, based on the spectrophotometric and electrochemical properties of the RS dye and PANI, depicted a photo-cathodic response for the PANI-RS composite electrode towards Hg^{2+} in the PEC. The proposed energy diagram proved adequate when the PEC containing the composite coated electrode had a photo-cathodic response to Hg^{2+} as low as 0.2 $\mu\text{g L}^{-1}$. The cell demonstrated analytical determination of Hg^{2+} in the range 10 to 150 $\mu\text{g L}^{-1}$ with a LOD of 6 $\mu\text{g L}^{-1}$.

The ITO/PANI-RS photoresponses were ideally measured between pH 6 and 9, with only a 3% error. The heterogeneous interaction on the ITO/PANI-RS electrode surface was strongly influenced by the formation of a positive double layer. The double layer increased the background response and reduced the selectivity of the PANI-RS composite towards Hg^{2+} to only three times that of the competing background ions. Although the complexation on the electrode surface was irreversible, the ITO plate could be cleaned and recoated. When compared to the 2-

bromoaniline copolymers, PANI has significantly more efficient charge separation ability and remains a favourable choice for use in the PEC.

6.5 References

- [1] C.T. Wang, H.H. Huang, *J. Non Cryst. Solids*, 354 (2008) 3336-3342.
- [2] V.E. Korobov, V.V. Shubin, A.K. Chibisov, *Chem. Phys. Lett.*, 45 (1976) 498-501.
- [3] G. Jones II, X. Wang, J. Hu, *Can. J. Chem.*, 81 (2003) 789-798.
- [4] P.C. Beaumont, D.G. Johnson, B.J. Parsons, *J. Photochem. Photobio. A: Chem*, 107 (1997) 175-183.
- [5] D.W. Wu, W. Huang, C. Duan, Z. Lin, Q. Meng, *Inorg. Chem.*, 46 (2007) 1538-1540.
- [6] A. Pud, N. Ogurtsov, A. Korzhenko, G. Shapoval, *Prog. Polym. Sci.*, 28 (2003) 1701-1753.
- [7] A. Pron, P. Rannou, *Prog. Polym. Sci.*, 27 (2002) 135-190.
- [8] M.Y. Chang, Wu, C. S. Chen, Y. F., B.Z. Hsieh, W.Y. Huang, K.S. Ho, T.H. Hsieh, Y.K. Han, *Org. Electron.*, 9 (2008) 1136-1139.
- [9] B. Gupta, R. Prakash, *Mater. Sci. Eng. , C*, 29 (2009) 1746-1751.
- [10] S. Tan, J. Zhai, B. Xue, M. Wan, Q. Meng, Y. Li, L. Jiang, D. Zhu, *Langmuir*, 20 (2004) 2934-2937.
- [11] W.J. Feast, J. Tsibouklis, K.L. Pouver, L. Groenendaal, E.W. Meijer, *Polymer*, 37 (1996) 5017-5047.
- [12] World Health Organization (2005), available at http://www.who.int/water_sanitation_health/dwq/chemicals/mercuryfinal.pdf, accessed 01-10-2009 .

- [13] M.C. Gupta, S.S. Umare, *Macromolecules*, 25 (1992) 138-142.
- [14] C.J. Harris, W.J. Belcher, P.C. Dastoor, *Sol. Energy Mater. Sol. Cells*, 91 (2007) 1127-1136.
- [15] J. Van de Lagemaat, N.G. Park, A.J. Frank, *J. Phys. Chem. B*, 104 (2000) 2044-2052.
- [16] W. Kubo, S. Kambe, S. Nakade, T. Kitamura, K. Hanabusa, Y. Wada, S. Yanagida, *J. Phys. Chem. B*, 107 (2003) 4374-4381.
- [17] H.G. Huang, Z.X. Zheng, J. Luo, H.P. Zhang, L.L. Wu, Z.H. Lin, *Synth. Met.*, 123 (2001) 321-325.
- [18] W. Shi, H. Ma, *Chem. Commun.*, 2008 (2008) 1856-1858.
- [19] J. Chen, A. Zheng, A. Chen, Y. Gao, C. He, X. Kai, G. Wu, Y. Chen, *Anal. Chim. Acta*, 599 (2007) 134-142.
- [20] C.C. Huang, H.T. Chang, *Anal. Chem.*, 78 (2006) 8332-8338.

Chapter 7

Photoelectrochemical determination of mercury (II) with a TiO_2 / polyaniline/rhodamine derivative composite electrode

7.1 Introduction

The spectrophotometric change of inorganic mercury (Hg^{2+}) selective small molecule chemosensors upon ligating Hg^{2+} was successfully converted to a photovoltaic response as described in Chapter 6. The photo-cathodic response of the indium tin oxide (ITO) electrode, coated with the polyaniline and rhodamine 6G hydrazone chemosensor composite (PANI-RS), towards Hg^{2+} was sensitive and could be quantified. The photon excitation was followed by charge separation, which resulted in an electron transfer through the electrolyte to the counter electrode. The fluorescent response of the chromophore with Hg^{2+} was converted to an electron current. The photoresponse of the Hg^{2+} selective chromophore was equivalent to the amount of Hg^{2+} in solution.

As polyaniline (PANI) is a hole separator and p-type semiconductor, charge could be conducted to the electrolyte. For a photo-anodic response charge separation needs to occur in the opposite direction towards the ITO back contact. For electron injection/conduction to the ITO back contact an n-type semiconductor is required. Chromophores based on rhodamine derivatives are popular for designing fluorescent chemosensors since the binding unit can easily be modified, while the fluorescent xanthene remains intact [1-6]. Derivatives of the rhodamine chromophores will have small band shifts compared to the parent rhodamine. It is expected that the fluorescent quenching or electron transfer to the semiconductor for the rhodamine 6G hydrazone derivative (RS) will be similar to that of rhodamine 6G (R6G).

The sensitization of semiconductor surfaces with rhodamine compounds for various applications has previously been investigated [7, 8]. Sensitization is achieved by adsorption of the dye molecules onto the semiconductor surface which, upon excitation, injects an electron into the semiconductor conduction band (CB). The dyes can adsorb via chemical, physical or electrostatic methods on semiconductors such as CdS [9, 10], ZnO [11, 12], silicates [13, 14] and TiO_2 .

The adsorption of xanthene-type molecules like R6G on porous silica gels takes place through the carbonyl group (acid or ester) [13]. The nitrogen substituents on the xanthene molecules (R6G, RB and R110) do not influence the adsorption patterns on porous silica but determine the separation between molecules. Asha Jhonsi *et al.* [9] found that xanthene dyes also adsorbed onto the surface of colloidal CdS through their anchoring group (-COO). The H-aggregate of R6G onto silicate surfaces depends on the amine group for effective electrostatic interaction with oxygen atoms [15]. Therefore, the anchoring group of the dye on these semiconductor surfaces play a major role in the adsorption and electron transfer processes.

TiO₂ is the most widely used and studied n-type semiconductor/electron acceptor used in photoelectrochemical cells (PECs) [16-18]. The scientific interest in dye-sensitized TiO₂ solar cells stems from their unusual features and mode of operation:

- Efficient charge separation due to ultrafast injection of electrons from the dye on picosecond and sub-picosecond timescales
- Conduction involving only injected electrons rather than electron-hole pairs, due to the wide-band-gap of the semiconductor TiO₂
- High optical density due to the large surface area of the dye-sensitised nanoporous semiconductor
- Negligible charge recombination with the oxidised dye
- High quantum yields [18].

The fluorescent quenching of various sensitizers by colloidal TiO₂ has also been reported [19-22]. The fluorescent quenching is attributed mainly to electron transfer from the excited state of the dyes to the CB of colloidal TiO₂. The most efficient dye sensitised solar cells are based on a nanoporous TiO₂ film that serves both as a substrate for the dye and as the electron conductor. In these films the TiO₂ sol-gel was baked to the anatase form on the ITO surface; the anatase form has a slightly higher Fermi-level and higher surface density of surface hydroxyl groups [23] when compared to the rutile or brookite phase.

The surface charge and therefore functionality is highly pH dependant in aqueous environments. Hydrated TiO₂ surface groups include Ti-OH (pH 10.7-4.3), Ti-OH₂

($\text{pH} < 10.7$), Ti-OH_2^+ ($\text{pH} < 5$) and $\text{Ti-OH}^+-\text{Ti}$ ($\text{pH} < 4.3$). The point of zero charge (PZC) or isoelectric point [24] is an intermediate pH at which the surface has a net zero charge. The Ti-OH group is formed at high pH and protonation to Ti-OH_2^+ begins at around the PZC. The Ti-OH-Ti group also begins to form about at the PZC, and both species contribute to the positive surface charge at low pH. At sufficiently low pH an oxide surface is expected to be protonated, giving a positive surface charge. At high pH the surface will be deprotonated, to leave a negative charge. The pH dependence of hydrous TiO_2 functional groups is shown in Figure 7.1.

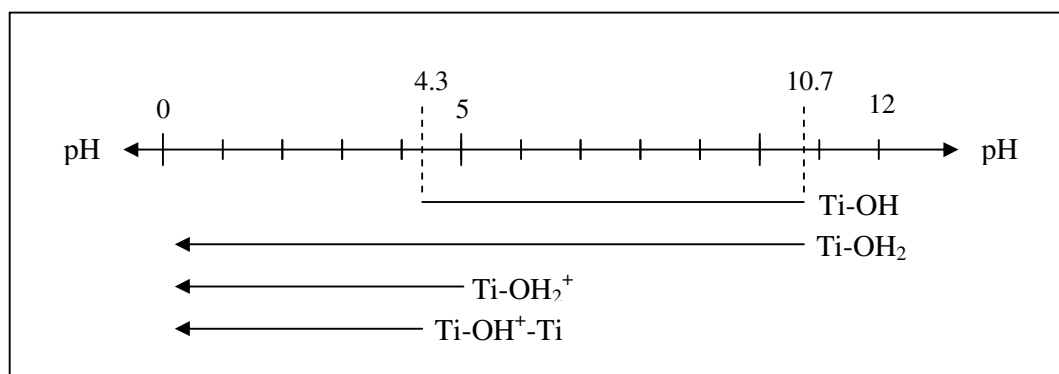


Figure 7.1: The surface functional groups of TiO_2 , depending on pH.

The polar, yet pH dependent, nature of colloidal TiO_2 surface facilitates the strong adsorption of charged dye molecules [25]. A certain degree of anisotropy or preferential orientation occurs for dye cations adsorbed on solid surfaces [26]. At higher pH the TiO_2 surface oxides become more negatively charged because Ti-OH groups are oxidised to TiO^- . Sánchez-Valencia *et al.* [27] described the formation of a double layer of charge on the TiO_2 surface by using an equivalent concentration of cations in the aqueous environment. Rhodamine cations can form part of this double layer. The electrostatic interaction between the negative surface and the rhodamine cation is crucial for adsorption of the R6G. According to Hamad *et al.* [28] R6G molecules will adsorb less onto the TiO_2 surface at $\text{pH} < 5$ due to the repulsion between the positively charged $-\text{OH}^+$ surface groups and the cationic R6G. Their simulations suggest that the phenyl moiety often inserts into the region previously occupied by the hydroxyl group, causing a near parallel adsorption on the TiO_2 surface. The carboxyphenyl group of the R6G molecule is perpendicular to the xanthene moiety, making it more sensitive to electrostatic interactions with the

surface. The intensity of the R6G dye absorption bands increased with increasing pH, but increasing pH also increased R6G dimerization and aggregate formation. The amount of R6G aggregate also increased with an increased layer charge.

The carbon structure of uncomplexed RS is relatively planar, and will adsorb onto a TiO_2 surface similar to that observed by Hamad *et al.* [28] for rhodamine 800 (R800). Because xanthene dye cations orient with their longest axis almost perpendicular to the host surface, R800 is planar and contains negative nitrogen groups. R800 adsorbs parallel to the TiO_2 surface, preferably under more basic conditions. R800 adsorbs far less than R6G. Upon binding Hg^{2+} , the spiro lactam ring of RS opens and the carbohydrazone binding unit rearranges to be approximately perpendicular to the xanthene moiety. In the complexed position, the RS- Hg^{2+} will then have as similar positioning to R6G.

In a photoelectrochemical detector the fluorophore will convert the binding process with the selected compound into an optical recognition [29]. Similar to dye-sensitized solar cells, PECs use photosensitization of wide-band-gap mesoporous oxide semiconductors to convert sunlight into an electrical current [30, 31]. Sensitization can be achieved by excitation of dye molecules adsorbed on the semiconductor surface by an electrostatic, hydrophobic or chemical interaction, and the subsequent electron injection into the CB of the semiconductor [32]. In the proposed Hg^{2+} photoelectrochemical detector, the Hg^{2+} -photosensitive dye is in composite form with the PANI [33]. PANI was implemented as a form of solid electrolyte or hole conductor. The composite was coated onto a porous TiO_2 layer with an ITO back contact. When activated, the spiro ring of the Hg^{2+} -selective RS sensor opened to establish a delocalised xanthene moiety that was identical to that of R6G. The dye was activated in the presence of Hg^{2+} and light; a photon was absorbed from the ground state (S/S^+) to an excited state (S/S^*). From the excited state in the composite, the electron was injected into the CB of TiO_2 . The electrons were shuttled from the dye through the semiconductor to the ITO electrode [34]. Charge separation was achieved with the sensitive dye between conductive PANI and anatase TiO_2 . In a closed cell, the electrons can move through the external circuit to the counter electrode and then to the electrolyte. The determination of Hg^{2+} was therefore based

on the photon-excitation of the Hg^{2+} -sensitive dye, followed by charge separation in a closed circuit.

7.1.1 Phosphate doped TiO_2

Attempts have been made to decrease the band-gap energy of TiO_2 to extend the photoactive wavelength region to visible light through surface modifications and/or the use of doping elements [35-37]. Phosphate anions are known to adsorb strongly on the surface of TiO_2 by the formation of a inner sphere surface complex, which can greatly influence the interfacial and surface chemistry of TiO_2 [38]. Phosphate modification of TiO_2 has been widely studied, with a range of results [39, 40]. Surface-bound phosphate affects the crystallization and aggregation of TiO_2 particles. According to Zhao *et al.* [41] the effect of phosphate modification is attributed to the surface-bound phosphate anion, rather than the change in the crystal structure or surface area of TiO_2 as a result of modification. The authors also suggested that phosphate modification inhibits the adsorption of other substrates and it can enhance the separation of photogenerated holes and electrons by a negative electrostatic field formed by the surface anion. Phosphonate groups have been used to bind photosensitisers to TiO_2 in solar conversion systems [42]. Five different adsorbed species can be observed on the TiO_2 surface: monodentate PO_4^{3-} , bidentate PO_4^{3-} , tridentate PO_4^{3-} , monodentate HPO_4^{2-} , monodentate H_2PO_4^- and bidentate HPO_4^{2-} . The adsorption of phosphate is accompanied by the loss of species from the surface of TiO_2 . The adsorption of phosphate is pH dependent, and increases with decreasing pH. At pH 5-6 the phosphate adsorbed species has a bidentate structure. The bidentate structure corresponds to a C_{2v} (most likely bidentate PO_4^{3-}) species at pH > 5-6, transforming to a protonated bidentate species with C_s symmetry (most likely monodentate H_2PO_4^-) at lower pH. The binding of phosphate species to TiO_2 under neutral aqueous conditions is bidentate [38].

The presence of anchoring groups such as carboxylate, sulphonate and phosphate groups broaden the absorption window for photons in the visible region and improve the electron injection efficiency of dyes into the CB of TiO_2 [22].

7.2 Materials and methods

7.2.1 Materials

ITO glass plates had a surface resistivity between 8 and $12\ \Omega\ \text{sq}^{-1}$, were purchased from Aldrich, South Africa. All chemicals and organic solvents used were of analytical reagent grade and were purchased from Sigma-Aldrich, South Africa. All aqueous solutions were prepared with ultrapure water obtained using a Milli-Q RO purification system.

7.2.2 Instrumentation

Surface imaging was performed with a Leo 1430VP scanning electron microscopy (SEM) and the surface thickness was determined with a Veeco Dektar 6M surface profiler. The spectrometric data of 0.03 mM RS- Hg^{2+} in 0.04 mM TiO_2 or 0.25 g L^{-1} was determined with a Cintra double beam UV-Vis spectrometer and a Perkin Elmer L550B in 1:1 aqueous dimethylformamide (DMF) solutions. A three-electrode set-up was used for the photoelectrochemical evaluation. It comprised a Pt counter electrode, an Ag/AgCl reference electrode and the coated working electrode. The electrolyte used was 0.05 M KNO_3 and various concentrations of HgCl_2 . An Elmo Omnigraphic 253 slide projector was used as a light source. The tungsten halogen lamp emitted $0.86\ \text{mW}\ \text{cm}^{-2}$ at the point of absorption by the electrode. The collimated beam was isolated in a steel casing to eliminate background light effects. The light was pulsed at 2 s intervals and the photovoltage signals were recorded by means of a DAX data acquisition system.

7.2.3 Coating of ITO electrodes

The synthesis of the PANI-RS dye composite followed the procedures as described by Chamier *et al.* [33]. The electrodes investigated were coated with TiO_2 and PANI. ITO glass plates were cut into approximately $8 \times 12\ \text{mm}$ segments and sonicated for 10 min in water, ethanol and acetone. Thereafter, all plates were dried at room temperature. The TiO_2 sol was made according to the procedure of Srikanth *et al.* [43] and then spin-coated onto the ITO surfaces, after which the plates were dried at $450\ ^\circ\text{C}$ for 30 min. A sample of 40 μL of a composite solution of 5 mg PANI and 5 mg RS in 5 mL DMSO was drop-coated onto the TiO_2 coated surface, and dried at room temperature. The TiO_2 colloidal nanoparticles used for the spectrophotometric

evaluation of RS- Hg^{2+} and used for coating of the electrodes was made in DMF [22] to eliminate the strong acidic environment seen with sol-gel [43].

The UV absorbance peak for the sensor- Hg^{2+} complex was observed at 536 nm (compared to 538 nm by Wu *et al.* [4]) and the emission peak was observed at 558 (compared to 560 nm by Wu *et al.* [4]).

7.3. Results and discussion

7.3.1 Electrode characterization

The SEM images of the ITO/ TiO_2 /PANI-RS electrode demonstrated that the electrode surface is relatively smooth. Figure 7.2 shows that the PANI composite penetrates into the pores of the TiO_2 and does not form a separate precipitate. The penetration of the composite into the TiO_2 increased the active surface area and prevented the dissolution of the composite into the water samples. The average layer thickness, measured with a surface image profiler, was ca. 2.56 μm .

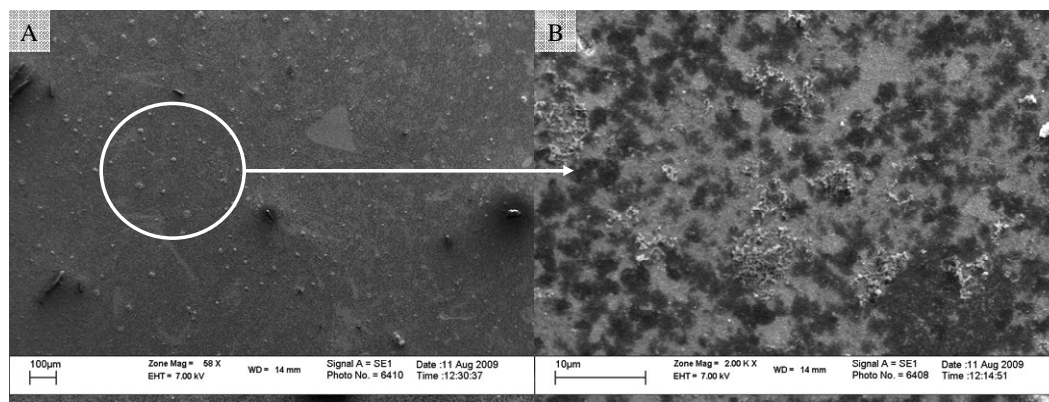


Figure 7.2: SEM images of the of ITO/ TiO_2 electrode surface coated with PANI-RS: A) magnification $\times 58$ and B) magnification $\times 2000$.

From the energy band-gap values for the various layers a proposed energy diagram is suggested, as shown in Figure 7.3. The RS- Hg^{2+} complex absorbed at 536 nm. Using the Planck equation, this value converted to a 2.35 eV energy band-gap. The energy band width for TiO_2 was taken as 3.055 eV with a flat band potential of -0.25 eV [44]. For PANI it was assumed that the emeraldine form would be the photoconductive part of the PANI layer as the leucoemeraldine and pernigraniline forms behave more like insulators [45]. The flat band potential for the emeraldine PANI was calculated by Huang *et al.* using the Mott Schottky plots to be 0.63 V (vs SHE) [45]. The energy

band-gap was determined to be 3.33 eV. The flat band potential for the PANI-RS composite was determined to be 0.63 V (vs SHE) [33].

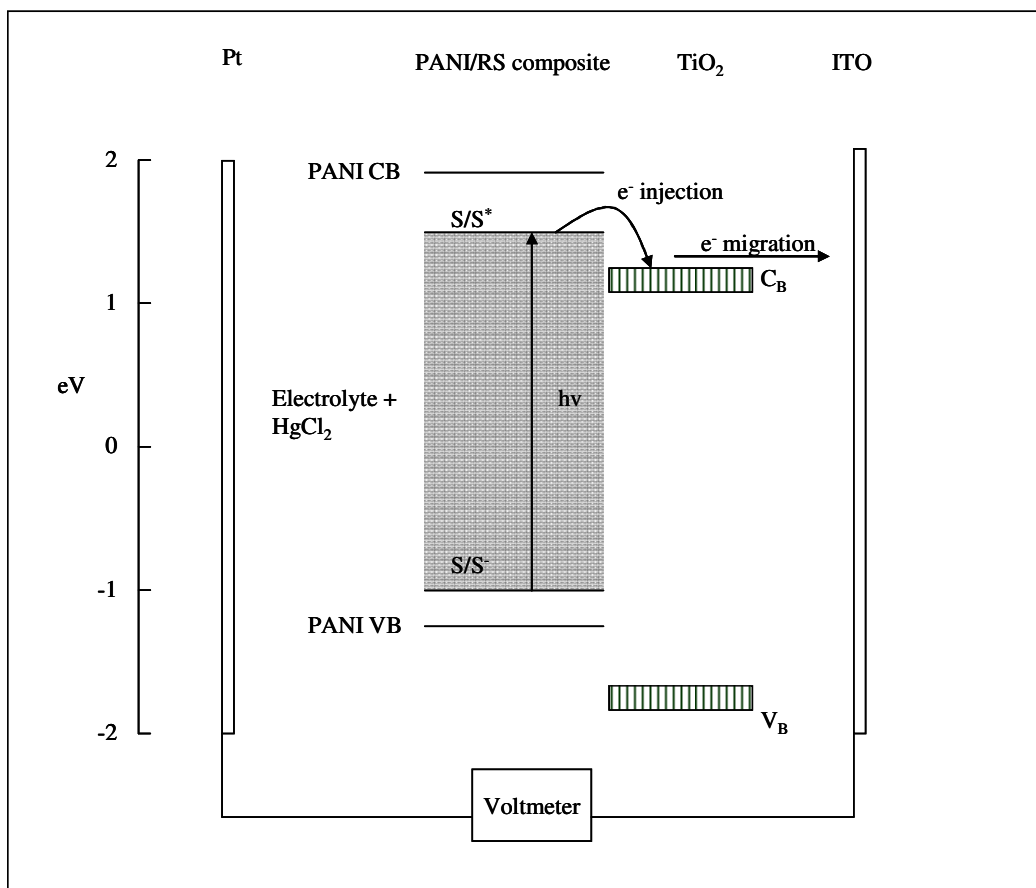


Figure 7.3: Proposed energy diagram for the photoelectrochemical detection of Hg^{2+} with an ITO/ TiO_2 /PANI-RS composite electrode.

The energy diagram in Figure 7.3 suggests that the excited electrons will be injected into the TiO_2 layer and will migrate to the back contact. The PANI assists in hole transport and behaved in a similar fashion as that of a solid phase electrolyte. The energy diagram suggests that the ITO/ TiO_2 /PANI-RS composite electrode will behave as a photo-anode.

7.3.2 Spectrophotometric responses of RS with PANI and TiO_2

The UV absorbance peak for the RS- Hg^{2+} complex was observed at 536 nm and the emission peak was observed at 558 after excitation at 500 nm (compared to 538 nm and 560 nm reported by Wu *et al.* [4]). The influence of PANI and TiO_2 on the UV

absorbance and fluorescence emission of the 0.03 mM RS- Hg^{2+} was investigated. Results are shown in Figure 7.4. The absorbance peak of RS- Hg^{2+} with PANI and TiO_2 in aqueous DMF (1:1) shifted to 533 nm due to a change in the solvent environment. The small shift in absorbance and the altered chemical environment change the excitation wavelength for maximum emission to 520 nm for TiO_2 and 530 nm for PANI. The uncomplexed RS dye was added to TiO_2 and PANI with no significant absorbance or emission. When either TiO_2 or PANI was added to RS- Hg^{2+} the absorbance of the activated complex increased slightly due to the wide band-gaps of both PANI and TiO_2 . The fluorescence emission of RS- Hg^{2+} was however significantly decreased when added to PANI and TiO_2 . A decrease in fluorescence emission may be attributed to electron transfer or energy transfer processes, as well as non-fluorescent complex formation. Use of fluorescent quenching techniques for the analysis of electron transfer in xanthene sensitised TiO_2 colloidal systems have been reported [20].

Kathiravan *et al.* [20] found that electron delocalization at carboxyl groups are coupled to the TiO_2 nanoparticles increasing the electron transfer efficiency. The polar nature of a colloidal TiO_2 surface facilitates the strong adsorption of charged dye molecules. The anchoring group plays a major role in the adsorption as well as electron transfer processes. As the fluorescence emission peak of RS- Hg^{2+} (558 nm) did not overlap with the absorbance of TiO_2 and the excited state energy of RS- Hg^{2+} (2.34 eV) was considerably lower than that of TiO_2 (3.2 eV [44]), quenching by energy transfer between TiO_2 and RS- Hg^{2+} could be excluded. The excited singlet state energy of RS- Hg^{2+} was determined from the normalised fluorescent excitation and emission spectra, with excitation at 500 nm.

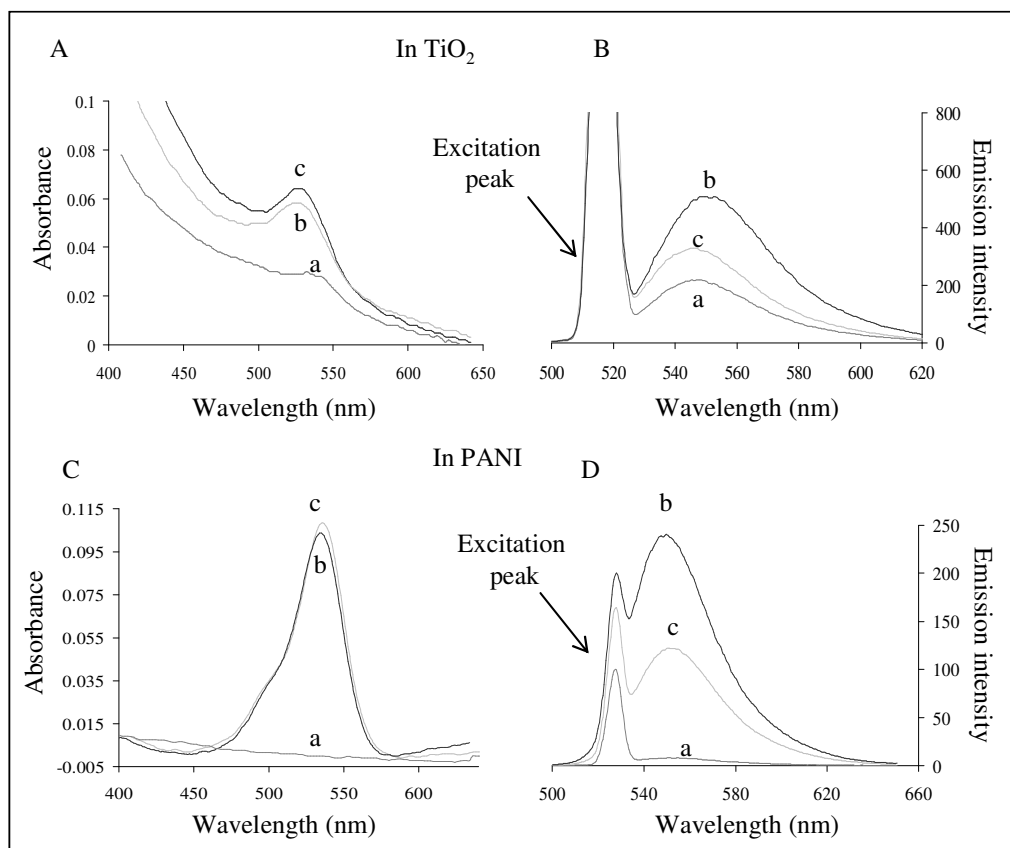


Figure 7.4: The absorbance A) and emission spectra (excitation 520 nm) B) of 0.04 mM TiO_2 with a) RS, b) RS- Hg^{2+} and c) of RS- Hg^{2+} alone in 1:1 aqueous DMF. The absorbance C) and emission spectra (excitation 530 nm) D) of 0.25 g L^{-1} PANI with a) RS, b) RS- Hg^{2+} and c) of RS- Hg^{2+} alone in 1:1 aqueous DMF. The emission spectra were measured for samples diluted 1:95.

In acidic environments ($\text{pH} < 2$) the TiO_2 surface was positively charged $\text{TiO}_2 (\text{Ti}^{\text{IV}}-\text{HO}_2^+)$ and the RS dye was protonated to form a zwitterion. The negative pole of the RS dye molecule chemically bonded with the TiO_2 surface causing ring opening of the spirolactam. The TiO_2 complexed RS dye had an increased absorbance and fluorescent emission compared to the RS- Hg^{2+} complex, but was no longer capable of Hg^{2+} determination. From the preliminary spectrophotometric evaluation it is suggested that the proposed photovoltaic response will be due to electron transfer between TiO_2 and RSHg^{2+} . Charge separation by PANI also facilitates the proposed electron transfer.

7.3.3 Photoresponse of ITO/ TiO_2 /PANI-RS composite coated electrodes

Figure 7.5 illustrates the photoresponse measured for short (± 2 s) light pulses, the sharp peaks, and rectangular responses for continuous illumination, measured for various concentrations of Hg^{2+} . The baseline for the voltage measurements remained relatively constant for increasing Hg^{2+} . The photoresponse for the ITO/ TiO_2 /PANI-RS electrode light pulses were similar, yet in the opposite direction of those observed for the ITO coated with the PANI-RS composite alone. Under constant illumination the excitation remained constant and the photoelectrochemical signal did not relax to the groundlevel or an intermediate energy level

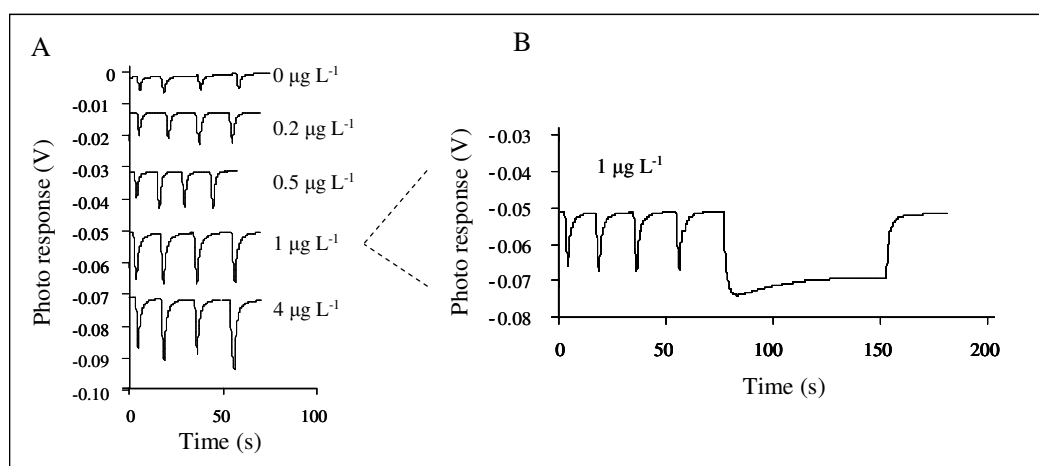


Figure 7.5: The photoresponse measured for an ITO/ TiO_2 /PANI-RS electrode for (a) short (± 2 s) light pulses for various Hg^{2+} concentrations and 0.05 M KNO_3 . (b) The photoresponse of an ITO/ TiO_2 /PANI-RS electrode for short pulses followed by continuous illumination in 1 $\mu\text{g L}^{-1}$ of added Hg^{2+} .

The photoresponse of ITO/ TiO_2 coated with a PANI-RS composite was evaluated in 0.05 M KNO_3 and HgCl_2 solutions, separately. As predicted from the energy diagram, the ITO/ TiO_2 electrode coated with PANI-RS behaves like a photo-anode. The photoresponse increased with an increasing amount of HgCl_2 in two ranges. The first range occurred between 0 and 4 $\mu\text{g L}^{-1}$, and the second range occurred between 5 $\mu\text{g L}^{-1}$ to 200 $\mu\text{g L}^{-1}$, after which the response decreased with an increasing concentration of Hg^{2+} . The limit at which the concentration of Hg^{2+} can be quantified with the ITO/ TiO_2 /PANI-RS electrode was 5 $\mu\text{g L}^{-1}$, as evidenced by the response, which was then only $3 \times$ (analyte photoresponse/background photoresponse). The detection limit

obtained compared well with the WHO guideline value for Hg^{2+} in drinking water of $6 \mu\text{g L}^{-1}$ [46].

As seen in Figure 7.6, the photoresponse increased with increasing Hg^{2+} concentration. Figure 7.6 shows two areas of linear response. The first and primary interaction is between Hg^{2+} and the most exposed dye active sites on the electrode surface. Therefore, the response increased sharply for Hg^{2+} concentrations below $4 \mu\text{g L}^{-1}$. With increasing Hg^{2+} concentration the outer layer of active sites became saturated and therefore diffusion into the TiO_2 /composite layer took place. The increase in photoresponse was smaller compared to the initial saturation below $4 \mu\text{g L}^{-1}$. It is likely that the response is determined by the access to active sites on the electrode surface.

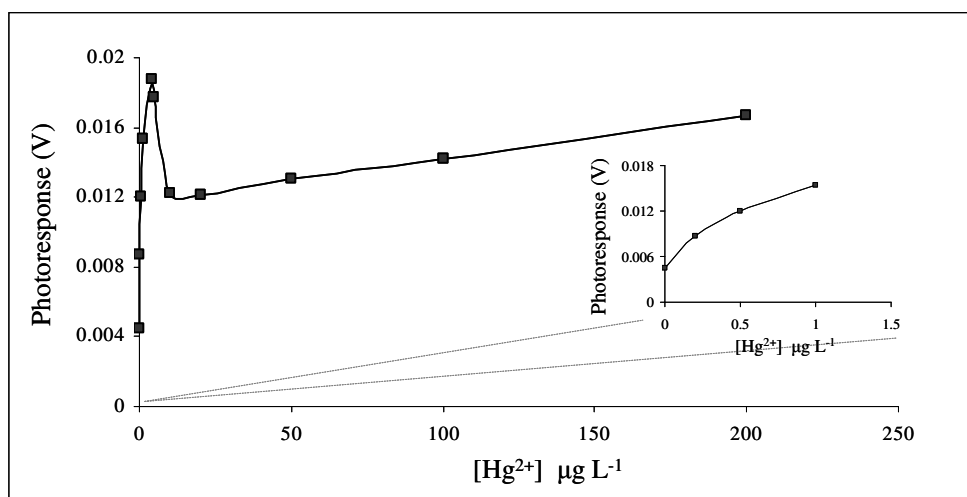


Figure 7.6: The photoresponse of an ITO/ TiO_2 /PANI-RS electrode measured at various Hg^{2+} concentrations in 0.05 M KNO_3 .

The sensitivity of the electrode can therefore be further increased by increasing the active surface area and/or increasing the number and size of the pores. The limit of detection obtained was $5 \mu\text{g L}^{-1}$ and the response increased linearly up to a maximum concentration of $200 \mu\text{g L}^{-1}$, whereafter the response became irregular. Under constant illumination the response peaks do not decay back to the baseline (ground state). The injected electrons successfully migrate to the back contact and are only minimally recombined with the hole in the electrolyte or trapped in the TiO_2 trapsites.

7.3.4 Selectivity of the ITO/ TiO_2 /PANI-RS electrode

The selectivity of the ITO/ TiO_2 /PANI-RS electrode in the presence of background anions was determined and results are shown in Figure 7.7. After submersion in aqueous solutions of Hg^{2+} , the electrode was evaluated in fresh 0.05 M KNO_3 to determine whether the electrode surfaces were fouled with bound Hg^{2+} .

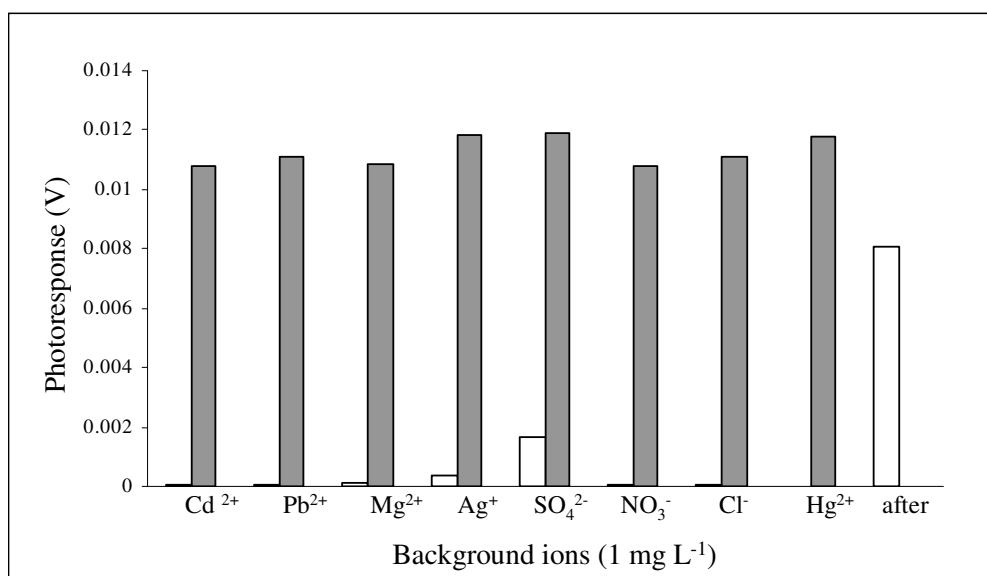


Figure 7.7: Photoresponse of the ITO/ TiO_2 /PANI-RS electrode in the presence of interfering ions in 0.05 M KNO_3 , with ■) and without □) $20 \mu\text{g L}^{-1}$ HgCl_2 .

Of the background ions evaluated only SO_4^{2-} and to a lesser extent Ag^+ had a significant influence on the photoresponse of the ITO/ TiO_2 /PANI-RS electrode. Therefore the excess presence of SO_4^{2-} and Ag^+ ions can cause false positive responses, thereby compromising the qualitative determination of Hg^{2+} . ITO/ TiO_2 /PANI-RS, had a higher selectivity than the ITO coated with PANI-RS alone.

The photoresponse of the ITO/ TiO_2 /PANI-RS was more pH dependent than the ITO coated with PANI-RS alone [33]. The photoresponse of the ITO/ TiO_2 /PANI-RS electrode towards Hg^{2+} was evaluated at various pH values between pH 4 and 9, in 0.01 M phosphate buffer in the presence and the absence of $10 \mu\text{g L}^{-1}$ Hg^{2+} . The photoresponse of the ITO/ TiO_2 /PANI-RS electrode at various pH values is shown in Figure 7.8. At $\text{pH} < 6$ the same pH dependence was observed for ITO/ TiO_2 /PANI-RS

as for ITO coated with the PANI-RS alone [33]. It can therefore be concluded that the speciation (protonated/deprotonated state) of the RS dye was strongly influenced by acidic conditions as PANI was at its most conductive at $\text{pH} < 4$. Between $\text{pH} 6$ and $\text{pH} 7$ the maximum response (subtracted from the free dye response) with minimum variation can be measured.

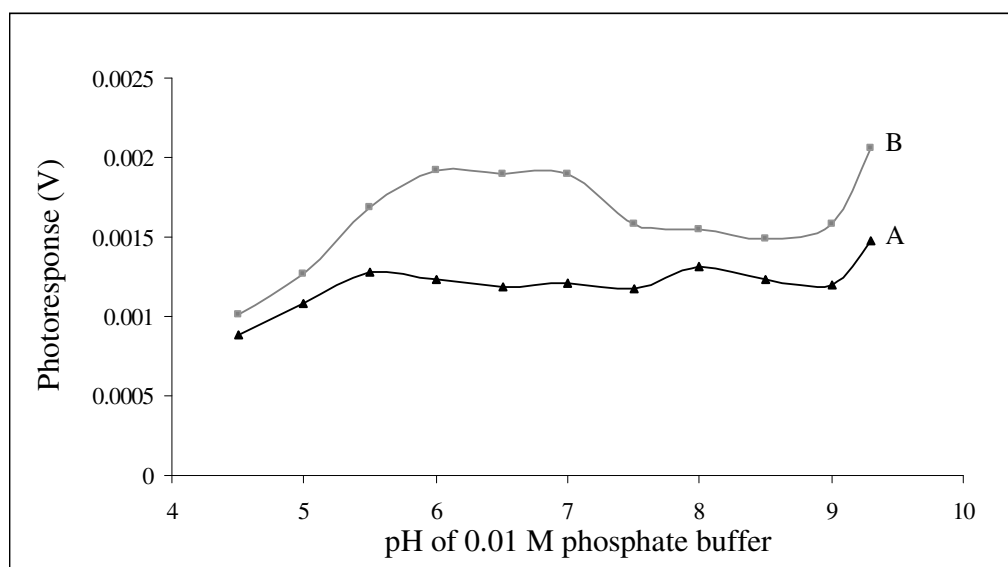


Figure 7.8: pH dependence of the ITO/ TiO_2 /PANI/RS electrode in A) 0.01 M phosphate buffer alone and B) 0.01M phosphate and $10 \mu\text{g L}^{-1} \text{Hg}^{2+}$.

The pH affects the properties of the TiO_2 surface and the speciation of the dye, and therefore the reaction mechanism and photon absorption [47]. The increased conductivity of PANI at lower pH ($\text{pH} < 4$) is well known [48]. The prepared PANI present in the composite occurs in its emeraldine salt (ES) state due to the presence of dopant acid. This form of PANI interacts efficiently with the RS dye in the absence of buffer solution. At higher pH values ($\text{pH} 7-14$) the ES form is deprotonated, transforming the polymer chains into their emeraldine base (EB) form. In the ES form the PANI/ TiO_2 composite will be more likely to degrade the dye, than assisting in electropositive hole transport. In aqueous solutions, radiation of the TiO_2 /PANI composite forms hydroxide radicals, which could degrade the RS dye molecules [49], especially in more acidic conditions (via a superoxide radical).

The photocatalytic behaviour of TiO_2 in terms of degradation or in sensor research [50] has been known to be optimal at pH 6-7 [51]. The TiO_2 particles tend to agglomerate under acidic conditions and the surface area available for dye adsorption and photon absorption is thereby reduced [52]. The PZC of the TiO_2 (Degussa P25) is at pH 6.8 [53]. Thus, the TiO_2 surface was positively charged in acidic medium (pH < 6.8), whereas it was negatively charged under alkaline conditions (pH > 6.8). At pH < 6, the strong adsorption of the RS dye on the TiO_2 particles was likely the result of the electrostatic attraction of the positively charged TiO_2 ($\text{Ti}^{\text{IV}}\text{-HO}_2^+$) with the anionic RS dye. At pH > 6.8 the density of TiO^- groups on the semiconductor surface is increased [54] and the RS dye molecules are negatively charged in alkaline media. Therefore, coulombic repulsion between the dye and TiO_2 surface occurs and the RS dye will be less absorbed, and then TiO_2 is far less likely to facilitate electron injection at pH > 7 [51, 55].

7.3.5 Hg^{2+} evaluation with RS and TiO_2 sol-gel in phosphate buffer

The phosphate group was investigated as a possible anchoring group for the RS dye onto the TiO_2 surface. The absorbance of RS was measured for increasing concentrations of phosphate buffer at pH 6.5. It was observed that the absorbance increased for decreasing phosphate concentration. The absorbance of phosphate was coupled to the loss of a hydroxyl group on the TiO_2 surface. Therefore, the increased phosphate concentration leads to a decrease in the available surface area for the dye- TiO_2 interaction.

The effect of phosphate was first observed during pH evaluation in phosphate buffer. In aqueous/DMF solutions of TiO_2 and RS no absorbance or fluorescence was observed. The spiro lactam ring remained intact, and no electron or energy transfer occurred between the TiO_2 colloidal particles and RS. In 0.005 M phosphate buffer/DMF 1:1 the RS xanthene is released and a distinct absorbance band is observed at 530 nm, with the emission band at 558 nm. The absorbance increased and fluorescence increased with increasing RS concentration. No absorbance was however observed with RS in phosphate alone. The absorbance of RS in TiO_2 /phosphate increased with decreasing phosphate concentration up to 0.001 M. However, as seen in Figure 7.9, the absorbance decreased non-linearly with the addition of Hg^{2+} for all concentrations of phosphate.

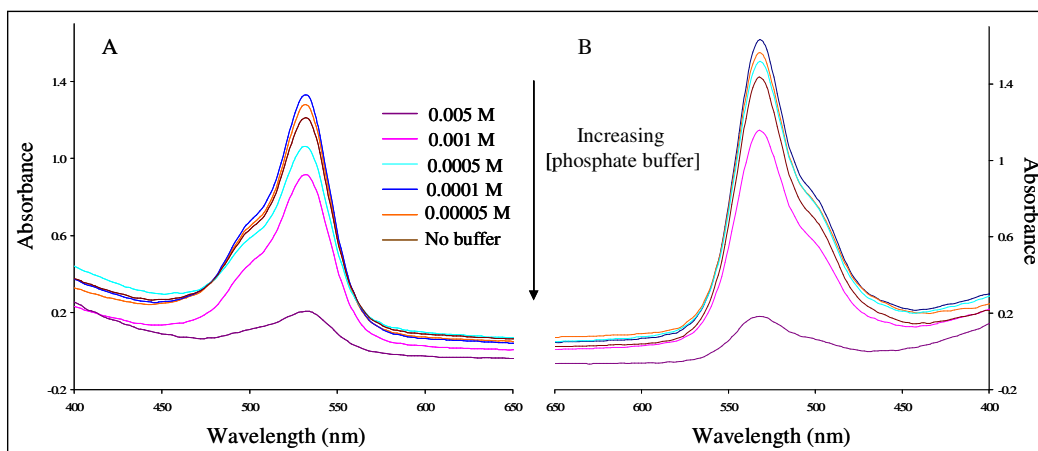


Figure 7.9: UV-vis spectra of A) RS in TiO_2 /phosphate in various concentration of phosphate buffer at pH 6.5, and B) RS in TiO_2 /phosphate with the addition of excess Hg^{2+} .

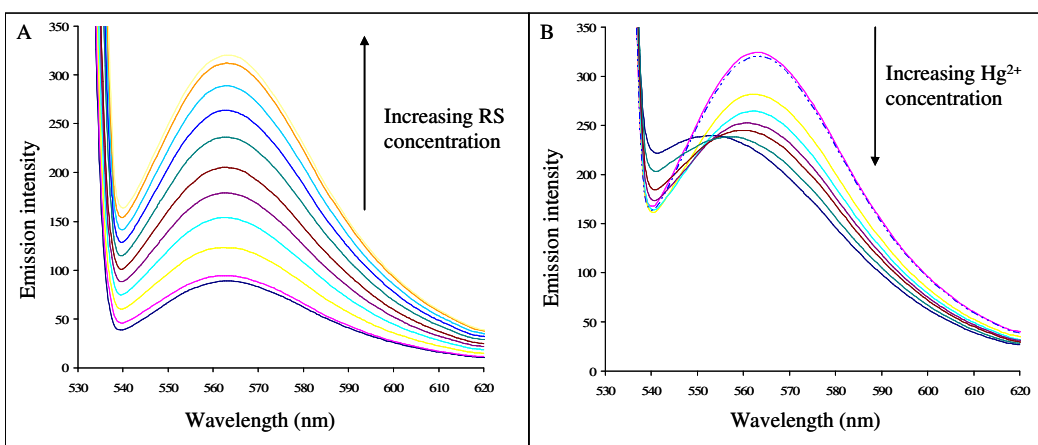


Figure 7.10: The fluorescent emission spectra for A) TiO_2 in phosphate buffer with increasing RS and B) TiO_2 and RS in phosphate buffer at pH 6.5 with increasing Hg^{2+} .

The spiolactam ring of RS was opened when added to TiO_2 either at low pH (< 4) or in phosphate buffer. Hg^{2+} was added to phosphate buffer containing TiO_2 and ring-opened RS. The absorbance peak did not decrease, but was “split” into two peaks. Figure 7.11 shows the absorption spectra of Hg^{2+} added to TiO_2 and RS in phosphate buffer.

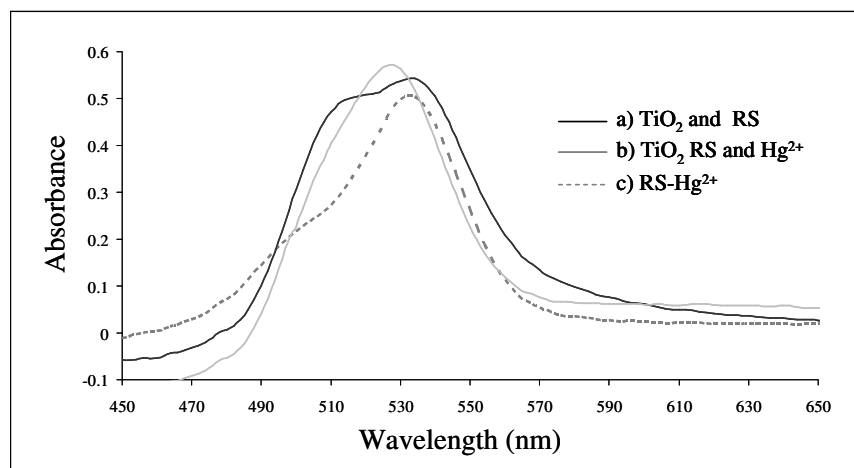


Figure 7.11: UV absorbance of a) TiO_2 and RS, b) TiO_2 , RS and Hg^{2+} , and c) RS- Hg^{2+} in 0.005 M phosphate buffer.

The absorbance peak of RS- Hg^{2+} was at 528 nm, which red shifted to 534 nm when RS was ringopened by TiO_2 . When Hg^{2+} was added to the TiO_2 and RS an additional absorbance peak appeared at 516 nm. The “peak splitting” and decrease in fluorescence that occurred when Hg^{2+} was added to TiO_2 -RS in 0.005 M phosphate buffer can be explained by dimerization of the RS ligand on the TiO_2 surface upon the addition of Hg^{2+} [56].

Results of the pH evaluations showed that the dimerization of the RS molecules by Hg^{2+} was favoured at lower pH. In Figure 7.12 it could be seen that the chromophore was completely quenched at higher pH values. These results indicated that the HPO_4^{2-} and H_2PO_4^- species were more actively involved phosphate species in the adsorption of the RS molecules onto the TiO_2 surface.

The dimerization of the RS sensor leading to the double absorption peak and quenched fluorescence was Hg^{2+} selective, except for high concentrations (millimolar) of Cu^{2+} . The second absorbance peak at 516 nm was not observed for TiO_2 -RS in phosphate buffer with Na^+ , Cd^{2+} , Mg^{2+} , Fe^{3+} , Fe^{2+} , Ag^+ , K^+ , Pb^{2+} , Cl^- , SO_4^{2-} , NO_3^- or Br^- . The Hg^{2+} and Cu^{2+} selectivity of the carbohydrazone binding unit of the RS chemosensor was first reported by Wu *et al.* [4], but the increase in absorbance and dimerization was significantly higher for Cu^{2+} than Hg^{2+} . Adding RS to phosphate-

rich TiO_2 offers another spectrophotometric method of Hg^{2+} determination in the presence of other background ions.

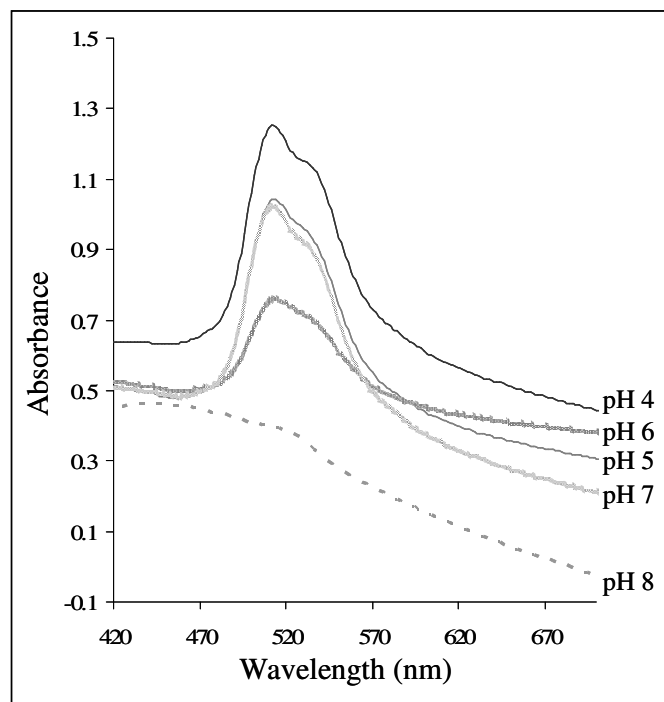


Figure 7.12: UV absorbance spectra of TiO_2 in phosphate buffer with 0.0015 M RS- Hg^{2+} measured at pH 4 to pH 8.

7.3.6 Photoelectrochemical evaluation of ITO/ TiO_2 coated with P[A-co-2-BrA]s

ITO/ TiO_2 electrodes were coated with composites of P[A-co-2-BrA] and RS and photoelectrochemically evaluated with Hg^{2+} . The photo-cathodic responses of these coated ITO/ TiO_2 electrodes are illustrated in Figure 7.13. The hole conductivity of the P[A-co-2-BrA]s was considerable lower compared to PANI. The observed photoactivity was due to the reduction of the Hg^{2+} containing electrolyte rather than the electron injection into TiO_2 . For the lower 2-bromoaniline content copolymers (10 and 25%), the photoactivity increased with increasing Hg^{2+} content up to $20 \mu\text{g L}^{-1}$. Copolymers with higher 2-bromoaniline content (50 and 70%) and poly-2-bromoaniline were relatively unaffected by the presence of Hg^{2+} .

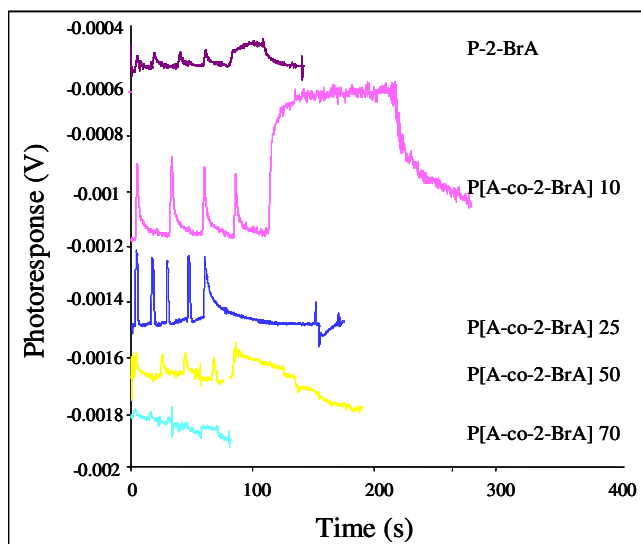


Figure 7.13: Photoresponses of the ITO/ TiO_2 coated with P[A-co-2-BrA]s and RS measured in $0.2 \mu\text{g L}^{-1} \text{Hg}^{2+}$ and 0.05 M KNO_3 .

ITO/ TiO_2 coated with the higher 2-bromoaniline content copolymers, had smoother coatings, which effectively sealed the TiO_2 surface, further inhibiting the charge separation. The photoresponses of the ITO/ TiO_2 /P[A-co-2-BrA]s-RS in $10 \mu\text{g L}^{-1} \text{Hg}^{2+}$ were compared to that of PANI-RS. Results are shown in Figure 7.14.

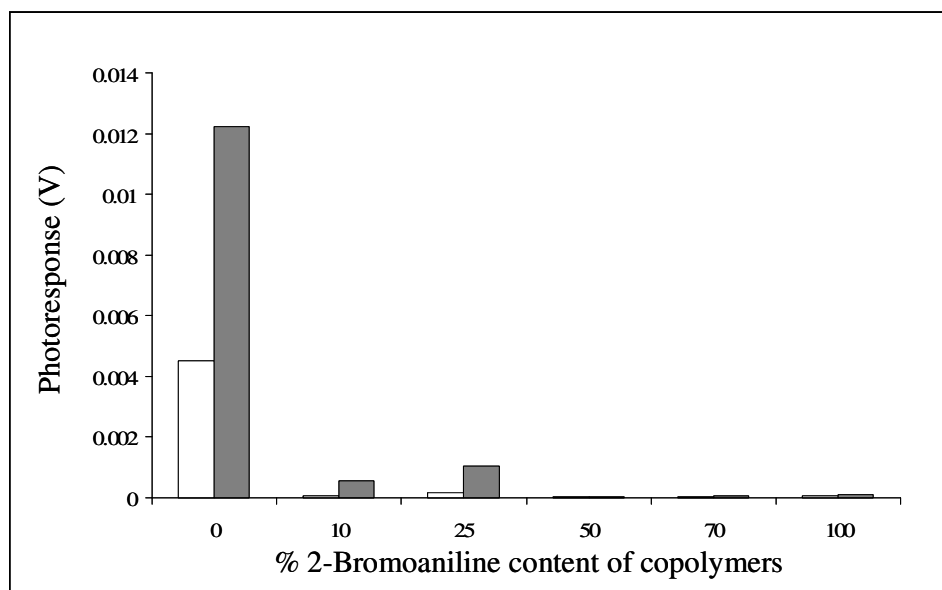


Figure 7.14: Photoresponses of ITO/ TiO_2 coated with P[A-co-2-BrA]s and RS in $10 \mu\text{g L}^{-1} \text{Hg}^{2+}$ and 0.05 M KNO_3 . Zero content 2-bromoaniline represents the photoresponse of PANI.

The photoresponse of the PANI-RS composite was more than 100-fold higher than that of P[A-co-2-BrA] 10, while P[A-co-2-BrA] 10 had a considerably lower background response, and therefore a greater increase (10-fold compared to 2.5-fold for PANI-RS) towards Hg^{2+} in solution. However, PANI remained the polymer of choice for coating ITO/ TiO_2 photoelectrodes for the detection of Hg^{2+} ; the significant response provided longer ranges of linearity in photoresponses with Hg^{2+} concentration with lower uncertainties.

7.4. Conclusions

The spectrophotometric change of the Hg^{2+} bound RS chemosensor was converted to a photovoltaic response through charge separation. TiO_2 , as an electron acceptor, and semiconductive PANI as the electron donor, facilitated the charge separation, and the coated ITO electrode therefore functioned as a photo-anode. The size of the photoresponse of the coated ITO electrode was determined by the amount of spiro-lactam-opened RS sensor on the surface of the electrode. The photoresponse of the ITO/ TiO_2 /PANI/RS electrode toward Hg^{2+} increased linearly between 10 and 200 $\mu\text{g L}^{-1}$ with a LOD of 5 $\mu\text{g L}^{-1}$. The Hg^{2+} adsorption is irreversible and detection can be done in aqueous solutions of buffer solutions with a pH between 6 and 7. The detection of Hg^{2+} with ITO/ TiO_2 coated with P[A-co-2BrA]10 and 25 resulted in a photo-cathodic response and was due to the reduction of the electrolyte under illumination. Although the photoresponses of the mentioned copolymers increased with increasing Hg^{2+} , the responses remained significantly smaller compared to ITO/ TiO_2 coated with PANI and RS.

The photoresponse of the ITO coated with a Hg^{2+} selective chemosensor and charge separators offers an analytical method for the determination of Hg^{2+} in aqueous solutions. In a closed PEC, the ITO coated electrodes offer the possibility for on-site Hg^{2+} screening, capable of providing important Hg measurement necessary for environmental health impact studies and surveys, for example.

7.5 References

- [1] W. Huang, C. Song, C. He, G. Lv, X. Hu, X. Zhu, C. Duan, *Inorg. Chem.*, 48 (2009) 5061-5072.
- [2] H.N. Kim, M.H. Lee, H.J. Kim, J.S. Kim, J. Yoon, *Chem. Soc. Rev.*, 37 (2008) 1465-1472.
- [3] J.S. Wu, I.C. Hwang, K.S. Kim, J.S. Kim, *Org. Lett.*, 9 (2007) 907-910.
- [4] D.W. Wu, W. Huang, C. Duan, Z. Lin, Q. Meng, *Inorg. Chem.*, 46 (2007) 1538-1540.
- [5] J. Chen, A. Zheng, A. Chen, Y. Gao, C. He, X. Kai, G. Wu, Y. Chen, *Anal. Chim. Acta*, 599 (2007) 134-142.
- [6] X. Chen, S.W. Nam, M.J. Jou, Y. Kim, S.J. Kim, S. Park, J. Yoon, *Org. Lett.*, 10 (2008) 5235-5238.
- [7] D.F. Watson, G.J. Meyer, *Annu. Rev. Phys. Chem.*, 56 (2005) 119-156.
- [8] J. Huang, D. Stockwell, A. Boulesbaa, J. Guo, T. Lian, *J. Phys. Chem. C*, 112 (2008) 5203-5212.
- [9] M. Asha Jhonsi, A. Kathiravan, R. Renganathan, *J. Mol. Struct.*, 921 (2009) 279-284.
- [10] G.G. Yordanov, G.D. Gicheva, C.D. Dushkin, *Mater. Chem. Phys.*, 113 (2009) 507-510.
- [11] W.J. Lee, H. Okada, A. Wakahara, A. Yoshida, *Ceram. Int.*, 32 (2006) 495-498.
- [12] J. Moser, M. Grätzel, *J. Am. Chem. Soc.*, 106 (1984) 6557-6564.
- [13] F. del Monte, J.D. Mackenzie, D. Levy, *Langmuir*, 16 (2000) 7377-7382.
- [14] T. Doussineau, S. Trupp, G.J. Mohr, *J. Colloid Interface Sci.*, 339 (2009) 266-270.

- [15] J. Bujdák, N. Iyi, *J. Phys. Chem. B*, 109 (2005) 4608-4615.
- [16] M. Gratzel, *Inorg. Chem.*, 44 (2005) 6841-6851.
- [17] F. Cao, G. Oskam, G.J. Meyer, P.C. Searson, *J. Phys. Chem.*, 100 (1996) 17021-17027.
- [18] J.S. Agnaldo, J.C. Cressoni, G.M. Viswanathan, *Phys. Rev. B*, 79 (2009) 35308.
- [19] A. Kathiravan, R. Renganathan, *Spectrochim. Acta, Part A*, 71 (2008) 1106-1109.
- [20] A. Kathiravan, V. Anbazhagan, M.A. Jhonsi, R. Renganathan, *Z. Phys. Chem.*, 221 (2007) 941-948.
- [21] A. Kathiravan, R. Renganathan, *Spectrochim. Acta, Part A*, 71 (2008) 1080-1083.
- [22] A. Kathiravan, R. Renganathan, *J. Colloid Interface Sci.*, 331 (2009) 401-407.
- [23] R.I. Bickley, T. Gonzalez-Carreno, J.S. Lees, L. Palmisano, R.J.D. Tilley, *J. Solid State Chem.*, 92 (1991) 178-190.
- [24] P.A. Connor, K.D. Dobson, A.J. McQuillan, *Langmuir*, 15 (1999) 2402-2408.
- [25] G. Ramakrishna, H.N. Ghosh, A.K. Singh, D.K. Palit, J.P. Mittal, *J. Phys. Chem. B*, 105 (2001) 12786-12796.
- [26] T. Fujita, N. Iyi, T. Kosugi, A. Ando, T. Deguchi, T. Sota, *Clays Clay Miner.*, 45 (1997) 77-84.
- [27] J.R. Sánchez-Valencia, A. Borrás, A. Barranco, V.J. Rico, J.P. Espinós, A.R. González-Elipe, *Langmuir*, 24 (2008) 9460-9469.
- [28] S. Hamad, J.R. Sánchez-Valencia, A. Barranco, J.A. Mejias, A.R. González-Elipe, *Mol. Sim.*, 35 (2009) 1140-1151.
- [29] P.A. Lieberzeit, F.L. Dickert, *Anal. Bioanal. Chem.*, 387 (2007) 237-247.

- [30] M. Grätzel, J. Photochem. Photobiol. C, 4 (2003) 145-153.
- [31] M. Grätzel, Nature, 414 (2001) 338-344.
- [32] H. Zhang, Y. Zhou, M. Zhang, T. Shen, Y. Li, D. Zhu, J. Colloid Interface Sci., 264 (2003) 290-295.
- [33] J. Chamier, J.J. Leaner, A.M. Crouch, Anal. Chim. Acta, 661 (2010) 91-96.
- [34] M.S. Wrighton, J. Chem. Educ., 60 (1983) 877-881.
- [35] S.Y. Ly, S.K. Kim, T.H. Kim, Y.S. Jung, S.M. Lee, J. Appl. Electrochem., 35 (2005) 567-571.
- [36] H. Luo, T. Takata, Y. Lee, J. Zhao, K. Domen, Y. Yan, Chem. Mater., 16 (2004) 846-849.
- [37] Y. Lv, L. Yu, H. Huang, H. Liu, Y. Feng, J. Alloys Compd., 488 (2009) 314-319.
- [38] P.A. Connor, A.J. McQuillan, Langmuir, 15 (1999) 2916-2921.
- [39] L. Korosi, S. Papp, I. Bertoti, I. Dekany, Chem. Mater, 19 (2007) 4811-4819.
- [40] H.P. Wu, T.L. Cheng, W.L. Tseng, Langmuir, 23 (2007) 7880-7885.
- [41] D. Zhao, C. Chen, Y. Wang, H. Ji, W. Ma, L. Zang, J. Zhao, J. Phys. Chem. C, 112 (2008) 5993-6001.
- [42] P. Péchy, F.P. Rotzinger, M.K. Nazeeruddin, O. Kohle, S.M. Zakeeruddin, R. Humphry-Baker, M. Grätzel, J. Chem. Soc., Chem. Commun. (1995) 65-66.
- [43] K. Srikanth, M.M. Rahman, H. Tanaka, K.M. Krishna, T. Soga, M.K. Mishra, T. Jimbo, M. Umeno, Sol. Energy Mater. Sol. Cells, 65 (2001) 171-177.
- [44] T. Bak, T. Burg, S.J.L. Kang, J. Nowotny, M. Rekas, L. Sheppard, C.C. Sorrell, E.R. Vance, Y. Yoshida, M. Yamawaki, J. Phys. Chem. Solids, 64 (2003) 1089-1095.

- [45] H.G. Huang, Z.X. Zheng, J. Luo, H.P. Zhang, L.L. Wu, Z.H. Lin, Synth. Met., 123 (2001) 321-325.
- [46] World Health Organization, available at http://www.who.int/water_sanitation_health/dwq/chemicals/mercuryfinal.pdf, Accessed 01-10-2009.
- [47] B. Neppolian, H.C. Choi, S. Sakthivel, B. Arabindoo, V. Murugesan, Chemosphere, 46 (2002) 1173-1181.
- [48] M.M. Ayad, N.A. Salahuddin, M.O. Alghaysh, R.M. Issa, Curr. Appl. Phys., 10 (2009) 235-240.
- [49] M.A. Salem, A.F. Al-Ghonemiy, A.B. Zaki, Appl. Catal., B, 91 (2009) 59-66.
- [50] A.K. Gupta, A. Pal, C. Sahoo, Dyes Pigm., 69 (2006) 224-232.
- [51] I.K. Konstantinou, T.A. Albanis, Appl. Catal., B, 49 (2004) 1-14.
- [52] M.A. Fox, M.T. Dulay, Chem. Rev., 93 (1993) 341-357.
- [53] I. Poullos, I. Tsachpinis, J. Chem. Technol. Biotechnol., 74 (1999) 349-357.
- [54] W.Y. Wang, Y. Ku, Colloids Surf. Physicochem. Eng. Aspects, 302 (2007) 261-268.
- [55] M. Stylidi, D.I. Kondarides, X.E. Verykios, Appl. Catal., B, 47 (2004) 189-201.
- [56] S.A. Tomás, R. Palomino, R. Lozada, E.F. da Silva, E.A. de Vasconcelos, W.M. de Azevedo, C. Persson, I. Pepe, D.G.F. David, A. Ferreira da Silva, Microelectron. J., 36 (2005) 570-573.

Chapter 8

Photoelectrochemical evaluation of an ITO/polyaniline-rhodamine 6G thiolactone composite electrode

8.1 Introduction

The structure and fluorescent properties are integral to the design of the photoelectrochemical cell (PEC). The previously described rhodamine 6G hydrazone derivative dye (RS) had the xanthene moiety from rhodamine 6G (R6G) and a carbohydrazone binding unit for Hg^{2+} selectivity. An investigation into the influence of ionophore modification on the electrochemical detection of Hg^{2+} is described in this chapter. As described in Chapter 3, the rhodamine 6G thiolactone derivative dye (RT) was synthesised from R6G and thiourea to give a fluoroionophore with a thiolactone moiety, which ring-opens upon binding with Hg^{2+} [1]. The design of RT takes advantage of both the high thiophilicity of Hg^{2+} and strong nucleophilicity of sulphur. This thiophilicity of Hg^{2+} has led to the design of various chemosensors that rely on desulphurization reactions of a variety of compounds, such as thioureas, thioethers or thioesters, to detect Hg^{2+} [2, 3]. Detection of Hg^{2+} by desulphurization has reduced false positive interactions but most desulphurization processes are irreversible and permanently change the structure of the chemosensor.

A rhodamine B derivative with the thiolactone unit similar to that of RT was synthesised by Shi and Ma [3]. According to Zhan *et al.* [4] the thiolactone has several advantages over other spirolactam centres, for example:

- Thiol groups have higher pH tolerances (pH 3 to 11)
- The presence of a thiol group enhances cyclization while remaining the centre for thiophilic attack by Hg^{2+}
- The thiolactone functionalised rhodamine compounds are easy to synthesise (one-pot synthesis from rhodamine B).

It is also reported that the binding event of Hg^{2+} with the thiolactone is reversible, and Hg^{2+} can be removed with KI [1, 3, 4].

In Chapter 7 the fluorescent quenching due to electron transfer of the RS chromophore in the presence of both TiO_2 , and polyaniline (PANI) was reported.

According to other authors [5, 6], the electron transfer to TiO_2 is only likely to occur when the sensitiser is linked to the TiO_2 surface. Amine and (especially) carbonyl linking of sensitisers to semiconductors are well documented [7-9]. Although thiols are more nucleophilic than hydroxyl and amine groups [4], linking by thiol or sulphur groups is more challenging, and has been limited to conductors such as Au particles [10]. The affinity of the TiO_2 surface hydroxyl groups for thiol functional groups is very unlikely and a reduced TiO_2 quenching is therefore expected for ligated RT as opposed to ligated RS. The adsorption of the RT dye onto the PANI or TiO_2 surface is assumed to undergo more physisorption than chemisorption.

Interaction of PANI with thiolactone groups has not been reported previously, but the deposition of PANI and thiol monolayers onto gold electrode surfaces has been extensively studied [11, 12].

As RS and RT have the same xanthene chromophore, the crucial differences will be observed in the Hg^{2+} -selective ionophore. Modification of the ionophore will influence:

- The adsorption of the chemosensor on PANI, polyaniline-co-2-bromoaniline copolymers (P[A-co-2BrA]s) and TiO_2 surfaces due to differences in polarity, and interactions between the chemosensor and the various surface coatings
- The binding event of the immobilised chemosensor with Hg^{2+} .

Figure 8.1 shows the three-dimensional images of the unbound and Hg^{2+} -ligated RT and RS structures. The ligated RT structure will have a more perpendicular binding event compared to RS, which may inhibit the binding event with Hg^{2+} in the immobilised state. Both RS and RT have a 2:1 binding event with Hg^{2+} , whereas RS has a delocalised bonding with the carbohydrazone. Hg^{2+} is bonded to two adjacent RT thiolactone sulphur atoms. When immobilised on the electrode surface, ring-opening of RS and RT is more likely to be a 1:1 binding event with Hg^{2+} .

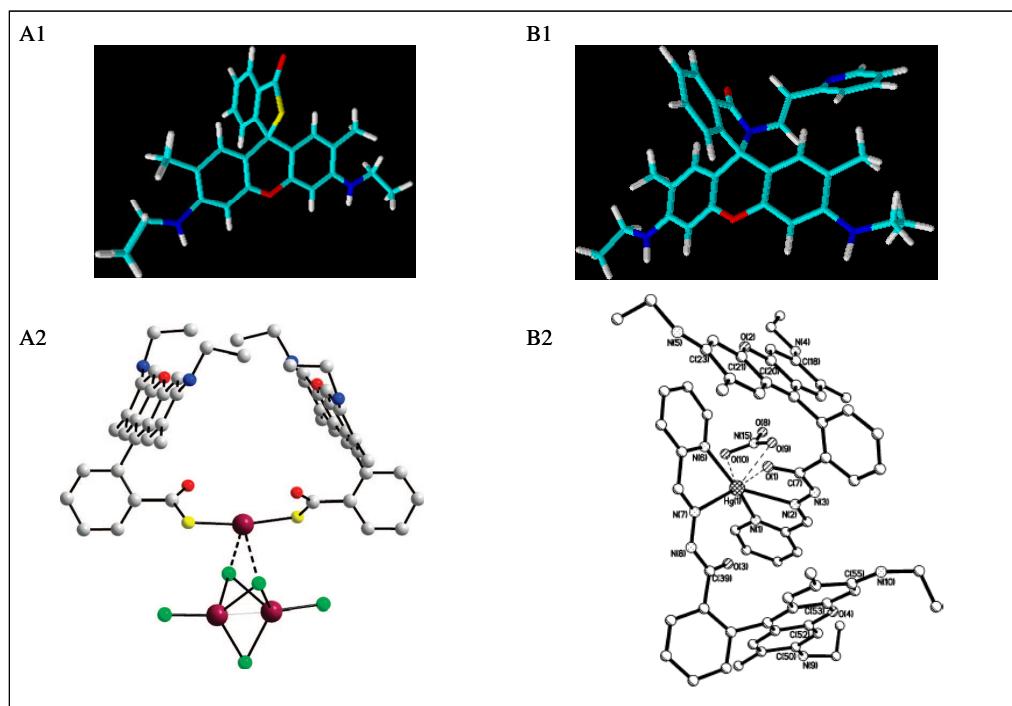


Figure 8.1: 3D images of A) RT and B) RS chemosensors in their 1) unbound and 2) ligated form with Hg^{2+} . A2 and B2 taken from references [1] and [13] respectively.

8.2 Material and methods

8.2.1 Materials

Indium tin oxide (ITO) glass plates, with a surface resistivity of between 8 and 12 $\Omega \text{ sq}^{-1}$, were purchased from Aldrich, South Africa. All chemicals and organic solvents used were of analytical reagent grade and obtained from Sigma-Aldrich, South Africa. All aqueous solutions were prepared with ultrapure water obtained using a Milli-Q RO purification system.

8.2.2 Instrumentation

Surface imaging of the coated electrodes was performed with a Leo 1430VP scanning electron microscope and surface thickness was determined with a Veeco DEKTAK 6M surface profiler. The spectrometric data of RT and RT- Hg^{2+} were determined with a Cintra double beam UV-Vis spectrometer and a Perkin Elmer L550B fluorimeter in 1:1 aqueous DMF solutions.

Electrochemical evaluations to determine the redox values of RT and RT-Hg were carried out in 0.005 M tetradecyltrimethylammonium bromide (TTAB) dissolved in

DMF to increase the potential window. A three-electrode cell was used with either an ITO plate or glassy carbon electrode as the working electrode, Pt wire as the counter electrode, and Ag/AgCl as the reference electrode. The measurements were conducted at room temperature at a scan rate of 50 mV s^{-1} .

8.2.3 Coating of the ITO electrodes

PANI and P[A-co-2-BrA]s were synthesised according to the procedure described in Section 5.2.2. The ITO electrodes were coated with $50 \mu\text{L}$ of 1 g L^{-1} PANI and $50 \mu\text{L}$ of 1 g L^{-1} RT and dried at $40 \text{ }^\circ\text{C}$. The copolymers were dissolved in DMF 5 g L^{-1} and drop-coated together with $50 \mu\text{L}$ of RT onto the ITO surface, and dried at room temperature.

8.3 Results and discussion

8.3.1 Characterization of PANI-RT composite electrode

The coated PANI-RT electrode surfaces are blue, with a very light pink tone. As seen in Figure 8.2, the PANI-RT composite dried to a relatively smooth surface. The particulates seen on the surface are clusters of excess RT. After the PANI-RT electrode had been used for Hg^{2+} evaluation, the particulates crystallised. The sizes of the crystals were in the region of $8 \mu\text{m}$ to $10 \mu\text{m}$, and were scattered across a relatively even surface. Although the crystals cannot contribute to the photoresponse of the PANI-RT electrode, the crystallization of the particulates after contact with Hg^{2+} in aqueous solutions indicated that the immobilised RT chemosensor complexed with Hg^{2+} and that the formed complex was insoluble in water.

Surface profiles were used to determine the average film thickness of the PANI-RT composite on the ITO electrode as well as obtain an idea of the surface roughness. Figure 8.3 shows the surface profiles for a PANI-RT composite electrode as well as a used electrode. The average film thickness of the PANI-RT composite electrode was $1.496 \mu\text{m}$, and $1.856 \mu\text{m}$ after being used for Hg^{2+} evaluation. The surfaces of both electrodes seemed relatively uniform, with peaks representing random particulates or crystals on the film surface.

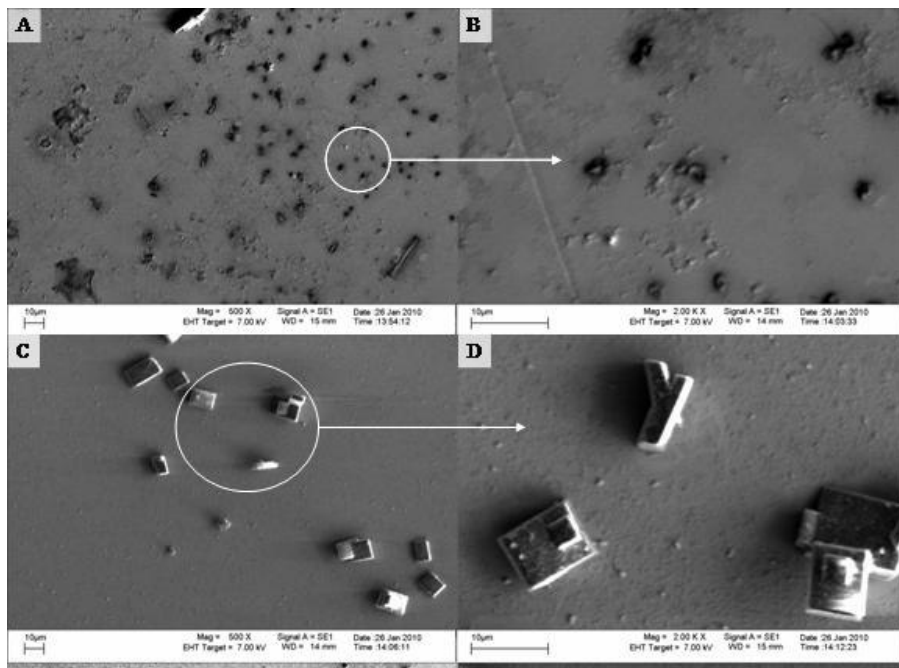


Figure 8.2: SEM images of the PANI-RT electrode: A) magnification $\times 500$ and B) magnification $\times 2000$. SEM images of PANI-RT electrode after Hg^{2+} evaluation: C) magnification $\times 500$ and D) magnification $\times 2000$.

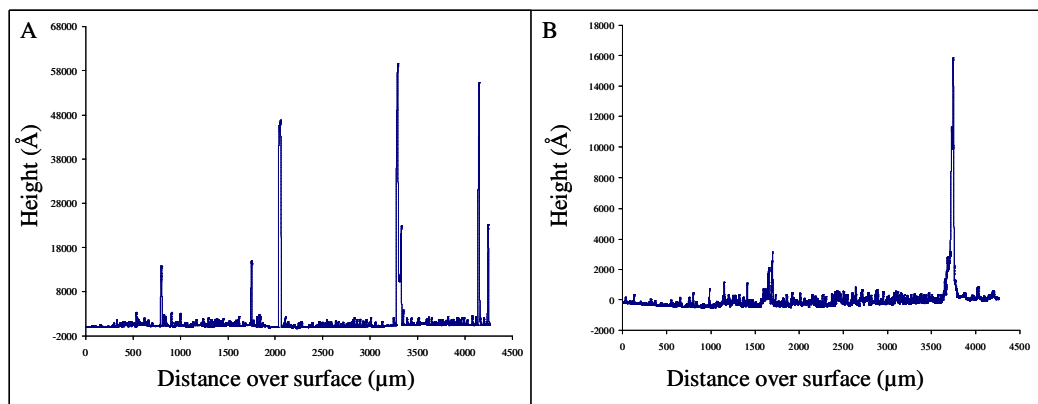


Figure 8.3: Surface profiles of A) PANI-RT composite coated onto ITO and B) a used ITO/PANI-RT electrode.

The redox potential of the RT dye was determined in 0.005 M TTAB/DMF. A colour change was observed at both the ITO and carbon electrode at the oxidation and reduction peaks. Figure 8.4 shows cross-over of the voltammograms before both the reduction and oxidation peaks on the ITO electrode. This was mainly attributed to the

chemical change of the RT molecule due to the applied potential, which is confirmed by the colour change observed at the electrodes in solution.

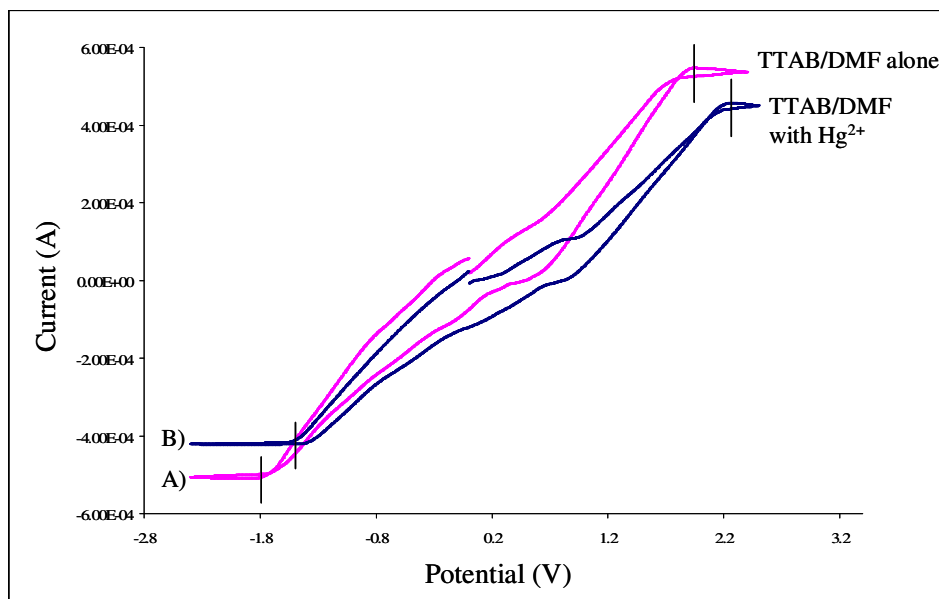


Figure 8.4: Cyclic voltammograms of ITO electrode in 0.005 M TTAB/DMF with A) 1 mM RT and B) RT-Hg²⁺.

The reduction peak for RT in DMF alone was -1.80 V (*vs.* SHE) and the oxidation peak was 1.92 V. Upon the addition of Hg²⁺, the reduction and oxidation peaks shifted to -1.59 V and 2.13 V, respectively. The peak separation between the uncomplexed RT and RT-Hg²⁺ complex remained the same (1.86 V) and, with an increasing number of voltammetric cycles the redox values of RT moved towards those of RT-Hg. The shift in redox potential with an increasing number of cycles indicates that the spirolactam ring opening occurred at the particular applied potential. The large peak separation between the oxidation and reduction peak as well as the anodic shift in the half peak potential ($E_{1/2}$) indicated low reversibility, which was most likely due to slow electron transfer kinetics as well as the chemical rearrangement of the molecule.

The energy band-gap is therefore the same for RT in the complexed and uncomplexed forms, but the complexed RT valence band (VB) and conductive band (CB) shifted to higher energies. The oxidation peak potential of RT was higher than that of RS (0.86 V), and the RT valence band moved to higher energy band values. The higher VB of

RT resulted in a higher Fermi band energy for the PANI-RT composite, but this did not alter the direction of electron transfer. Therefore, it was predicted that electron transfer would occur from the CB of the PANI-RT composite to the electrolyte upon the absorption of a photon, i.e. a photocathodic response.

8.3.2 Photoresponse of PANI-RT composite electrode

In Section 3.4 it was reported that the RT-Hg complex had an absorbance at 523 nm and an emission at 552 nm, indicating only a 5 nm difference when compared to RS-Hg²⁺. The RT chemosensor in solution alone is, however, considerably more stable than RS, with far less ring-opened tautomer.

The photoresponses of PANI-RT coated on ITO in Hg²⁺ were photocathodic and similar to those of the PANI-RS composite electrodes. The photoresponses of the RT composite electrode towards Hg²⁺ are shown in Figure 8.5.

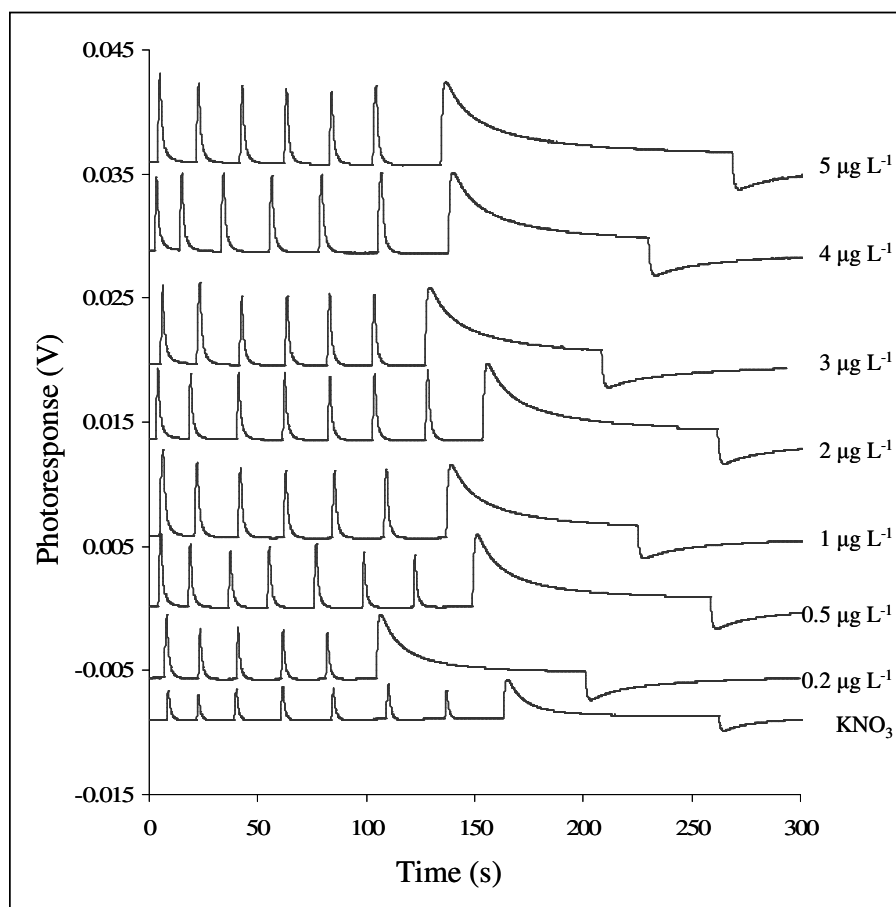


Figure 8.5: Photovoltammetric responses of ITO coated with the PANI-RT composite electrode in 0.05 M KNO₃ and 0.2 to 5 µg L⁻¹ Hg²⁺.

The PANI-RT photoresponses towards Hg^{2+} increased linearly from $0.2 \mu\text{g L}^{-1}$ to $5 \mu\text{g L}^{-1}$, after which the surface was saturated and the response remained relatively constant. Due to interaction between the PANI and the RT molecules, more RT molecules were ring-opened on the electrode surface, thereby causing a higher background response.

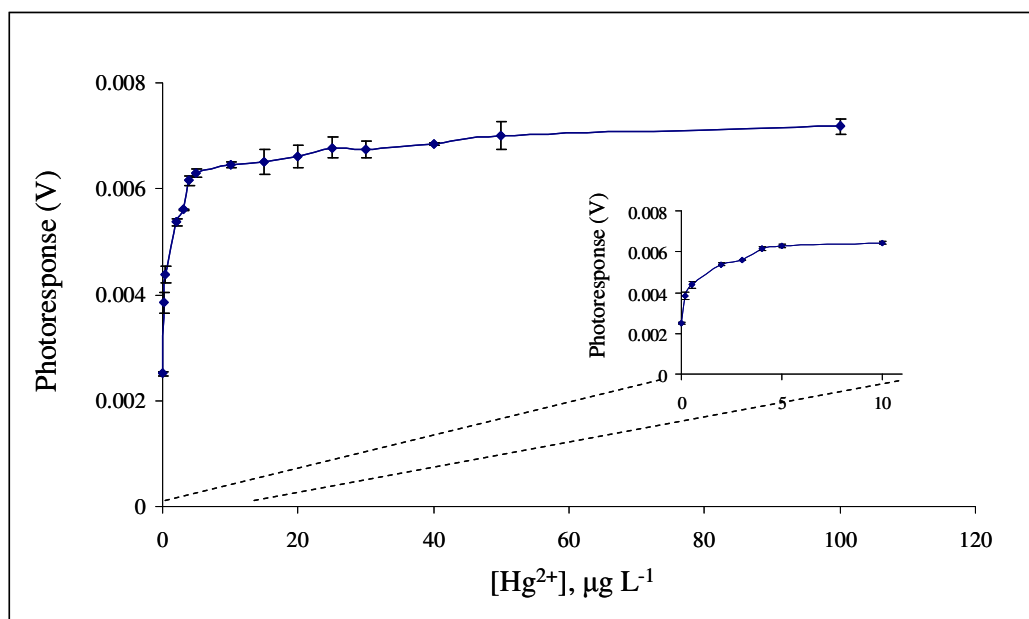


Figure 8.6: The photoresponses of ITO coated with a PANI-RT composite.

The PANI-RT composite electrode's photoresponse was measured in 0.005 M phosphate buffer at various pHs. Figure 8.7 shows no trend in the response of the composite electrode at increasing pH.

The photoresponse of the PANI-RT composite electrode towards Hg^{2+} at increasing pH also seemed quite stable, except at $\text{pH} > 7.5$. The decrease in photoresponse at higher pH is most likely due to a decreased amount of ring-opened RT spirolactam. The photoresponse of the PANI-RT composite seemed independent of the conductivity of PANI, which was prevalent at lower pH. The photoresponse of the PANI-RT composite on ITO/ TiO_2 did not have a qualitative or quantitative response towards Hg^{2+} in aqueous solutions.

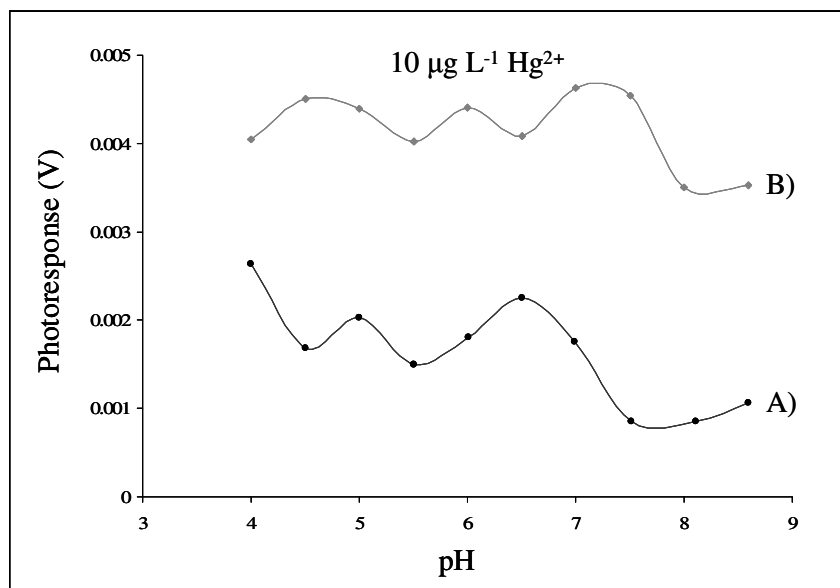


Figure 8.7: The photoresponses of PANI-RT on ITO measured at various pHs in 0.005 M phosphate buffer in A) the absence of Hg²⁺ and B) in 10 µg L⁻¹ Hg²⁺.

Although the energy diagram predicted photoanodic behaviour for the composite ITO/TiO₂, electron transfer due to ring opening of a Hg²⁺ ligated chemosensor was not observed. It can be assumed that electron injection did not occur for one or more of the following reasons:

- Repulsion between the TiO₂ surface groups and sulphur on the RT binding unit
- No orbital overlap of the TiO₂ and the RT binding unit
- The arrangement of the RT molecules on the TiO₂ surface.

The selectivity of the PANI-RT coated ITO electrode was tested with 1 mg L⁻¹ of background cations. Figure 8.8 shows that the immobilised RT had reduced selectivity towards Hg²⁺ when compared to the RT chemosensor alone. However, the coated electrode reached a maximum photoresponse when immersed in the aqueous solutions that contained the background ions, with the exception of 1 mg L⁻¹ Ag⁺. The PANI-RT photoresponse towards Hg²⁺ reached an electrode to electrode maximum value of 2 to 3.5 mV. Although the maximum of each electrode was established in 10 µg L⁻¹ Hg²⁺, quantitative analysis in the presence of background ions was not possible. The high photoresponse of Ag⁺ is due to strong thiophilicity of Ag⁺ [1, 3] and the affinity of Ag⁺ for rhodamine compounds. The effect of Ag⁺ is much higher

with the immobilised chemosensor, which could be due to delocalization in the ionophore, thereby making the thiolactone more susceptible to nucleophilic attack.

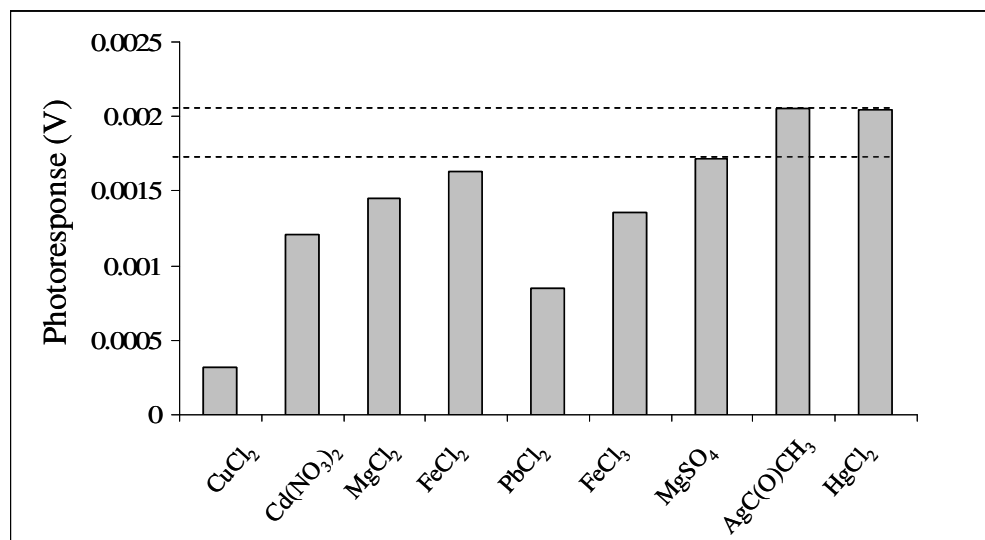


Figure 8.8: The photoresponse of ITO/PANI-RT in 1 mg L⁻¹ background ions, and 10 µg L⁻¹ Hg²⁺.

8.3.3 Photoelectrochemical evaluation of RT copolymer composites

ITO was coated with composites of P[A-co-2-BrA] copolymers that contained increasing amounts of 2-bromoaniline monomer in the synthesis stock. The P[A-co-2-BrA] copolymers were dried onto the ITO electrode surface in composite with RT and the photoresponses were compared to those of PANI-RT in Hg²⁺. The photoresponses were measured for increasing amount of Hg²⁺ in 0.05 M KNO₃. The results are shown (and compared) in Figure 8.9 A.

As with P[A-co-2-BrA] 50 and 70 composites with RS, the photoresponse was unaffected by the presence of Hg²⁺. P[A-co-2-BrA] containing 10% 2-bromoaniline monomer had the highest response to Hg²⁺ over a wide range, from 0.2 µg L⁻¹ to 30 µg L⁻¹ Hg²⁺. The photoresponse of the various polymers in 0.05 M KNO₃ and towards 10 µg L⁻¹ Hg²⁺ are shown in Figure 8.9 B

The photoresponse of the P[A-co-2-BrA] 10-RT composite is 10-fold lower than that of PANI-RT, but had the highest ratio increase of background response in electrolyte to Hg²⁺. The photoresponse of PANI-RT towards 10 µg L⁻¹ Hg²⁺ increased 2.5 fold

from baseline response in electrolyte alone, when compared to that of P[A-co-2-BrA] 10-RT, which increased 15-fold.

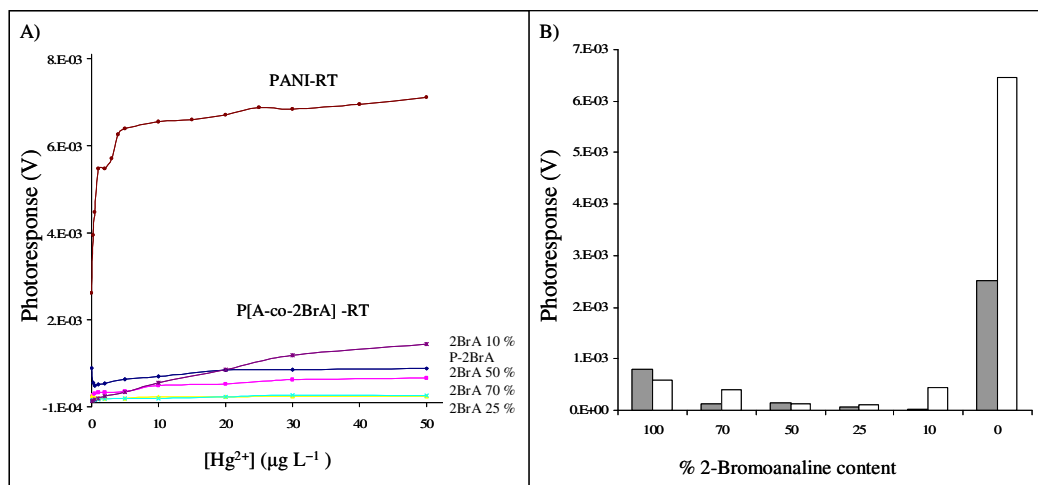


Figure 8.9: The A) photoresponses of the P[A-co-2-BrA] copolymers in 0.05 M KNO₃ and increasing Hg²⁺ concentration [Hg²⁺]. B) The photoresponse of the P[A-co-2-BrA] copolymers towards 10 µg L⁻¹ Hg²⁺.

8.4 Conclusions

The PANI-RT composite ITO electrode had a photocathodic response that was similar to that of PANI-RS. Although the photoresponse of ITO coated with PANI-RT was higher than that of PANI-RS, the PANI-RT electrodes had a higher background response in solution. Hence, the PANI-RT electrodes can only be used for the qualitative determination of Hg²⁺ in the presence of other background ions. Although P[A-co-2-BrA] 10-RT showed a photoresponse to Hg²⁺ over a wide linear range, with a low detection limit (0.2 µg L⁻¹), the voltage measurements were in the micro-volt region which has greater perturbations due to the presence of background ions.

8.5. References

- [1] X. Chen, S.W. Nam, M.J. Jou, Y. Kim, S.J. Kim, S. Park, J. Yoon, *Org. Lett.*, 10 (2008) 5235-5238.
- [2] B. Liu, H. Tian, *Chem. Commun.* (2005) 3156-3158.

- [3] W. Shi, H. Ma, Chem. Commun. (2008) 1856-1858.
- [4] X.Q. Zhan, Z.H. Qian, H. Zheng, B.Y. Su, Z. Lan, J.G. Xu, Chem. Commun. (Camb) (2008) 1859-1861.
- [5] M. Asha Jhonsi, A. Kathiravan, R. Renganathan, J. Mol. Struct., 921 (2009) 279-284.
- [6] A. Kathiravan, V. Anbazhagan, M.A. Jhonsi, R. Renganathan, Z. Phys. Chem., 221 (2007) 941-948.
- [7] T.A. Heimer, S.T. D'Arcangelis, F. Farzad, J.M. Stipkala, G.J. Meyer, Inorg. Chem., 35 (1996) 5319-5324.
- [8] J. Rochford, D. Chu, A. Hagfeldt, E. Galoppini, J. Am. Chem. Soc., 129 (2007) 4655-4665.
- [9] M.T. Spitler, B.A. Parkinson, Acc. Chem. Res., 42 (2009) 2017-2029.
- [10] T. Vossmeier, A. Yasuda, R.E. Bauer, K. Mullen, Chemical sensors from nanoparticle/dendrimer composite materials, 10/197,905 (2002) 1-15.
- [11] M. Mazur, P. Krysinski, Thin Solid Films, 396 (2001) 131-137.
- [12] M. Mazur, P. Predeep, Polymer, 46 (2005) 1724-1730.
- [13] D.W. Wu, W. Huang, C. Duan, Z. Lin, Q. Meng, Inorg. Chem., 46 (2007) 1538-1540.

Chapter 9

Prototype photoelectrochemical mercury detector

9.1 Introduction

Current techniques for sensitive and accurate inorganic mercury (Hg^{2+}) determination are immobile, require trained operators and the sophisticated instrumentation is expensive to use and maintain. The photoelectrochemical evaluation of Hg^{2+} offers a method for on-site Hg^{2+} screening, as well as a quantitative analysis after sample preparation.

In this chapter a prototype for a small portable instrument that is capable of Hg^{2+} determination is designed, constructed and tested. The prototype is representative of the design of a photoelectrochemical mercury detector (PEMD). The working electrodes were coated with the Hg^{2+} -selective chemosensors and charge separators and were positioned into a unit cell that included a counter electrode that closes the circuit. The prototype is designed to read a photoresponse of the closed circuit in the presence and absence of Hg^{2+} , under illumination pulses.

9.2 Materials and methods

9.2.1 Materials

Indium tin oxide (ITO) glass plates that had a surface resistivity ranging between 8 and $12 \Omega \text{ sq}^{-1}$ were purchased from Aldrich, South Africa. All chemicals and organic solvents used were of analytical reagent grade and were obtained from Sigma-Aldrich, South Africa. All aqueous solutions were prepared with ultrapure water that was deionised using a Milli-Q RG purification system. The unit cells used in the PEMD were $12.5 \times 12.5 \times 45$ mm polymethylmethacrylate (PMMA) disposable cuvettes, Plastibrand. A digital panel meter LCD-GB701 voltmeter, with a display range between -200 and 200 mV was used. The voltmeter had a four-digit display, set with an amplifier to measure -200 to 200 μV . The Hg^{2+} selective sensor, rhodamine 6G hydrazone derivative (RS) and rhodamine 6G thiolactone derivative (RT) were synthesised according to the procedures described in Chapter 3.

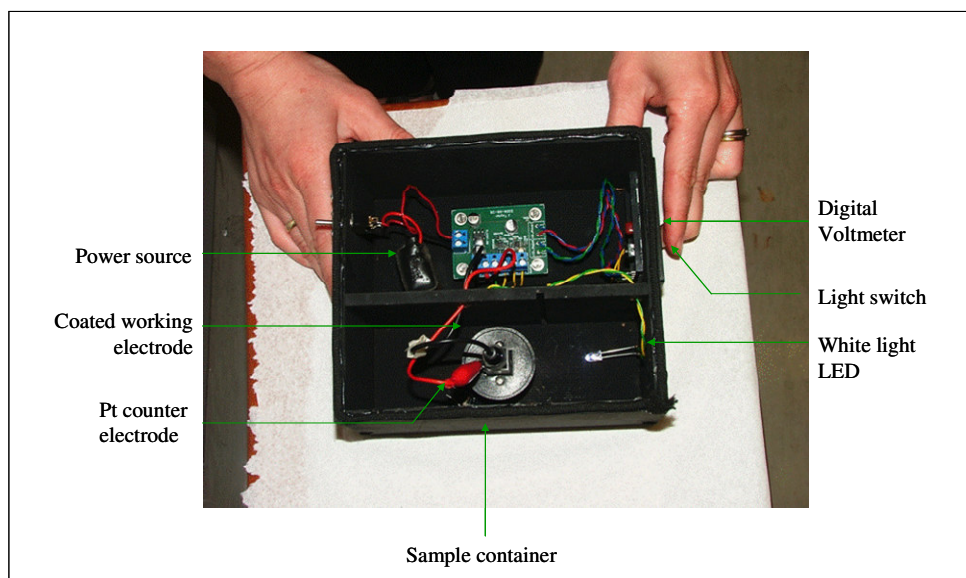


Figure 9.2: The PEMD prototype.

9.2.3 Electrode evaluation with the PEMD

The electrodes used in the evaluation were ITO coated with a) PANI-RS, b) PANI-RT and c) $\text{TiO}_2/\text{PANI-RS}$. The electrodes were coated according to the procedures described in Sections 6.2, 7.2 and 8.2. The unit cells were $12.5 \times 12.5 \times 45$ mm disposable cuvettes containing 2 mL 0.05 M KNO_3 electrolyte and increasing concentrations of Hg^{2+} prepared from HgCl_2 in deionised water. A Pt wire was used as counter electrode.

9.2.4 Sample collection and preparation

Water samples ($n = 3$) were collected from different sampling locations along the Eerste River in Kuilsriver ($33^\circ 57' 12''\text{S}$; $18^\circ 39' 52.0''\text{E}$) in the Western Cape, RSA. The water samples were scooped into HCl cleaned glass bottles, transported to the laboratory at the University of Stellenbosch where it was frozen at -12°C for 7 days. All samples were thawed, filtered and heated at 70°C for 30 min, after which it was filtered again. The conductivity of the water samples was modified by the addition of 20 mg of KNO_3 to 20 mL of sample (0.01 M KNO_3). The Hg^{2+} concentrations of the environmental samples were determined with a Milestone DMA-80 direct mercury analyzer (DMA).

9.3 Results and Discussion

9.3.1 Electrode evaluation of PANI-RS and PANI-RT in the prototype PEMD

The photoresponses of ITO coated with PANI-RS and PANI-RT were determined using the PEMD for increasing Hg^{2+} concentrations. The photoresponses of the electrodes are tabulated in Table 9.1 and 9.2.

Table 9.1: Voltage responses of the PANI-RS coated ITO electrodes towards Hg^{2+} exposure in the custom PEMD prototype

Sample	PANI-RS		
	E1 (100 μV)	E2 (100 μV)	E3 (100 μV)
0.05 M KNO_3	0.7	0.9	0.5
0.2 $\mu\text{g L}^{-1}$	0.8	1	0.9
2 $\mu\text{g L}^{-1}$	1.2	1.2	1.2
10 $\mu\text{g L}^{-1}$	1.0	1.0	1.0

Table 9.2: Voltage responses of the PANI-RT coated ITO electrodes towards Hg^{2+} exposure in the custom PEMD prototype

Sample	PANI-RT		
	E1 (100 μV)	E2 (100 μV)	E3 (100 μV)
0.05 M KNO_3	1	0.8	0.8
0.2 $\mu\text{g L}^{-1}$	2	1.1	1.4
2 $\mu\text{g L}^{-1}$	1.5	1.6	1.7
10 $\mu\text{g L}^{-1}$	1.5	1.4	1.6

The responses of the coated electrodes in the absence of Hg^{2+} were less than 100 μV , and were due to the immobilised ring-opened RS and RT molecules. The photovoltage increased upon exposure to 200 ng L^{-1} Hg^{2+} , and yielded responses that did not increase linearly with increasing Hg^{2+} concentration. For most of the electrodes evaluated the maximum response was reached at 2 $\mu\text{g L}^{-1}$ Hg^{2+} , after which

the response decreased. The maximum response was determined by the available surface area of the coated electrode to the electrolyte containing Hg^{2+} . Overall, the photoresponses of PANI-RT were higher than the PANI-RS in 0.05 M KNO_3 alone, which corresponds to evaluations as discussed in Sections 6.3.4 and 8.3.2 for the PANI electrodes without Hg^{2+} . The photoresponses towards Hg^{2+} were higher for PANI-RT than PANI-RS. The preliminary measurements using the prototype PEMD, in association with the PANI chemosensor composites on ITO, indicated that the PEMD is suitable for the screening of Hg^{2+} in aqueous samples.

The photovoltage responses for ITO/ TiO_2 coated electrodes could not be determined with the PEMD. This was mainly due to the responses to Hg^{2+} being higher than 1 mV, which was higher than the resolution of the voltmeter. The photovoltage of ITO/ TiO_2 coated with PANI-RS measured 150 μV in 0.05M KNO_3 , in the absence of Hg^{2+} . There was a significant increase in the photoresponse for the TiO_2 /PANI-RS electrode towards Hg^{2+} , i.e. 0.15 V to 1 mV. From these initial evaluations, it is evident that the TiO_2 /PANI-RS electrode could be used as a Hg^{2+} indicator for concentrations higher than 200 ng L^{-1} .

9.3.2 Evaluation of environmental samples

Water samples ($n = 3$) collected from the Eerste River were evaluated for Hg^{2+} . The environmental parameters measured at the sampling locations included temperature (19.8 $^\circ\text{C}$), as well as, pH and conductivity which are presented in Table 9.3.

Table 9.3: The pH and conductivity values for the collected environmental samples

	pH	Conductivity ($\mu\text{S.cm}^{-1}$)	pH 0.01 M KNO_3	Conductivity (mS cm^{-1}) 0.01 M KNO_3
Sample 1	7.70	459	7.83	2.12
Sample 2	8.10	677	8.09	2.02
Sample 3	7.75	323	7.96	2.62

The photovoltage results as well as the estimated Hg^{2+} results obtained for the samples with the PEMD prototype are presented in Table 9.4 and were compared to the measurements obtained by DMA analysis.

Table 9.4: The photovoltage responses of the PANI-RS and PANI-RT electrodes in the PEMD toward environmental samples compared to the Hg^{2+} concentrations determined by DMA

	Photovoltage (100 μV)		$[\text{Hg}^{2+}]$, $\mu\text{g L}^{-1}$	
	PANI-RS	PANI-RT	Prototype	DMA
Sample 1	0.8	1.1	> 0.2	4.04
Sample 2	1	1.1	> 0.2	4.01
Sample 3	0.8	1	> 0.2	5.71

The prototype photovoltage responses towards Hg^{2+} in the environmental samples were lower compared to the expected values for the electrodes in the reference samples. The Hg^{2+} values measured by DMA include inorganic as well as organic Hg, whereas the PEMD would exclusively complex with Hg^{2+} . The concentration of Hg^{2+} in environmental water samples range between 0.7 to 52% of the total Hg content, depending on the water source (i.e. wetland, estuary etc) [1-3]. The observed PEMD photovoltage value was lower due to a combination of the following:

- The exclusion of particulate and organic Hg in the measurements of the PEMD prototype.
- The pH values for the environmental samples (ca pH 8) were slightly higher than those of the reference samples (pH 7.5).
- The sample matrix contained inorganic and organic molecules which could quench the photoresponse of the coated electrodes in the PEMD.
- The matrix of the sample influenced the translucency of the sample for UV and visible light.
- The influence of oxygen content and micro organisms on the photovoltage response of the PEMD was not previously evaluated and may have an unaccounted affect on the PEMD response towards Hg^{2+} in environmental samples.

As seen with the reference samples, the photoresponse of the PANI-RT electrode was higher when compared to that of PANI-RS. An additional $2 \mu\text{g L}^{-1} \text{Hg}^{2+}$ was added to the environmental samples to determine if the photovoltage was Hg^{2+} selective and

whether the electrode surface had been saturated. The photovoltage results for the spiked samples are presented in Table 9.5.

Table 9.5: The photovoltage responses of the PANI-RS and PANI-RT electrodes in the PEMD toward environmental samples with $2 \mu\text{g L}^{-1}$ additional Hg^{2+} compared to the Hg^{2+} concentrations determined with DMA

	Photovoltage (100 μV)		$[\text{Hg}^{2+}]$, $\mu\text{g L}^{-1}$	
	PANI-RS	PANI-RT	Prototype	DMA
Sample 1	1.2	1.4	> 2	6.09
Sample 2	1.1	1.2	> 2	6.62
Sample 3	1.1	1.1	> 2	7.78

The photoresponses for the PANI-RT and PANI-RS electrodes in the PEMD increased with the addition of $2 \mu\text{g L}^{-1}$. The electrode surfaces were therefore not fouled during the initial evaluation of the environmental samples. The increases in photoresponse were not the same for each of the electrodes, and were most likely influenced by the unique matrix of each sample. Although the environmental analysis indicated many challenges in the quantitative determination of Hg^{2+} , the prototype provides an inexpensive, on-site method for prescreening of Hg^{2+} in aqueous solutions.

9.4 Conclusion

The photoresponses of PANI-RS and PANI-RT coated electrodes used in the PEMD were used to detect Hg^{2+} at concentrations up to $2 \mu\text{g L}^{-1}$. As the photoresponses were not linear with increasing Hg^{2+} concentration, no quantitative analysis could be undertaken using the PANI composite electrodes. ITO/ TiO_2 coated with the PANI-RS composite had a significant photovoltage response towards Hg^{2+} , but the response could not be quantified due to limitations in the sensitivity of the instrument.

The prototype was capable of Hg^{2+} screening only, due to the following limitations:

- High background responses in the absence of Hg^{2+}
- Limited electrode to electrolyte contact
- Quick electrode surface saturation after exposure to $2 \mu\text{g L}^{-1}$ Hg^{2+}
- Low sensitivity and the limited range of the voltmeter.

The electrode to electrode photovoltage responses measured within 0.1 mV of each other, thereby suggesting that the responses were reasonably reproducible. Water samples collected in the Eerste River (Western Cape, South Africa) were measured using the prototype PEMD and the results were compared to measurements made using the DMA. From the initial results obtained from the PEMD, it is evident that the PEMD prototype provides a robust method for trial prescreening of aqueous Hg^{2+} .

9.5 References

- [1] K. Kannan, R.G. Smith Jr, R.F. Lee, H.L. Windom, P.T. Heitmuller, J.M. Macauley, J.K. Summers, Arch. Environ. Contam. Toxicol., 34 (1998) 109-118.
- [2] N.M. Lawson, R.P. Mason, Water Res., 35 (2001) 4039-4052.
- [3] N.M. Lawson, R.P. Mason, J. Laporte, Water Res., 35 (2001) 501-515.

Chapter 10

Conclusions and recommendations for future work

10.1 Conclusions

An alternative method for inorganic mercury (Hg^{2+}) determination in aqueous solutions was developed and evaluated. This involved the detection of Hg^{2+} by using a fluorescent chemosensor, charge separation of the excited photons, and the measurement of the resulting electron current.

10.1.1 The selection, synthesis and characterization of the chemosensor

Two rhodamine 6G derivative chemosensors were selected for use in the photoelectrochemical evaluation of Hg^{2+} . The first chemosensor contained a carbohydrazone ionophore and spirolactam ring, a rhodamine 6G hydrazone derivative (RS), which opened to release the xanthene chromophore in the presence of Hg^{2+} . The second chemosensor contained a thiolactone function ring, rhodamine 6G thiolactone derivative (RT), which also opened to bind Hg^{2+} from solution. The chemosensors were synthesised according to established procedures and characterised by ^{13}C and ^1H NMR, UV absorbance, fluorescence and mass spectrometry. The chemosensors were also evaluated in their complexed form with Hg^{2+} .

10.1.2 Electrochemical evaluation of polyaniline and substituted polyaniline copolymers

The photoresponse of the photoelectrochemical detection method relies on the effective charge separation by the n- and p-type semiconductors. Polyaniline (PANI), which is a well documented conductive polymer, and copolymers of PANI and 2-bromo substituted copolymers (P[A-co-2-BrA]s) were immobilised on indium tin oxide (ITO) and were electrochemically evaluated to establish their suitability as charge separators. The electrodes were evaluated in terms of their energy band gaps, surface morphology, half peak potential ($E_{1/2}$), peak separation (ΔE), diffusion coefficients and charge transfer coefficients. The electrodes were evaluated at pH 3.5 and pH 7.5.

The energy band-gaps of the copolymers decreased with increasing 2-bromoaniline content. The electrochemical capabilities of PANI and P[A-co-2-BrA]s were increased at lower pH, which is consistent with the known characteristics and pH dependence of PANI. At pH 7.5 the electrochemical properties of P[A-co-2-BrA]s were less influenced by the PANI content, and their electrochemical properties averaged those of semi-conductors.

The ITO plates were coated with TiO₂, baked to anatase structure, and then coated with PANI and the P[A-co-oBrA]s. Thereafter, the electrodes were subjected to electrochemical evaluation. The electrochemical capabilities were slightly favoured at pH 7.5, and were dependent on the 2-bromoaniline content at pH 3.5. The repulsion between the negative charge on PANI and the electronegative species in solution combined with the protonation of the T=O surface at lower pH caused delays in the electron transfer leading to quasi-reversible electron transfer processes.

Electrochemical evaluations indicated that PANI and P[A-co-2-BrA] 10 and 25 have favourable electrochemical properties, which assist in the charge separation in the photoelectrochemical cell (PEC).

10.1.3 Photoelectrochemical evaluation of ITO coated with PANI and P[A-co-2-BrA] copolymers in composite with RS

The PANI-RS composite was deposited onto the ITO surface that was characterised and photoelectrochemically evaluated. After characterization with cyclic voltammetry (CV) and UV absorbance an energy diagram was proposed, in which the PANI-RS electrode would behave as a photo-cathode in a PEC. During the photoelectrochemical evaluation the PANI-RS composite electrode had a linear photocathodic response towards Hg²⁺ in water over the range 10 to 150 µg L⁻¹, with a detection limit of 6 µg L⁻¹. The photoresponses of PANI-RS were pH independent in the pH range 6-9, and had a three fold response towards Hg²⁺ compared to other background cations.

The P[A-co-2-BrA]s were also coated onto the ITO surface in composite with RS. The photoresponses of the electrodes were determined by the PANI content of the copolymers. P[A-co-2-BrA] 50 and 70 were not influenced by the amount of Hg²⁺,

but P[A-co-2-BrA] 10 and 25 showed a linear response towards Hg^{2+} in the range 0.2 to $5 \mu\text{g L}^{-1}$, and had a lower background response compared to that of PANI-RS. The photoresponse of PANI-RS was, however, more than 10-fold greater than that of the copolymers.

10.1.4 Photoelectrochemical evaluation of ITO/TiO₂ coated with PANI and P[A-co-2-BrA] copolymers in composite with RS

The polymer-RS composites were coated onto the ITO/TiO₂ surfaces and were photoelectrochemically determined. The proposed energy diagram suggested that the ITO/TiO₂ coated with PANI-RS would behave as photo-anode in a PEC containing Hg^{2+} . The photoanodic response of the PANI-RS composite on ITO/TiO₂ was linear towards Hg^{2+} in the range 10 to $200 \mu\text{g L}^{-1}$, with a limit of detection of $\mu\text{g L}^{-1}$. The pH range was, however, limited to pH 6 - 7 due to the protonation of the Ti=O groups.

The influence of phosphate on the detection of Hg^{2+} was also determined. The phosphate groups were found to be linked to the TiO₂ surface hydroxyl groups. Upon the addition of RS the spirolactam ring opened and the fluorescent xanthene was released. In the presence of Hg^{2+} a second absorption peak was observed as well as a decrease in the fluorescence of the aqueous solutions. The addition of Hg^{2+} to phosphate modified TiO₂ and RS caused dimerization of the RS chemosensor. The dimerization was Hg^{2+} selective and provided another method for Hg^{2+} screening.

ITO/TiO₂ coated with the P[A-co-2-BrA]s produced photocathodic responses, which indicated that electron transfer occurred from the composite to the electrolyte. The photoresponses of the higher 2-bromoaniline content copolymers (P[A-co-2-BrA] 50 and 70) were uninfluenced by the Hg^{2+} content, whereas P[A-co-2-BrA] 10 had a linear response to Hg^{2+} at an LOD of $0.2 \mu\text{g L}^{-1}$. P[A-co-2-BrA] 10 had a lower background response when compared to ITO/TiO₂ coated with PANI-RS, whereas PANI-RS had a 100-fold higher voltage response.

10.1.5 Photoelectrochemical evaluation of ITO coated with PANI and P[A-co-2-BrA] copolymers in composite with RT

Composites of PANI and the P[A-co-2-BrA]s and RT were coated onto ITO, after which the coated electrodes were characterised and photoelectrochemically evaluated.

The RT composite electrodes showed higher photoresponses when compared to the photoresponses observed for RS. However, the PANI-RT and P[A-co-2-BrA]s showed significant background responses in the absence of Hg^{2+} . The PANI-RT composite electrode showed a linear photocathodic response towards Hg^{2+} in the range 0.2 to 5 $\mu\text{g L}^{-1}$ after which the electrode surface was saturated. The photoresponse was less pH dependent when compared to RS, while the immobilised RT chemosensor was more vulnerable to nucleophilic attack by other interfering background ions. RS in composite with PANI is preferred, as opposed to the RT composite in the PEC, for measuring natural water samples containing Hg.

PANI-RT was coated onto TiO_2 but the coated electrode showed no response towards the presence of Hg^{2+} . No orbital or chemical overlap occurred between the chemosensor and the TiO_2 layer, and TiO_2 could not assist in the charge separation process.

A similar trend was observed for P[A-co-2-BrA]s-RT composites, as opposed to P[A-co-2-BrA]s-RS. The photoresponses of P[A-co-2-BrA] 50 and 70 were not influenced by Hg^{2+} , and the responses of P[A-co-2-BrA] 10 and 25 increased from 0.2 to 5 $\mu\text{g L}^{-1}$. The background responses were lower for the copolymers than for PANI, with P[A-co-2-BrA] 10 showing a 15-fold increase from the background response to 10 $\mu\text{g L}^{-1}$ Hg^{2+} .

The photoresponses for all the coated electrodes were strongly surface dependent; roughness, surface coverage and double layer effects demonstrated the greatest photometric influences.

10.1.6 The prototype photoelectrochemical mercury detector

A prototype photoelectrochemical mercury detector (PEMD) was designed, built and tested. The design was simple and used the electrodes that were coated with PANI-RS, PANI-RT and TiO_2 , followed by PANI-RS. The PANI composite electrodes showed high background responses, but were sensitive up to 2 $\mu\text{g L}^{-1}$ Hg^{2+} , after which the electrode surfaces were saturated. Quantitative analysis of Hg^{2+} with the PEMD prototype could not be performed, but the prototype PEMD could be used to pre-screen Hg^{2+} in aqueous environmental samples.

10.2 Scientific contribution

A novel yet simple method for Hg^{2+} detection was developed. The fluorescent chemosensors were combined with photoelectrochemical technology to produce electrodes that are capable of selective Hg^{2+} determination. P[A-co-2-ABr]s, which are easier to dissolve and process than PANI, were electrochemically and photoelectrochemically evaluated. Although this study showed that PANI had superior charge separation and conductive properties to P[A-co-2-ABr]s, P[A-co-2-BrA] 10 and 25 had semiconductive properties and sufficient electron donating abilities for use in PECs. The photoanodic and photocathodic behaviours of the coated electrodes were determined as well as the Hg^{2+} concentration ranges in which Hg^{2+} can be determined.

The photoelectrochemical responses of all the electrodes were highly surface and pH dependent. The electron accepting nature of TiO_2 could only be used when the chemosensor contained carbonyl or amine groups in which orbital overlap or positive interaction occurs.

10.3 Recommendations for future work

The efficiency of the photoelectrochemical detection relies on many variables including;

- The efficiency of the charge separators
- Interaction between the charge separators and the chemosensor and
- Selectivity, sensitivity, pH dependence and fluorescent intensity of the chemosensor.

Any of the above-mentioned variables could be modified to improve the selectivity and sensitivity of the photovoltammetric response of the coated electrodes.

Investigations of different modes of immobilization of the chemosensor on the electrode surface would be a major consideration for future work. Chemisorption of the chemosensor onto the n-type semiconductor would result in an improvement of the electron transfer capabilities of the PEC. Results of the phosphate modified TiO_2 evaluation with RS indicated that linking of the sensor would significantly improve the selectivity of the photoresponse and reduce the background response in the absence of Hg^{2+} .

In the prototype PEMD, the efficiency could also be improved by inserting a voltmeter that has a higher sensitivity as well as a more intense light source.